INFORMATION TO USERS

This manuscript has been reproduced from the microfilm master. UMI films the text directly from the original or copy submitted. Thus, some thesis and dissertation copies are in typewriter face, while others may be from any type of computer printer.

The quality of this reproduction is dependent upon the quality of the copy submitted. Broken or indistinct print, colored or poor quality illustrations and photographs, print bleedthrough, substandard margins, and improper alignment can adversely affect reproduction.

In the unlikely event that the author did not send UMI a complete manuscript and there are missing pages, these will be noted. Also, if unauthorized copyright material had to be removed, a note will indicate the deletion.

Oversize materials (e.g., maps, drawings, charts) are reproduced by sectioning the original, beginning at the upper left-hand corner and continuing from left to right in equal sections with small overlaps. Each original is also photographed in one exposure and is included in reduced form at the back of the book.

Photographs included in the original manuscript have been reproduced xerographically in this copy. Higher quality 6" x 9" black and white photographic prints are available for any photographs or illustrations appearing in this copy for an additional charge. Contact UMI directly to order.

UMI®

Bell & Howell Information and Learning
300 North Zeeb Road, Ann Arbor, MI 48106-1346 USA
800-521-0600

CHARACTERIZATION AND OPTIMIZATION OF THE MAGNETRON DIRECTIONAL AMPLIFIER

A

THESIS

Presented to the Faculty

of the University of Alaska Fairbanks

for the Degree of

DOCTOR OF PHILOSOPHY

By

Michael Craig Hatfield, M.S.E.E.

Fairbanks, Alaska

August 1999

CHARACTERIZATION AND OPTIMIZATION OF THE MAGNETRON DIRECTIONAL AMPLIFIER

By

Michael Craig Hatfield

RECOMMENDED:

Advisory Committee Chair

Department Head

APPROVED:

Dean, College of Science, Engineering & Mathematics

Dean of the Graduate School

7-12-99

Date

Abstract

Many applications of microwave wireless power transmission (WPT) are dependent upon a high-powered electronically-steerable phased array composed of many radiating modules. The phase output from the high-gain amplifier in each module must be accurately controlled if the beam is to be properly steered. A highly reliable, rugged, and inexpensive design is essential for making WPT applications practical.

A conventional microwave oven magnetron may be combined with a ferrite circulator and other external circuitry to create such a system. By converting it into a two-port amplifier, the magnetron is capable of delivering at least 30 dB of power gain while remaining phase-locked to the input signal over a wide frequency range. The use of the magnetron in this manner is referred to as a MDA (Magnetron Directional Amplifier). The MDA may be integrated with an inexpensive slotted waveguide array (SWA) antenna to form the Electronically-Steerable Phased Array Module (ESPAM). The ESPAM provides a building block approach to creating phased arrays for WPT. The size and shape of the phased array may be tailored to satisfy a diverse range of applications.

This study provided an in depth examination into the capabilities of the MDA/ESPAM. The basic behavior of the MDA was already understood, as well as its potential applicability to WPT. The primary objective of this effort was to quantify how well the MDA could perform in this capacity. Subordinate tasks included characterizing the MDA behavior in terms of its system inputs, optimizing its performance, performing sensitivity analyses, and identifying operating limitations. A secondary portion of this study examined the suitability of the ESPAM in satisfying system requirements for the solar power satellite (SPS). Supporting tasks included an analysis of SPS requirements, modeling of the SWA antenna, and the demonstration of a simplified phased array constructed of ESPAM elements.

The MDA/ESPAM is well suited for use as an amplifier or an element in a WPT phased array, providing over 75% efficiency and a fractional bandwidth exceeding 1.7% at 2.45 GHz. The results of this effort provide the WPT design engineer with tools to predict the MDA's optimum performance and limitations.

Table of Contents.

List of Figures.

List of Tables.

List of Appendices.

Acknowledgments

I would like to express my sincere thanks to the late Bill Brown for all of his help. He made immeasurable contributions to the field of wireless power transmission and in magnetrons, in general. He provided us with the hardware, technical support and advice to get our program (and my research) off to a solid start. I particularly want to give thanks for Bill's genuine concern for his fellow man. His life work demonstrated a sense of responsibility to all, even those he would never know. Bill was a good man and will be deeply missed.

I would like to thank Gene Eves of Ferrite Components, Inc. for his help with the project. Gene's hardware support made this project possible. His advice and support made it interesting and fun.

Thank you to my committee members at UAF: Joe Hawkins, Charlie Mayer, John Olson, and Vikas Sonawalkar. Their guidance and support was crucial in accomplishing this task. I would particularly like to convey my gratitude to Joe Hawkins for his outstanding mentoring. His own work ethic and his patience with others energized my motivation for the project. His clear insight and determination ensured the effort stayed on track.

A special thanks to a few individuals at UAF that supported this effort out of professional courtesy and the kindness of their hearts: Joann Neumaier, Darlette Powell, Bob Merritt and Steve Stevens. I owe a very large debt of gratitude to each of these for their help and friendship. Better people simply cannot be found.

Thanks to those folks that prepared the UAF Beam Steering Demonstration and stood out in the weather with me for two days. Participants included UAF graduate students

Shawn Houston and Joann Neumaier. Assisting were Mimi Houston (Shawn's wife) and Darlene Hatfield (my wife). Also, thanks to the UTEP summer students for helping out.

Finally, I would like to thank the most competent and giving person I have ever known, my wife Darlene. I can never repay you for all you've done and all you are. ♥

1.0 Introduction

1.1 Background

Ultimately, man's ever-increasing need for energy will outpace our planet's ability to produce it. In the case of fossil fuels, either the energy source itself will become depleted, or the processing of the energy into a usable form will pollute our environment past its healing capacity. Some studies project the depletion of known oil reserves within 65 years and the natural gas reserves within 120 years. Coal deposits are likely to last until the year 2225. However, this energy source poses a serious threat to our ecological system. Current renewable sources such as wind, geothermal, and tidal energy may ease energy requirements in some areas, but will do little to solve large-scale urban energy requirements. Nuclear fusion holds promise, but to date has not proven to be a viable alternative. Even nuclear fission reactors have shown limited ability to meet our power needs, with environmental contamination in processing fuel and waste a concern [1].

Another energy alternative is needed to meet our long-term demands — one that can be obtained economically, safely, and abundantly. One proposed energy system is the solar power satellite (SPS). In this system, the earth is encircled by a number of satellites in geostationary orbit or low earth orbit, depending upon the proposed design. The satellites use photovoltaic (PV) cells to convert sunlight to DC electricity. This is then converted to radio frequency (RF) energy and beamed to earth via a high-gain directional antenna. The RF energy is reconverted to electricity and used to feed power grids, or to power fuel cells through the electrolysis of water into hydrogen and oxygen [2].

Obviously, a system capable of satisfying the electrical requirements for a large urban area would be of enormous proportion. To design a system to meet the energy needs of the world is almost unimaginable. It would easily surpass our largest space endeavors to date (and most ground-based achievements, as well), requiring a vast logistical structure

to implement and operate. The SPS is not without significant technical hurdles as well, such as (1) the means to get the structures or materials to orbit without destroying the earth's atmosphere in the process, and (2) a method of controlling very large flexible and sparsely filled transmitting antenna arrays. Though these problems have not yet been solved, they are being considered seriously by some governments, aerospace industries, and utility companies [2].

A necessary step in any large research and development acquisition program is that of concept demonstration and validation. The program is structured to minimize the company's (or government's) risk by demonstrating key components or elements of the proposed system design prior to obligating large production-level resources. This approach would most assuredly be used on a program such as the SPS. Fortunately, the unit-level resources to construct a prototype solar power satellite exist today, as COTS (commercial off-the-shelf) items. This greatly increases the program's chance of progressing to a production phase.

The magnetron directional amplifier (MDA) is analyzed in this dissertation as one possible high-power RF source for the SPS. Though the magnetron is not generally considered state-of-the-art, it possesses many desirable qualities for space applications. The primary advantage of the MDA is its high efficiency, which may exceed 75% when the magnetron is tuned properly to the load. The magnetron has also been vigorously tested in harsh environments. As it has served as the RF engine in many applications, such as airborne radar, it is known to be rugged, durable, and reliable. Part of this quality is the magnetron's good heat rejection capability. Since heat dissipation is low in the space environment, the magnetron has an advantage in that it may operate at higher temperatures (~300° C) than existing electronic RF generating devices (~150° C). The high temperature allows heat to be radiated away from the magnetron more efficiently, since heat transfer is proportional to T^4 (Stefan-Boltzmann law) [3].

1.2 Potential Applications

Just as the choice to field a multi-billion dollar production SPS will certainly require the successful demonstration of a smaller-scale prototype, generating the momentum to build the prototype itself will likely require even smaller technology demonstrations. The applications that generate the most interest will be those that clearly illustrate the ability to improve man's condition and pocketbook. To garnish the support of investors, they must have low risk and a short payback period.

Each application of wireless power transmission (WPT) serves as a paving stone in reaching the postulated SPS, shoring up support and improving related technology along the way. Whether or not the SPS is viewed as (or ever becomes) the cure for our energy concerns, developing WPT technology serves to increase our proficiency in energy conversion, transmission, and storage.

The term WPT, as its constituent words denote, refers to any transmission of power between two points without the constraint of wires. This can provide significant advantages over other systems in certain types of applications, whether land-based or space-based. This is particularly apparent for (1) sustained operations with limited space/weight, (2) operations with limited or difficult access, (3) environmentally hazardous areas, and (4) providing surge capability where batteries are not practical.

Since a system powered by WPT possesses an 'indefinite' time-on-task, it can substantially reduce task time and cost by eliminating or reducing equipment refueling and transit time. This in turn reduces energy storage requirements and planning complexities for refueling and task integration. As a result, the amount of equipment and manpower for a given task may be reduced. Each of these equates to an increase in productivity and reduction in operating costs. In addition, it can be strongly argued that

the components comprising the WPT portion of the system would generally have a higher end-to-end efficiency than their gas-powered or battery-powered cousins.

1.2.1 Non-terrestrial Applications

The operating characteristics of the magnetron make it ideally suited for space applications. The harsh environment of space and the large financial costs of fielding space systems require the use of rugged and dependable components.

Space provides unique challenges in controlling the thermal environment. Since spacecraft are not protected by the moderating effects of the earth's atmosphere, they may be subjected to potentially extreme temperatures (under –200° C to over 1200° C) from solar effects alone [4]. In addition, internally generated heat must be considered, which is significant in the high power DC to RF conversion process. A carefully designed thermal control system, including a judicious choice of spacecraft coatings, can help minimize the effects of this environment. Selecting components with tolerance to high operating temperatures such as the magnetron can greatly simplify system design.

Charged particles streaming from the sun (at 300 – 700 km/sec) impact the spacecraft, causing a number of potential problems [4]. These include sandblasting of solar arrays and sensors, single event phenomenon (SEP), and spacecraft charging. Sandblasting erodes exposed components over time, eventually degrading spacecraft performance. The cumulative effects of this erosion are known and accounted for in the spacecraft design by adding extra capacity to carry the system through its intended lifetime. A potentially more devastating effect of charged particles is that of single event phenomenon. SEP occurs when a particle impacts a component of the spacecraft's electronics, causing the malfunction in the spacecraft's operation. This may range in severity from a software 'hick-up' to permanent physical damage to the device, either of which may render the spacecraft inoperable. Another effect of charged particles is

spacecraft charging, where charge builds up gradually between different locations on the spacecraft. The sudden discharge (arcing) of this energy can also destroy spacecraft components. Though any modern spacecraft will necessarily contain electronic components, these must be shielded or minimized to limit the risk of charged particle bombardment [4].

WPT systems would seem to lend themselves to space applications, by the very nature of these operations. Since large-scale space operations are quite expensive ventures, reducing the time to complete tasks is a prime consideration. This is especially true for manned operations, where it is essential to minimize the risk associated with exposure to this hostile environment. Here it is critical to reduce the amount of time and additional risk spent accomplishing support functions, such as recharging batteries. Another substantial cost in extended space operations is in the transportation of personnel, equipment, and supplies to the desired location. Decreasing the amount of energy re-supply and storage equipment can have an enormous positive affect on the length and cost of an operation.

One example of extraterrestrial application of WPT includes the assembly and operation of a space station. Autonomous or semi-autonomous robots could be used to attach segments of the station. In addition, WPT could be used to power manned vehicles in close proximity of the station for construction, repairs, or experiments. Other possible applications for WPT include lunar mining/colonization and providing transportation between LEO and GEO [5].

1.2.2 Terrestrial Applications

Not only must the scientific aspects of WPT be first proven sound on earth, but its viability as a profitable commercial venture will be demonstrated here as well. The most

likely applications of this technology would be within the aerospace and communications industries, power utilities, and military.

The aerospace industry is seen as a potentially large user of WPT technology, because of the diverse range of applications within this field. This industry tends to validate research efforts that eventually become commercial ventures. Some anticipated uses of WPT include providing power/telemetry links for scientific vehicles such as balloons, helicopters, aircraft, or rockets. The advantage of WPT to this field is its ability to provide long term power with nearly instantaneous control. It may also provide clean power (no pollutants) in regulated environments.

Once WPT has been demonstrated to be useful in certain processes, the fast-paced communications industry is likely to be a chief benefactor of this technology. A ground-based phased array may be quickly configured to power an airborne platform for temporary surges in wireless communications demand. This would most likely be used for planned special events such as the Olympics at first. As the technology matures, it might eventually be provided as a service to other wireless communications companies during upgrades.

Power utility companies might also eventually benefit from WPT by providing portable power transmission components for remote locations. This industry has traditionally been more conservative in its operations and is not as likely to become involved in a leading edge technology. However, as WPT becomes more orthodox, it may be used for satisfying special needs for power distribution. This approach may be taken where it is cost/environmentally prohibitive to run power lines or use generators, such as the project proposed for Reunion Island [6]. Because of its mobile nature, WPT is also well suited for short-term usage requiring quick setup. It also provides a means to power remote equipment which otherwise would require portable generators or solar-charged batteries,

either of which requires preventative maintenance and can be impacted by temperature extremes.

Military applications for WPT may be extensive. In fact, one of the first perceived uses for WPT was the U.S. Air Force's interest in an indefinitely hovering drone vehicle [7]. Such a vehicle could be employed for communications, reconnaissance, or delayed attack. Other uses include remote ground vehicles for land-mine detection/detonation and nuclear/biological agent/hazardous materials cleanup.

2.0 Past Work

2.1 Magnetron Directional Amplifier (MDA)

The MDA was originally developed by William C. Brown, the father of modern microwave wireless power transmission [8]. The term *magnetron directional amplifier* refers to the magnetron's ability to lock onto a low-level signal near its free-running frequency and amplify it (Section 3.0). Brown's work provided the first end-to-end demonstration of microwave power transmission, furthering the earlier works of Hertz and Tesla. Brown laid the foundation for work in this area, both making enormous contributions in the development of microwave oscillator devices, and in pioneering the application of these devices to WPT [7], [9].

The concept of using an ordinary magnetron to generate the RF energy for WPT is credited to Richard Dickinson in 1975 [7]. Brown modified the concept and brought its design to fruition. He incrementally developed the capabilities of a magnetron-based RF power source that would ultimately drive a WPT phased array. For his work, Brown chose magnetrons operating in the 2.4 – 2.5 ISM (International Science and Medical) band. This provided an operating frequency with low atmospheric attenuation that was available for scientific experimentation, and was based upon a low-cost RF engine as microwave ovens were already becoming popular.

Brown's early work included the demonstration of a beam-riding helicopter [10]. This exhibition gave credence to the concept of WPT, moving it from the realm of speculation and theory to that of practical demonstration. However, for society to realize the full benefit of this technology, larger-scale demonstrations would have to be constructed. To this end, Brown desired to build a phased array that would provide a high-power, steerable microwave beam.

To document the capability of the MDA, Brown categorized its functionality by classes [8]. The Class I MDA provided an inexpensive, high-gain (~30 dB) RF amplifier. This was accomplished solely by injecting a reference signal into the magnetron. Unfortunately, in this configuration, the magnetron could only amplify a very narrow frequency range (1 – 2 MHz). This was simply not enough tuning to overcome the inherent characteristics of the tube, which can cause much larger frequency variances. Some of these observed during the characterization effort are shown in Table 2-1.

Table 2-1. Frequency Variance in MDA Operation.

Cause	Variance Observed
difference in loads (same magnetron)	6 MHz
heating effects (change during warmup period)	8 MHz
manufacturing tolerances (same load)	7 MHz
combined effects (two similar MDA units)	14 MHz

The Class II MDA was not so much a change in configuration, but more a change in the way the equipment was operated. By varying the relative magnitudes of the injected reference signal and the input power to the magnetron, it was possible to provide control of the signal phase [11]. This was accomplished by varying the input anode current, using a current-regulated power supply. However, it also had the undesired effect of changing the magnetron's output power. For the MDA to be of use in a phased-array application, it would be necessary to achieve independent control of the frequency, phase, and amplitude.

The Class III MDA provided another means to affect the magnetron output. Brown used an aluminum slug in the output path of the magnetron, suspended in the center of the waveguide by a ceramic rod. The metallic slug has a very low resistance and may be

modeled as a reactance in parallel with the load impedance. This provided a simple mechanism for tuning the magnetron output by varying its load impedance. Using a feedback path, the output signal phase and operating frequency could be independently controlled within a certain range. This process was automated by adding a servomotor and an error signal amplifier. The result of the Class III MDA was a phase-locked RF amplifier with a much wider bandwidth (~15 MHz demonstrated by Brown). However, the output power was also affected by the presence of tuning slug and could not be controlled independently [8].

The Class IV MDA added the ability to independently control the output signal power. This was accomplished by augmenting the magnetron's permanent magnet with a variable electromagnet. Changing the magnetic field had the effect of changing the magnetron's output power and frequency. By simultaneous operation of both feedback loops, independent control of all signal parameters was achieved. This also allowed multiple MDA units to be operated from a common power supply, making the system much more practical [8].

2.2 Electronically Steerable Phased-Array Module (ESPAM)

One of the hurdles to overcome in developing a practical SPS system was the construction of a simple, cost-effective power transmission module. Brown formed the ESPAM by combining his MDA RF engine with a slotted waveguide array (SWA) antenna, as described in Section 6.1 [12]. The SWA could be easily fabricated from metal sheet stock, utilizing simple processes of punching, bending and spot welding [13]. The ESPAM provided a conceptual building block approach for designing tailor-made WPT systems. Modules could be arranged as needed to furnish the power levels and beamwidths required for a given application.

To gain support for WPT system development, Brown constructed prototype slotted arrays for use in a portable demonstration kit, which he showcased to numerous audiences since 1990. The kit included an array of rectifying antennas (*rectennas*) used to convert the beamed microwave energy back into DC electricity, thereby providing a demonstration of the end-to-end transmission capability [13]. The rectenna was also of simple construction, consisting of a dipole with a rectifying diode (Section 6.1). This could be fabricated from bent sheet metal stock for large-scale earth uses, or etched on mylar sheet stock for light-weight deployable space applications. The rectenna elements were then used to power a simple load, such as a bank of automotive light bulbs.

Brown's endeavors included the development of larger scale WPT demonstrations to emphasize its potential for high-power applications. In one such experiment conducted at JPL's Goldstone facility in 1975, microwave power was beamed across 1 mile using a parabolic antenna [7]. At this distance, the receiving panels were able to collect 32 kW of the transmitted power, which was used to power a bank of lights. The rectenna element panels were calculated to be 84% efficient in converting the RF energy to DC. This provided a vivid demonstration of the ability to beam large amounts of power, as the lights were easily visible across the desert in the noonday sun.

2.3 Solar Power Satellite (SPS)

The concept of the solar power satellite is to place a number of satellites in orbit around the earth which will gather solar energy, convert this to microwave energy, and transmit this to the earth. The first viable concept for the SPS was provided by Peter D. Glaser in 1968 [7]. The fuel shortages of the 1970's then created the catalyst for interest in finding alternative energy sources. This resulted in the 1977 – 1980 DOE/NASA study to examine the fuel shortage and possible means of satisfying energy demands [14]. The study concluded that while the SPS was technically feasible, it was not currently practical.

The 1995 NASA Fresh Look Study ended with much the same conclusions with regard to the reference system described in the 1980 study [1]. Fielding a large constellation of GEO satellites capable of satisfying a significant portion of the earth's energy requirements was not deemed viable, at least presently. One of the largest technical hurdles to overcome is still finding a suitable launch vehicle that can deliver the components to orbit at minimal cost and pollution. However, the concept of the large GEO 'reference system' has not been abandoned.

The 1995 study examined numerous alternatives with a strategy of incrementally proving the concept of SPS. The acquisition approach shifted from a monolithic government controlled program towards a lower-risk phased program designed to encourage commercial participation. As such, the number of SPS configurations considered has increased to account for different levels of power production, coverage, and timelines [1], [2].

2.4 Focus for Research Effort

The objectives for this dissertation project flow from the previous work performed in the field, as mentioned in this chapter. In a general sense, the goal of this effort is to summarize what is known of the behavior of the MDA, further that body of knowledge, and identify design constraints/considerations useful for implementing the MDA in prototype WPT applications.

3.0 MDA System Description

The term Magnetron Directional Amplifier refers to the use of a magnetron as a frequency and amplitude stabilized source [8]. Historically, the magnetron has been used as a RF energy source operating at a select frequency within its design bandwidth. Since the magnetron is a tuned cavity oscillator, its frequency and output power vary with both the DC input power and the load.

Devices such as circulators are typically used to isolate the magnetron from changes in the load, thereby stabilizing its output signal. Therefore, the magnetron is generally considered a one-port device, as shown in Figure 3.0-1. It is powered at a *roughly* constant level and operates into a *roughly* constant load, and as a result, outputs a *roughly* constant amplitude and frequency.

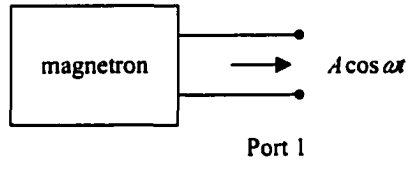

Figure 3.0-1. Magnetron as a One-Port RF Source.

However, the operation of the Magnetron Directional Amplifier (MDA) differs from this traditional approach. Its key purpose is to provide a building block approach to constructing phased arrays for wireless power transmission. For this application, the MDA must provide precise control of the output signal power level, frequency, and phase. These requirements are satisfied by actively altering the load impedance and input power to the magnetron.

Rough power and frequency control of the free-running oscillator can be obtained using three methods [8]: (1) internally change the resonant frequency of the magnetron, (2) change the current flow through the tube, or (3) change the reactance of the load into

which the magnetron operates. The first method requires some type of electromechanical tuning scheme and is therefore not applicable to the simple magnetrons studied. The second and third methods are employed in this research effort and will be discussed in detail in the following sections.

Phase control of the MDA is accomplished by injecting a low-level reference signal into the magnetron RF probe. When this signal is close to the free-running frequency, the magnetron locks to the signal and amplifies it [11]. In addition to the phase control capability, the injected signal also provides a degree of control over the MDA operating frequency and output power. Used in this fashion, the magnetron may be modeled as a two-port device, as shown in Figure 3.0-2.

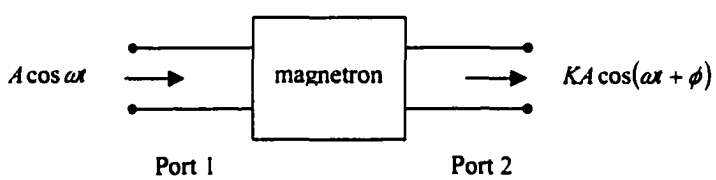

Figure 3.0-2. Magnetron as a Two-Port RF Amplifier.

This effort characterizes the relative control provided by each of the tuning methods. The capabilities are examined in accordance with the four MDA classifications defined by Brown [8]:

Class I: frequency locking
Class II: Class I + phase control by changing magnetron anode current
Class III: Class I + reactance tuning (phase-locked amplifier)
*_Class III OL: Class III Open-Loop (manual reactance tuning)_*
*_Class III CL: Class III Closed-Loop (automatic reactance tuning)_*
Class IV: Class III + amplitude control loop.

*Sub-category not broken out in Brown's work.

3.1 Basic Magnetron Configuration

The basis for the Magnetron Directional Amplifier is the magnetron itself. The behavior that will be encountered with the increasingly complex MDA classes can ultimately be attributed to the characteristics of the magnetron, its power supply, and the load.

3.1.1 Functional Description

A core set of microwave components is common to all of the MDA configurations. These include a magnetron, the magnetron launching section, at least one circulator, and some type of load. A functional diagram of the components is shown in Figure 3.1-1.

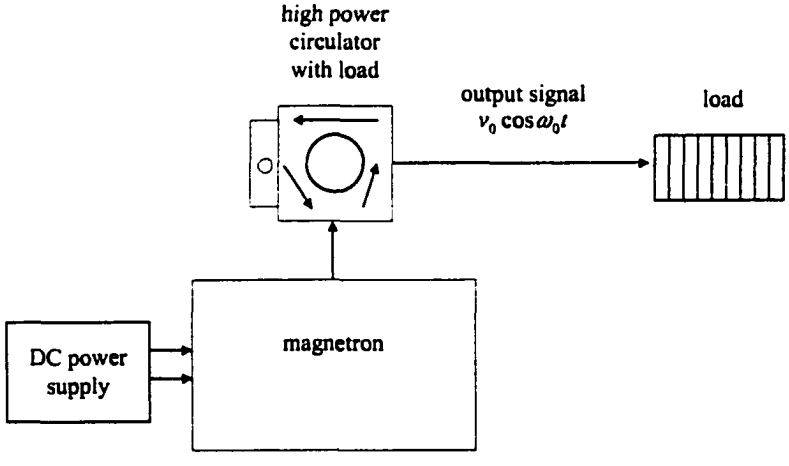

Figure 3.1-1. Simple Block Diagram for a Magnetron.

The magnetron investigated is a microwave oven-type tube rated at ~1 kW. The current-regulated power supply provides a maximum current of ~350 mA at an operating voltage of ~3.5 – 4 kV. The magnetron converts this to RF energy, typically at an efficiency in the range of 50 – 70%. This is then transmitted through the circulator to the load.

The circulator isolates the magnetron from any reflected RF power that might affect the magnetron's operating frequency or output power. This unwanted power is instead routed to a secondary load, which will effectively attenuate the remainder of the signal. Typical circulators provide 15 – 30 dB of isolation, and therefore multiple circulators are sometimes necessary to provide adequate isolation.

The load is any device that removes a large percentage of the RF energy from the system. This may be accomplished by transmitting the energy out of the system via an antenna. Alternately, the load may transform the RF energy to some other form such as heat, which is then removed from the system. This is called a *dummy load* and usually takes the form of an air-cooled or water-cooled load.

3.1.2 Theory of Operation

In its simplest form, the magnetron may be modeled as having only two inputs — its DC operating power and effective load impedance, as shown in Figure 3.1-2. Any variation in the output signal may be attributed to changes in one or both of these inputs. The remainder of this dissertation will analyze the components of these inputs and their effects upon the output signal. For details on the development of the magnetron model, see Chapter 4 and Appendix A.3.

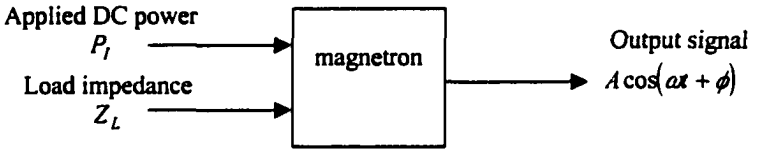

Figure 3.1-2. Control Mechanisms for the Magnetron.

Although either of these inputs affects both the magnetron's output power and operating frequency, controlling the magnetron output is generally described in terms of its affects on frequency. Using the applied power to drive the magnetron to a particular operating

frequency is called frequency *pushing*. Varying the load to affect a change is called frequency *pulling*. Either of these methods may be used to control the frequency, but each also affects the output power. Since the power must also be controlled for phased array applications, some combination of both techniques must be employed.

The basic theory governing these relations is provided in Chapter 4. Pertinent equations are again presented as needed in the explanation of the MDA behavior throughout Chapter 5.

3.1.3 Physical Configuration

The magnetron was characterized using two different test configurations. In the first arrangement, the objective was merely to obtain rudimentary data on the operation of the magnetron — rough power and frequency readings. For this, the magnetron was connected to a waterload. The configuration used for the waterload testing is shown in Figure 3-1.3.

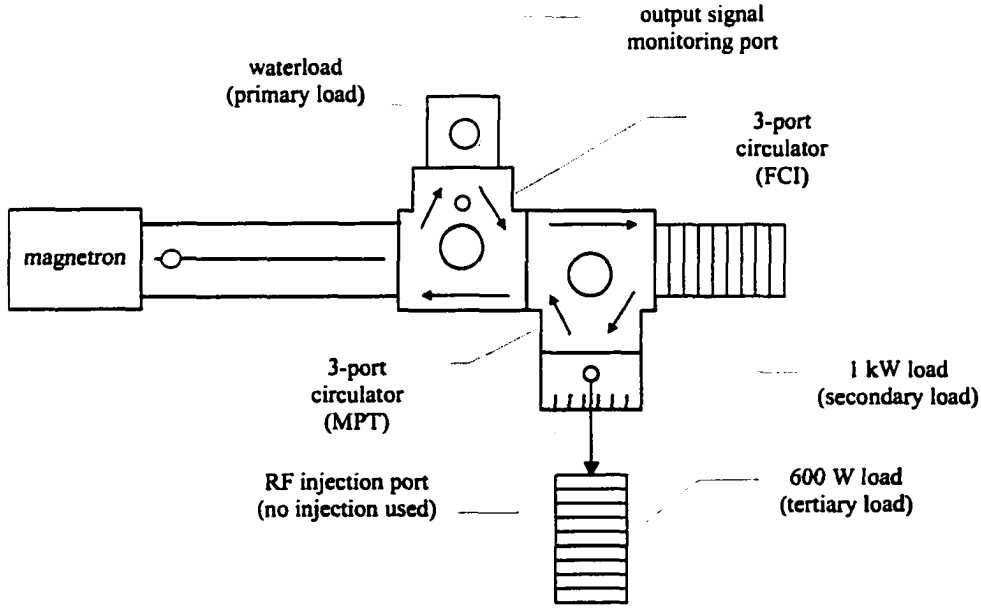

Figure 3.1-3. Test Configuration for Magnetron with Waterload.

The magnetron's output energy is routed by the first circulator to the water load. Energy reflected from the water load due to impedance mismatches is routed to the secondary load (1 kW waveguide load), then to the tertiary load (600 W coaxial load). These circulators and loads isolated the magnetron from reflections and provided the signal monitoring and injection ports needed for subsequent configurations.

The free-running frequency of the magnetron was measured at the output signal monitoring port. The power output may be calculated by measuring the water flow rate through the water load and the temperature differential of the water between the input and output ports. The equation governing this calculation is

$$Q = mc\Delta T \tag{3.1-1}$$

where

Q = heat absorbed by load $[\mathrm{J}]$

m = mass $[\mathrm{kg}]$

c = specific heat capacity of water $= 4186.8\left[\dfrac{\mathrm{J}}{\mathrm{kg}\cdot\mathrm{deg\,C}}\right]$

ΔT = temperature differential $[\mathrm{deg\,C}]$.

Using a flowmeter to determine the flow rate f of the water in gallons per hour, the equivalent mass flow rate is

$$\frac{m}{t} = 1.0515\times10^{-3} f\left[\frac{\mathrm{kg}}{\mathrm{sec}}\right]. \tag{3.1-2}$$

In terms of flow rate, the heat capacity equation is

$$P = \frac{Q}{t} = \frac{m}{t}c\Delta T = 4.4024 f\Delta T\,[\mathrm{W}]. \tag{3.1-3}$$

For example, suppose the flowmeter measures a flow rate of $f = 48.5$ gallons per hour. If the temperature difference between the input and output of the water load is $\Delta T = 4.0°$ C, then the power absorbed by the water load is $P \approx 850$ W.

This configuration was useful in determining the maximum power available from the magnetron for delivery to a load. It was also helpful in calibrating the actual power output to relative power level readings taken at the output monitoring port. After this was completed, the water load configuration was replaced with a simplified air-cooled load arrangement, as shown in Figure 3.1-4. This was the configuration used for the majority of the magnetron characterization effort.

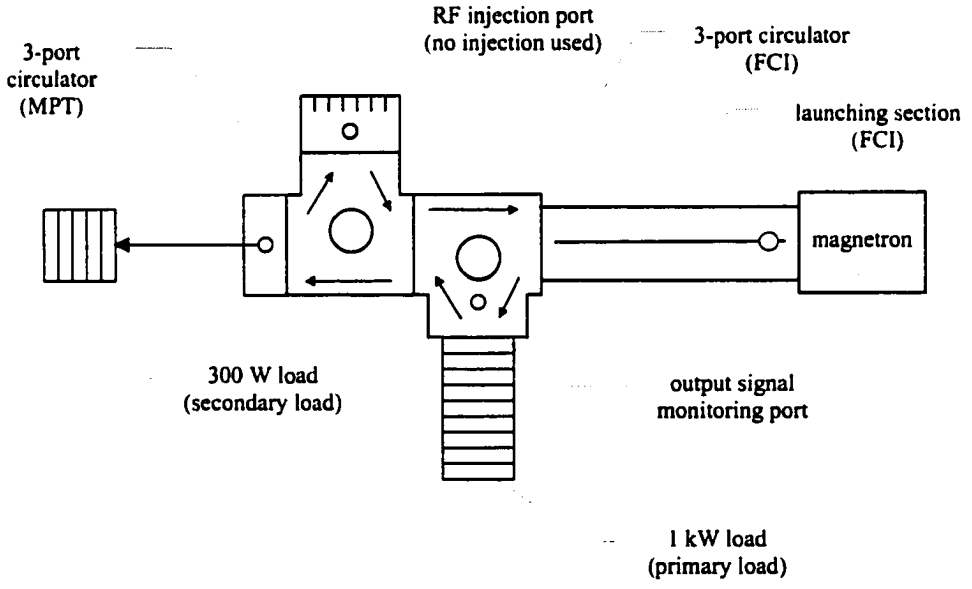

Figure 3.1-4. Primary Test Configuration for Magnetron.

The magnetron temperature verified the output power measurements. The temperature was measured externally at the case, as shown in Figure 3.1-5. The mounting scheme of the magnetron provided good thermal contact with the tube, although some slight delay was introduced. The thermal environment was kept as constant as possible. The ambient

room temperature was approximately 29° C. Cooling fans were kept at constant settings and positioning relative to the magnetron and dummy load.

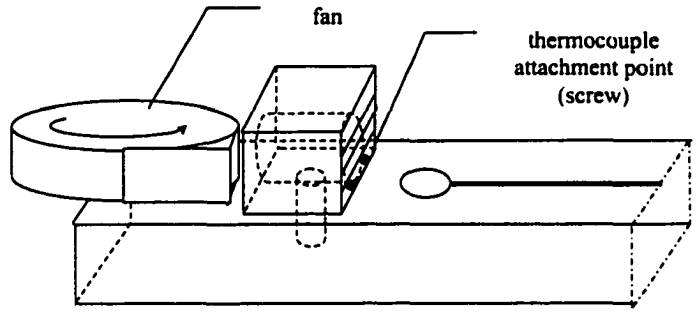

Figure 3.1-5. Measurement Scheme for Magnetron Temperature.

The operating characteristics of the magnetron in a static environment (fixed input power and load impedance) are provided in Section 5.1.

3.2 Class I MDA

The Class I MDA provides an inexpensive high-gain RF amplifier, whose output power level is that of the magnetron used. Amplification is accomplished solely by injecting a reference signal into the magnetron. However, this provides only a limited tracking bandwidth. For magnetrons operating at 2.45 GHz, a 1 – 2 MHz locking bandwidth is typical, depending upon the total load impedance. If the injected signal is within this bandwidth, it may be used to command the MDA operating frequency and phase. Additional bandwidth may be achieved at the expense of gain by increasing the injected signal strength or decreasing the output power level.

3.2.1 Functional Description

The Class I MDA is formed by simply adding an injected signal source to the basic magnetron configuration. A functional diagram of the components is shown in Figure

3.2-1. These include a stable frequency generator, a RF amplifier, and an additional low-power circulator.

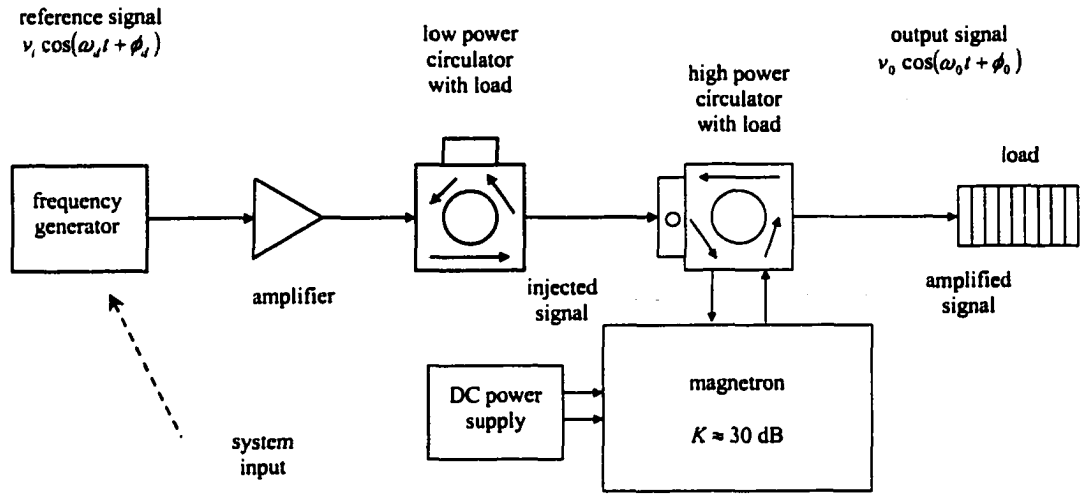

Figure 3.2-1. Class I MDA Functional Diagram. Frequency generator is the only system input.

The signal generator provides the reference signal necessary to control the MDA frequency and phase. The reference signal is amplified to reach the desired drive power level, roughly 20 – 40 dB below that of the magnetron output power level. This is defined as the gain K of the MDA. The amplified RF signal is then passed through a series of microwave circulators before being injected into the magnetron.

The circulators are 3-port devices that act as traffic routers, allowing RF signals to pass in one direction only at each junction. The first circulator is a low-power coaxial type configured as an isolator by attaching a matched load at the third port. The function of this isolator is to protect the RF amplifier output port from reflected power. The second circulator is a high-power waveguide type, which serves three purposes: (1) provides a path for the high-power magnetron output to the load, (2) isolates the magnetron from the load by routing reflected energy to the third port, and (3) provides a path for the injected signal into the magnetron.

The reference signal is then injected into the magnetron. If it is close enough to the free-running magnetron frequency, it is amplified and sent back out into the waveguide. The output signal is then routed through the high-power circulator to the load (antenna or dummy load).

3.2.2 Theory of Operation

The operation of the MDA as a RF amplifier may be explained with the aid of the expression for a frequency-locked oscillator given by E. E. David [11]. For further details, see Section 4.2. The phase difference between the injected and free-running signals is given by

$$\sin\phi = \left[\sqrt{\frac{P_O}{P_I}} \cdot \frac{f - f_I}{f} \cdot Q_E\right] \tag{3.2-1}$$

where

ϕ = phase shift between the output and input signals of the amplifier
f = free running frequency of the magnetron
f_I = frequency of the input drive signal
P_I = power in from the drive signal
P_O = power out of the amplifier
Q_E = external qualify factor Q of the circuit.

The phase shift between the input and output terminals of the frequency-locked oscillator is a function of (1) the frequency difference between the locking signal and the free running oscillator, (2) the external Q of the device, and (3) the ratio of the output power to input locking power. Varying any of these inputs will alter the output signal phase.

Figure 3.2-2 shows the effect of the injected signal upon the magnetron. The electric and magnetic fields may be equated to corresponding voltages and currents, so that

transmission line theory may be used to analyze the magnetron behavior. The reference plane represents the total voltage and current at the magnetron RF probe (shown near probe for illustration purposes).

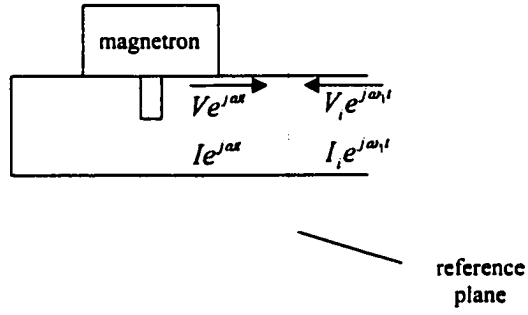

Figure 3.2-2. Magnetron-Load Interface (Transmission Line Equivalent).

The injected signal has the effect of changing the total voltage and current signals, thereby altering the load admittance. From Section 4.2, the total admittance seen by the magnetron is

$$Y = \frac{1}{Z} = \frac{I_T}{V_T} \approx \frac{I}{V}\left(1 + \frac{I_I}{I} - \frac{V_I}{V}\right)e^{j\Delta\omega t} \tag{3.2-2}$$

where

Y, Z = admittance, impedance at the magnetron port
I, V = current, voltage out of the magnetron
I_i, V_i = current, voltage incident at the port from the load and the injected signal
I_I, V_I = current, voltage incident at the port from the total load
I_T, V_T = total current, voltage at the port
$\Delta\omega t$ = phase shift between the incident and free - running signals.

Since the magnetron operating point is dependent upon the load admittance, the injected signal alters the magnetron operation. The relatively low drive level limits the tuning ability of the injected signal.

Note that for the Class I MDA, the output power can be considered relatively constant. The frequency of the injected signal only slightly affects the output power (~5% at 25 dB gain). Therefore, for this hardware configuration, the Class I MDA provides limited frequency-locking capability for a modest change in power output.

3.2.3 Physical Configuration

The physical configuration used to implement the Class I MDA is shown in Figure 3.2-3. The signal generator used was a HP 8780A Vector Signal Generator, which can output a maximum signal strength of 40 mW. To achieve the necessary input signal levels for the 1 kW magnetron (~60% efficient) requires a RF amplifier which can produce 60 mW – 6 W output power. However, the actual amplifiers used were limited to ~1.5 W maximum.

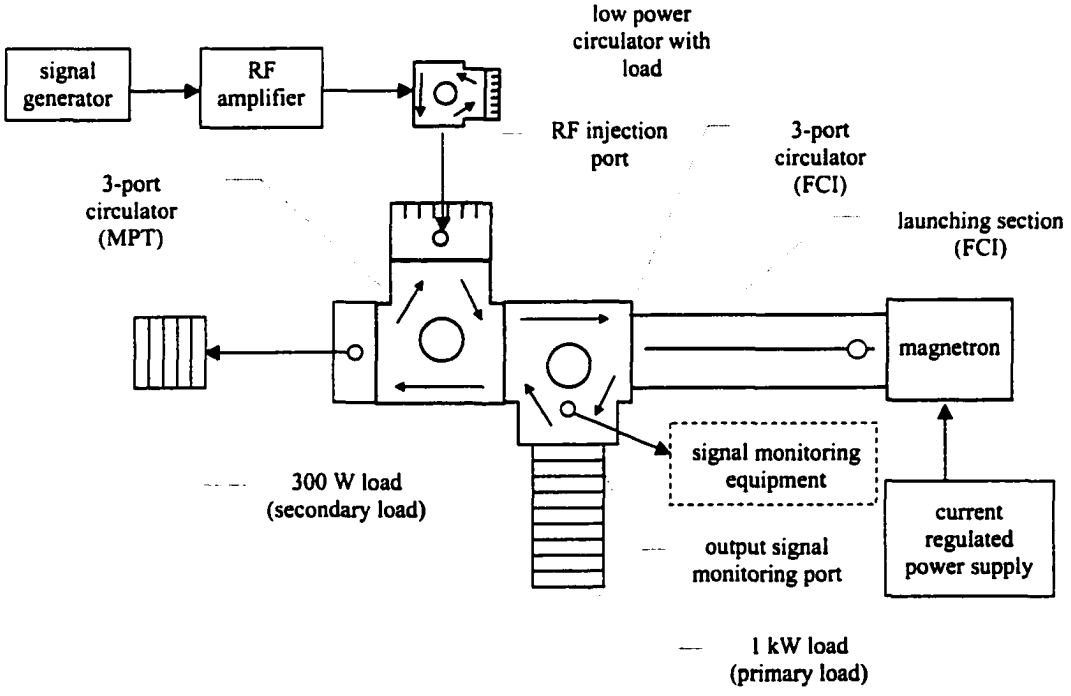

Figure 3.2-3. Physical Configuration of a Class I MDA.

The components discussed so far utilize coaxial connectors — either Type N or SMA. To inject the signal into the magnetron requires coupling the signal into the waveguide. This is accomplished using the probe located at the RF injection port. Note that the physical diagram shows two high-power waveguide circulators, instead of the one shown in the block diagram of Figure 3.2-1. This is due to the physical limitations imposed by the actual hardware. The second circulator provides the injection port and further isolates the injected signal from errant power reflections within the waveguide.

The adapter probe on the left circulator is a high-power design capable of coupling a larger fraction of the injected power into the waveguide. These larger probes tend to be frequency sensitive, which must be accounted for if the probe is operate over a wide range. In comparison, the low-power probe located at the output signal monitoring port is designed not to disturb the main power flow. This probe has low power coupling ability and is relatively insensitive to frequency changes.

Using the input probe to couple the injected power requires adding the low-power coaxial circulator to protect the RF amplifier. Unwanted RF power can come from two different sources. The first cause of concern is power bled through from the magnetron to the probe. In this configuration, the two high power circulators provide a total of ~35 – 40 dB protection from the magnetron's output power. Therefore, a magnetron outputting 750 W can leak up to 190 mW of power through to the output of the RF amplifier, posing a danger to the amplifier. The other source of unwanted RF energy is from the amplifier itself. If the amplifier is producing 1.5 W and sees a reflection coefficient of 8 dB, it will cause 237 mW of power to be reflected. These signals can be enough to burn out the output stage of the RF amplifier. Therefore, the low-power circulator should always be used to protect the amplifier output stage.

The Class I MDA utilized a variable current-regulated DC power supply. However, it was operated at a nearly constant power level. Control of the Class I MDA was limited

to variations in the injected signal power and frequency provided by the signal generator. Although not part of the MDA configuration itself, the interface to the signal monitoring equipment is shown. This equipment is necessary to monitor output signal strength and frequency (Appendix A.2). It also provides the equipment necessary to measure the phase between the injected reference signal and the MDA output. The performance characteristics of the Class I MDA are presented in Section 5.2.

3.3 Class II MDA

The Class II MDA has the same capability as the Class I MDA, but also uses changes in input power levels to affect the output signal. The result is an amplifier that may be rough-tuned to some power/frequency pair with the DC input power, then fine-tuned with the injected signal. With the improved gain control, the Class II MDA has an increased ability to trade locking bandwidth for gain and to control the output signal phase.

3.3.1 Functional Description

The functional components of the Class II MDA are shown in Figure 3.3-1.

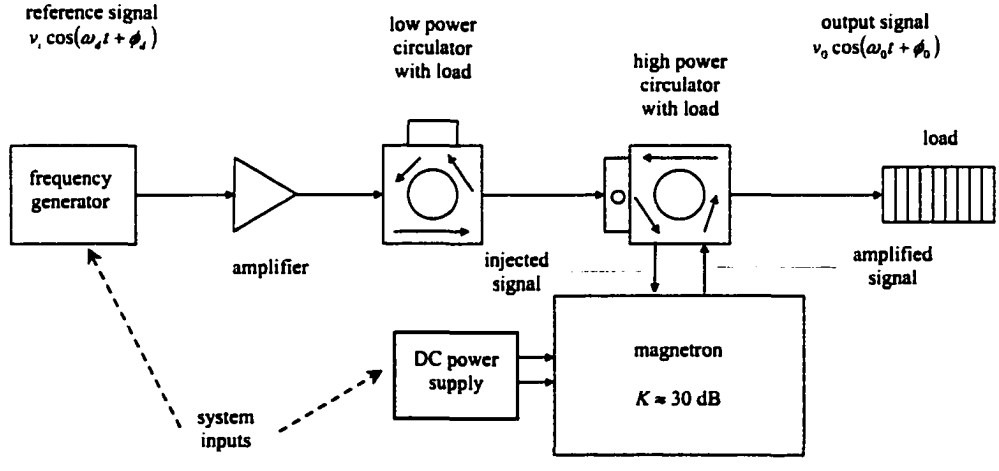

Figure 3.3-1. Class II MDA Functional Diagram. Input parameters are the injected reference signal and DC power.

The Class II MDA is identical to the Class I, except for the addition of the DC power as a control input. Altering the input anode current changes both the output power and frequency.

3.3.2 Theory of Operation

The magnetron's operating frequency and output power are functions of the input power and load impedance. However, the relationships between the parameters are not independent, as implied by the simple block diagram in Figure 3.1-2. For example, a change in applied power will cause the output power to change. The waveguide and load will react to this change in output power by expanding or contracting, which will affect the load impedance. The altered load impedance then causes another change in output power, completing the cycle. Likewise, a change in the load impedance indirectly causes a change in the applied power. These relations are discussed further in Section 5.3.

The adjustable DC power supply provides a means to control the magnetron frequency. The relationship between anode current and operating wavelength is given by [15]:

$$\Delta\lambda \approx \frac{1}{SY_c}\frac{\lambda}{2}\left(\frac{dB_e}{dI}\right)\Delta I \qquad (3.3\text{-}1)$$

where

$\Delta\lambda$ = change in wavelength
S = frequency stabilization circuit = 1 (not used)
Y_c = characteristic admittance of the resonant circuit
λ = operating wavelength
B_e = electronic susceptance associated with the phase of the DC power supply
I = anode current.

The operating frequency is almost linearly proportional to the electronic susceptance, and therefore varies with the anode current. However, the slope of the susceptance changes with the current. Depending upon the magnetron characteristics, the effects of the varying slope may be significant. This may cause the frequency to eventually roll over and change sign, as seen in Figure 5.3-1.

Power control of the magnetron proves difficult, unless augmented by some other tuning means. The magnetron has a very flat *V-I* characteristic curve, as shown in Figure 3.3-2. It will not operate below a threshold voltage, where the current changes vary rapidly with small changes in operating voltage.

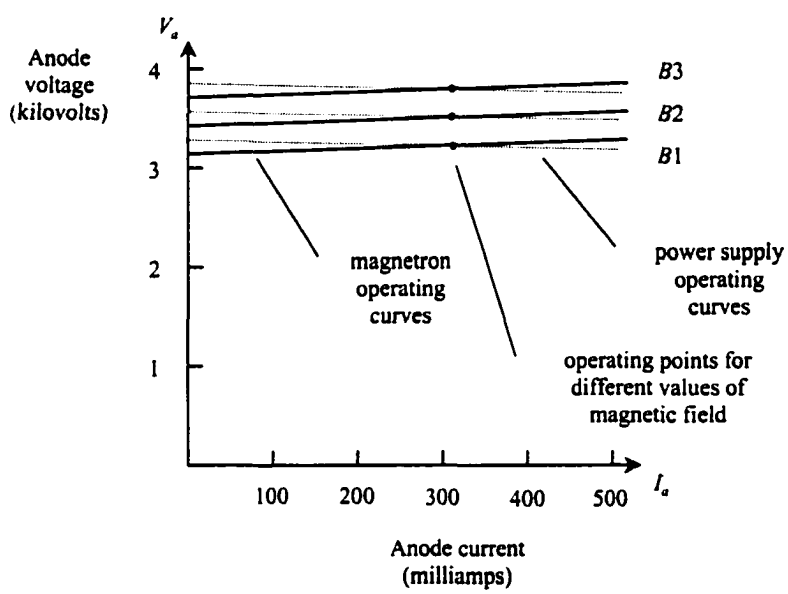

Figure 3.3-2. *V-I* Characteristic Curve for Magnetron.

Both the magnetron output power and operating frequency are proportional to the anode current. Therefore, the magnetron must have a constant current source to provide desirable control characteristics. Otherwise, small changes in voltage can produce large fluctuations in output power and frequency. This is particularly important when

operating multiple MDAs from a common bus voltage. In this case, it is necessary to isolate each magnetron from the bus voltage changes induced by other units.

In the Class IV MDA, a separate amplitude control system is introduced to automatically adjust the magnetron's magnetic field via an electromagnet (Section 3.6). As the output power level fluctuates, the electromagnet coil is energized to either augment or cancel a portion of the normal magnetic field, thereby restoring the output power to the desired level. However, the generic magnetrons used in the Class I – III MDA do not possess this capability, and therefore require the constant current power supply.

The phase control of the Class II MDA is also governed by David's equation, as described in Section 3.2. However, the ability to change the output power level provides much greater control over the MDA gain. In this manner, the locking bandwidth of the MDA may be effectively traded against gain. Rewriting David's equation to highlight this, the fractional locking bandwidth is

$$\Delta BW = \frac{f - f_I}{f} = \frac{BW}{f} = \frac{2}{Q_E}\sqrt{\frac{P_I}{P_O}} \tag{3.3-2}$$

where

ΔBW = fractional locking bandwidth
BW = locking bandwidth.

3.3.3 Physical Configuration

The physical configuration used for the Class II MDA is shown in Figure 3.3-3. This is the same configuration as the Class I MDA, but now the current regulated power supply is also used as a control input. Details of the test instrumentation are provided in Appendix A.2.

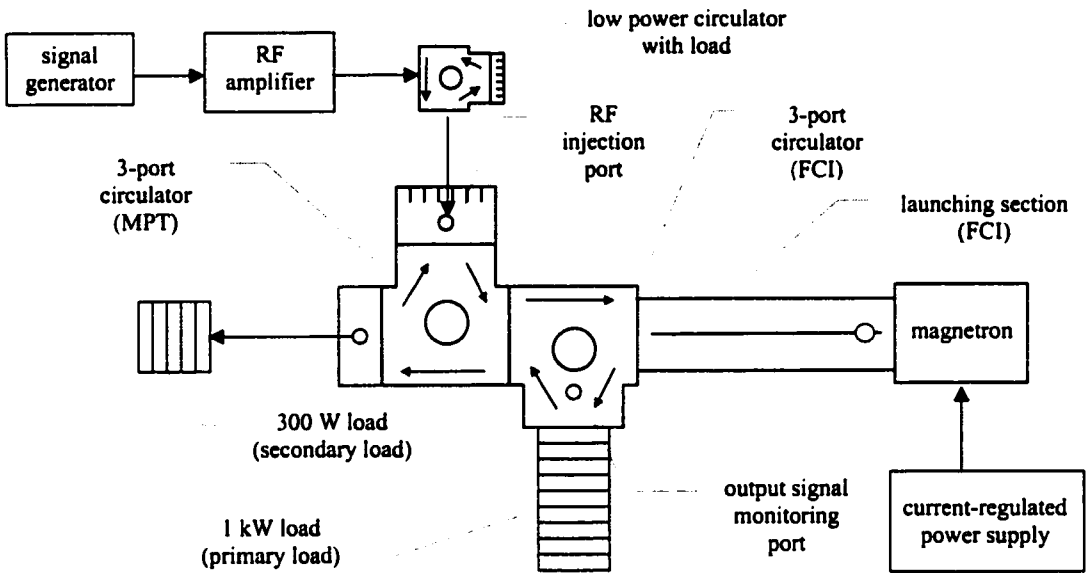

Figure 3.3-3. Physical Configuration of a Class II MDA.

The signal generator was adjusted to provide a range of input frequencies and power levels at the injected signal port. This has the effect of varying the load seen by the magnetron over a limited range. The anode current of the current-regulated power supply was also varied. Both of these inputs and their effects on the output frequency and power of the MDA were measured. The performance characteristics of the Class II MDA are presented in Section 5.3.

3.4 Class III Open-Loop (OL) MDA

The Class III OL MDA has the same capability as the Class II MDA, but adds a tunable load reactance to the output of the magnetron. The result is a RF amplifier with controllable output power, frequency, and phase.

3.4.1 Functional Description

The functional components of the Class III MDA are shown in Figure 3.4-1.

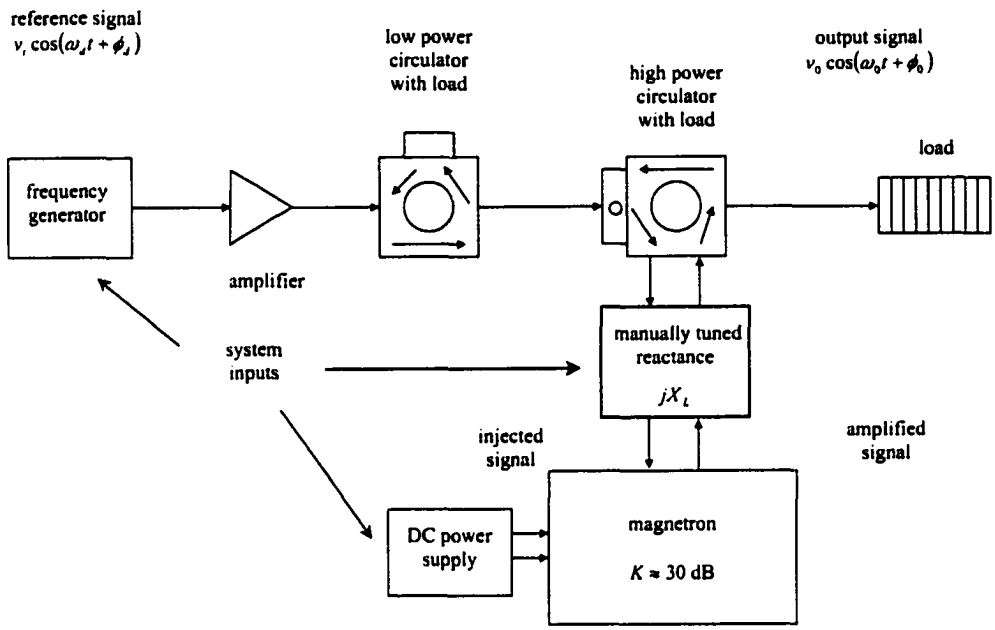

Figure 3.4-1. Class III OL MDA Functional Diagram.

The Class III MDA adds a load reactance tuning capability to that of the Class II MDA. Reactance tuning provides a second means to change the output power and frequency. Varying the input DC power and load concurrently provides independent control of the power and frequency. The injected reference signal provides phase control of the MDA, thereby obtaining all three desired output signal parameters.

3.4.2 Theory of Operation

The reactance tuning slug is a cylindrical shaped aluminum object centered within the waveguide cavity. Its purpose is to tune the total load seen by the magnetron by altering the standing wave ratio in this section of the waveguide. The reflected wave either reinforces or cancels the output of the magnetron according to its relative phase. This changes the load admittance seen by the magnetron, thereby tuning the MDA output. The signal components are shown in Figure 3-4.2.

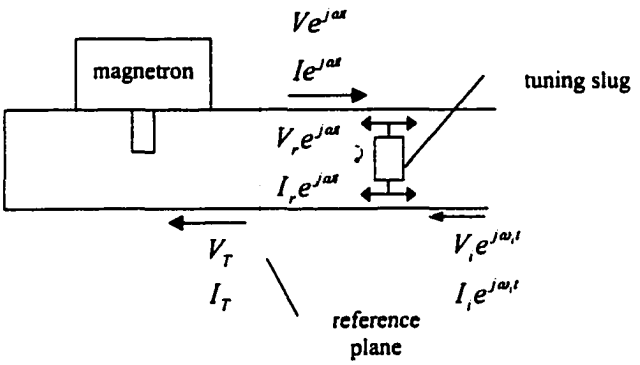

Figure 3.4-2. Magnetron/Tuning Slug Interface.

The new signals are defined as:

V_r, I_r = voltage, current of the signal reflected from the tuning slug.

This consequently alters the voltage applied to the magnetron probe, changing the impedance at the driving point. The effective changes in load resistance and reactance alter the MDA operating power and frequency, respectively.

For completeness, the injected reference signal is also shown in the figure above. Note that this signal acts in an identical manner as does the reflected signal from the tuning slug. It has the same effects upon the magnetron, but of a much lesser magnitude (for the signal strengths and slug sizes studied). The tuning slug can then be thought of as providing coarse load tuning, with refinements being made by the injected signal.

3.4.3 Physical Configuration

The physical configuration used for the Class III MDA is shown in Figure 3.4-3. The reactance tuning slug is inserted into the section of slotted waveguide near the magnetron. Details of the test instrumentation are provided in Appendix A.2.

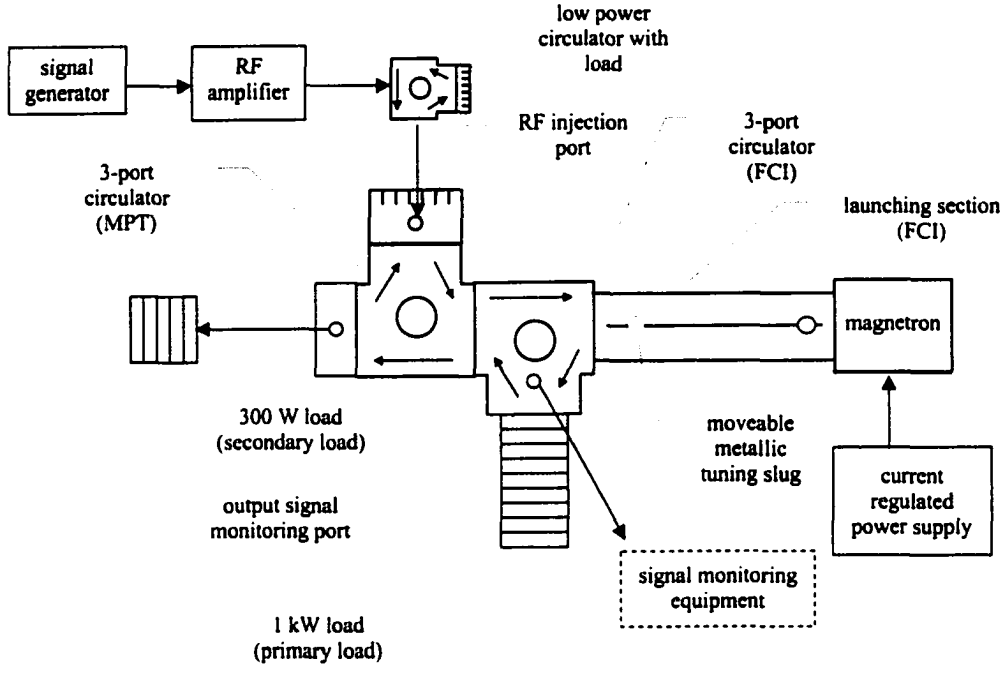

Figure 3.4-3. Physical Configuration of a Class III OL MDA.

The addition of the metallic tuning slug provides another means for tuning the output of the MDA. The slug's primary effect is on the frequency of operation, though it also changes the output power of the MDA. The tuning slug pulls the magnetron output in the same manner as does the injected signal (Section 5.3). However, the tuning slug exhibits much more control over the MDA, as the magnitude of the reflected signal greatly exceeds that of the injected reference signal. Referring to Figure 3.4-2, in general $V_r, I_r >> V_i, I_i$.

A number of different sized slugs were constructed for this purpose. The aluminum slugs are cylindrical in shape, ranging from ¼ " to 5/8" in diameter and ¼" to ¾" in length. The different sizes examined are shown in Table 3.4-1.

Table 3.4-1. Tuning Slug Sizes.

Slug Number	Size (diameter x length) (in)	Slug Number	Size (diameter x length) (in)
1	5/8 x ¼	9	3/8 x ¾
2	5/8 x ½	10	¼ x ¼
3	5/8 x ¾	11	¼ x ½
4	½ x ¼	12	¼ x ¾
5	½ x ½	13	¼ x 5/8
6	½ x ¾	14	3/8 x 5/8
7	3/8 x ¼	15	½ x 5/8
8	3/8 x ½	16	5/8 x 5/8

The slug was attached to a teflon or ceramic rod and inserted into the waveguide so that it was suspended in the center of the guide, as shown in Figure 3.4-4. This location was chosen to provide maximum coupling of the slug with the electric field within the guide. The slot location provided minimal disturbance of the surface currents.

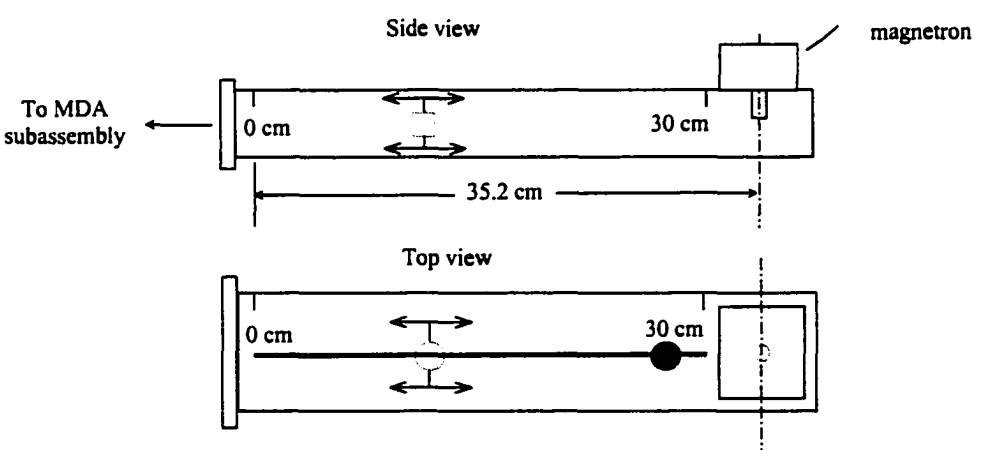

Figure 3.4-4. Tuning Slug Position within Waveguide.

For each data set, the slug was initially positioned at the far left away from the magnetron. It was then incrementally moved towards the magnetron, noting the operating frequency and output power at each point. At each new operating point, data collection was delayed for a sufficient amount of time to permit the MDA to reach thermal equilibrium. The performance characteristics of the Class III OL MDA are presented in Section 5.4.

3.5 Class III Closed-Loop (CL) MDA

The Class III CL MDA contains the same features as the Class III OL MDA, but provides much improved functionality by incorporating an automatic phase control feedback loop. This enhancement allows the MDA to track a much broader range of frequencies, and to track reference signal phases.

3.5.1 Functional Description

The functional components of the Class III CL MDA are shown in Figure 3.5-1. The input signal from the frequency generator contains the reference phase information required of the MDA unit for multi-unit beam steering. The reference phase is compared with the actual phase of the MDA output signal. The resulting low-level error signal is amplified and used to drive the tunable reactance mechanism, which repositions the tuning slug to force the error signal to zero.

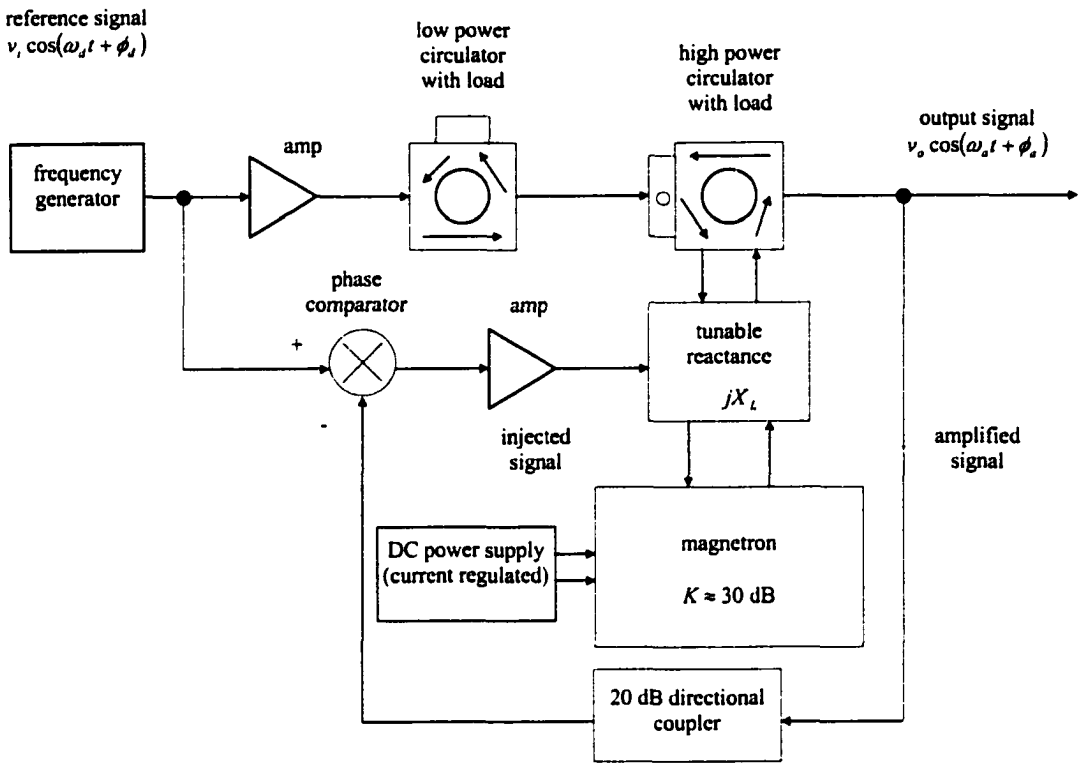

Figure 3.5-1. Class III CL MDA Functional Diagram.

3.5.2 Theory of Operation

The operation of the magnetron itself is unchanged by the addition of the phase control loop. Its control inputs are the input power level and the load impedance presented at the RF port. Therefore, it responds as before to impedance changes, regardless of the method by which the tuning slug is positioned.

However, behavior of the overall MDA *is* modified by automatically repositioning the tuning slug. The tendency of the control system is to return the tuning slug to a point of equilibrium satisfying the phase condition imposed by the injected signal. This causes the slug to trace out the normal ($\Delta\phi = 0$) curve centered between the frequency limits, as shown in Figure 5.4-14.

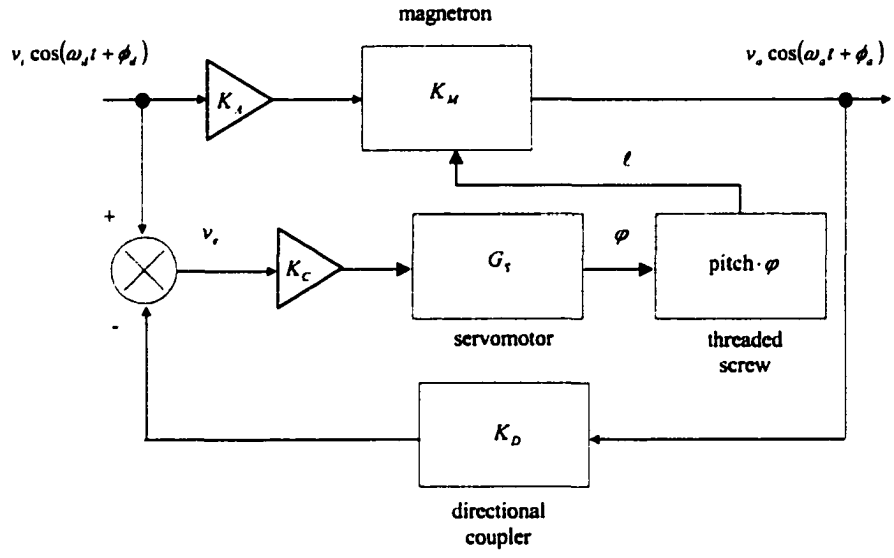

Figure 3.5-2. Control Block Diagram for Class III CL MDA.

The control loop of the Class III MDA has its own set of operating characteristics that affect its performance. These determine the speed, stability, and error of the system response. A block diagram of the components is given in Figure 3.5-2. For more details on the phase control loop, see Appendix A.3.

3.5.3 Physical Configuration

Figure 3.5-3 shows the major components used to implement the Class III CL MDA. The reference signal from the HP 8780A Vector Signal Generator is split into two streams. The portion of the signal to be injected into the MDA is first amplified up to 1.6 W maximum. A low-power coaxial circulator protects the RF amplifier output from reflected power due to the coax-to-waveguide probe impedance mismatch. The second half of the split reference signal is routed through the phase control circuitry. The signal is first manually shifted via a rotary-type phase shifter. The shifted signal is then passed to the phase comparator, which generates a low-level signal voltage that is proportional to the phase difference of the inputs.

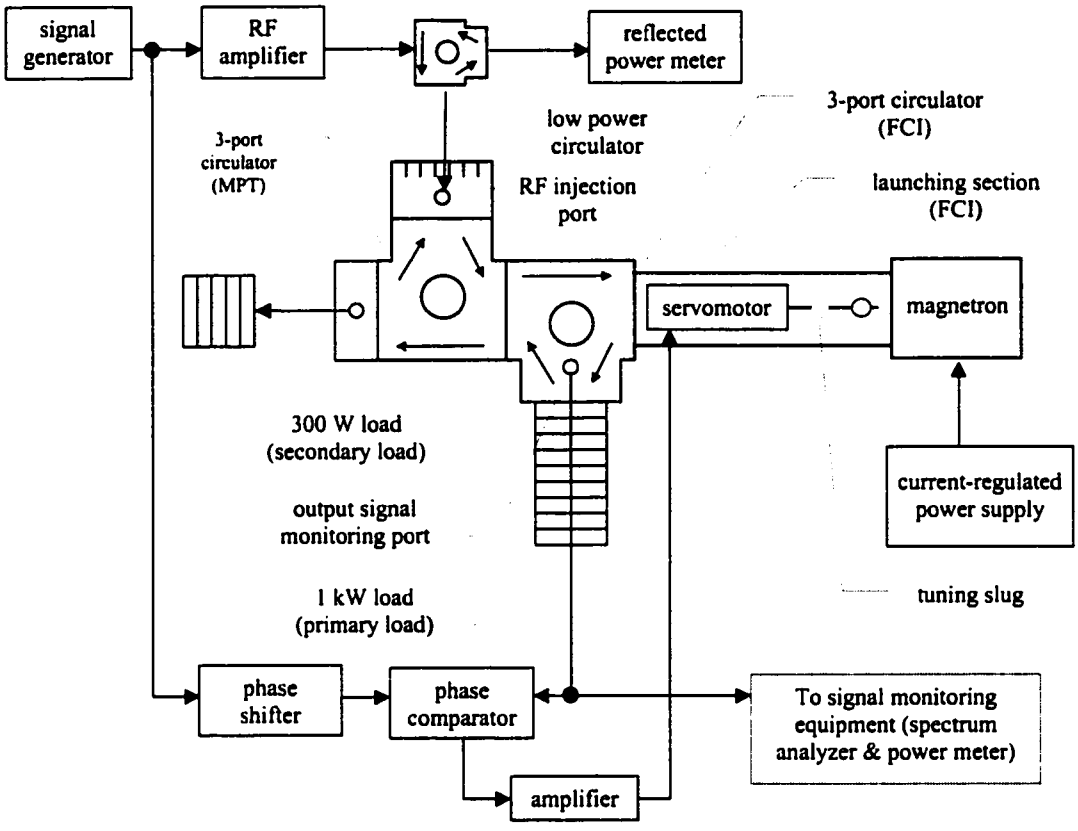

Figure 3.5-3. Physical Configuration of a Class III CL MDA.

The phase error signal is then amplified to drive a DC servomotor, which positions the tuning slug at the appropriate location to meet the desired frequency or phase condition. The mechanism for positioning the slug is shown in Figure 3.5-4.

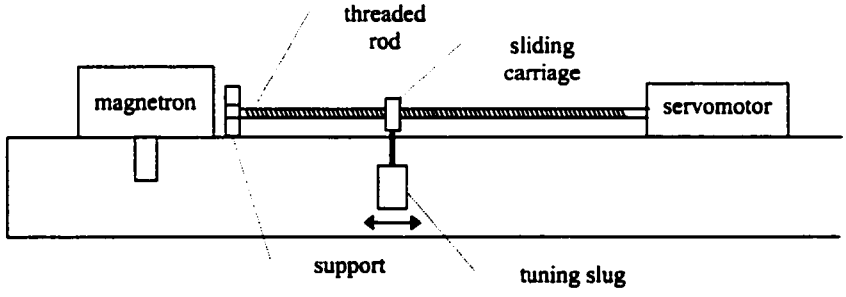

Figure 3.5-4. Tuning Slug Positioning Arrangement.

The servomotor is connected to the tuning slug using a slide-screw arrangement, converting the servomotor angular rotation into a linear displacement. A longitudinal slot centered in the top waveguide wall permits the tuning slug to move relative to the magnetron RF probe. This provides a symmetric waveguide cross-section picture to the magnetron, while minimizing RF current losses.

To test the MDA performance, a manual rotary phase shifter was introduced to vary the reference phase relative to the injected signal (this could alternatively be placed in the RF amplifier path). Note that the phase shifter may or may not be considered an integral element of the MDA. Since the MDA will track any input phase while frequency-locked, the input signal is assumed to contain the desired phase information. Any phase adjustment required of the reference signal would occur just prior to the MDA input. However, a phase shifter shown in the location above might be incorporated for small-scale phase trimming purposes.

The phase control loop is activated by first positioning the tuning slug at the approximate location corresponding with the desired operating point (power and frequency). The MDA frequency is noted on the spectrum analyzer and selected on the reference signal generator. The open-loop MDA will lock to the injected signal if the strength is sufficient to overcome the initial frequency separation. The phase shifter is then manually tuned to zero the output of the phase comparator. At this point, the servomotor amplifier is turned on to engage the phase control loop.

This feedback loop may then be used to control either the operating frequency or phase. The frequency is controlled using the signal generator; the phase by the phase shifter. The performance characteristics of the Class III CL MDA are presented in Section 5.5.

3.6 Class IV MDA

The Class IV MDA adds an amplitude control system to the Class III MDA configuration. This consists of an electromagnet that 'boosts' the value of the normal magnetic field for the magnetron (also called a buckboost coil). By varying the magnetic field, the output power of the magnetron may be controlled. This enhancement provides the capability for independent control of the MDA output power and operating frequency.

3.6.1 Functional Description

It should be noted that no laboratory measurements were accomplished on a Class IV MDA as part of this effort. This section is provided to complete the discussion of MDA types. The functional components of the Class IV MDA are shown in Figure 3.6-1.

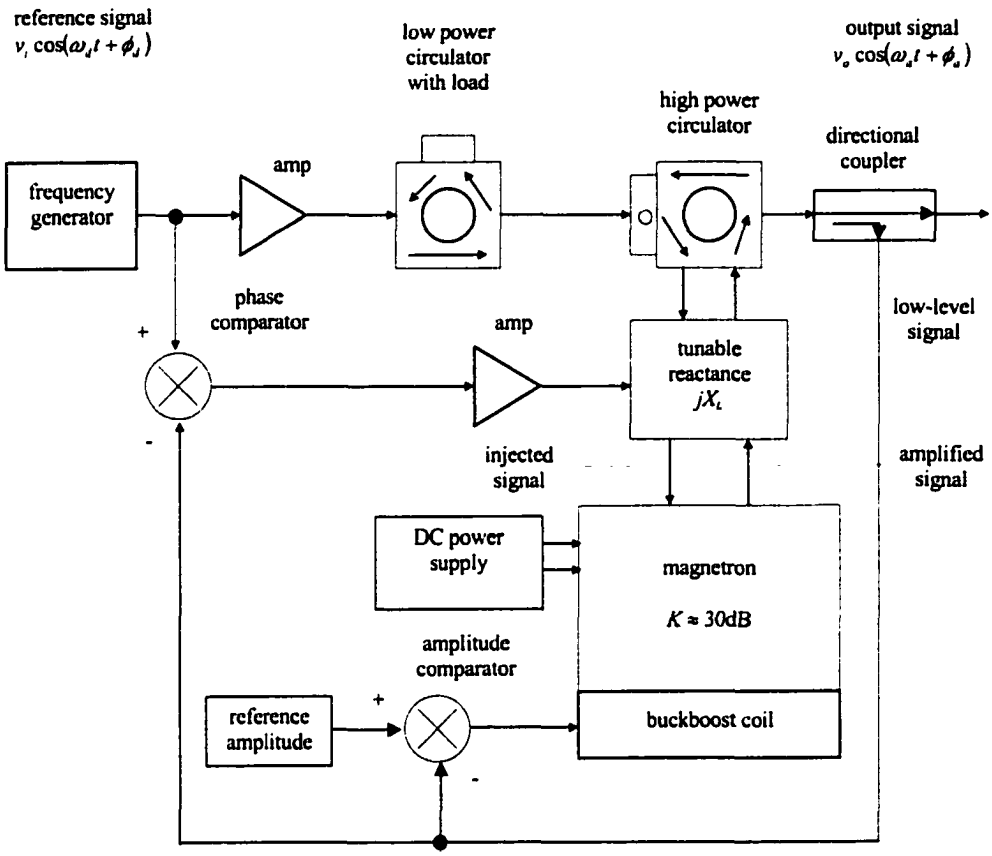

Figure 3.6-1. Class IV MDA Functional Diagram.

3.6.2 Theory of Operation

The buckboost coil is an integral part of the magnetron. It can either be used to supply the entire magnetic field needed by the magnetron, or may be used in conjunction with a permanent magnet to provide a given range of adjustment. A conceptual arrangement of the electromagnet and permanent magnet is shown in Figure 3.6-2.

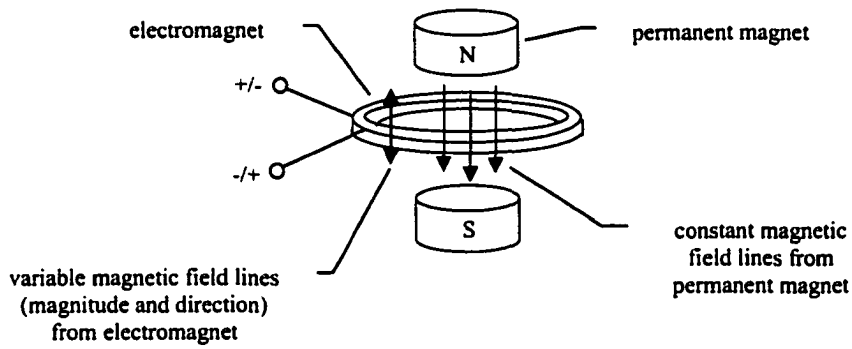

Figure 3.6-2. Magnetic Flux Lines from Permanent Magnets & Electromagnet.

Hartree's equation governing the relation between the magnetic field and voltage required for oscillation of a magnetron is given in Equation 4.1-12. This may be solved in terms of Hull's voltage or magnetic field cutoff equations.

The system model for the Class IV MDA is provided in Figure 3.6-3. Partial details of the model are available in Appendix A.3.

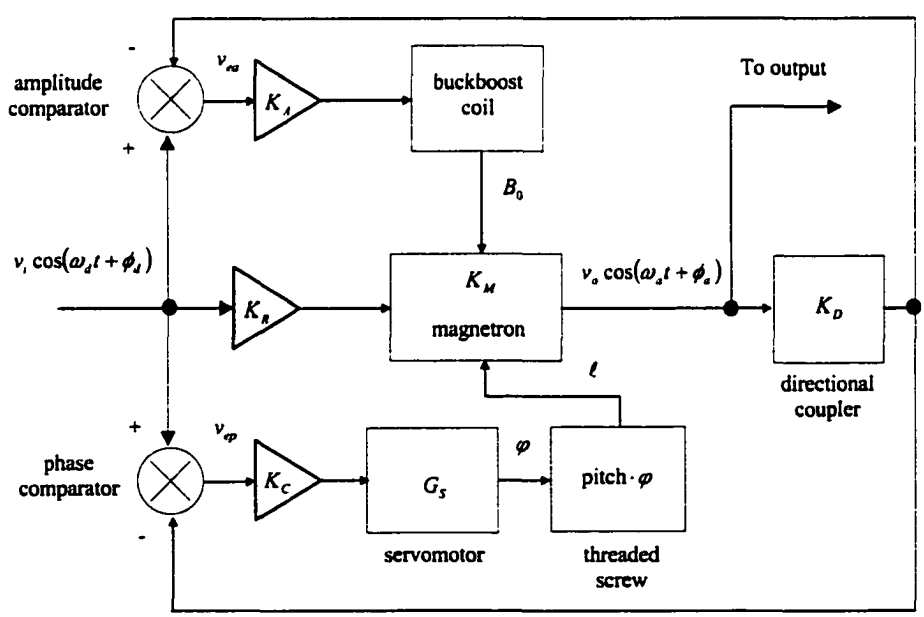

Figure 3.6-3. Control Block Diagram for Class IV MDA.

3.6.2 Physical Configuration

Figure 3.6-4 shows the major components used to implement the Class IV MDA. This diagram shows a simplified physical configuration, which includes only major components. Not shown are miscellaneous components used to distribute and protect signals, such as power splitters, low-power circulators, and attenuators. Additional details are provided in Appendix A.2.

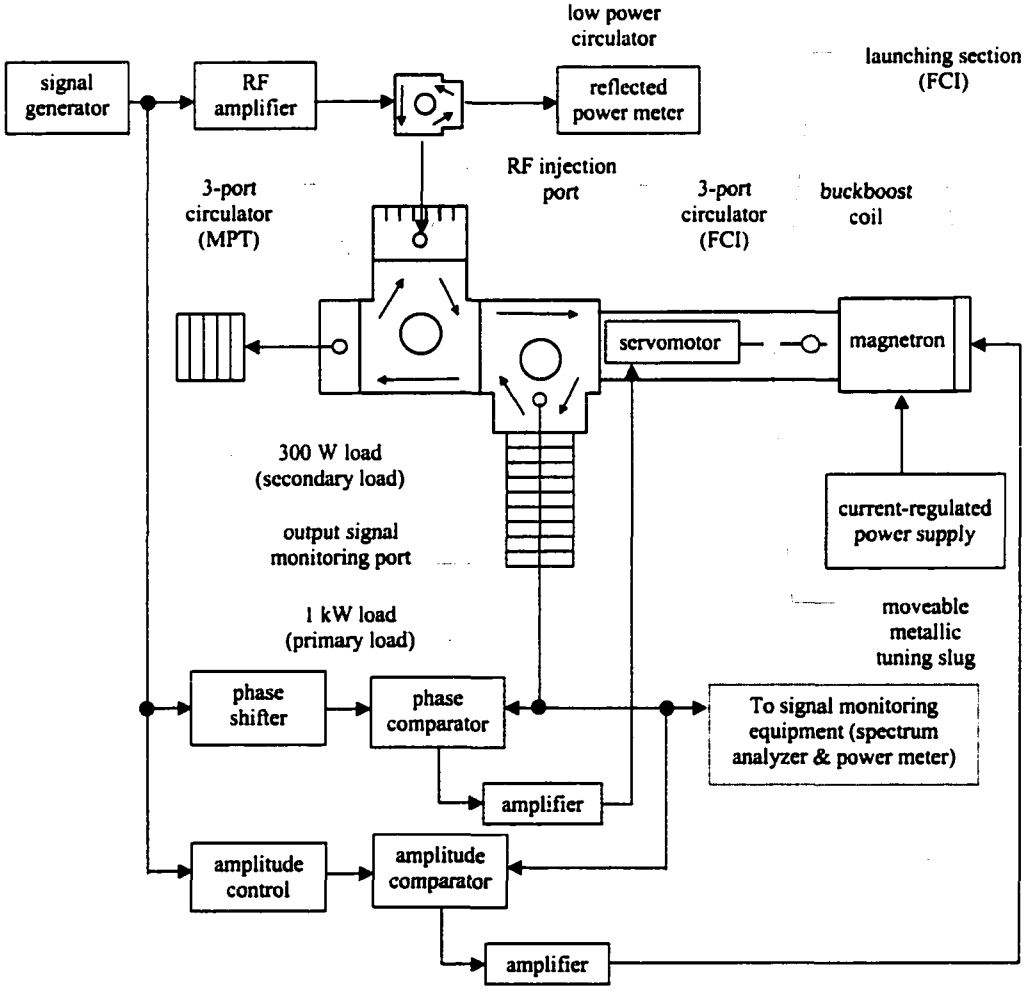

Figure 3.6-4. Physical Configuration of a Class IV MDA.

4.0 Theory of Magnetron Operation

This chapter describes the operation of the magnetron. This includes its electron beam interaction with the slow-wave structure, its resonant circuit, and its coupling to the output load. Additional information on modeling the magnetron empirically is provided in Appendix A.3.

4.1 Governing Equations

The magnetron is a member of the class of *crossed-field* devices, meaning that the magnetic and electric fields are perpendicular to each other. These come in different shapes, with specific rules governing the operation of each. However, most are some variant of the generic type shown in Figure 4.1-1.

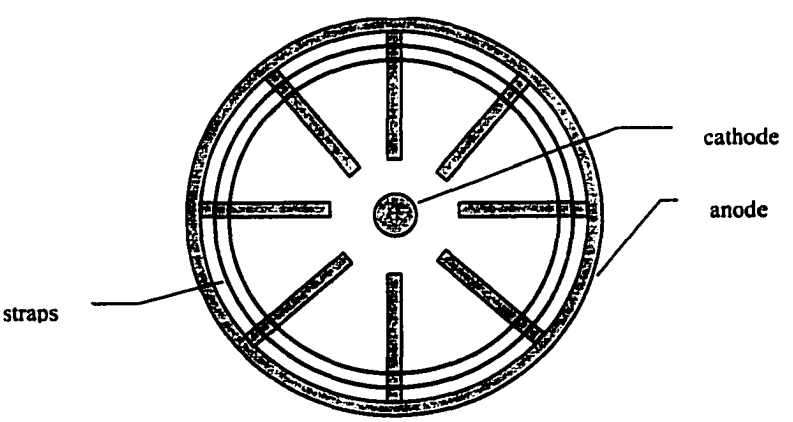

Figure 4.1-1. Cross-Section of a Strapped Magnetron [15].

The magnetron consists of a tuned cavity with equal angular spacing between vanes. In general, this structure is the anode of the magnetron. The cathode is a central rod with a filament that supplies a source of electrons. The electric field is established radially between the cathode and anode, as shown in Figure 4.1-2. A magnet provides an axial magnetic field perpendicular to the electric field.

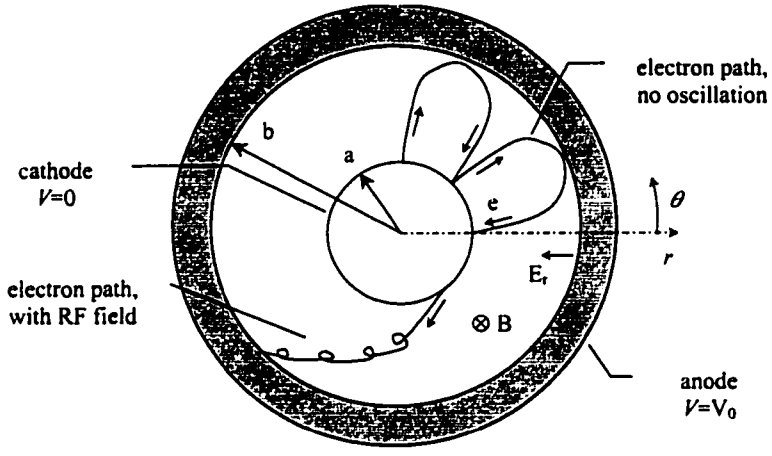

Figure 4.1-2. Simplified Magnetron Cavity. Cathode has radius *a* and anode radius *b*. Electron path shown before and during oscillation [15], [16].

The magnetron equations are developed by analyzing the effects of the electric and magnetic fields upon an electron in the cavity. The force experienced by an electron in an electric field is given by

$$\overrightarrow{F_E} = -e\vec{E} \tag{4.1-1}$$

where

$$\overrightarrow{F_E} = \text{force on electron due to electric field}\,[\text{N}]$$
$$\vec{E} = \text{electric field intensity}\left[\frac{\text{volt}}{\text{m}}\right]$$
$$e = \text{electron charge} = 1.6022\times10^{-19}[\text{C}].$$

The force due to the transverse magnetic field is

$$\overrightarrow{F_M} = -e\vec{v}\times\vec{B} \tag{4.1-2}$$

where

$\overrightarrow{F_M}$ = force on electron due to magnetic field [N]

$\vec{v}$ = electron velocity $\left[\frac{\text{m}}{\text{sec}}\right]$

$\vec{B}$ = magnetic flux density [Teslas].

The combined force on the electron due to both fields is given by Lorentz's equation,

$$\vec{F} = \overrightarrow{F_E} + \overrightarrow{F_M} = -e\left(\vec{E} + \vec{v} \times \vec{B}\right). \tag{4.1-3}$$

The electron's path through the crossed-field is shown in Figure 4.1-2. As the electron accelerates from the cathode toward the anode, the magnetic field acts upon it to change its direction. The acceleration a experienced by the electron is

$$\vec{a} = \frac{\vec{F}}{m} = -\frac{e}{m}\left(\vec{E} + \vec{v} \times \vec{B}\right) \tag{4.1-4}$$

where

$$m = \text{electron mass} = 9.1094 \times 10^{-31}[\text{kg}].$$

Equation 4.1-4 is expanded in cylindrical coordinates to obtain the equations of motion for the magnetron. Noting that the only fields existing are the radial electric field and the axial magnetic field,

$$\begin{aligned} E_\theta &= E_z = 0 \\ B_\theta &= B_r = 0 \end{aligned} \tag{4.1-5}$$

the equations are simplified to [16], [17]:

$$\frac{d^2 r}{dt^2} - r\left(\frac{d\theta}{dt}\right)^2 = \frac{e}{m} E_r - B_z r \frac{d\theta}{dt} \tag{4.1-6a}$$

$$\frac{1}{r}\frac{d}{dt}\left(r^2\frac{d\theta}{dt}\right)=\frac{e}{m}B_z\frac{dr}{dt}. \tag{4.1-6b}$$

Summing the radial forces on the electron at equilibrium (just grazing the anode), the centripetal force from the electron motion is counterbalanced by the force of the magnetic field,

$$\frac{mv^2}{r}=evB. \tag{4.1-7}$$

This may be rewritten in terms of the cyclotron angular frequency,

$$\omega_c=\frac{eB}{m}. \tag{4.1-8}$$

Manipulating Equation 4.1-6b and incorporating Equation 4.1-8 yields

$$\frac{d}{dt}\left(r^2\frac{d\theta}{dt}\right)=\frac{1}{2}\omega_c\frac{d}{dt}\left(r^2\right). \tag{4.1-9}$$

Since the magnetic field exerts a force that is perpendicular to the electron velocity, the total work upon the electron is zero. Therefore, the kinetic energy of the electron is equal to the work done by the electric field,

$$\frac{1}{2}mv^2=eV. \tag{4.1-10}$$

Upon emission by the filament, the electron leaves the cathode perpendicular to its surface and travels as discussed above. If the field strengths are set correctly, the electron will almost graze the anode at the apex of its trajectory prior to making contact

with the anode or accelerating back toward the cathode. The associated boundary conditions for the initial and final electron states are

$$\left.\frac{d\theta}{dt}\right|_{r=a} = 0, \left.\frac{dr}{dt}\right|_{r=b} = 0. \tag{4.1-11}$$

Writing Equation 4.1-10 in terms of cylindrical coordinates, applying the boundary conditions, and substituting into Equation 4.1-9 leads to Hartree's condition [15], [16]

$$\frac{V_0}{B_0^2} = \frac{e}{8m} b^2 \left(1 - \frac{a^2}{b^2}\right)^2, \tag{4.1-12}$$

where

V_0 = anode voltage [V]
B_0 = magnetic flux density [Teslas]
b = radius to anode surface [m]
a = cathode (filament) radius [m].

This equation may be solved in terms of Hull's cutoff voltage V_{0C}. If the anode voltage is less than this for a given magnetic field, the electrons will not reach the anode. Conversely, the equation may be solved for a particular value of the magnetic field B_{0C} needed for oscillation (Hull cutoff magnetic equation). If the value of the magnetic field exceeds this for a specific value of the applied voltage, the electrons will not reach the anode of the magnetron.

For the magnetron to oscillate, the electron cloud must add constructively as it rotates about the cathode. This type of reentrant structure requires the total phase shift around the magnetron to be a multiple of 2π radians. The period of revolution is given by

$$T = \frac{2\pi}{\omega_c} = \frac{2\pi m}{eB}. \tag{4.1-13}$$

For a magnetron with N cavities, the phase shift θ_n between adjacent cavities is given by

$$\theta_n = \frac{2\pi n}{N}, \tag{4.1-14}$$

where

n = mode number of oscillation
N = number of cavities.

Magnetrons are normally operated in the π-mode, which means the phase is opposite between adjacent cavities ($\theta_n = \pi$). This corresponds to a mode number of $n = N/2$. An example of a vaned magnetron operating in the π-mode is shown in Figure 4.1-3.

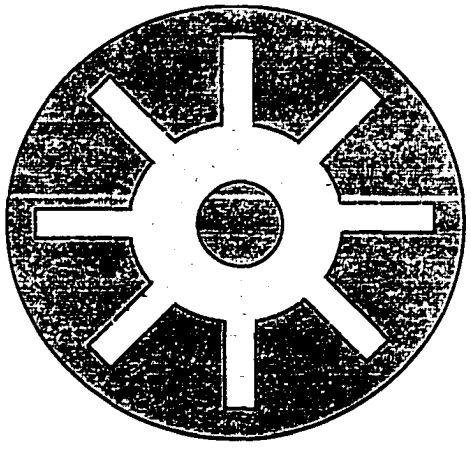

Figure 4.1-3. Lines of Force in a 8-cavity, π-mode Magnetron [16].

In this mode, the electromagnetic fields are primarily excited in the cavities. As the field strength increases, then decreases with each cavity, it creates a slow wave that rotates around the magnetron. Energy is transferred from the electrons to the traveling slow

wave (RF field) when the cyclotron frequency of the electrons equals that of the angular frequency of the field,

$$\frac{eB}{m} = \omega_c = \beta_0 \frac{d\theta}{dt} \tag{4.1-15}$$

where

β_0 = phase constant of the slow wave structure
θ = phase angle of the slow wave.

The phase constant of the slow wave structure β_0 is defined to be

$$\beta_0 = \frac{2\pi n}{NL} \tag{4.1-16}$$

where

L = mean separation between cavities [rad].

A diagram of the electron cloud and RF field interaction is shown in Figure 4.1-4. As oscillation begins, the electrons bunch into $N/2$ groupings resembling spokes of a wheel. These spokes rotate clockwise about the cavity space. As the electrons impact the anode wall, they cause a migration of the electrons in the walls of the anode structure. This causes a voltage to be applied across the magnetron vane. As the electron cloud continues to rotate, the polarity of the voltage is reversed. The resulting sinusoidal wave is coupled to the waveguide via the magnetron RF probe [15].

A certain number of the electrons will be accelerated ahead of or behind the spoke. Some of these will be reintegrated into the spoke, while others will strike the cathode. This action breaks new electrons free from the cathode to sustain the process, allowing the filament current to be turned off after oscillation is established.

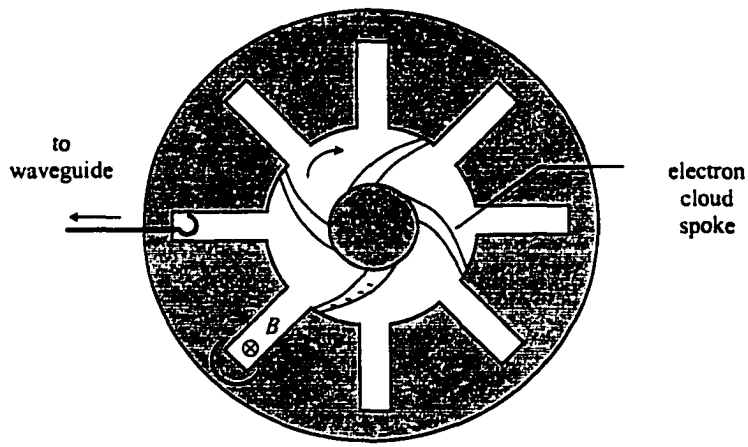

Figure 4.1-4. Interaction of Electron Cloud and RF Field [15].

4.2 Equivalent Circuit Models for the Magnetron and Load

The operation of the MDA as a RF amplifier may be explained with the aid of David's expression for a frequency-locked oscillator [11],

$$\phi = \sin^{-1}\left[\frac{(f - f_I)}{f} \cdot Q_E \cdot \sqrt{\frac{P_O}{P_I}}\right] \tag{4.2-1}$$

where

ϕ = phase shift between the output and input signals of amplifier
f = free running frequency of magnetron
f_I = frequency of input drive signal
P_I = power in from input drive signal
P_O = power out of amplifier
Q_E = external Q of circuit.

The phase shift between the input and output terminals of the frequency-locked oscillator is a function of (1) the frequency difference between the locking signal and the free running oscillator, (2) the external quality factor Q_E of the device, and (3) the ratio of the

output power to input locking power. The phase difference will be forced to a value between ±90° when the oscillator is locked to the input drive frequency.

From transmission line theory, the waveguide electric and magnetic fields may be defined in terms of equivalent voltages and currents. Therefore, David's equation may be analyzed in terms of the equivalent circuit shown in Figure 4.2-1.

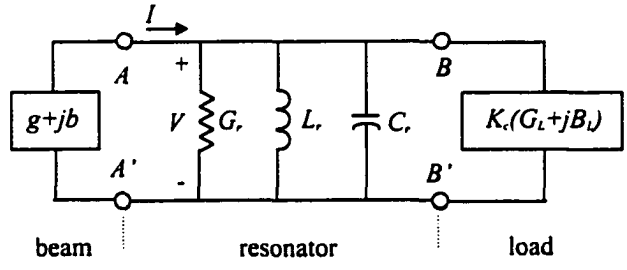

Figure 4.2-1. Equivalent Circuit for a Magnetron and Load [11].

The circuit parameters are defined to be:

$Y_e = g + jb$ = electronic admittance of electron beam
G_r = conductance of resonator
L_r = inductance of resonator
C_r = capacitance at vane tips
$Y_L = G_L + jB_L$ = load admittance seen by resonator
K_c = transformer constant (coupling cofficient) between load and resonator.

Then the admittance of the unloaded resonator is

$$Y_r = G_r + j\left(\omega C_r - \frac{1}{\omega L_r}\right). \tag{4.2-2}$$

For the unloaded circuit, resonance occurs at a frequency where the reactive components cancel and the input impedance is purely resistive,

$$\omega_0 = \frac{1}{\sqrt{L_r C_r}}. \tag{4.2-3}$$

At this point, the equivalent RF voltage V and current I at the vane tips (port AA' in Figure 4.2-1) are in phase.

The quality factor Q_0 of the unloaded circuit is [16], [17]

$$Q_0 = 2\pi \frac{\text{maximum energy stored}}{\text{energy dissipated per cycle}} = 2\pi \frac{[w_L(t) + w_C(t)]}{P_G T} \tag{4.2-4}$$

where

$w_L(t)$ = instantaneous energy in inductor
$w_C(t)$ = instantaneous energy in capacitor
P_G = power dissipated in resistor (conductance)
T = time period.

The energy stored in each reactive element is given by

$$w_{C(t)} = \frac{1}{2} C v^2 = \frac{I_m^2 R^2 C}{2} \cos^2 \omega_0 t \tag{4.2-5a}$$

$$w_{L(t)} = \frac{1}{2} L i^2 = \frac{1}{2} L \left(\frac{1}{L} \int_0^t v dt \right)^2 = \frac{I_m^2 R^2 C}{2} \sin^2 \omega_0 t . \tag{4.2-5b}$$

The total energy stored by the reactive elements is

$$w(t) = w_C(t) + w_L(t) = \frac{I_m^2 R^2 C}{2}. \tag{4.2-6}$$

The energy dissipated by the resistor is

$$P_R T = \frac{I_m^2 R}{2}\frac{1}{f_0} = \frac{I_m^2 R}{2f_0}. \tag{4.2-7}$$

The quality factor Q_0 of the unloaded circuit is

$$Q_0 = \frac{\omega_0 C_r}{G_r}. \tag{4.2-8}$$

The external quality factor Q_E for the resonator is defined as that looking at the load, assuming the conductance of the resonator is zero [18],

$$Q_E = \frac{\omega_0 C_r}{K_c G_L}. \tag{4.2-9}$$

Note that the electronic admittance of the driving network (electron beam) must be equal and opposite to that of the total load admittance seen (combination of the resonator and external load). As a condition of oscillation,

$$Y_e = -(Y_r + Y_L). \tag{4.2-10}$$

Expanding this equation into its component terms yields

$$-(g + jb) = \frac{1}{1/j\omega C_r} + G_r + \frac{1}{j\omega L_r} + K_c(G_L + jB_L), \tag{4.2-11}$$

where the electronic admittance provides a negative resistance to the load circuit at this point. Equating the real components of Equation 4.2-11 yields

$$-g = G_r + K_c G_L . \tag{4.2-12}$$

These components determine the power delivered to the load. This is commonly rewritten in terms of the quality factors,

$$\frac{|g|}{\omega_0 C_r} = \frac{1}{Q_0} + \frac{1}{Q_E} = \frac{1}{Q_{loaded}}, \tag{4.2-13}$$

The power delivered to the load is given by

$$P_L = \frac{V^2 G_L}{2}. \tag{4.2-14}$$

Equating the imaginary components of Equation 4.2-11 yields

$$-b = \omega C_r - \frac{1}{\omega L_r} + K_c B_L . \tag{4.2-15}$$

These components govern the frequency of operation of the magnetron under load. In terms of the resonant frequency, this may be rewritten as (with normalized load, $G_L = 1$)

$$\frac{|b|}{\omega_0 C_r} = 2\left(\frac{\omega^2 - \omega_0^2}{\omega_0}\right) + \frac{B_L}{Q_E G_L}, \tag{4.2-16}$$

Analyzing the circuit near resonance,

$$\omega = \omega_0 + \Delta\omega . \tag{4.2-17}$$

Then the normalized electronic susceptance is

$$\frac{|b|}{\omega_0 C_r} = \frac{(\omega_0 + \Delta\omega)^2 - \omega_0^2}{\omega_0(\omega_0 + \Delta\omega)} + \frac{B_L}{Q_E G_L} . \tag{4.2-18}$$

Discarding higher order terms,

$$\Delta\omega^2 \approx 0, \omega_0 \Delta\omega \approx 0 \tag{4.2-19}$$

then Equation 4.2-18 may be approximated as

$$\frac{|b|}{\omega_0 C_r} \approx \frac{2\Delta\omega}{\omega_0} + \frac{B_L}{Q_E G_L} . \tag{4.2-20}$$

Solving for the frequency of oscillation,

$$\omega' = \frac{|b|}{2C_r} + \omega_0 - \frac{\omega_0 B_L}{2Q_E G_L} . \tag{4.2-21}$$

To explain the interaction of the injected signal with the magnetron, we define a set of transmission equations at the output. An imaginary reference plane is established corresponding to the magnetron RF probe, as shown in Figure 4.2-2.

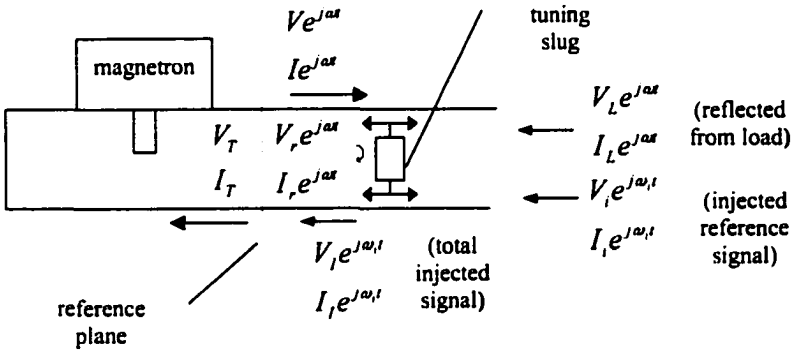

Figure 4.2-2. Magnetron-Load Interface (Transmission Line Equivalent).

This total 'injected' signal V_I may be the result of an injected reference signal V_i, the reflected signal from a tuning slug V_r, or the reflected signal due to a load mismatch V_L. The total voltage at the reference plane is the sum of the magnetron output and the injected waveforms,

$$V_T = Ve^{j\omega t}\left(1+\frac{V_I}{V}e^{j\Delta\omega t}\right) \tag{4.2-22}$$

where

$$V_I = V_i e^{j\omega_i t} + V_r e^{j\omega t} + V_L e^{j\omega t}$$
$$\Delta\omega = \omega_i - \omega.$$

Likewise, the total current at the reference plane is

$$I_T = Ie^{j\omega t}\left(1+\frac{I_I}{I}e^{j\Delta\omega t}\right). \tag{4.2-23}$$

For a relatively low-level input signal ($I_I << I$, $V_I << V$), the load admittance at the terminals is approximated as

$$Y = \frac{I_T}{V_T} \approx \frac{I}{V}\left(1 + \frac{I_I}{I} - \frac{V_I}{V}\right)e^{j\Delta\omega t}. \tag{4.2-24}$$

This is equivalent to a complex time-varying admittance,

$$Y = G'_L + jB'_L = G_L + jB_L + 2\rho G_L e^{j\Delta\omega t} \tag{4.2-25}$$

where

$G'_L + jB'_L$ = total load admittance with injected/reflected signal
$G_L + jB_L$ = passive load admittance
ρ = reflection coefficient.

Writing this equation in terms of its real and imaginary components,

$$Y = (G_L + 2\rho\cos\Delta\omega t) + j(B_L + 2\rho\sin\Delta\omega t). \tag{4.2-26}$$

Substituting Y'_L for Y_L in Equation 4.2-7 and equating the imaginary components yields

$$\frac{|b|}{2C_r} + \omega_0 - \frac{\omega_0 B_L}{2Q_E G_L} = \omega + \frac{\omega_0 \rho G_L \sin\Delta\omega t}{Q_E G_L}. \tag{4.2-27}$$

Using Equation 4.2-21, the frequency of oscillation with the injected signal becomes

$$\omega' = \omega + \frac{\omega_0 \rho \sin\Delta\omega t}{Q_E}. \tag{4.2-28}$$

The difference in the drive and free-running frequencies is related to the phase of the signal. The time varying term in Equation 4.2-28 provides the feedback that nudges the magnetron frequency towards that of the injected signal. Substituting $\phi = \Delta\omega t$ yields David's equation [11],

$$\frac{\omega - \omega'}{\omega_0} = \frac{|\rho| \sin \phi}{Q_E}. \tag{4.2-29}$$

The reflection coefficient is defined as

$$|\rho| = \frac{V_I}{V_O} = \sqrt{\frac{P_I}{P_O}} \tag{4.2-30}$$

where

V_I = magnitude of the incident (injected) wave
V_O = magnitude of the reflected (amplified) wave.

By this definition, the reflection coefficient is actually an amplification factor. If the injected signal frequency is near enough to the free-running frequency, the magnetron will lock ($f' = f_I$). Noting that the resonant frequency of the unloaded magnetron is approximately equal to its free-running frequency ($f_0 \approx f$), David's equation may be written in the form of Equation 4.2-1 given by Brown [8].

This equation may then be used to experimentally determine Q_E. The phase limits where $\sin(\phi) = \pm 1$ occur at the upper and lower locking frequencies (f_u and f_l, respectively), which can be measured. Equations 4.2-31a and 4.2.31b can be solved simultaneously,

$$-1 = \frac{(f - f_u)}{f} \cdot Q_E \cdot \sqrt{\frac{P_O}{P_I}}, \tag{4.2-31a}$$

$$+1 = \frac{(f - f_l)}{f} \cdot Q_E \cdot \sqrt{\frac{P_O}{P_I}}. \tag{4.2-31b}$$

Subtracting these and solving for Q_E yields

$$Q_E = \frac{2f}{BW}\sqrt{\frac{P_I}{P_O}}. \tag{4.2-32}$$

where

$$BW = \text{locking bandwidth} = f_u - f_l.$$

In a similar fashion, the effects on power output may be determined. Equating the real parts of Equations 4.2-6b and 4.2-16 two equations results in a modified equation for Q. The electronic conductance is given by

$$-g = G_r + K_c G'_L = G_r + K_c\left(G_L + 2\rho G_L \cos\Delta\omega t\right). \tag{4.2-33}$$

However, to find the optimum load impedance, the source impedance of the magnetron must first be determined. This may be analytically determined only through intimate knowledge of the magnetron's internal geometry. Generally, this information is not available to the application engineer desiring to model the magnetron. Therefore, the source impedance must be determined empirically.

4.3 Impedance Effects on Magnetron Operation

This section discusses the effects of load impedance on the operation of the magnetron. The output of the magnetron is dependent upon the load presented at the output port, as modeled in Figure 4.2-2. The total impedance presented to the magnetron is a combination of the primary load, the tuning slug, the injected signal, and reflections from any components in the system. All of these add some contribution to the total E and H fields (or equivalent V and I for the transmission line representation). Each must be accounted for in analyzing the effects on the magnetron.

A common means to graphically analyze the magnetron performance is through the use of a Rieke diagram [19], [20]. Plotting a Rieke diagram for a magnetron requires

measuring the magnetron's operating frequency and power at various load impedances. The impedance (reflection coefficient) data is plotted on the Smith chart, then contours of constant frequency and output power are overlayed on the load impedance data points. The resulting plots appear throughout the discussion of results in Chapter 5 and in Appendix A.4. These are similar to the Rieke diagram shown in Figure 4.3-1.

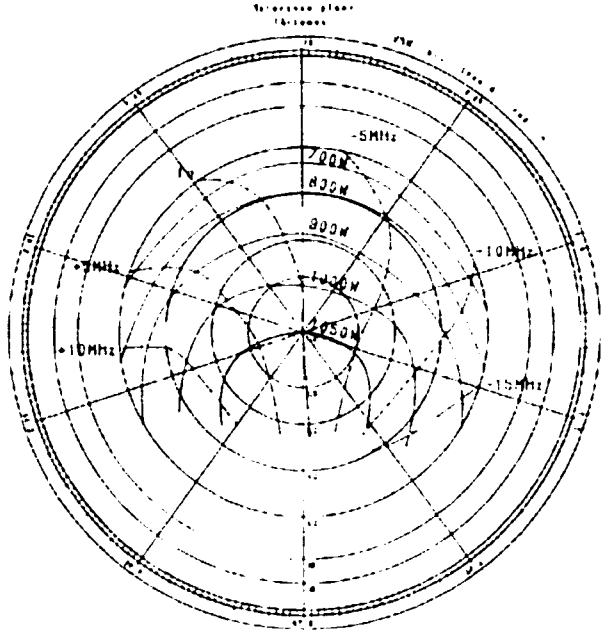

Figure 4.3-1. Manufacturer's Rieke Diagram for Sanyo 2M218 Magnetron [21].

The sink region of the Rieke diagram is located at the bottom of the graph. Constant frequency curves (dashed lines) radiate out from this point, output power curves wrap around it. This region provides the largest changes in magnetron output power and operating frequency for a given amount of impedance tuning. Traversing this region provides sharp changes in frequency and power, as will be shown in Section 5.4.

The method for creating the Rieke diagram, and tools for analyzing it are provided in Appendices A.4.1 and A.4.2.

5.0 MDA Performance Characteristics

This chapter details the performance characteristics of the Magnetron Directional Amplifier (MDA). Each class of MDA is investigated experimentally and the measured results are compared with analytic models. The overall objective of this research was to demonstrate that the MDA provides adequate power, frequency, and phase control for phased-array wireless power transmission (WPT) applications. Specific data collection objectives are outlined in subsequent sections.

5.1 Magnetron Operating Characteristics

The first step in examining the operation of the MDA is the analysis of a single magnetron. The understanding of its behavior is crucial, as it will serve as the foundation for developing increasingly complex layers of added components. The hardware configuration used to test the magnetron behavior is illustrated in Figure 3.1-4. Unless otherwise noted, the magnetron used is a Samsung 2M181 (S/N 5194) operating at 300 mA anode current.

Wireless power transmission applications will require multiple MDA units to be integrated together. The aggregate beam pattern is dependent upon the signal output from each of the contributing units. Individual magnetrons may at times be affected by power or load fluctuations, causing their outputs to change or to drop out completely. Therefore, it is desirable to understand how magnetrons respond to temperature fluctuations.

To determine the temperature sensitivity of the magnetron, the following parameters were measured as the magnetron approached its steady state operating temperature: (1) case temperature, (2) operating frequency, and (3) output power. The temperature was measured externally at the case, as shown in Figure 3.1-5.

Time to Achieve Operating Temperature. Figure 5.1-1 shows the amount of time necessary for a Samsung 2M181 magnetron to reach thermal equilibrium for a given configuration and thermal environment. This is useful, since the frequency of operation for the magnetron corresponds strongly with its measured case temperature.

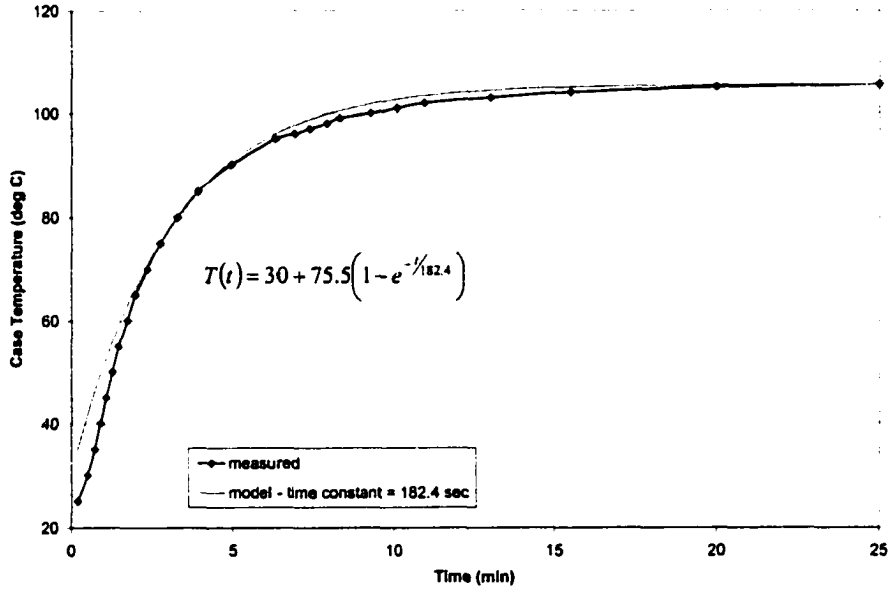

Figure 5.1-1. Case Temperature Heating as a Function of Time for Samsung 2M181 Magnetron. Anode current I_{anode} = 300 mA; anode voltage $V_{anode} \approx 4$ kV.

The magnetron case temperature may be roughly modeled by the first order heat equation,

$$T(t) = T_{offset} + T_{\circ}\left(1 - e^{-t/\tau}\right)[\text{deg C}] \qquad (5.1\text{-}1)$$

where τ = thermal time constant.

For cooling, the magnetron follows the curve shown in Figure 5.1-2. The cooling curve is modeled by

$$T(t) = T_{offset} + T_o e^{-t/\tau} [\text{deg C}]. \qquad (5.1\text{-}2)$$

The thermal time constants for heating and cooling are approximately 200 seconds.

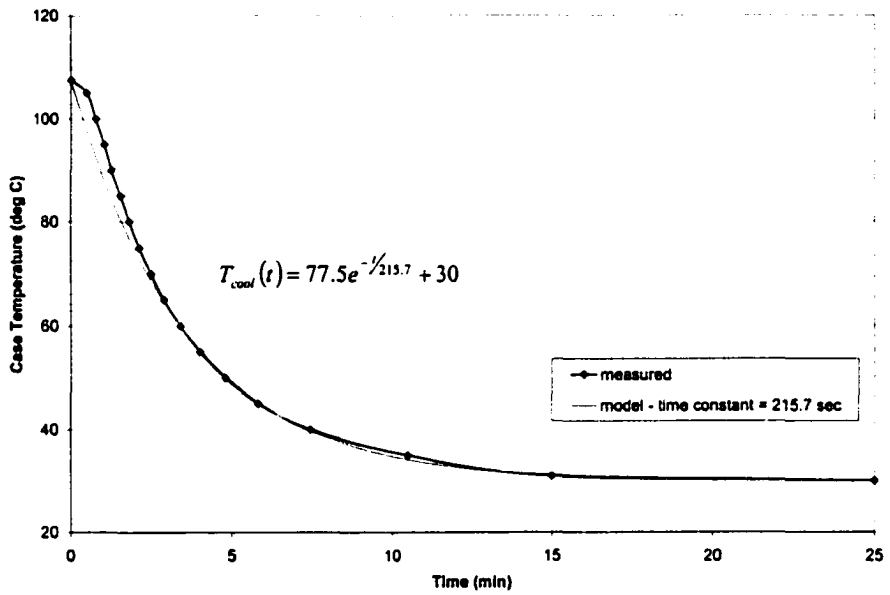

Figure 5.1-2. Case Temperature Cooling as a Function of Time for Samsung 2M181 Magnetron. Anode current removed.

Frequency Correlation with Temperature. The magnetron's operating frequency and output power both depend upon the input power and load impedance. Figure 5.1-3 shows how the magnetron's frequency varies with its temperature. The steady-state temperature at which the magnetron operates is correlated to a specific free-running frequency f_0 for a given load. The temperature of the magnetron in effect changes the total load seen. This is explained by the expansion of the waveguide components caused by heat absorption.

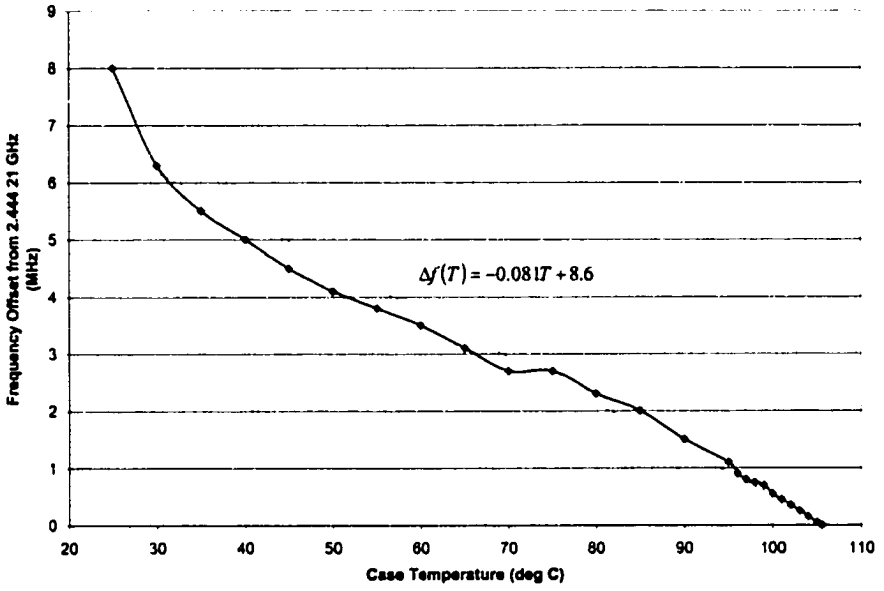

Figure 5.1-3. Operating Frequency versus Magnetron Case Temperature.

This particular magnetron varies its frequency by approximately 8 MHz before reaching its steady state temperature. As shown in Figure 5.1-1, the majority of this shift occurs early in the warmup. The linear nature of the curve suggests the magnetron cavity size, and therefore impedance, varies linearly with temperature. This assertion is supported by general design equations for the magnetron. The depth of the cavity is generally one-quarter wavelength at its resonant frequency,

$$h = \frac{\lambda_0}{4} = \frac{c}{4f_0} \tag{5.1-3}$$

where

$$\lambda_0 = \text{resonant wavelength of cavity}[\text{m}]$$
$$f_0 = \text{resonant frequency of cavity}[\text{Hz}]$$
$$c = \text{speed of light} = 3\times10^8\left[\frac{\text{m}}{\text{sec}}\right].$$

Therefore, an increase in temperature increases the cavity depth, thereby decreasing the resonant frequency,

$$\Delta T \uparrow \Rightarrow \Delta h \uparrow \Rightarrow \Delta f_0 \downarrow . \tag{5.1-4}$$

This assertion is confirmed by the magnetron design equation [15]

$$\Delta \lambda = \lambda \alpha \Delta T \tag{5.1-5}$$

where α = thermal expansion coefficient .

Output Power Correlation with Temperature. The same temperature-induced impedance changes also cause variations in output power. As the magnetron heats up, the surface resistivity R_s of the walls increases. This causes more power to be dissipated as heat energy, and therefore decreases the MDA output power and efficiency,

$$\Delta T \uparrow \Rightarrow R_s \uparrow \Rightarrow P \downarrow \Rightarrow \varepsilon \downarrow . \tag{5.1-6}$$

Figure 5.1-4 shows the magnetron RF output power and DC input power versus temperature. The power delivered by the magnetron shows the same dependency on operating temperature as does the frequency. As the magnetron heats up to normal operating temperature, the power output steadily drops. This is also the case for the DC power demanded of the power supply.

An efficiency curve for the magnetron is shown in Figure 5.1-5. Since the power output of the magnetron drops off faster than does the power supplied, the efficiency of the system decreases with temperature. The steps in the efficiency waveform are caused by the low resolution of the input current reading compared to the output power meter.

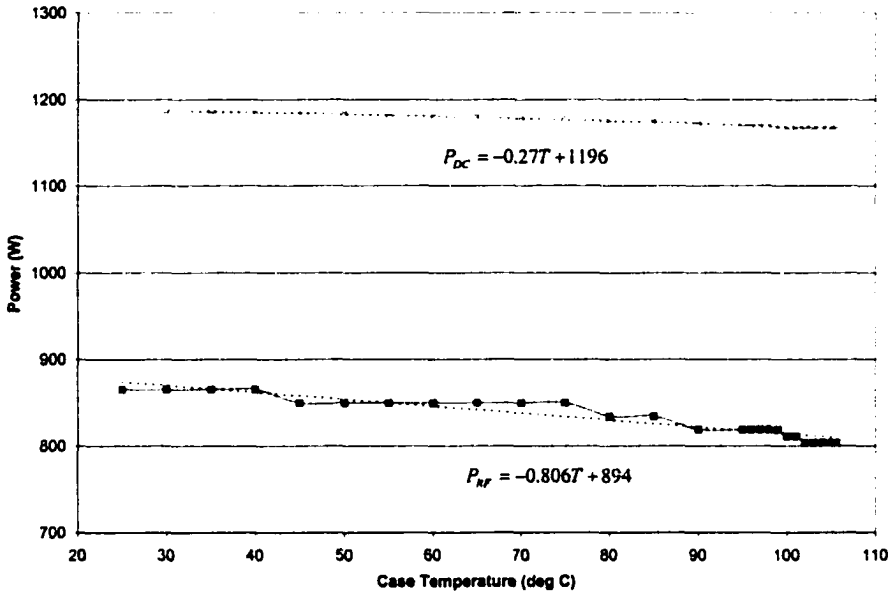

Figure 5.1-4. Power versus Magnetron Case Temperature.

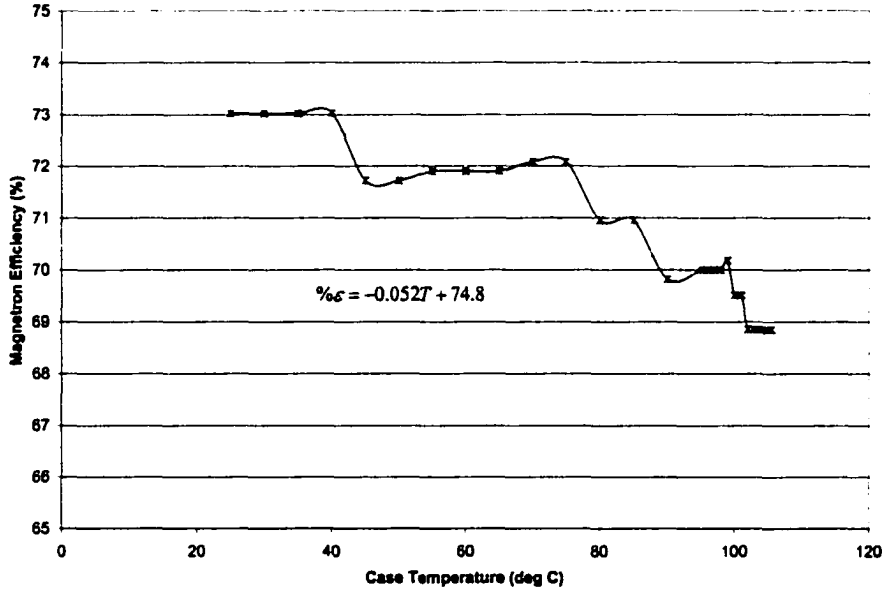

Figure 5.1-5. Efficiency versus Magnetron Case Temperature.

Since the impedance of the resonant cavity is dependent upon its physical dimensions, it is also a function of temperature,

$$Z_r(T) = \frac{1}{Y_r} = \frac{1}{G_r + jB_r} \tag{5.1-7}$$

where

Z_r = impedance of magnetron resonant cavity
T = temperature
Y_r = admittance of resonator
G_r = conductance of resonator
B_r = susceptance of resonator.

This fact may be of use in explaining the mode jumps seen in the MDA operation. Appendix A.4.6 contains the same performance data collected above for a Hitachi 2M170 magnetron used earlier in the MDA characterization effort. The performance of this magnetron reflects greater temperature dependence than the Samsung 2M181 examined here. It appeared to have two operating curves — one during warmup, another for sustained operations. This phenomenon is sometimes referred to as *moding* [15]. Additional data is presented in Appendix A.4.6 for the National 2M107A-605 magnetron, which also displayed moding effects.

5.2 Class I MDA Operation

The Class I MDA uses an injected RF signal to control the magnetron output. The hardware configuration used to characterize the Class I MDA is provided in Figure 3.2-3. Unless otherwise noted, the magnetron used is a Samsung 2M181 (S/N 5194) operating at 300 mA anode current.

When the combination of the injected signal's frequency and power level is sufficient to overcome the initial separation from the magnetron's free-running frequency, then the magnetron will lock to the injected signal. Once the magnetron is locked to the drive

signal, the frequency of the signal may be varied within a certain envelope for the injected power level.

On one hand, it is desirable to make the frequency pulling envelope of the Class I MDA as large as possible, as this provides a RF amplifier with the broadest possible frequency response. Such an amplifier may be useful as a high power RF source for some applications, or as a component in a limited capability phased array. In the latter case, a large frequency pulling range can provide more flexibility in frequency locking dissimilar elements of the array. This may not be a serious concern when constructing large-scale production arrays, but can be significant when operating within in a lab-type environment. Additionally, if the frequency of transmission may be varied, the frequency pulling range may translate into an increased beam steering capability for the phased array.

At the same time, it is also advantageous to minimize the drive signal strength required to lock the amplifier. This provides the highest gain operation of the MDA. If the MDA is used as a RF amplifier, lowering the drive signal level may avert the need to introduce intermediate amplifiers to boost the signal. If used as an element in a large phased array, this savings would be particularly important.

To quantify the sensitivity of the magnetron operation on these competing requirements, the following parameters were measured: (1) locking bandwidth versus injected signal strength and (2) output power versus injected signal frequency.

Locking Bandwidth versus Injected Signal Strength. Figure 5.2-1 shows how the injected signal strength affects the frequency locking range. As the drive signal is increased, the magnetron may be pulled further from its free-running frequency f_0 = 2.4429 GHz. This eventually leads to a point of diminishing returns, where an increase in injected signal strength provides relatively little additional locking bandwidth.

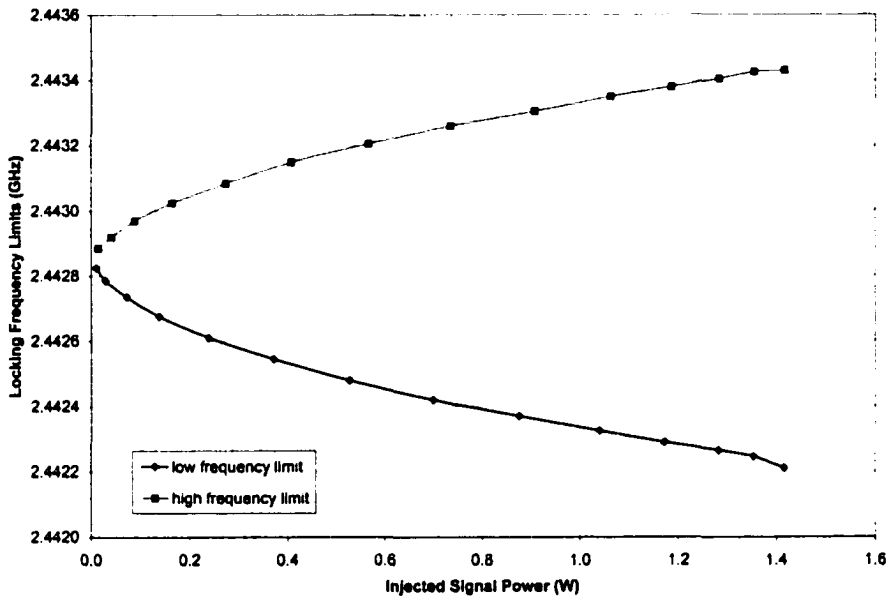

Figure 5.2-1. Locking Frequency Limits versus Injected Signal Power for a Class I MDA.

From this data, it was demonstrated that the Class I MDA behaves according to David's equation governing a phased-locked amplifier developed in Section 4.2. Solving Equation 4.2-32 for the projected bandwidth yields

$$BW_{projected} = \frac{2f}{Q_E}\sqrt{\frac{P_I}{P_O}}. \tag{5.2-1}$$

The value of the external quality factor was estimated from the performance chart shown in Figure 5.2-2, which utilizes the measured BW data to calculate Q_E in Equation 4.2-32. Note that two values for Q_E were calculated in Figure 5.2-2, the other being calculated by the average from Equations 4.2-20a and 4.2-20b. This calculation was added to provide verification of the low injected power range.

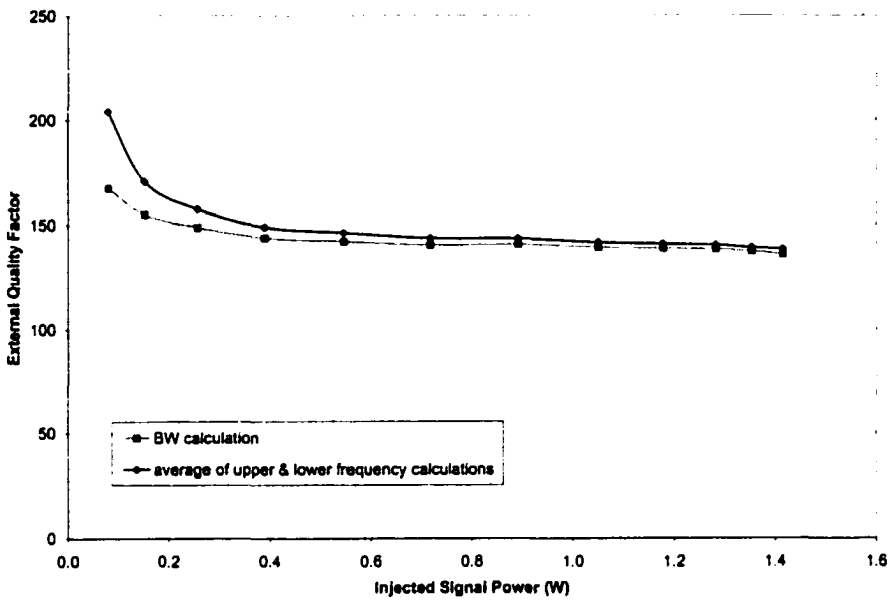

Figure 5.2-2. Quality Factor versus Injected Signal Strength for a Class I MDA.

Substituting in the appropriate values for the parameters: P_0 = 1227 W, f = 2.4429 GHz, and $Q_E \approx 140$, the equation for the projected bandwidth becomes

$$BW_{projected} = 0.996\sqrt{P_I}\,. \tag{5.2-2}$$

This model closely approximates the value for the locking bandwidth, as shown in Figure 5.2-3. The results matched to within 3% at the higher injected power levels. At the lower injected power levels, the analytical curve has a greater departure from the measured bandwidth curve due to the errors in approximating Q_E as a constant value. As can be seen in Figure 5.2-3, the value for Q_E is not constant in the lower injected signal range. This is partly due to error in measuring the injected and output signals, particularly at low power levels (Equation 5.2-1). The low power levels introduce errors in the power and frequency readings that impact the Q_E calculation,

$$P_I \downarrow \Rightarrow \Delta f \downarrow \Rightarrow \Delta f_{error} \uparrow \Rightarrow Q_{E\,error} \uparrow . \tag{5.2-3}$$

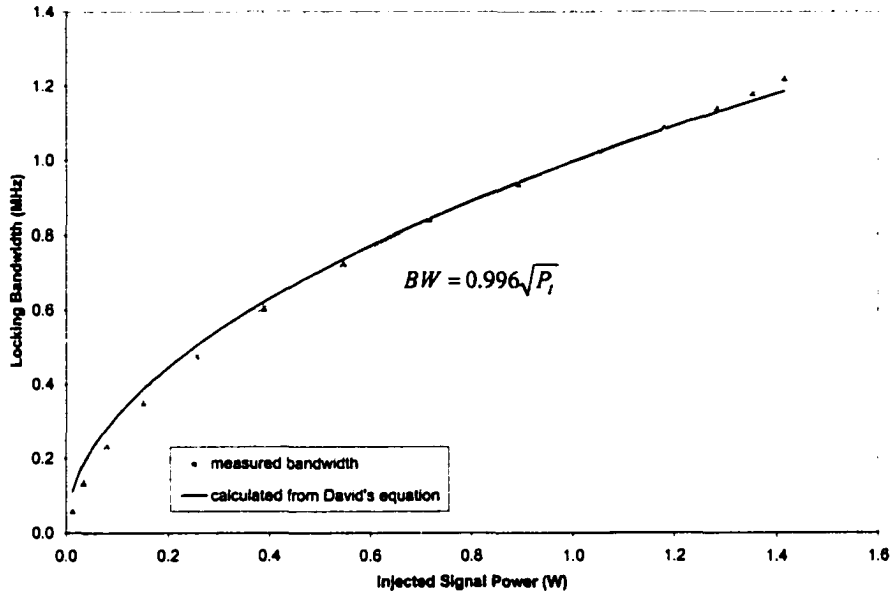

Figure 5.2-3. Comparison of Experimental and Theoretical Locking Bandwidth for a Class I MDA.

The preceding measurements are also subject to hardware limitations, including the RF amplifier response and reflection losses from the injection probe/waveguide mismatch. Figure A.2-4 shows that the reflection coefficient for this frequency range is $\Gamma \approx 0.24$, with an amplifier output power of 1.495 W. The actual power injected is therefore roughly 1.41 W (~95% of the 1.5 W used above), which impacts the calculations for low injected power levels. Additional sources of error are introduced from a slight frequency sensitivity of the output probe and associated components, and also in the reading of equipment scales. However, these are not considered significant to the overall results presented above.

Output Power versus Injected Signal Frequency. The frequency of the injected signal also has a slight affect on the output power of the MDA, as shown in Figure 5.2-4.

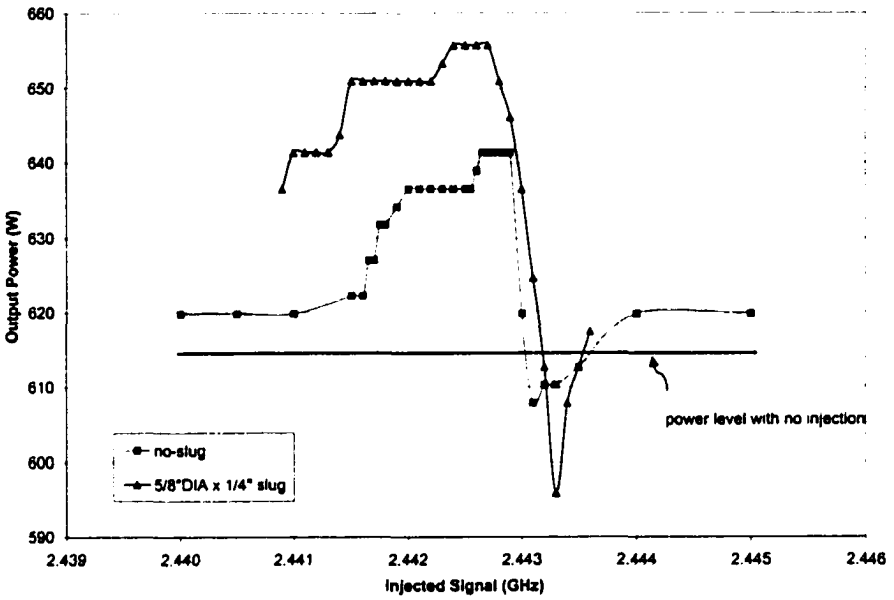

Figure 5.2-4. Output Power as a Function of Injected Signal Frequency for a Class I MDA. Injected reference power P_I = 1.6 W. Performance is compared to a Class III OL MDA using slug 1.

The behavior exhibited reflects that of a magnetron being pulled through the sink region Rieke diagram (discussed in Section 4.3). The Class I MDA power profile is compared with that of a Class III OL MDA. Differences in the curves may be explained by the difference in the impedances seen by the magnetron. Both curves appear to be stepped, but this is actually due to the limited resolution at which the data was read.

The slight variation in power (less than 5%) for the Class I MDA is produced solely by frequency change in the injected signal. The change in frequency causes a corresponding phase shift between the drive signal and that of the free-running magnetron. This phase shift may be viewed as a change in the impedance seen by the magnetron. If the MDA is locked, the reference signal will either constructively or destructively add to the free-running signal. The interface between the input and output waveforms at the magnetron RF probe is shown in Figure 3.2-2.

5.3 Class II MDA Operation

The Class II MDA has the same capabilities as a Class I MDA, but adds a variable DC input to control the magnetron output. The hardware configuration used to characterize the Class II MDA is provided in Figure 3.3-3. Unless otherwise noted, the magnetron used is a Samsung 2M181 (S/N 5194) operating at 300 mA anode current.

The primary focus of this section was on characterizing the effects of the input power control on the MDA operation. The first portion of this section deals with the effects of the power control alone. The combined effects of the input power control in conjunction with the injected reference signal are examined later in the discussion.

5.3.1 Effects of Input Power Control

Varying the input power provides another means to tune the magnetron. This is especially useful for implementing amplitude control in a phased array to reduce beam sidelobes. Unfortunately, changing the output power level also affects the frequency of operation. Therefore, it necessary to quantify the effects of the power control on the MDA. This data consists of the following parameters as a function of input power: (1) frequency, (2) output power, (3) efficiency, and (4) magnetron case temperature.

Operating Frequency versus Input Power. The frequency of the magnetron varies with the power applied, as shown in Figure 5.3-1. The frequency is plotted versus the anode current, as this adjustment was the means of controlling the input power. For this magnetron, the curve is equally balanced with respect to the maximum frequency. The experimental data is fit with a 3^{rd} order polynomial to show that it may easily be modeled. This curve may be broken into three separate regions — a linear front, a roughly parabolic top, and a linear back. Since both the front and back regions are linear for this magnetron, a pushing figure may be assigned for each. Breaking the curve into

these regions provides a simple means to calculate the expected performance of the Class II MDA. This can be helpful when tuning the MDA output signal using a combination of control inputs.

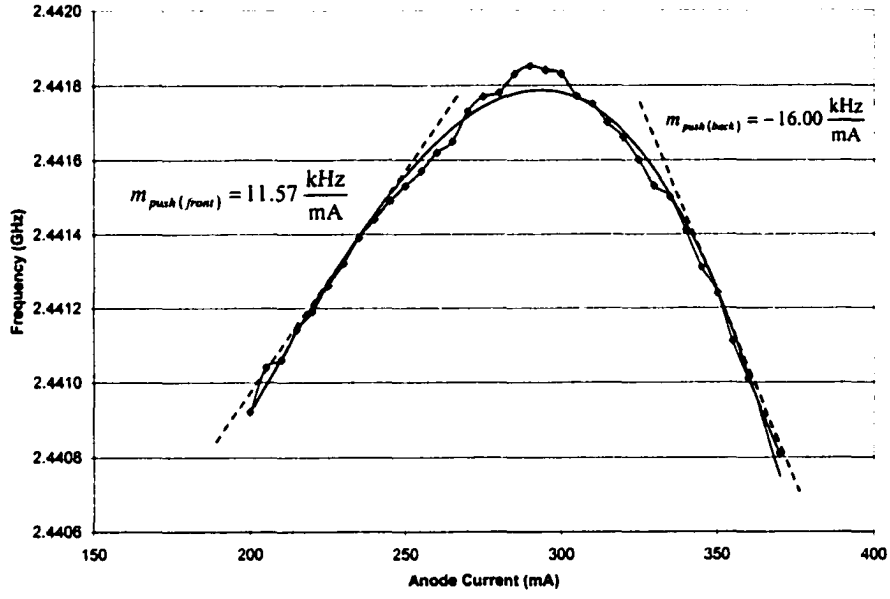

Figure 5.3-1. Operating Frequency versus Anode Current for a Class II MDA.

For most magnetrons, this curve appears roughly linear on the front with a shallow positive slope, then falling off sharply above the maximum frequency. An example of a more typical magnetron frequency curve is shown in Figure 5.3-2. Though this frequency response is not linear (instead monotonically increases), its behavior is more representative of generic magnetrons.

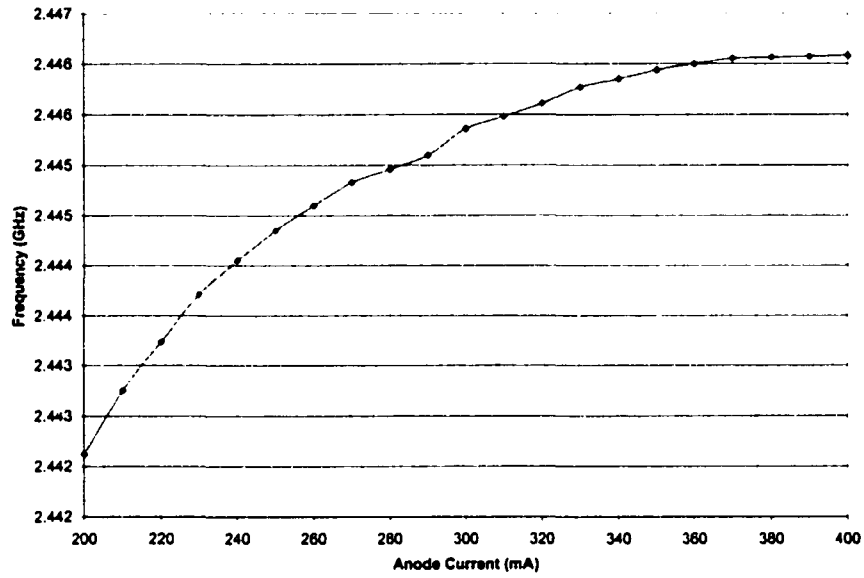

Figure 5.3-2. Operating Frequency versus Anode Current for a National 2M107A-605 Magnetron.

Output Power versus Input Power. The characteristic curve for the Class II MDA is shown in Figure 5.3-3.

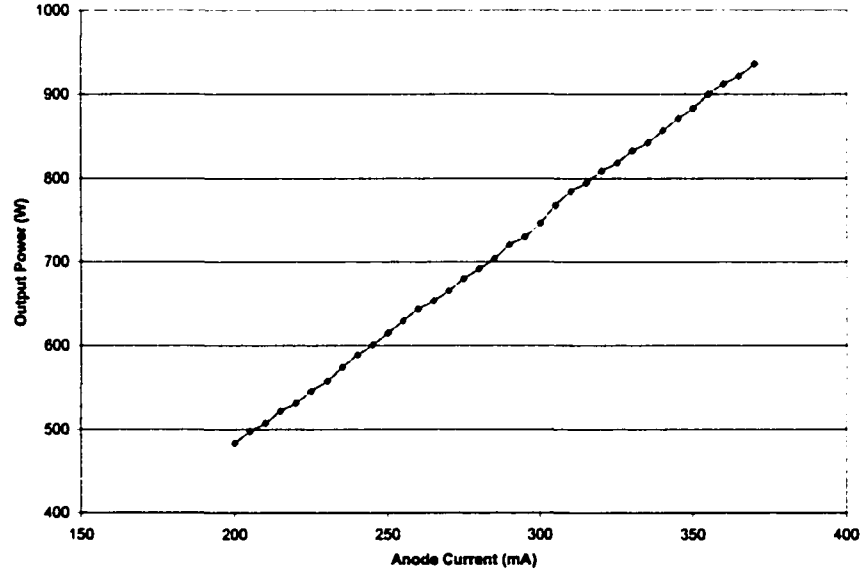

Figure 5.3-3. Output Power versus Anode Current for a Class II MDA.

The magnetron may be thought of as a RF generator that converts DC electrical power to RF power. The MDA operating efficiency is defined by each point on the curve and may vary slightly. However, the overall linearity of the curve shows the efficiency is relatively unaffected by changes in input power. This provides a measure of reassurance that tuning the MDA across relatively large operating power levels will not substantially alter its efficiency, which is important for amplitude control of phased arrays.

Efficiency versus Input Power. The efficiency of the power conversion is often a prime concern in optimizing the MDA operation. As mentioned above, the efficiency may be considered to be roughly constant over a particular operating range. But for applications involving large amounts of power such as WPT, these relatively small changes in efficiency can translate into large power losses. Therefore, it is important to analyze all potential means of maximizing this parameter.

The magnetron efficiency generally depends upon the power level at which it is driven. This can usually be maximized by operating the magnetron at a relatively high power level (this should be balanced with the lifetime requirements for the particular magnetron design or application). For precise measurements, the characteristics of the power supply driving the MDA must also be accounted for. Imperfections in the power supply *V-I* curve may cause fairly substantial differences in efficiency over a relatively small range. This is the case for the plots shown in Figure 5.3-4.

In this chart, the efficiency of a magnetron is compared using two different power supplies. These yield substantially different curves, varying in peak efficiency values and in stability. Power supply #1 yields a fairly flat efficiency response overall, but has a significant dip in the 270 – 300 mA region. Power supply #2 does not flatten until reaching approximately 300 mA and has similar instabilities in the 245 – 275 mA range.

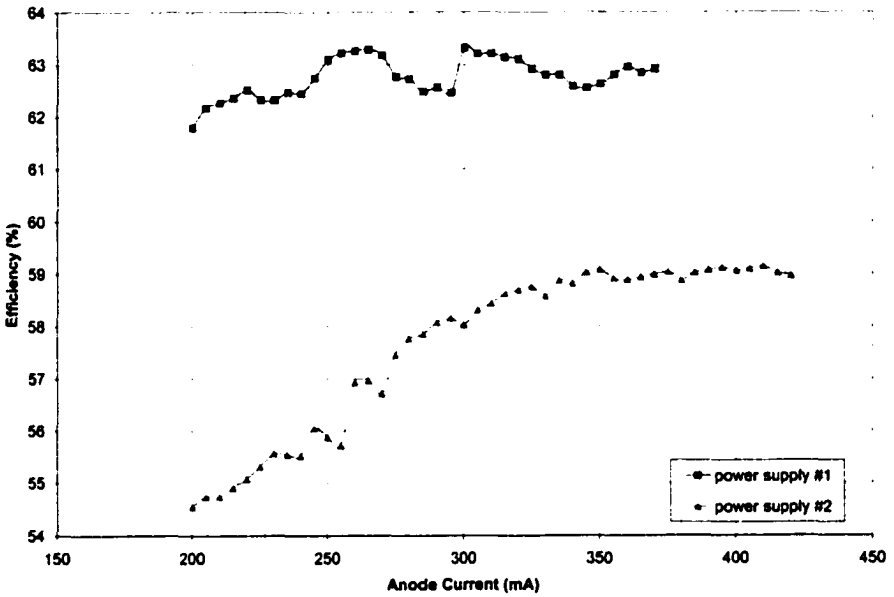

Figure 5.3-4. Efficiency as a Function of Anode Current for a Class II MDA Using Current-Regulated Power Supplies.

These measurements were made using an otherwise identical hardware configuration, showing a calibration error to exist between the units (mainly attributed to PS 2). The characteristic waveforms above have been shown to be repeatable over different data collection sets. Overall power levels may vary by ~2 – 3% between data sets, according to thermal loading conditions (Appendix A.4.8). However, the distinguishing shapes for each power supply are maintained.

The irregularities in the above efficiency data may be explained by examining the corresponding *V-I* curves for the power supplies, as shown in Figure 5.3-5. Spikes in the voltages correspond to regions of relatively low efficiency from Figure 5.3-4. These variations are not due to metering errors, but indicate nonlinearities in the power supplies' operation. The MDA output power confirms this behavior — normalizing this to the anode current provides a mirror image of the efficiency curves in Figure 5.3-4. These curves are of interest in analyzing the MDA behavior, as its operating point is defined by the intersection of these with the magnetron *V-I* curves. Their shapes may be

useful in explaining 'mode' shifts, where the MDA output jumps or moves between two distinct states. This phenomenon is discussed in Section 5.4 and Appendix A.4.6.

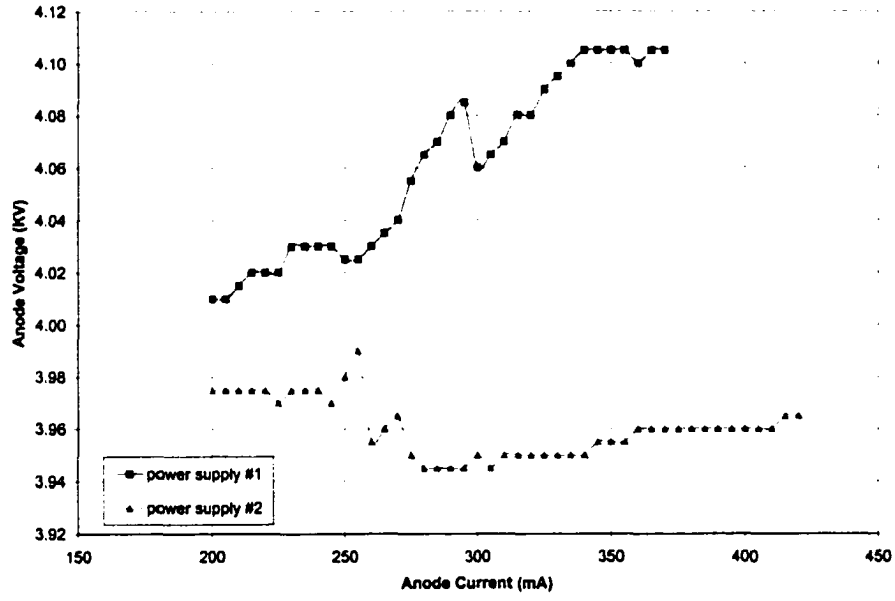

Figure 5.3-5. Current-Regulated Power Supply Characteristics.

Magnetron Temperature versus Input Power. The magnetron is a power converter with a finite efficiency, the remainder being converted to heat energy. As seen from the performance charts above, the efficiency of the magnetron is relatively independent of operating power. Thermal energy produced is directly proportional to the power applied,

$$Q_{heat} = P_{applied}(1-\varepsilon) \tag{5.3-1}$$

where

$$Q_{heat} = \text{heat energy}\,[\text{W}]$$
$$P_{applied} = \text{DC input power}\,[\text{W}]$$
$$\varepsilon = \text{magnetron efficiency.}$$

This heat energy is related to the magnetron temperature by

$$Q_{heat} = mc\Delta T \tag{5.3-2}$$

where

m = mass of anode block [kg]

c = specific heat capacity for block $\left[\frac{\text{kJ}}{\text{kg} \cdot \text{deg C}}\right]$

ΔT = temperature differential [deg C].

Therefore, its steady state operating temperature is a linear function of the power applied. The measured case temperature is shown in Figure 5.3-6.

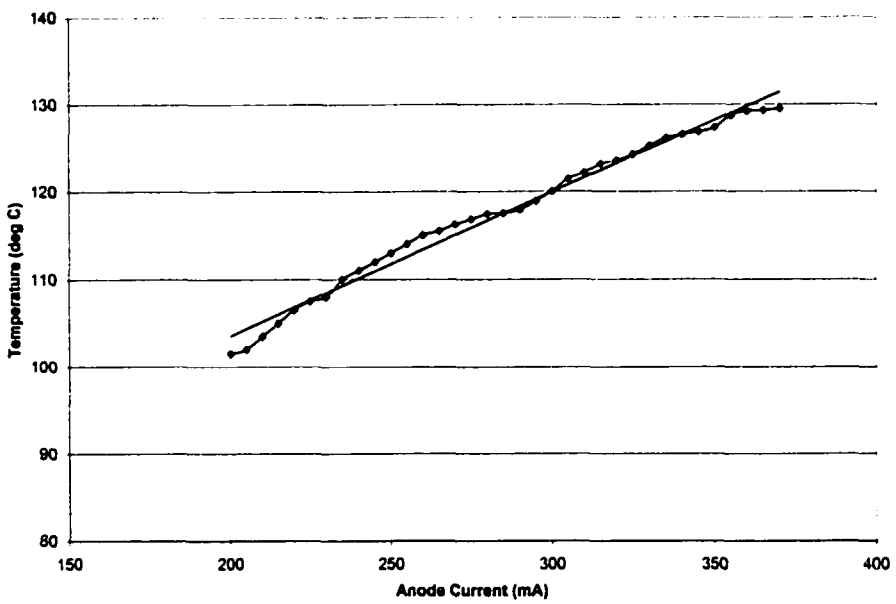

Figure 5.3-6. Case Temperature versus Anode Current for a Class II MDA.

In Section 5.1 it was shown that the magnetron operating frequency and power vary with its temperature. Applying a change in the anode current has the effect of a step input to the system, creating a transient response in its output power and frequency. The effect of an input power change is shown in Figure 5.3-7.

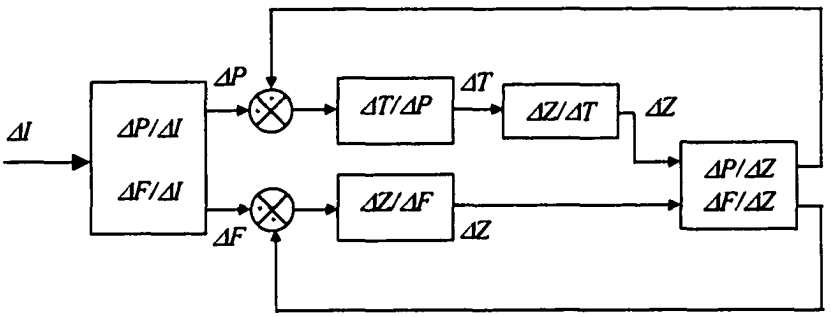

Figure 5.3-7. MDA Operating Point Selection.

A change in anode current sets a new initial operating point (frequency and power) for the MDA, given by Figures 5.3-1 and 5.3-3. Because of the change in operating power, the temperature of the magnetron will adjust according to Figure 5.3-6. The change in frequency also affects the load impedance seen by the magnetron, as shown in Figure A.4.2-7. The temperature change causes the waveguide and load to change size, thereby altering the load impedance. The load impedance then shifts the magnetron operating point from its initial position. The loop continues until thermal equilibrium is reached.

This transient behavior should be considered when designing and testing WPT systems. During open-loop operation, the system must be allowed adequate time to reach thermal equilibrium, as the power and frequency will drift. For normal closed-loop operation, the phase and amplitude feedback systems must provide sufficient control to overcome these effects while the system temperature stabilizes. This will be especially important for system startup. In this case, it may be necessary to determine an appropriate startup time prior to engaging control of the array.

5.3.2 Combined Effects of Input Power Control and Injected Reference Signal

Power control provides a second means to vary the gain of the system. Previous efforts to characterize the system for gain less than 30 dB were hampered by the limited power provided by the RF amplifier (~1.5 W maximum). Reducing the operating power of the

magnetron decreases the system gain, providing access to the larger locking bandwidth operation of the MDA. By varying both the injected and output power levels, the following effects may be quantified: (1) phase shift versus frequency, (2) locking bandwidth versus gain, and (3) Q_E versus gain.

Phase Shift versus Frequency. In Section 5.2, the locking bandwidth for the Class I MDA was determined. This was accomplished by injecting an amplified RF reference signal into the MDA and measuring the maximum frequency locking range. The resultant bounds for the frequency range correspond to the limits of phase of shift (±90°). It is also possible to measure the phase difference between the free-running and injected signals for any signal falling within the allowable range. To accomplish this, it is necessary to augment the equipment shown in Figure 3.3-3. The additional equipment includes a phase shifter, a phase comparator, a multimeter, and associated components needed to connect these. The modified test configuration is described in Appendix A.2.

The phase shift was measured by first noting the free-running frequency of the MDA, and matching the injected signal to this value. The phase shifter was then adjusted so that the phase comparator provided an output of zero (no phase shift between the input and output signals). Then the injected signal was incrementally displaced from the free-running frequency, noting the amount of phase shift required to re-zero the phase output. This same process was repeated for different values of injected power and output power.

The experimental data was verified by calculating the theoretical values of phase shift using David's equation (Equation 4.2-1). The injected signal level P_I was first adjusted for the probe impedance mismatch and RF amplifier response in Appendix A.2. Figure A.2-4 shows that the reflection coefficient for this frequency range is approximately constant with $\Gamma \approx 0.24$, allowing ~95% of the power injected to reach the magnetron. With few exceptions, the resulting calculated phase was identical to the measured data.

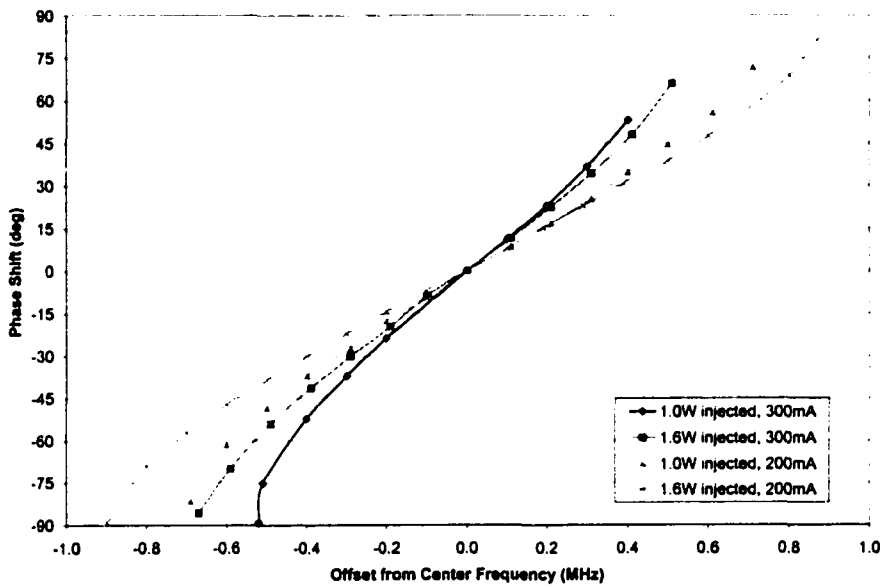

Figure 5.3-8. Phase Shift versus Frequency for a Class II MDA.

Figure 5.3-8 shows that the lower phase limit is essentially achieved. However, the upper phase limit falls short of the theoretical value. The shortfall is related to the gain of the MDA, according to Table 5.3-1.

Table 5.3-1. Phase Shortfalls for Various Power Ratios.

Anode current (mA)	Output Power (W)	Injected Power (W)	Power Ratio (dB)	+90° Shortfall (deg)
200	802	1.510	27.25	8.63
200	802	0.945	29.29	18.41
300	1218	1.510	29.07	24.01
300	1218	0.945	31.10	26.97

The largest shortfall of the +90° phase limit occurs for the largest value of gain, whereas the closest value occurs for the lowest system gain. The gain of the system is directly

related to the strength of the injected signal versus that of the reflected power at the magnetron probe (or injection probe). Higher output signals reflect more unwanted energy back towards the probe, thereby drowning out the injected signal more quickly.

The external quality factor Q_E may be re-calculated using Equation 5.2-1. The resulting curves are plotted in Figure 5.3-9. Differences between this data and that of Figure 5.2-2 are due to changes in the hardware configuration (Appendices A.4.3, A.4.5, and A.4.8). Note that the data near the center frequency is unreliable due to the proximity of free-running and injected frequency values. This region may be clarified by providing additional measurements.

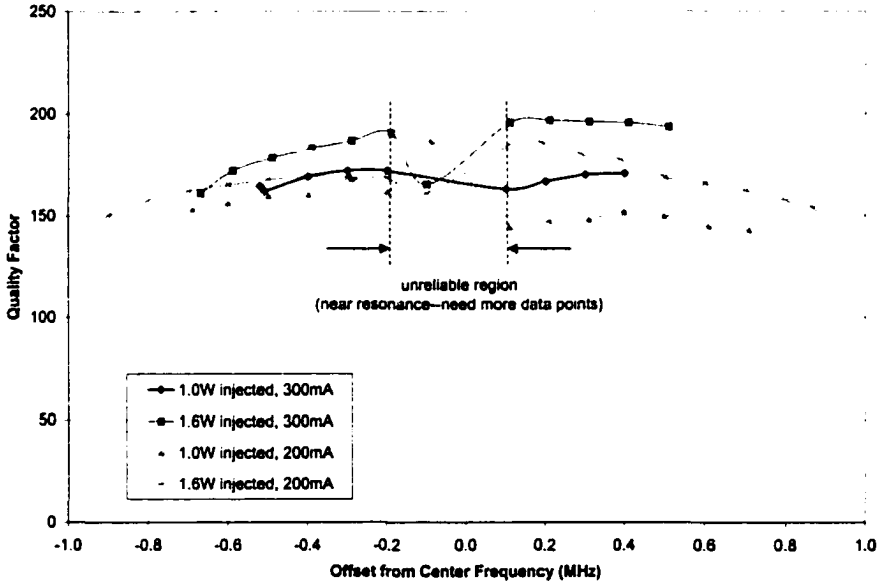

Figure 5.3-9. External Quality Factor Q_E for Class II MDA.

Locking Bandwidth versus Gain. As was seen in Figure 5.2-2, the locking bandwidth of the Class II MDA is a function of gain (in this case, entirely controlled by the injected signal strength). The low gain amplifier provides larger locking bandwidth due to the lower relative reflected power levels inside the waveguide,

$$P_O \downarrow \text{or } P_I \uparrow \Rightarrow BW \downarrow . \tag{5.3-3}$$

The gain may be altered by changing either the DC input power or the injected drive signal. If the MDA is to be operated at various power levels, it is necessary to determine the impact of these changes on its frequency locking capability. The plots in Figure 5.3-10 demonstrate these effects. These show that the locking bandwidth is not only a function of amplifier gain, but also of its operating power. This is explained by the increase in reflected power incident upon the injection probe at higher operating powers. As the strength of the load reflections increase relative to the injected signal, the locking bandwidth is degraded.

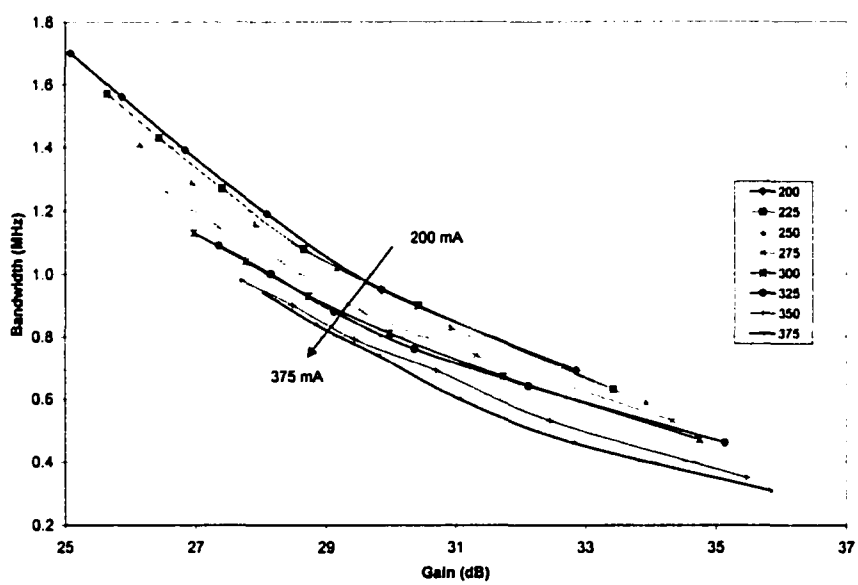

Figure 5.3-10. Locking Bandwidth versus Gain for a Class II MDA.

Quality Factor versus Gain. Using the bandwidth data from above, the external quality factor may be calculated using Equation 5.2-1.

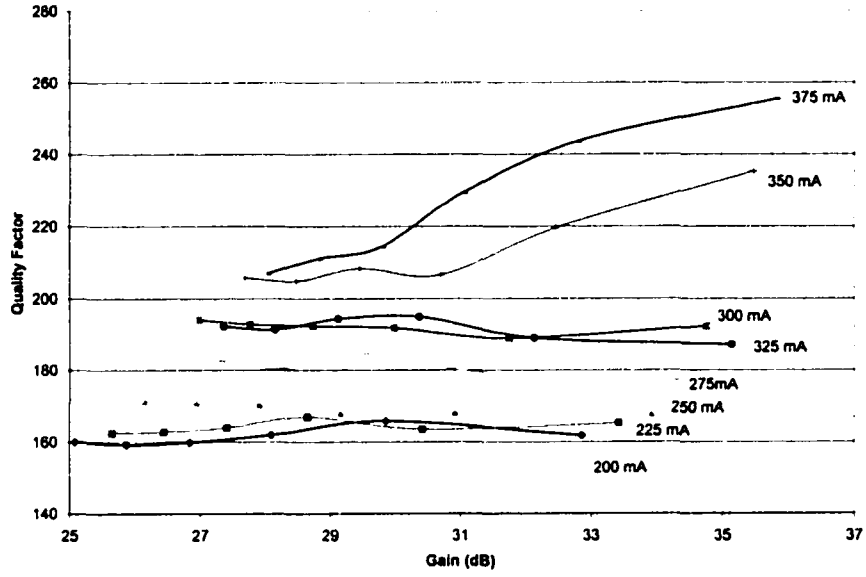

Figure 5.3-11. Quality Factor versus Gain for a Class II MDA.

Figure 5.3-11 shows the effects of changing gain upon the quality factor. The quality factor for the circuit is roughly constant with the gain, showing little sensitivity to the injected signal level except at high power levels. Distortion in the 350 mA and 375 mA curves is likely due to errors caused by scale resolutions, as in Equation 5.2-3.

5.4 Class III Open-Loop MDA Operation

The Class III Open-Loop (OL) MDA provides the same capabilities as a Class II MDA, but adds a metallic reactance tuning slug to control the magnetron's frequency, phase, and output power. The hardware configuration used to characterize the Class III MDA is provided in Figure 3.4-3. Unless otherwise noted, the magnetron used is a Samsung 2M181 (S/N 5194) operating at 300 mA anode current. The primary focus of this section is to characterize the effects of the tuning slug on the MDA operation. The first portion of the discussion deals with the effects due to the slug alone. Later portions describe the combined effects of the reactance slug in conjunction with the previous tuning methods.

5.4.1 Tuning Slug Effects

To characterize the effects of the tuning slugs, a data set was collected for each size slug using an identical hardware configuration and power settings. For each tuning slug, the following data was collected as a function of the slug position: (1) frequency, (2) output power, (3) efficiency, (4) magnetron temperature, and (5) load impedance.

Frequency versus Tuning Slug Position. The frequency response of the Class III OL MDA to three different tuning slugs is shown in Figure 5.4-1. The slug sizes are given in Table 3.4-1. The position scale shown corresponds to that referenced in Figure 3.4-4. The origin (0 cm) is located to the far left away from the magnetron; 30 cm is located nearest the magnetron at ~5.2 cm from the center of the RF probe.

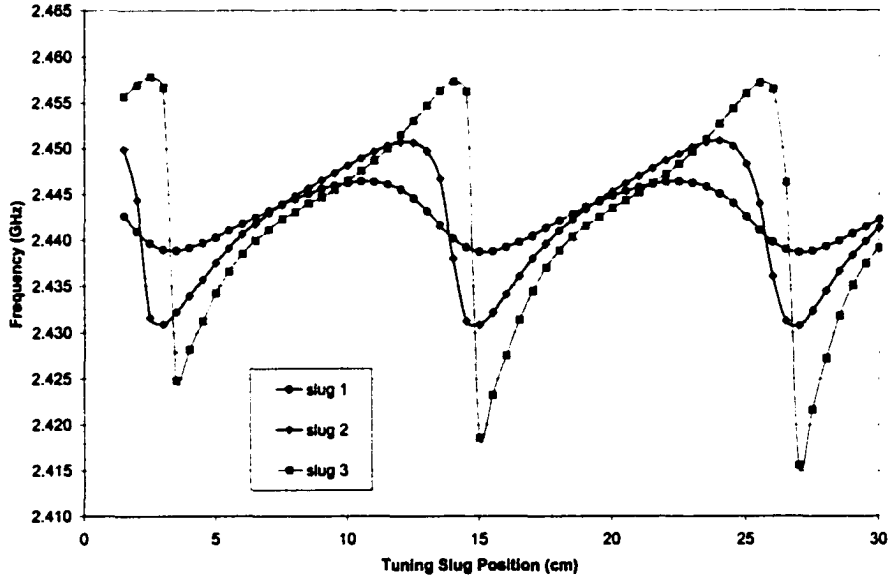

Figure 5.4-1. Effects of Tuning Slug Location on Operating Frequency for a Class II MDA. Larger slugs produce greater frequency pulling range.

The tuning slugs cause the MDA frequency to vary cyclically, repeating every ½ guide wavelength. The normal operating frequency without a tuning slug is ~2.442 GHz. Each

slug provides a roughly equal amount of positive and negative frequency pull, proportional to the size of the slug. The steep regions of the curves correspond to the sink of the Rieke diagram, described in Section 4.3 and Appendix A.4.1.

Increasing the size of the tuning slug shifts the locations of frequency maxima/minima closer together, eventually creating a discontinuity between them. The slug size also alters the location of the transition region, larger slugs pulling this closer to the magnetron. Sufficiently large slugs create a pronounced hysteresis effect, yielding different frequency crossover locations depending upon the direction of approach, as shown in Figure 5.4-2.

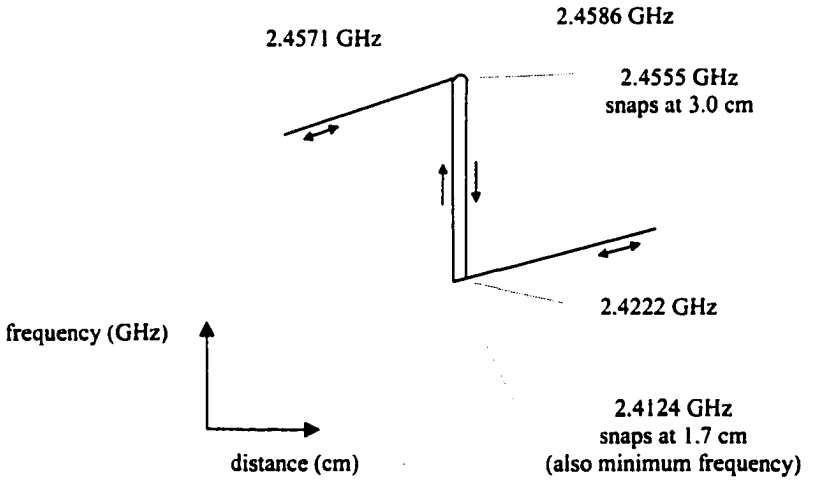

Figure 5.4-2. Frequency Hysteresis Loop for Class III MDA Using a Large Tuning Slug. Numerical values shown for slug 3.

When approaching the sink region from the left, the operating frequency increases to its maximum value of 2.4586 GHz, then begins to roll off. At a value of 2.4555 GHz, the frequency of oscillation then 'snaps' to a much lower value of 2.4222 GHz. If the left to right motion of the tuning slug is continued, the frequency response increases along the next cycle of the waveform. If the motion is reversed, the discontinuity is shifted to the

left. The frequency is then pulled to an even lower value before snapping back to the top curve. The physical overlap of the two discontinuities is substantial (1.3 cm).

The physical separation of the discontinuities may be explained by examining the guide wavelengths for the two frequencies [22],

$$\lambda_g = \frac{\lambda}{\sqrt{1-\left(\frac{f_c}{f}\right)^2}} \tag{5.4-1}$$

where

λ_g = wavelength in guide [cm]
λ = wavelength in free space = 12.24 cm
f_c = cutoff frequency = 2.078 GHz
f = operating frequency [GHz].

The guide wavelengths at the discontinuities are $\lambda_{g\,(2.455\ \mathrm{GHz})}$ = 22.99 cm and $\lambda_{g\,(2.412\ \mathrm{GHz})}$ = 24.11cm. The distance for the discontinuity may be expressed in terms of wavelengths from the magnetron probe: $l_{\lambda\,(2.455\ \mathrm{GHz})} = 1.35\lambda_g$ and $l_{\lambda\,(2.412\ \mathrm{GHz})} = 1.34\lambda_g$. Therefore, the location of the discontinuity (moding) is constant from the perspective of the magnetron.

This hysteresis effect was experimentally noted during the early phases of the UAF MDA characterization effort, and later validated by theory [15]. The operating point of the magnetron is defined by the intersection of the load admittance and electronic admittance curves. The above condition arises when these two curves move in such a manner as to cause the intersection to be broken. This situation is illustrated in Figure 5.4-3.

In this case, the load admittance has been altered by a change in tuning slug location. The original load impedance is shown by the solid line, with the operating point shown by the black dot. Repositioning the tuning slug causes a deformation of the load

admittance curve, shifting the operating point. This causes a corresponding change in the operating frequency and output power of the MDA. At some point, the intersection of the curves is broken and oscillation momentary ceases. The magnetron reestablishes oscillation at the next stable operating point having the lowest load conductance G_L (shown by the gray dot).

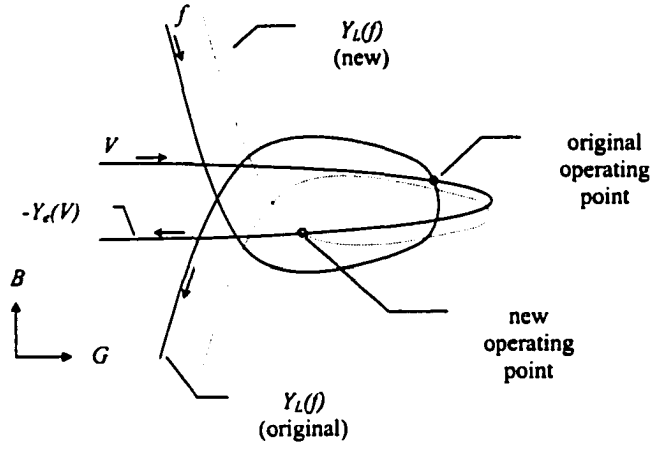

Figure 5.4-3. Intersection of Load and Electronic Admittance Curves [15].

Note that the slope of the steep frequency regions (Figure 5.4-1) tends to lessen nearer to the magnetron. This behavior is referred to as *short-line effects* (more often called *long-line effects* in the U.S.) [15]. This is caused by frequency dispersion for the long line, forcing differences in the group velocity for the different frequencies,

$$v_g = \frac{c\lambda}{\lambda_g} = c\sqrt{1-\left(\frac{f_c}{f}\right)^2} \tag{5.4-2}$$

where

$$v_g = \text{group velocity}\left[\frac{\text{m}}{\text{sec}}\right]$$

$$c = \text{speed of light} = 3\cdot 10^8\left[\frac{\text{m}}{\text{sec}}\right].$$

For slug 3 in Figures 5.4-1 and 5.4-2, the difference in the maximum and minimum frequencies corresponds to a ~2% change in group velocity (and guide wavelength). Therefore, the slope of the frequency in the sink region should vary by ~2% with each successive cycle. The slope becomes more negative with increasing line length until the frequency transition becomes discontinuous in the sink region, as shown in Figure 5.4-2.

Output Power versus Slug Position. Tuning slug position also affects the output power of the MDA. For the frequency response of Figure 5.4-1, the corresponding power curves are shown in Figure 5.4-4.

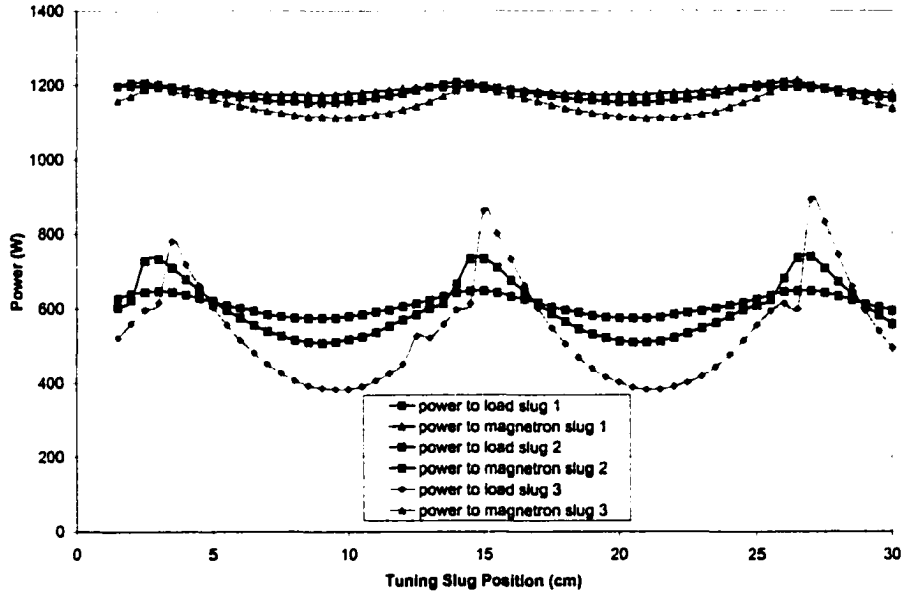

Figure 5.4-4. Output Power versus Tuning Slug Position for a Class III MDA. Larger slugs have more affect on power levels. Input power curves at top show loading on the power supply.

This curve shows the output and input power curves for the Class III OL MDA using slugs 1 – 3. Both curves are affected by the slug position by an amount proportional to the size of the slug. The output power without a tuning slug is ~610 W. Small tuning slugs provide a roughly symmetric waveform with equally positive and negative affects

on the output power (~± 35 W for slug 1). Larger slugs heavily load the magnetron, distorting the output power pattern. These provide much more output power in the sink regions, but on the average provide less power. For slug 3, the output power is boosted to ~890 W in the sink region, but provides an average power of only 540 W. The sink regions also correspond to regions of high efficiency and low magnetron case temperatures (Figures 5.4-4 and 5.4-6).

Efficiency versus Slug Position. The efficiency waveform for the Class III MDA retains the characteristic shape of the output power curve, as seen in Figure 5.4-5. Though the input power is also affected, this amount is relatively minor with respect to the output.

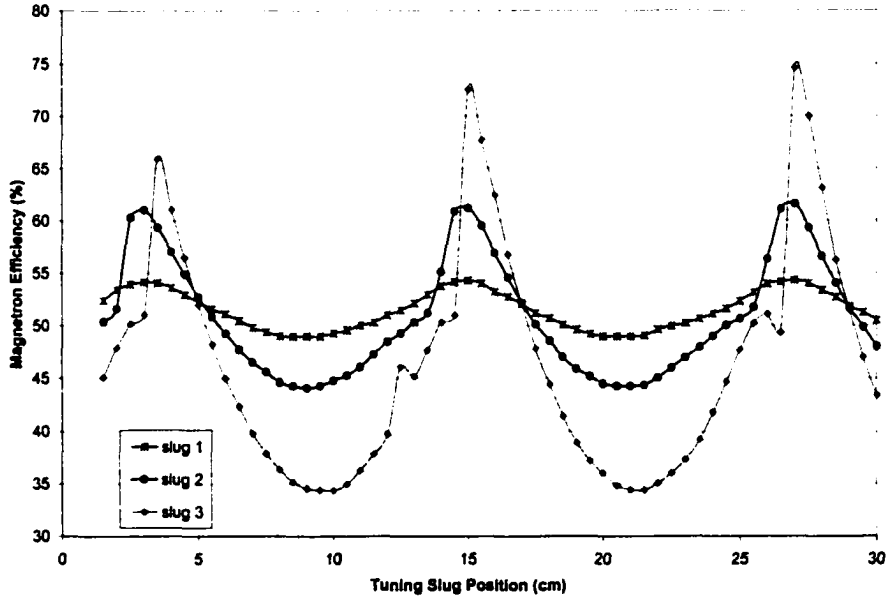

Figure 5.4-5. Efficiency versus Tuning Slug Position for a Class III MDA.

This curve shows the large effect that the tuning slug can have on power transmission efficiency. The MDA efficiency without a tuning slug is ~51%. Slug 1 only slightly affects the efficiency. The resulting waveform is relatively symmetric, providing about ±2.5% pull. The waveform for slug 3 is significantly distorted, with narrow regions of

improved efficiency and wide regions of decreased efficiency. This slug heavily loads the magnetron, providing an efficiency swing exceeding ±20%.

The magnitude of efficiency changes associated with the larger tuning slugs were initially a source of concern. The size of the effect and the resonant quality of the sink region made these results suspect. This behavior had not been noted in previous MDA works, and therefore required verification.

An extensive study was undertaken to substantiate the efficiency measurements. The MDA output was examined for a number of load configurations in an attempt to confirm the behavior. Summarizing the results of this investigation, it was found that the efficiency data could at least be partially supported. It was determined that the total load seen by the magnetron is dependent upon the characteristics of the constituent hardware, including the waveguide size used to implemented the MDA. These effects are described in Appendices A.4.2 and A.4.7.

It was found that the resonant waveform of the efficiency curves could be confirmed by temperature measurements made at the load and the magnetron. The exact magnitude of the peaks remained inconclusive from this perspective, but a trend analysis of the MDA performance seems to support the data. This argument is provided later in the discussion (Figures 5.4-8 and 5.4-10). The resonant behavior was also confirmed by examining the effect of the shorting plate on the MDA. These results are provided in Appendix A.4.8.

Magnetron Temperature versus Slug Position. The case temperature of the magnetron was measured for various slug locations and sizes, as shown in Figure 5.4-6. As expected, the smaller tuning slugs impact the magnetron operating temperature less. Normal operating temperature for this configuration was ~97° C with no tuning slug. Low magnetron case temperatures in the sink region are caused by low reflected power associated with a good impedance match. Regions of high temperature correspond to

inefficient operation of the MDA, which are elevated for the larger slugs. This confirms that large tuning slugs can degrade the impedance match, and therefore lower the efficiency at some locations.

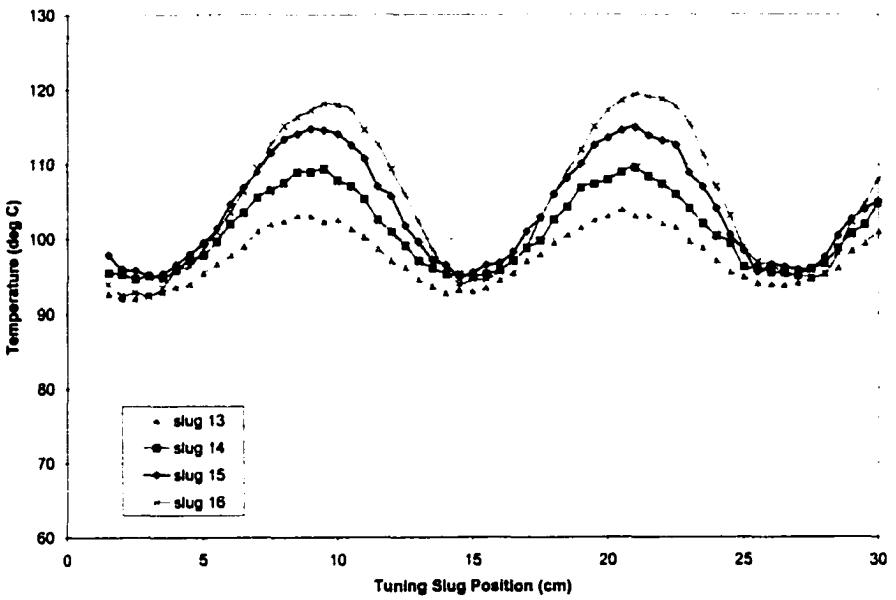

Figure 5.4-6. Magnetron Case Temperature versus Tuning Slug Position for a Class III MDA. Larger slugs provide more variation in temperature.

However, the shape of these curves does not support the resonant efficiency for the large slugs. This is partly due to the relative size of some of the slugs, combined with the time intervals in which the data was collected. The thermal time constant of the MDA is relatively long, which has the effect of smoothing the data. This demands that sufficient time be allowed for the magnetron to reach its final temperature at every data point.

As part of the power investigation, the MDA was operated in numerous load configurations to detremine whether the apparent efficiency resonance was real. In one experiment, the MDA temperature was permitted to stabilize for 10 minutes between data points (total of 10 hours per set). This was accomplished twice for each power supply. The comparative output power and load temperatures for these data sets are shown in

Figure A.4.7-8. These curves exhibited the same characteristic waveform, and were therefore considered to be related. Using the heat capacitance equation, the load temperature was modeled in terms of the output power level

$$Q = mc\Delta T, \tag{5.4-3}$$

where

Q = heat absorbed by load [J]
m = mass [kg]
c = specific heat capacity for load material $\left[\frac{\text{J}}{\text{kg} \cdot \text{deg C}}\right]$
ΔT = temperature differential [deg C].

An example of the resulting temperature and power curves is shown in Figure 5.4-7.

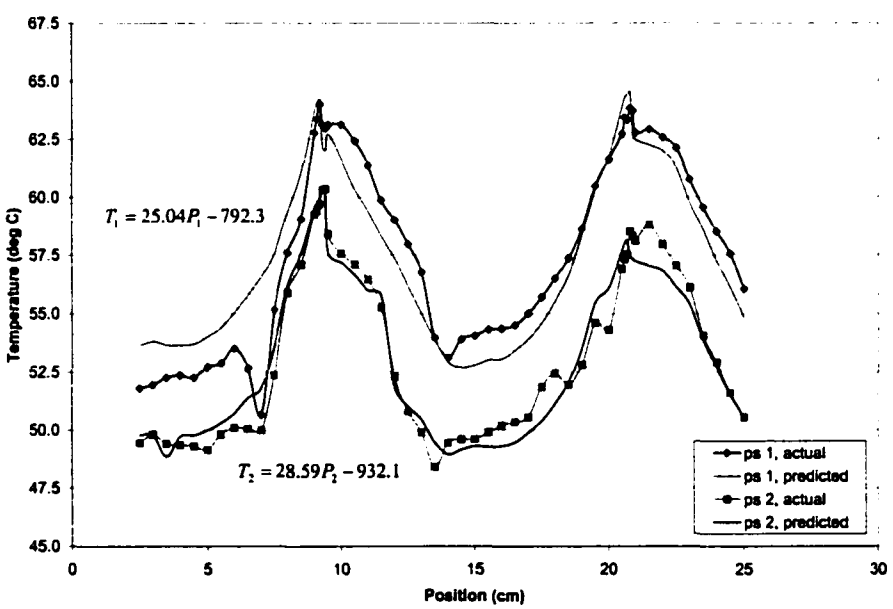

Figure 5.4-7. Expected versus Actual Load Temperatures. Each plot shows one data run for each power supply. Actual data shown by data points. Modeled results based upon output probe power level, shown by smoothed curves.

These curves verify that a reasonably linear relationship exists between the output probe power and the load temperature. Therefore, the resonant peak in efficiency for large tuning slugs (Figure 5.4-4) is shown to be real.

The MDA was characterized using all 16 tuning slugs identified in Table 3.4-1. This resulted in plots of operating frequency, power, and efficiency for each slug similar to those shown above. Analyzing the responses revealed trends in the MDA behavior, which are summarized in the following plots. These may be used as design tools for estimating the required slug size when designing specific MDA applications.

Figure 5.4-8 shows the maximum frequency pull provided for a given slug size.

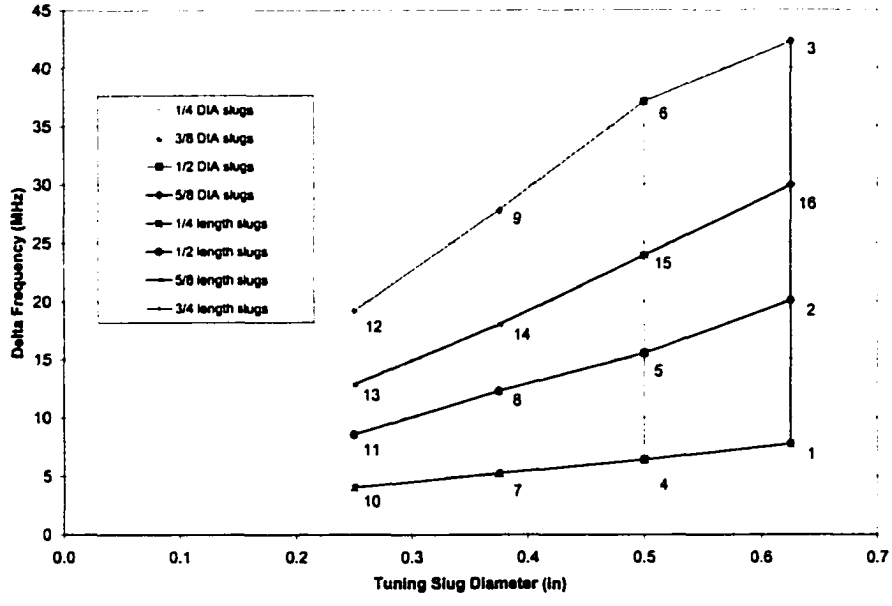

Figure 5.4-8. Maximum Frequency Tuning versus Slug Size for a Class III MDA. Vertical lines represent constant diameter tuning slugs. Slanted lines show constant length slugs. Slugs are labeled according to Table 3.4-1. Frequency pulling is given in terms of maximum range, $f_{\text{upper limit}} - f_{\text{lower limit}}$.

This chart shows linear relationships between the tuning slug dimensions and the maximum frequency pull. For a tuning slug of a given diameter, the pulling range is directly proportional to the slug length (vertical lines); slugs of constant length are represented by the family of slanted lines. Increasing the diameter of the slug increases the frequency pulling according to the slope of the curve.

The chart also provides a means to estimate the size slug needed to attain a certain value of frequency pulling. For example, an earlier version of this chart was created to summarize the effects of slugs 1 – 12. It showed a large gap in the data, and was used to select the size of slugs 13 – 16. These were added later, which accounts for the break in the numbering scheme. This chart was also used to determine an appropriate slug size for the UAF 2-element phased array demonstration discussed in Section 6.4.

The performance effects on MDA efficiency may likewise be summarized for the slugs. Maximum and minimum efficiencies obtained are shown in Figures 5.4-9a and 5.4-9b. Larger slugs provide the possibility for increased efficiency, but only in a limited region. If not positioned properly, these quickly degrade the efficiency of the MDA. The larger the tuning slug, the more critical it is to position the slug accurately. For these slugs, it is generally necessary to stabilize the frequency through use of an injected reference signal. It may also be necessary to employ a phase control loop, as described in Section 5.5.

The data from Figures 5.4-8 and 5.4-9 may be re-plotted to show the relation between the locking bandwidth required of the MDA and the difference in its maximum and minimum efficiencies. This is shown in Figure 5.4-10. The significance of the chart is that it provides insight into the character of the Class III MDA, which may be used to tradeoff competing performance requirements. The chart quantifies the efficiency penalty to be paid if the MDA is not tuned properly.

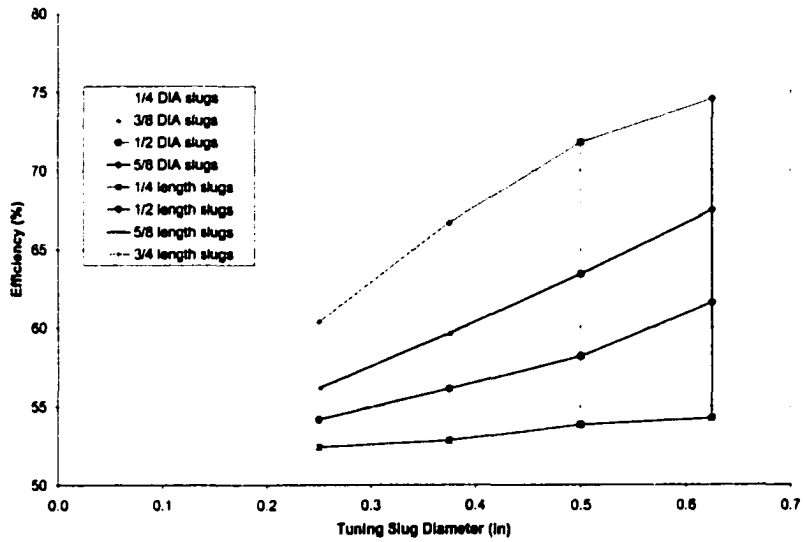

(a) maximum efficiency

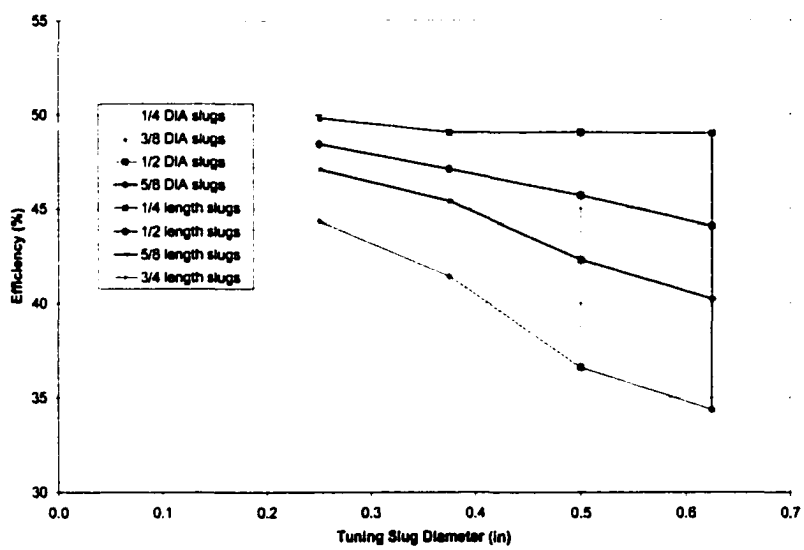

(b) minimum efficiency

Figure 5.4-9. Maximum and Minimum Power Efficiencies versus Slug Size for a Class III MDA.

For example, it may be desired to modify the MDA to provide a locking bandwidth of 20 MHz. In the matched position, the MDA will be capable of 60% maximum efficiency. However, if it is not operating at the tuned position, the magnetron efficiency may drop

as low as 45%. As another example, suppose that it is desired to tune the MDA to a maximum efficiency of 70%. This may be accomplished, but only for a very limited frequency band (even though this MDA would be capable of ~34 MHz pulling range). If the MDA were to be operated at some other frequency, the efficiency would quickly fall off. The potential minimum efficiency of this MDA would be ~37%.

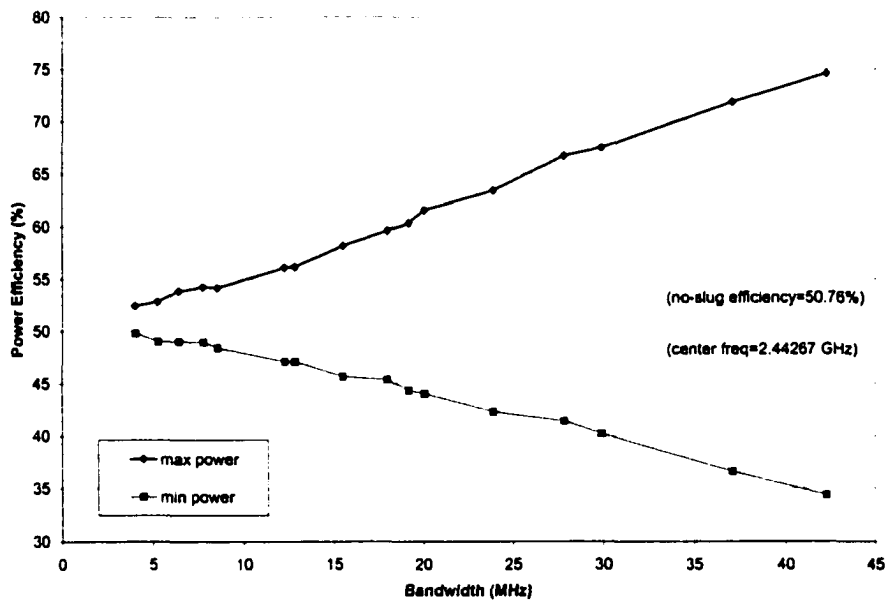

Figure 5.4-10. Power Efficiency Range for Desired Locking Bandwidth of a Class III MDA. Large slugs provide the best and worst possible efficiencies, and largest frequency tuning range.

Figure 5.4-10 is used in conjunction with the frequency and efficiency charts (Figures 5.4-8 and 5.4-9) to determine a suitable slug size. It also requires an understanding of how the magnetron frequency and efficiency vary with each other. This may be accomplished through examining the frequency and efficiency versus slug position charts (Figures 5.4-1 and 5.4-5) for the particular slug.

To ease in this analysis, the frequency and efficiency data may instead be plotted on one chart. One format for this is the Rieke diagram (Section 4.3), which will be presented

shortly. In this format, the load impedance is plotted on the Smith chart with constant frequency and power or efficiency contours overlaid. Another form for the same data involves a direct plot of magnetron efficiency versus operating frequency, shown below.

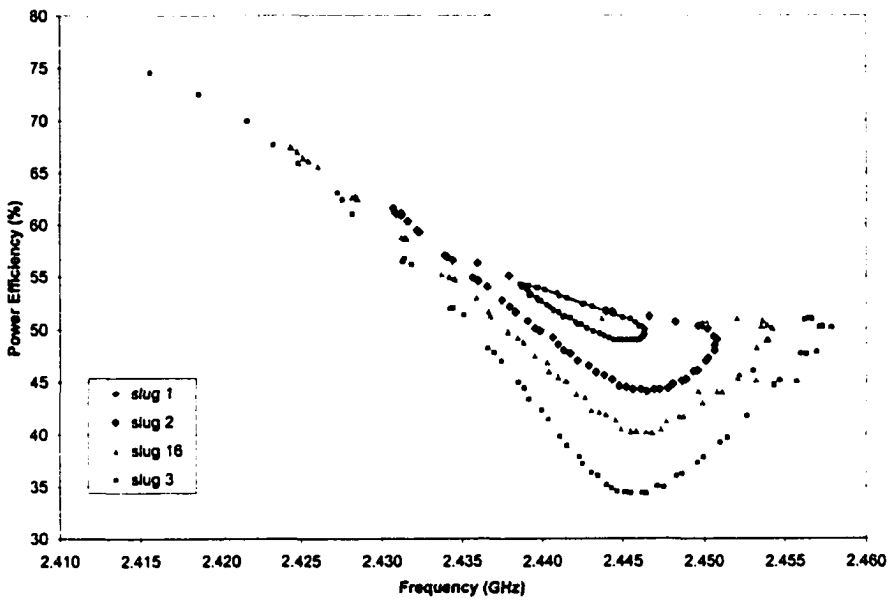

Figure 5.4-11. Efficiency versus Operating Frequency for a Class III MDA. Large slugs provide most tuning range. Sink region of Rieke diagram corresponds to top of curve.

The efficiency is plotted as a function of frequency for all data points using four different sized tuning slugs. Slug 1 is relatively small from a reactance point of view, and therefore affects the efficiency very little. The no-slug operating point is located at the centroid of the loop (f = 2.443 GHz, ε = 50.8%). As the slugs increase in size, the efficiency pattern becomes distorted. More of the operating points are eventually pulled down to lower operating efficiencies. However, the data points occupying the upper region of the curves do not extend directly upwards. Instead, these points are stretched across a comparatively large frequency range, forming a boundary. This boundary represents the sink region of the Rieke diagram.

Sparseness of the high efficiency data points on the 'handle' (sink) can be viewed as a relative measure of stability. Points located near the top of the handle are difficult to achieve, requiring heavy loading of the magnetron and precise control. A large enough tuning slug for a given waveguide size will eventually exceed the magnetron's ability to operate. High temperatures associated with the low efficiency region may damage the magnetron RF probe. Alternately, operation in the very high efficiency region may cause destruction of the magnetron or the DC power supply.

Load Impedance versus Tuning Slug Position. The operation of the MDA may be explained through an analysis of its load impedance. Figure 5.4-3 outlined the concept of load impedance as a determinant of the MDA behavior. The measurement of the actual load impedance data provides additional insight into the magnetron's operating characteristics. Correlation of the impedance data with the magnetron's output power and operating frequency is commonly analyzed by means of the Rieke diagram.

Constructing the Rieke diagram requires an independent measurement of the MDA load impedance. The method for accomplishing this is detailed in Appendix A.4.1. The load impedance data is then plotted on a Smith chart, as shown in Figure A.4.1-6. The Rieke diagram results from overlaying contours of constant frequency and output power. An example of this is shown in Figure A.4.1-7. An alternate form of the diagram may be constructed by plotting all load data in contiguous bands, as shown in Figures A.4.1-8 and A.4.1-9. Behavior of the MDA may then be analyzed in terms of the impedance data and the Rieke diagram.

5.4.2 Combined Effects of Tuning Slug and Injected Reference Signal

After characterizing the performance of the MDA with a tuning slug, the combined effects of the slug with the other tuning methods may be examined. This portion of the discussion analyzes the tuning capability of the Class III MDA using a combination of

the tuning slug and an injected reference signal. The data collected for this analysis included: (1) frequency locking limits versus tuning slug position, (2) locking bandwidth versus slug position, (3) efficiency variations with frequency locking limits, and (4) quality factor versus slug position.

Frequency Locking Limits versus Tuning Slug Position. As the tuning slug is moved along the slotted waveguide section, the load impedance presented to the magnetron changes. At each point, the locking bandwidth of the injected reference signal may be measured. If the injected power level is varied, a set of curves similar to that shown in Figure 5.2-1 result. The width of each curve will vary according to the relative impedance match presented by each operating point. Assuming the parameter of interest is the maximum locking range for the slug, the above data sets may be simplified. Figure 5.4-12 shows the frequency locking range attainable for an injected signal of 1.6 W.

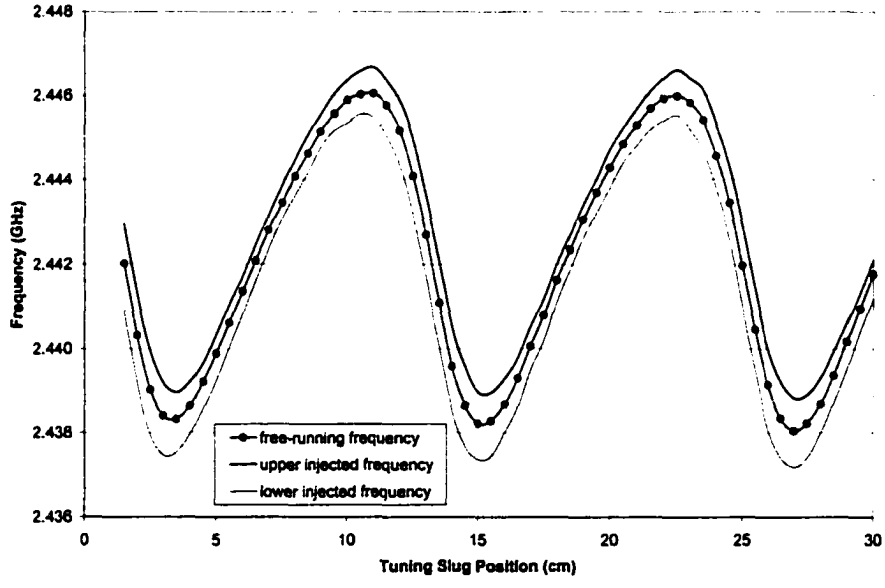

Figure 5.4-12. Frequency Attainable Using Reactance Tuning Slug and Injected Reference Signal for a Class III MDA. Data shown is for slug 1. Center curve shows normal operating frequency. Locking range is bounded by upper and lower frequency curves.

This chart shows how frequency locking limits are affected by a relatively small tuning slug. The locking limits appear to be roughly symmetric about the operating (free-running) frequency. At first glance, the areas of maximum and minimum frequency seem to have the highest locking bandwidths. However the slope of the sink region actually provides the largest value.

For a larger tuning slug, the locking bandwidth becomes less symmetric, as seen in Figure 5.4-13. The larger tuning slug provides a steeper frequency slope in the sink regions, and therefore more locking bandwidth than the smaller slug. In contrast, the areas away from the sink have a lower locking bandwidth. This is caused by reflected RF energy canceling out the injected reference signal at the input to the magnetron.

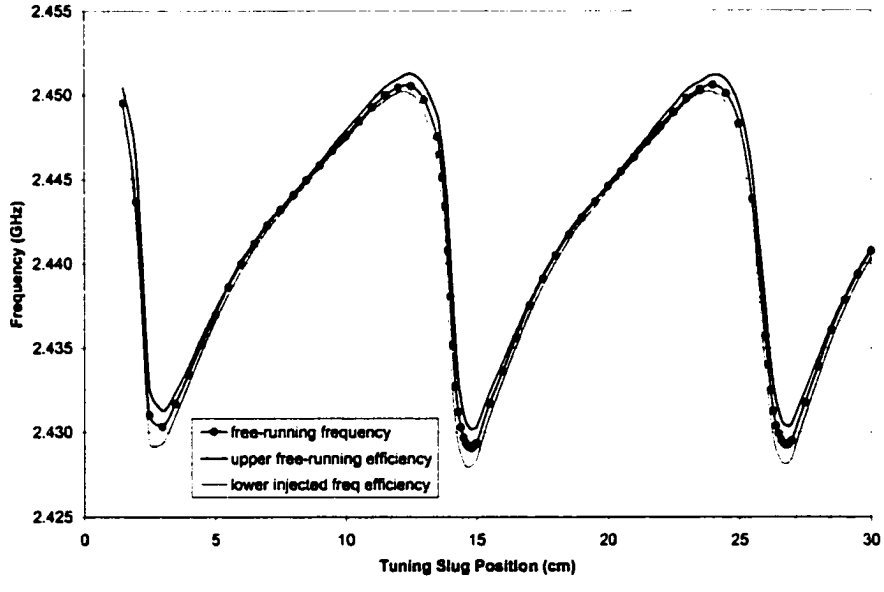

Figure 5.4-13. Frequency Attainable Using Reactance Tuning Slug and Injected Reference Signal for a Class III MDA. Data shown is for slug 2. Center curve shows normal operating frequency. Locking range is bounded by upper and lower frequency curves.

The relative magnitude of the frequency range in the plot above begins to obscure the injected locking range. For larger slugs, the locking limits become indistinguishable from the free-running frequency. Plotting the bandwidth directly shows the effects more clearly, as shown in Figure 5.4-14.

This plot shows the frequency locking bandwidth for tuning slugs 1 – 3 as a function of slug position. The shapes of the curves are affected by both slug size and position. Larger bandwidth is provided in the sink region due to the slope of the frequency versus tuning slug curves. Less locking bandwidth is available outside the sink region due to the load impedance mismatch. In this region, the reflected power interferes with the injected reference signal, lowering the locking range.

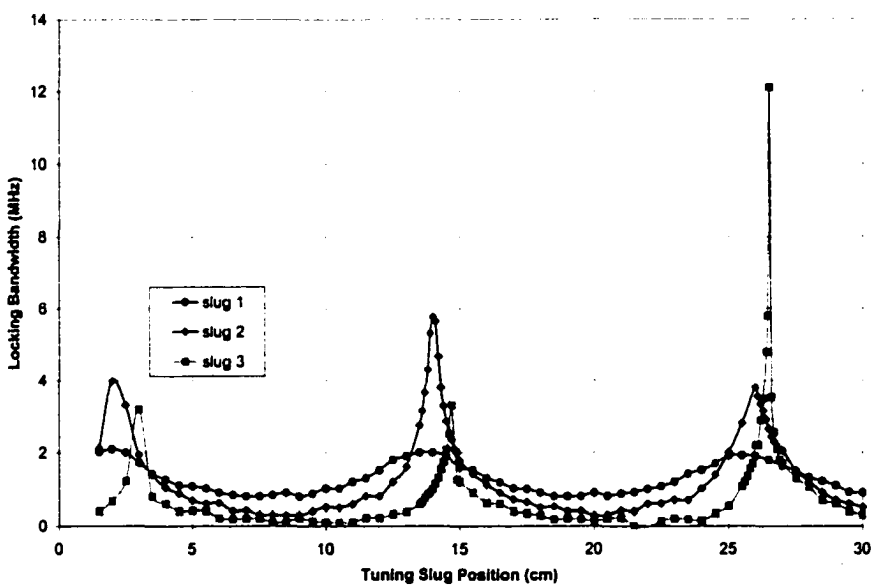

Figure 5.4-14. Locking Bandwidth Using Reactance Tuning Slug and Injected Reference Signal for a Class III MDA. Larger slugs provide the most locking bandwidth, but over a more limited range. Locking bandwidth due to the injected signal alone was ~1.2 MHz.

These results may be compared against the frequency response of the Class III MDA using the slug alone. From Figure 5.4-8, the maximum frequency pulling range for each of the three slugs is 7.7 MHz, 20.1 MHz, and 42.3 MHz, respectively. These values should roughly equal the theoretical bandwidth that might be achieved using a combination of the tuning slug position and injected reference signal level.

Whether this maximum range may be obtained depends upon the exact slope of the frequency curve at that slug position. In most cases the slope will not permit the entire frequency range to be controlled from one location. If the slope is too shallow, then one or both extrema will be blocked. If the slope is too steep, as in the hysteresis condition mentioned in Figure 5.4-4, then the frequency will jump between the two extremes. The possible cases for the slope are shown in Figure 5.4-15.

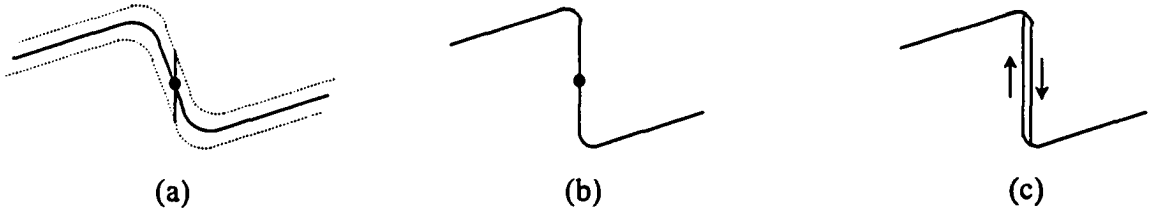

Figure 5.4-15. Effect of Frequency Curve Shape on Locking Bandwidth. (a) BW limited by slope of curve, (b) full BW available, (c) no BW available.

Referring to Figure 5.4-14, the locking bandwidth for slug 1 is roughly symmetrical, reaching a maximum value of 2 MHz in the sink region and dropping to a minimum of 0.8 MHz. Slug 2 provides an increase to almost 6 MHz in the middle sink region, but drops to only 0.3 MHz opposite the sink region. The value of 4 MHz near the magnetron may be partly in error, the result of not taking data in adequate resolution to capture the peak. However, it is expected that the decreased slope of this sink region also played a part in the decreased value.

Slug 3 provides over 12 MHz of locking bandwidth in the sink nearest the magnetron, but the locking bandwidth is practically absent outside of this region. In this case, the lesser peak encountered for the middle sink region (3.3 MHz) is due to the instability of the discontinuity. The slope of the middle sink is in fact greater than for the sink region nearest the magnetron. However, the inability to stabilize the slug in this location limits its locking bandwidth. Even on the nearest sink region, the effects of this tuning slug are difficult to control — bandwidths of the entire 20 MHz frequency range have been demonstrated, but are difficult to repeat consistently.

The shape of the bandwidth curves above is explained by considering the total fields in the waveguide near the magnetron shown in Figure 3.4-2. The tuning slug acts to either reinforce or cancel a portion of the injected signal tuning ability, depending upon its location. The shape of the bandwidth curves above results from the relative magnitudes of these voltages. As the slug size is increased, the magnitude of V_r increases with respect to V_i. For slug 1, the frequency pulling range is ~8 MHz compared to the injected signal range of ~1.2 MHz. Assuming the amount of frequency pull is proportional to the signal voltage, then the reflected voltage V_r would be

$$V_r\big|_{\text{slug 1}} \approx \frac{8\ \text{MHz}}{1.2\ \text{MHz}} V_i = 6.7 V_i . \qquad (5.4\text{-}4)$$

Therefore, the two voltages would seem to be of at least comparable magnitude. For the larger slugs, the tuning effect of the slug quickly dominates over that of the injected signal. For slugs 2 and 3 the relative pulling capability would be roughly $V_{r\ (\text{slug } 2)} \approx 16.7 V_i$ and $V_{r\ (\text{slug } 3)} \approx 35 V_i$. These estimates are admittedly rough, but their relative magnitudes provide at least some sense of the values for the above bandwidth curves.

Efficiency Variations with Frequency Locking Limits. While determining the frequency locking limits of the Class III MDA, the corresponding output power for each point was

recorded. This data was used to calculate the efficiency range obtained by sweeping the injected signal through the locking bandwidth at each slug position. The resulting data is shown in Figure 5.4-16.

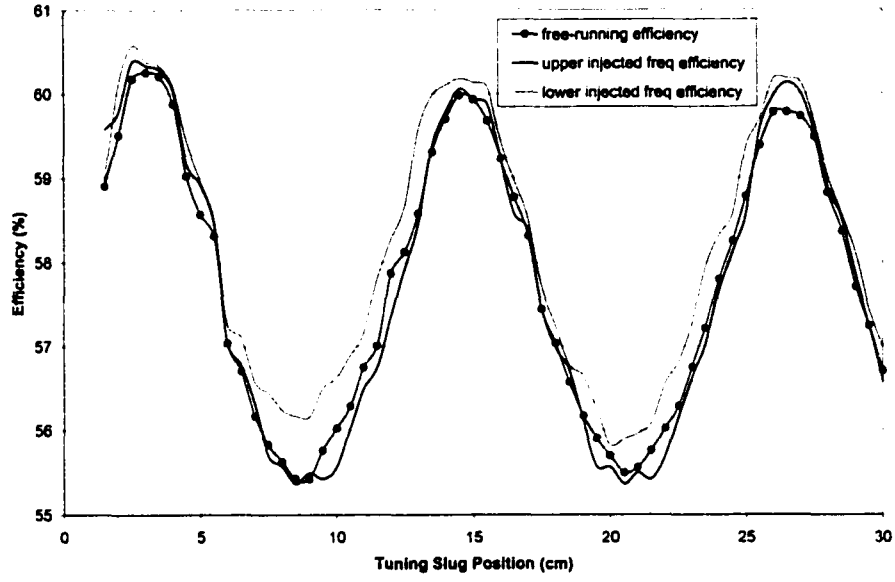

Figure 5.4-16. Efficiency Range Using Reactance Tuning Slug and Injected Reference Signal for a Class III MDA. Data shown is for slug 1. Center curve shows normal operating efficiency. Locking range is 'bounded' by upper and lower curves. High value curve corresponds to low frequency limit.

The information provided from this particular data set is of questionable value. These curves lack the smooth characteristics seen in the corresponding frequency data. For some portions of the plot, the injected curves do not bound the free-running signal as would be expected. In addition, the maximum efficiency changes would be expected to occur in the sink regions. However, the opposite appears to be true here.

Some of the pattern irregularities may be attributed to the limited resolution of the equipment. Although the curve for the free-running efficiency is relatively smooth, it contains slight pattern distortions. This is compounded with distortions in the injected

efficiency waveforms, which appear to be more aggravated than for the free-running curve. The output power resolution was limited to ~2.4 W, corresponding to an efficiency error of ~0.35% for this output power range (685 W average). Another factor contributing to the curve shapes may be the power level of the injected signal, which represents ~0.22% of the average output power.

For larger tuning slugs, the curves appear smoother. The efficiency response for tuning slug 2 is shown in Figure 5.4-17. The efficiency response for this combination of tuning slug and injected signal appears to be better behaved. This may be partially attributed to the compressed efficiency scale. The injected signal exerts more influence over the efficiency in the sink region, as expected. Overall, the injected curves appear to be more stable, but still demonstrate some pattern distortion opposite the sink regions. Instead of bounding the free-running signal, the injected curves both exhibit lower efficiencies in these regions.

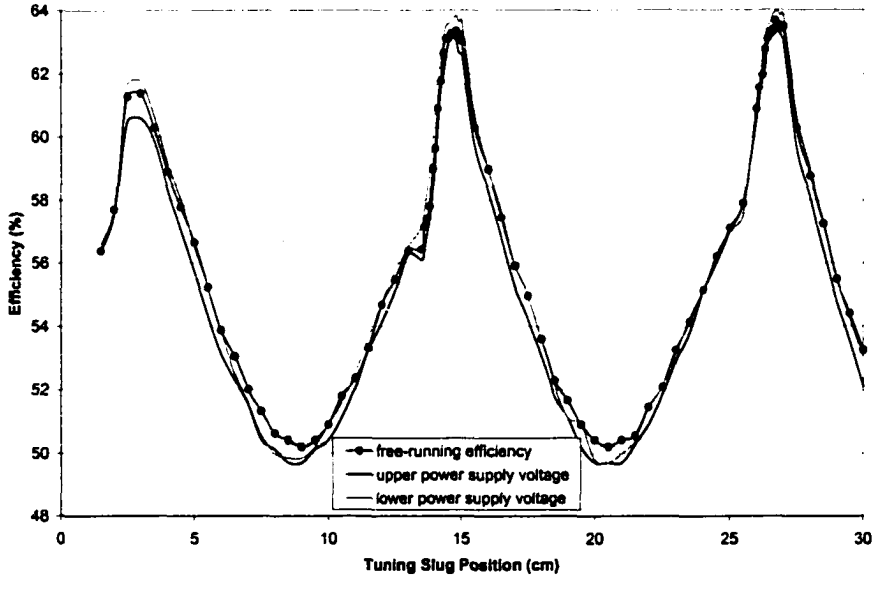

Figure 5.4-17. Efficiency Range Using Reactance Tuning Slug and Injected Reference Signal for a Class III MDA. Data shown is for slug 2.

Part of the error in the curves above is due to limitations in the output power resolution. At the low efficiency points, this corresponds to ~0.42% of the output power (575 W). Additional error is introduced in reading the locking frequency limits in Figure 5.4-14. As the tuning slug departs a sink region and enters a low efficiency region, the locking bandwidth falls off sharply. At this point, the accuracy of the frequency locking measurements becomes limited by the resolution of the scale used for the readings. As a consequence, the power output corresponding to the injected frequency is also affected.

However, the behavior displayed by the injected signal waveforms opposite of the sink regions appears to be consistent. This would indicate that the injected reference signal has a negative effect on the efficiency. The magnitude of the injected signal represents ~0.28% of the output power at this point. By comparison, the difference in efficiency between the injected and non-injected signals is noted to be 0.5%. Therefore, it seems plausible that the phase of the injected signal is responsible for the decreased efficiency.

It is desired to examine the efficiency swing attainable for a number of tuning slugs, similar to that done for locking bandwidth. Unfortunately, this becomes more difficult because of (1) errors introduced in power measurements, and (2) the instabilities of the output power waveform itself discussed in Appendix A.4.6. This is especially true for large slugs that load the magnetron heavily.

However, it is still possible to provide a comparison of the efficiency 'pulling' effects for two other slugs from the midsize range. Figure 5.4-18 shows this data for tuning slugs 9 and 16 (Table 3.4-1). This chart is the efficiency equivalent of the locking bandwidth plot shown in Figure 5.4-16. The empirical results shown here will be discussed shortly. However, the results of the Class III MDA for these slugs without the injected signal will be reviewed first.

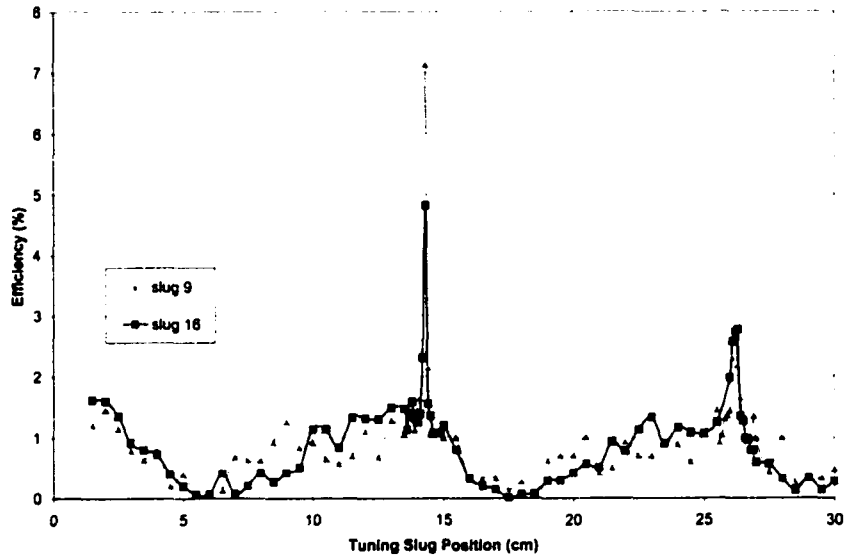

Figure 5.4-18. Efficiency Range Using Reactance Tuning Slug and Injected Reference Signal for a Class III MDA. Data shown is for slugs 9 and 16.

From the data in Figure 5.4-9, the difference in maximum and minimum efficiency for slugs 9 and 16 is $\Delta\varepsilon_{(\text{slug } 9)} = 25.3\%$ and $\Delta\varepsilon_{(\text{slug } 16)} = 27.3\%$, respectively. These values set a theoretical limit on the maximum efficiency pull that might be obtained using a combination of the tuning slug and injected reference signal. Unlike the frequency waveform, the efficiency curve does not instantaneously jump between its maximum and minimum values. The actual amount of efficiency pull will therefore never reach this upper bound. However, the efficiency waveform for large tuning slugs does present a resonant waveform in the vicinity of the peak value. This resonance may provide a substantial jump resembling that of the frequency waveform, but to a lesser degree. As an example, the efficiency curves for slugs 9 and 16 are shown in Figure 5.4-19.

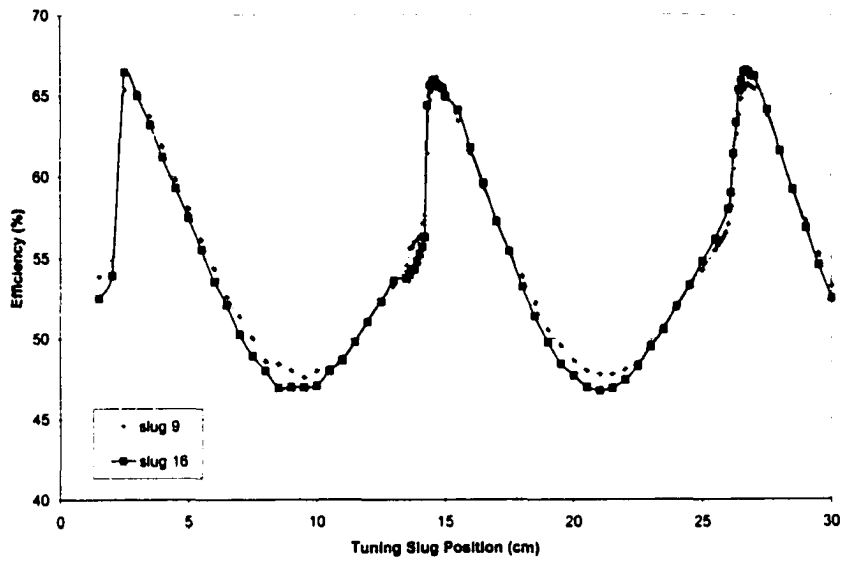

Figure 5.4-19. Efficiency versus Tuning Slug Location for a Class III MDA. Data shown for is slugs 9 and 16. Plot demonstrates efficiency jump near resonance.

Comparing these results with those obtained for Figure 5.4-18, the efficiency pulling waveforms for the slugs are similar. This is expected due to the similarity in the size of the two slugs. The difference in the peak values (7.1% versus 4.8%) obtained in the center sink region is understandable, given the steep slope of the curves near resonance. It has been noted that the precise positioning of the tuning slugs is critical to obtaining repeatable results for these larger slugs. Running these two data sets multiple times would likely result in nearly identical results.

The peak values for the nearest sink region provide a good picture of how similar the two slugs are electrically. Since this sink region tends to be more stable, the slopes of the efficiency curves are more gradual. This results in the same behavior for the injected reference signal, making the efficiency difference more repeatable. The same analysis may be performed for the frequency response of the MDA using these two slugs and the injected signal. The corresponding locking bandwidth curves are shown below.

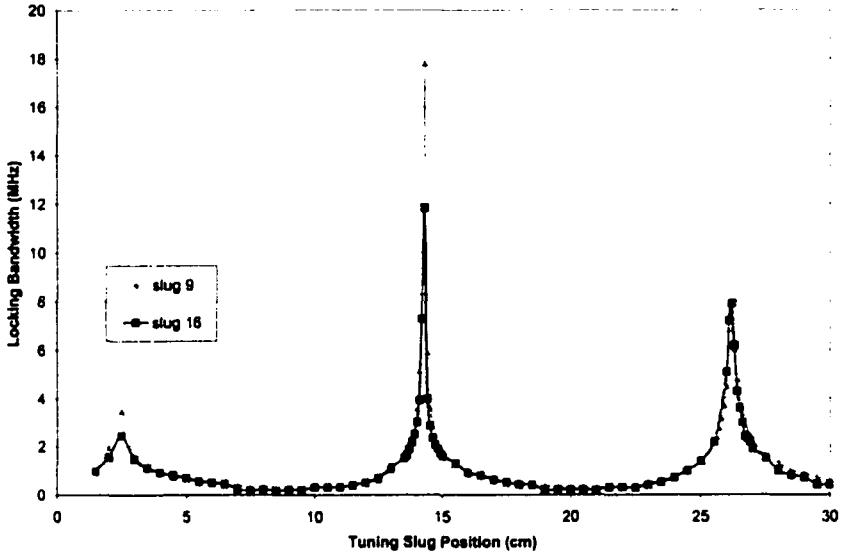

Figure 5.4-20. Locking Bandwidth Using Reactance Tuning Slug and Injected Reference Signal for a Class III MDA. Data shown for slugs 9 and 16.

From Figure 5.4-8, the maximum frequency pulling range provided by the tuning slugs alone is 19 MHz for slug 12 and 30 MHz for slug 16. The locking bandwidth for slug 9 comes quite close to the theoretical maximum of 17.8 MHz. The bandwidth obtained using slug 16 is less (11.8 MHz), but again, this may be explained by the slope of the frequency versus slug position curves. The steep slope requires the slug to be precisely located to take advantage of the full locking bandwidth. To demonstrate this point, the frequency curves for the two slugs are shown in Figure 5.4-21 below.

This figure helps explain the locking bandwidth results seen in Figure 5.4-20. Though the two slugs have nearly identical frequency responses, the locking bandwidth obtained for slug 16 in the middle sink region was substantially less than that for slug 9. The high value for slug 16 corresponds to the point nearly midway in the sink region — no such point occurred for slug 9. The sink region nearest the magnetron is less steep, as evidenced by the number of data points located in this area. Locking bandwidth is essentially identical for the two slugs in this sink region.

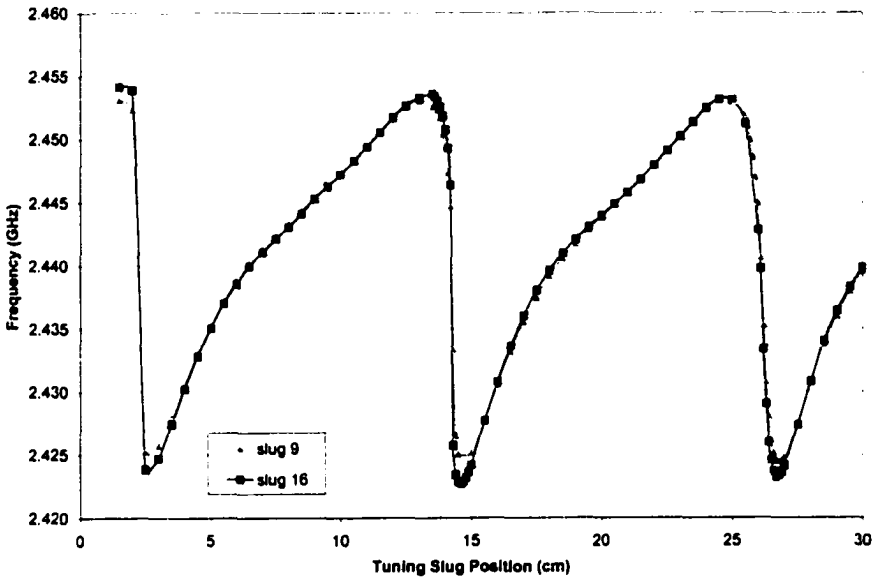

Figure 5.4-21. Frequency versus Tuning Slug Location for a Class III MDA. Data shown for slugs 9 and 16. Plot demonstrates relative slope of sink regions.

Quality Factor versus Tuning Slug Position. Using David's equation governing the operation of a frequency-locked amplifier, the external quality factor Q_E may be determined (Equation 5.2-3). By calculating the value of Q_E as a function of tuning slug position, it is possible to model the efficiency of the Class III MDA. The quality factor changes with tuning slug position, as seen in Figure 5.4-22. The shape of these curves is affected by the narrow locking bandwidth associated with the low efficiency regions. As noted in Figure 5.4-5, large tuning slugs can result in inefficient operation if not properly positioned. Power reflected from the load interferes with the injected signal, thereby lowering the locking bandwidth. In these regions, the resolution used to measure the locking bandwidth causes the distorted patterns above.

The maximum efficiencies obtained for the tuning slugs may be correlated to a minimum value of Q_E. Similar to the efficiency curves in Figure 5.4-9, a maximum Q_E chart is constructed in Figure 5.4-23, corresponding to the low efficiency case for each slug.

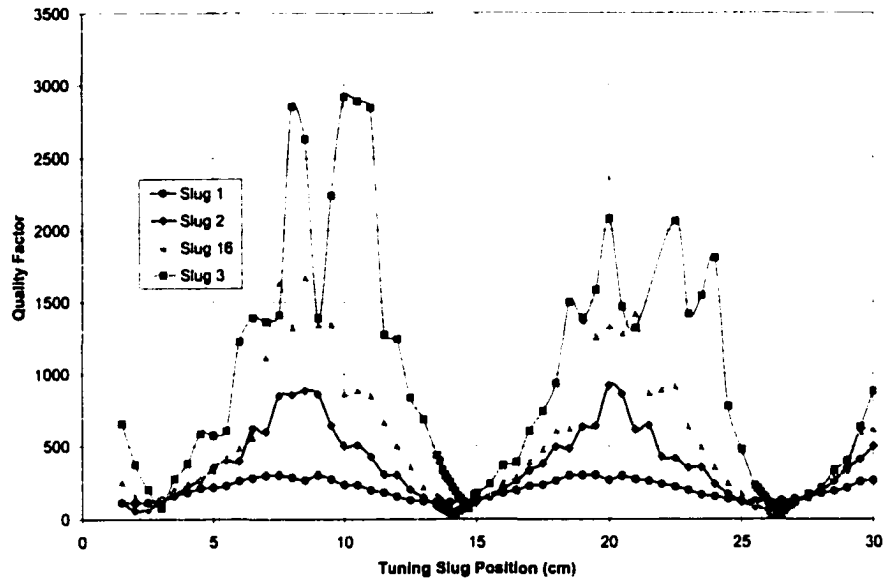

Figure 5.4-22. Quality Factor Using Reactance Tuning Slug and Injected Reference Signal for a Class III MDA. Low Q_E corresponds to high efficiency.

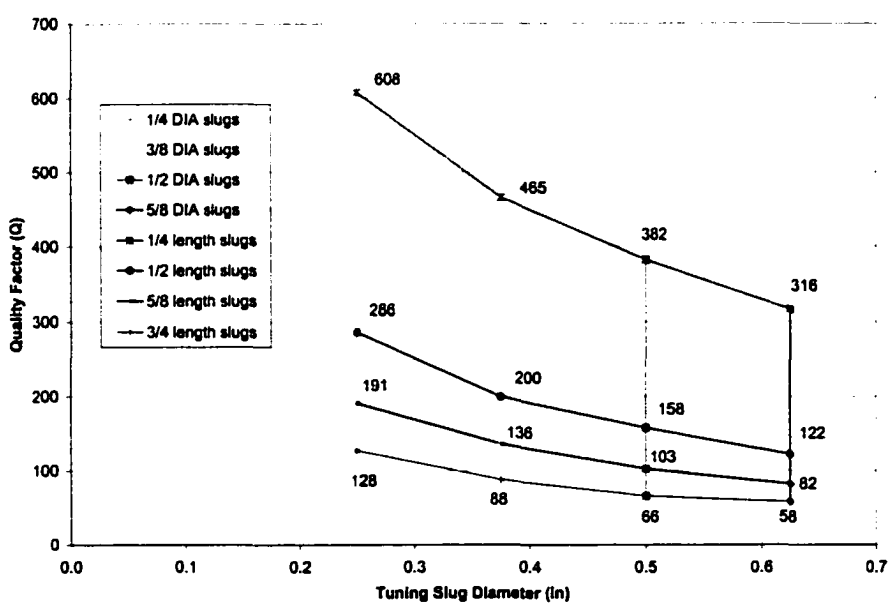

Figure 5.4-23. Quality Factor versus Tuning Slug Size for a Class III MDA. Low Q_E provides high efficiency operation.

5.4.3 Combined Effects of Tuning Slug and Power Control

This portion of the discussion analyzes the tuning capability of the Class III MDA using a combination of the tuning slug (frequency pulling) and power control (frequency pushing). The data collected for this analysis included: (1) output power versus tuning slug position, (2) efficiency versus slug position, and (3) frequency versus slug position.

Output Power versus Tuning Slug Position. The output power of the Class III MDA is well-behaved with respect to changes in the DC input power. Figure 5.4-24 shows the MDA output profile for several different input power levels.

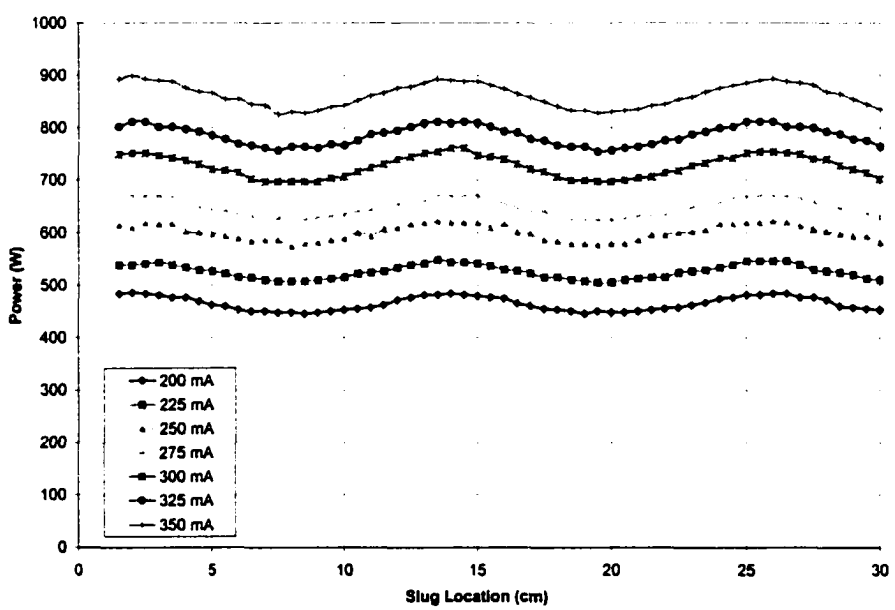

Figure 5.4-24. Effect of Power Control on Output Power for a Class III MDA. Data shown is for slug 1. Anode current incremented by 25 mA (~100 W).

These waveforms are basically parallel and proportional to input power, stretching slightly with increased output power. The variation in power versus slug position remains roughly at 8% for all power levels. This demonstrates that the power

characteristics are relatively unaffected by the operating level. The Class III MDA therefore retains its linear relationship between input and output power.

The same results are obtained for larger tuning slugs, as shown in Figure 5.4-25. The relative change with respect to the average power level remains roughly constant at 26% for all power levels.

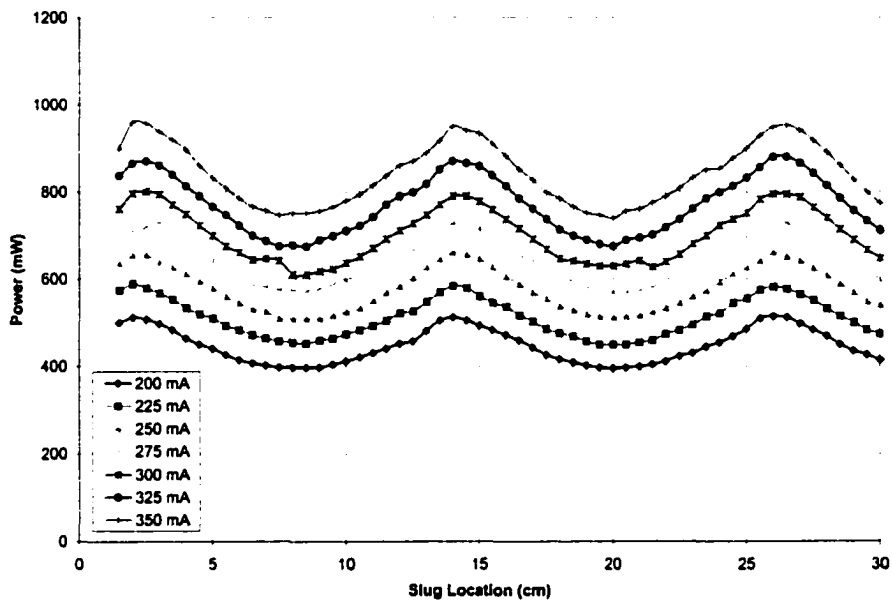

Figure 5.4-25. Effect of Power Control on Output Power for a Class III MDA. Data shown is for slug 2. Anode current incremented by 25 mA (~100 W).

The relative change (or controllability) in the power output is unaffected by its operating level. This is instead a function of the tuning slug size. Power control of the Class III MDA can therefore be broken into two components — an offset value established by the operating power level, and a tuning range selected by the slug size. The selection of the magnitudes for these components is based upon other desired performance characteristics for the MDA, such as efficiency and frequency.

Efficiency versus Tuning Slug Position. It has already been noted that the efficiency data is subject to errors stemming from power scale resolutions and waveform instabilities. However, the shape and trends of the curves may still shed light on the character of the MDA. The efficiency plot for the MDA with tuning slug 1 is shown in Figure 5.4-26.

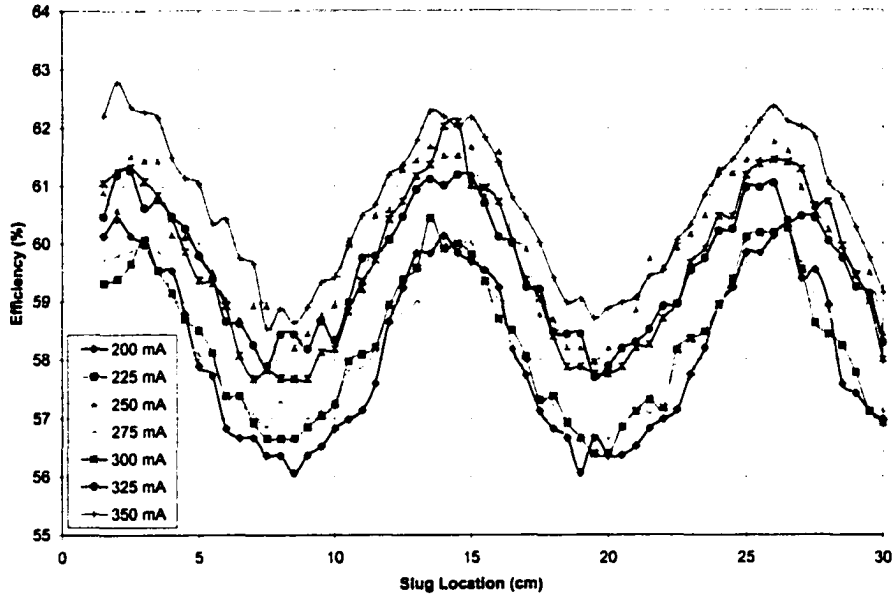

Figure 5.4-26. Effect of Power Control on Efficiency for a Class III MDA, Slug 1.

The curve shapes reveal that the slug provides roughly 4% efficiency pulling regardless of the power level. The exact values of efficiency deviate somewhat from the expected sequence, but overall the efficiency is shown to vary with the power level. This supports the power supply characterization accomplished for the no-load condition discussed in Section 5.4.1. The results are confirmed by the MDA performance using the larger slug 2, as shown in Figure 5.4-27.

In addition, it is seen that high power levels tend to drive the MDA into the sink region harder. This is evidenced by the sharpening of the peak resonance in the sink region nearest the magnetron (right). The effect is not overwhelming in this case, but is consistent with the higher peak efficiency values obtained in the sink.

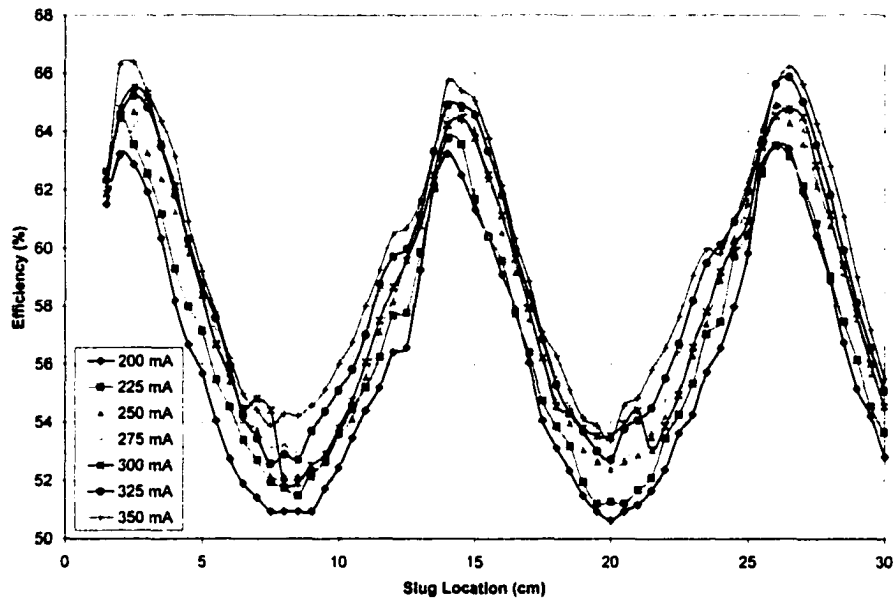

Figure 5.4-27. Effect of Power Control on Efficiency for a Class III MDA, Slug 2.

Frequency versus Tuning Slug Position. An examination of the Class III MDA frequency response shows that its behavior is not as straightforward, as shown in Figure 5.4-18. A quick look shows that the curves do not display the parallel behavior seen in the power output. Instead, the frequency curves have different peak locations and magnitudes. This results in the curves crossing in many locations. An expanded section of this chart is shown in Figure 5.4-29.

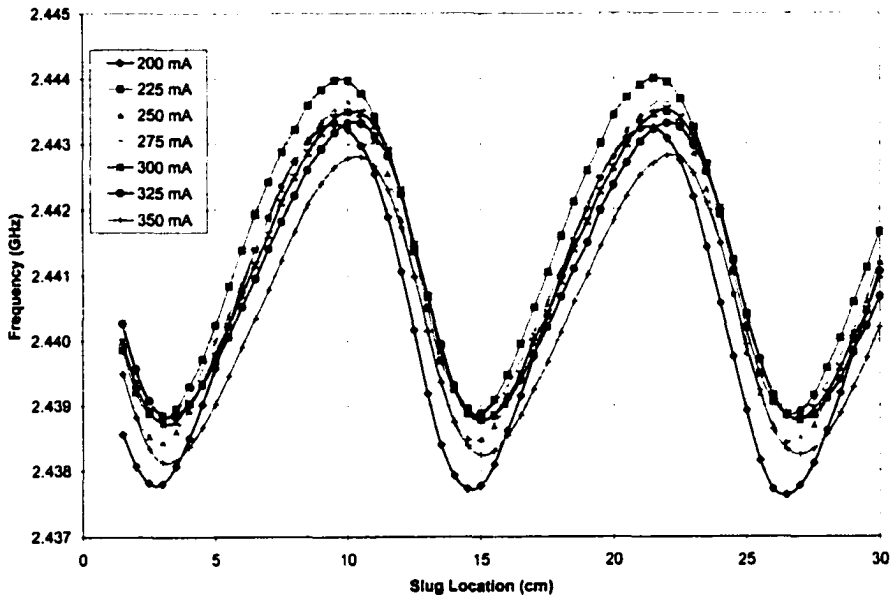

Figure 5.4-28. Effect of Power Control on Frequency Response for a Class III MDA, Slug 1. Chart intended to illustrate chaos of curves. An expended scale chart is shown in Figure 5.4-29.

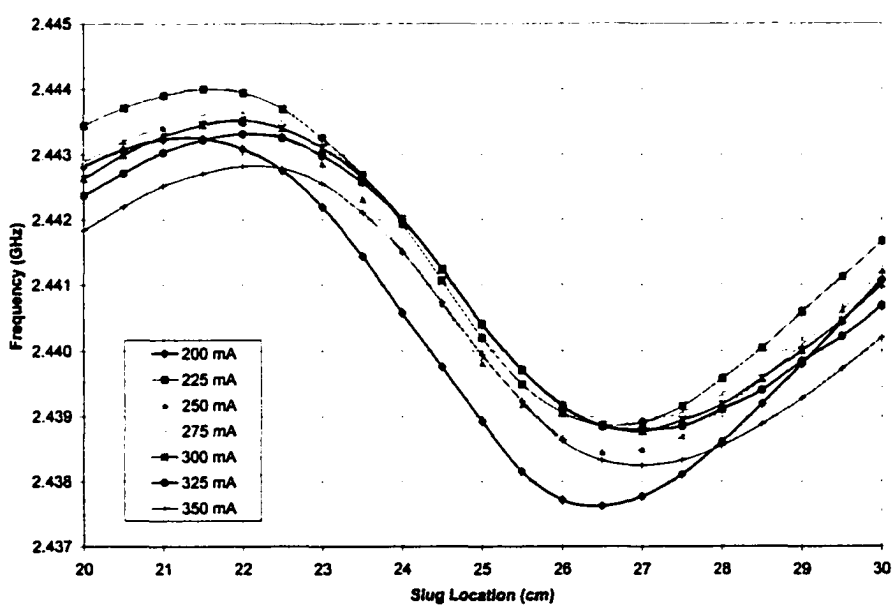

Figure 5.4-29. Effect of Power Control on Frequency Response for a Class III MDA (Expanded), Slug 1.

As the power is increased, the maximum frequency pulling range is compressed slightly, from ~5.5 MHz at 200 mA to ~4.5 MHz at 350 mA. This effect is explained by referring to the Figure 4.2-2. As the power of the magnetron increases, the temperature of the waveguide and load are increased. The resultant change in dimensions alters the load impedance, providing increased reflected power V_L at the magnetron port. This competing signal lessens the effectiveness of V_r, causing the MDA to break lock sooner.

Note that the frequency versus anode current profile shown in Figure 5.3-1 is not sufficient to describe the relative placements of the frequency bands in Figure 5.4-29. This curve only provides the frequency response for one given load impedance, in this case with no tuning slug. Positioning the tuning slug in the waveguide changes the load seen by the magnetron for each new slug location. Therefore, the relative magnitudes of the frequency curves at a particular slug location define the same frequency versus anode current profile for that point. This yields the family of curves shown in Figure 5.4-30.

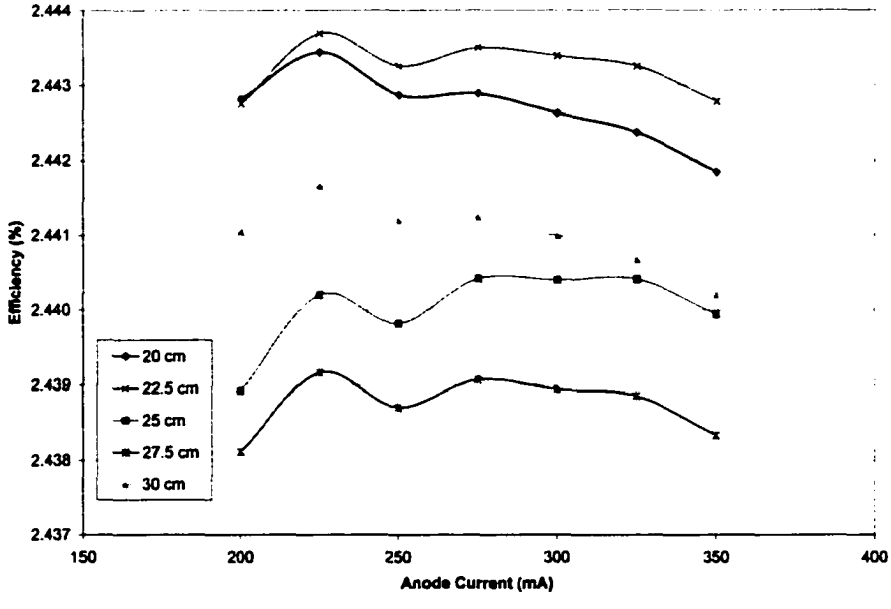

Figure 5.4-30. Frequency versus Anode Current at Different Slug Locations for a Class III MDA, Slug 1.

For comparison purposes, the same frequency analysis may be accomplished for tuning slug 2. The frequency response of the resulting MDA is shown in Figure 5.4-31. The frequency curves for this tuning slug are more consistent. Peak values of frequency are roughly constant, but the minimum frequency limits still vary with power level. Increasing the input power flattens the frequency response. Arrows in the figure above indicate the direction of increasing power. At higher powers, the waveform takes on a more pronounced sawtooth shape. The low frequency response is truncated and the transition region (sink) is pushed further right (closer to the magnetron). These effects are due to the larger effective injected signal ($V_i + V_L$) caused by reflections from the total load seen by the magnetron.

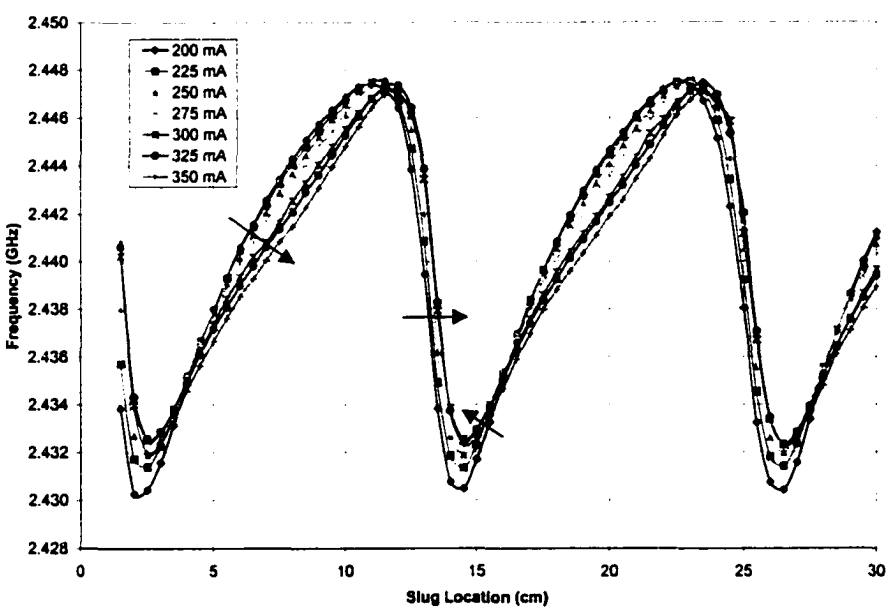

Figure 5.4-31. Effect of Power Control on Frequency Response for a Class III MDA, Slug 2.

Lower operating powers correlate to dirtier, less stable oscillating frequencies. The relatively unstable output is more easily affected by an injected reference signal. Higher operating powers displayed cleaner output signal qualities and therefore less locking

bandwidth for the same injected signal. Figure 5.4-32 shows the details for an expanded area. This plot shows frequency curves in the sink region nearest the magnetron.

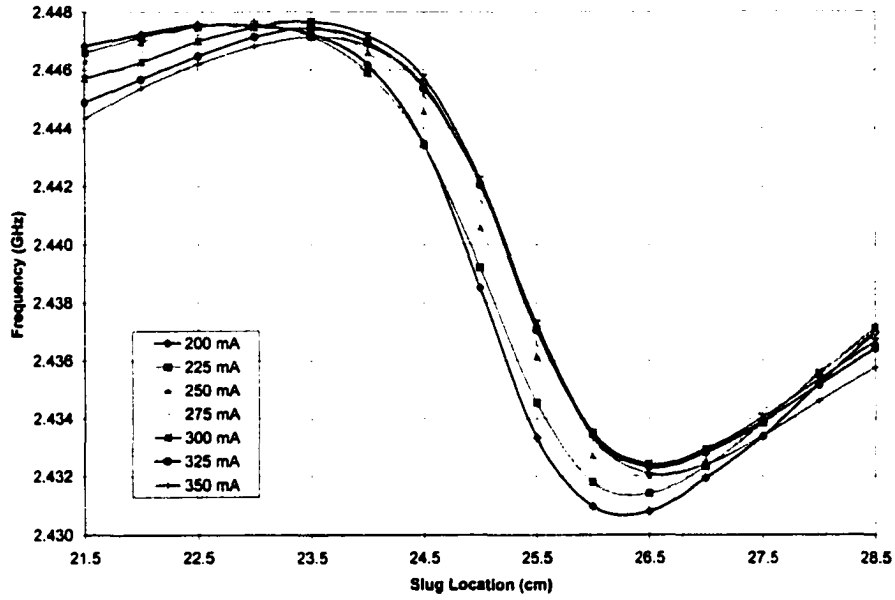

Figure 5.4-32. Effect of Power Control on Frequency Response for a Class III MDA (Expanded), Slug 2.

The sink location has been shifted, as was the case for slug 1. However, crossover points for the curves are now largely constrained to two distinct locations. For this slug, the increase in power constricts the maximum frequency pulling range from ~17.2 MHz at 200 mA down to ~15.1 MHz at 350 mA.

The frequency versus anode current curves for the MDA using slug 2 are shown in Figure 5.4-33. Note that due to the location of the crossover points, the slope of the curve would be positive for all values in the range of ~23.5 to 27.5 cm, as is the case for the 25.0 cm curve.

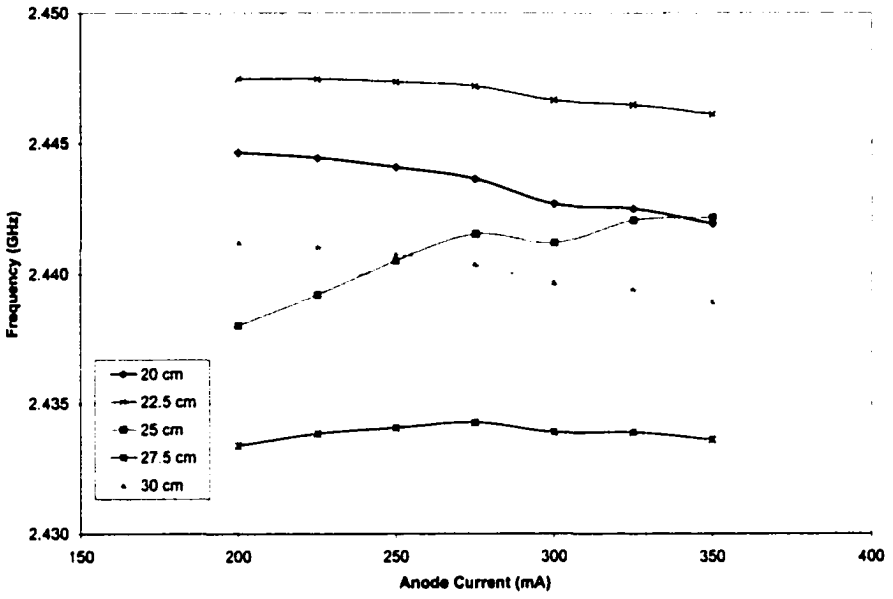

Figure 5.4-33. Frequency versus Anode Current at Different Slug Locations for a Class III MDA, Slug 2.

Power versus Frequency. For the MDA, the power versus frequency response is of prime concern. As discussed above, the input DC power provides an effective means to control the output power. Unfortunately, it also has some affect on the operating frequency. This may be counterbalanced by the use of a tuning slug, however, the slug also affects the output power. To view the relative magnitude of the effects, it is helpful to plot the output power versus frequency for the slugs of interest. The set of curves for slug 1 is shown in Figure 5.4-34; corresponding curves for slug 2 are shown in Figure 5.4-35.

These curves provide a measure of power stability across the frequency operating range. The upper portion of the curves represents the sink region(s) of the magnetron for that combination of output power and load impedance. The flatness of these curves defines the operating characteristics possible for the MDA.

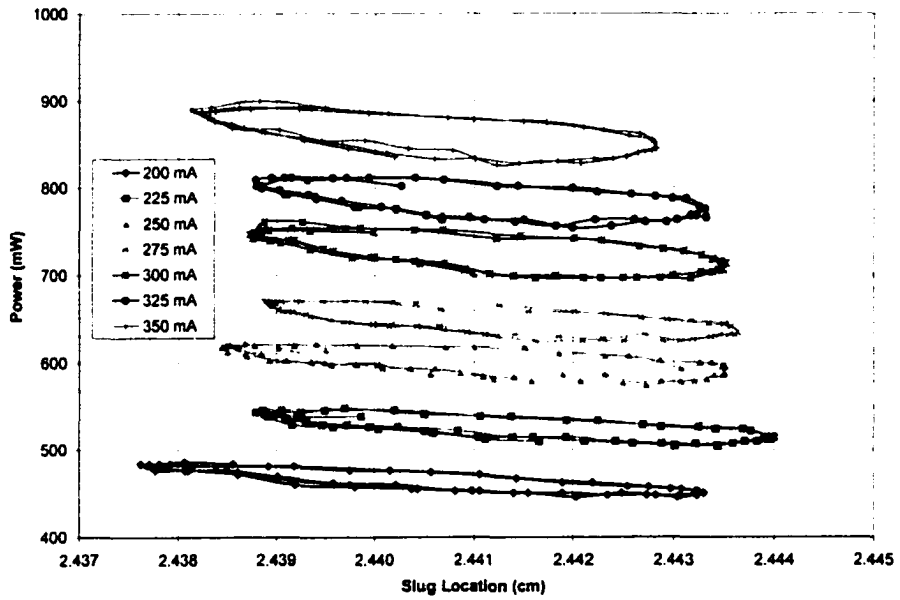

Figure 5.4-34. Output Power versus Operating Frequency for a Class III MDA Using Input Power Control, Slug 1.

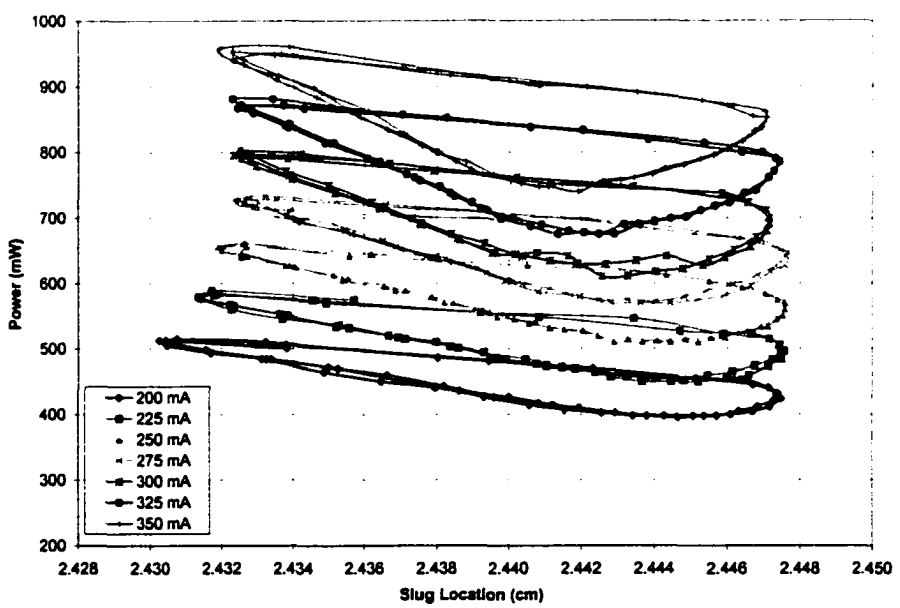

Figure 5.4-35. Output Power versus Operating Frequency for a Class III MDA Using Input Power Control, Slug 2.

Some adjustment in tuning range is possible by altering the power level. However, assuming that power is to be kept relatively constant to maximize efficiency or for stability in a phased array, then this method is undesirable. Additional frequency tuning would then require using a larger slug, but this also increases the effect on output power.

Therefore, the design of the Class III MDA boils down to a design choice balancing the stability and tunability of the system. Large slugs provide more tuning range and a higher maximum power output (and efficiency). However, they also load the magnetron more heavily and require more precise positioning to achieve the desired operating point. To highlight the relative influence of the two slugs, their effects are compared in the same plot, shown in Figure 5.4-36.

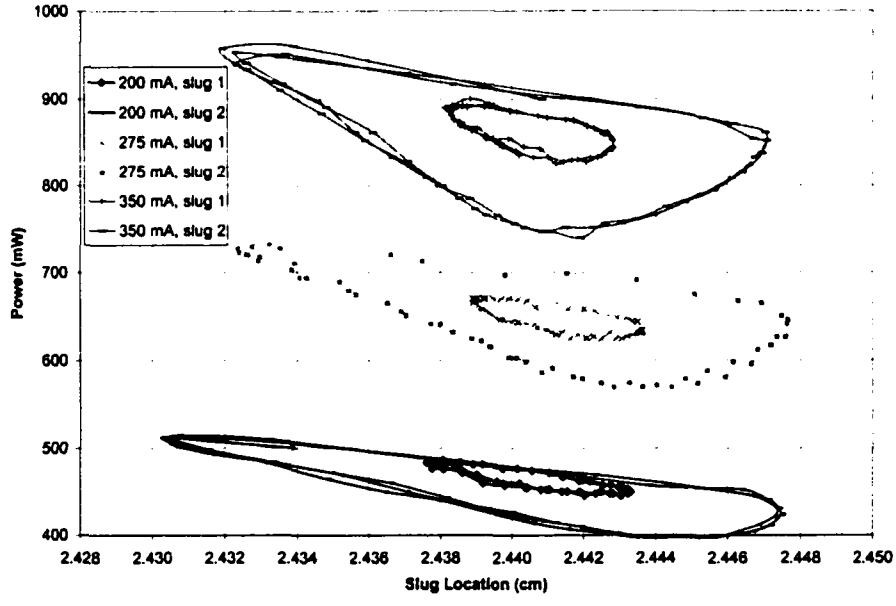

Figure 5.4-36. Comparative Output Power versus Operating Frequency for a Class III MDA Using Input Power Control. Data shown for slugs 1 and 2.

The large contours represent the possible output states of the MDA for the tuning slug 2; the inner contours slug 1. The larger slugs pull the magnetron further upward into the sink region and provide more frequency tuning capability. An increase in power has the

effect of compressing the curves to a more circular state. The frequency range is reduced with power, but the magnitude of power control is increased.

5.4.4 Combined Effects of Tuning Slug, Power Control, and Injected Reference Signal

This portion of the discussion briefly explores the effects of the tuning slug and power control on locking bandwidth. In the previous subsection it was shown that the tuning capability of the slug was degraded with an increase in operating power. This was attributed to an increase in reflected power caused by the waveguide expansion, shown in Figure 5.4-29. Since the slug tuning range ($\propto$ to V_r) is reduced by this phenomenon, it is logical that the locking ability of the injected signal V_i will be affected in the same way.

Figure 5.4-37 indicates that the increased power level does lower the locking bandwidth. The effects of increasing the power are highlighted by presenting the data incrementally.

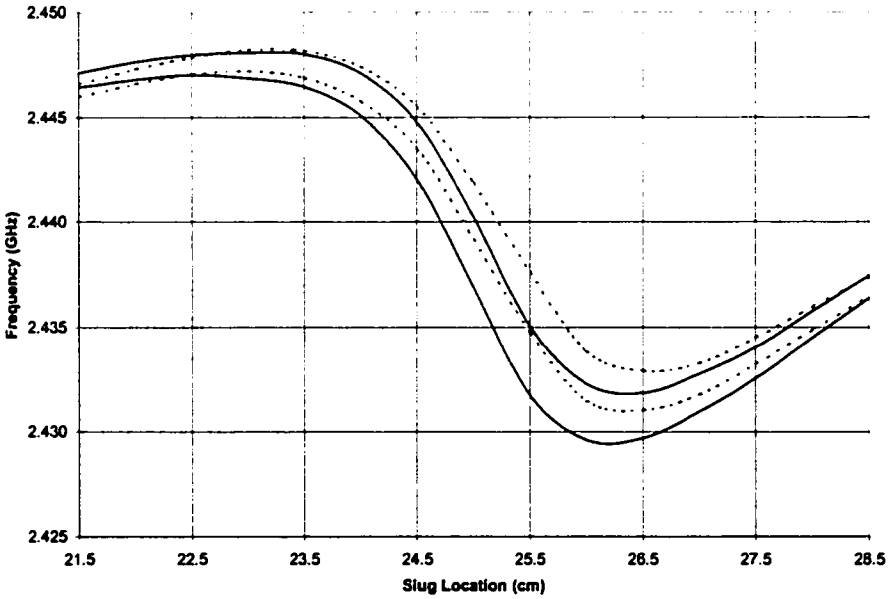

(a) Solid line: I_{anode} = 200 mA, Dashed: I_{anode} = 250 mA

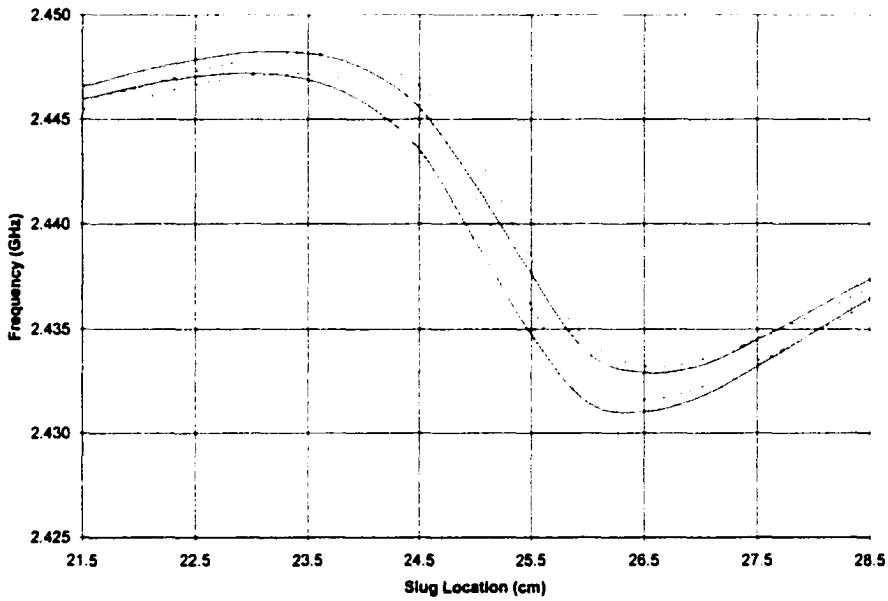

(b) Solid line: I_{anode} = 250 mA, Dashed: I_{anode} = 300 mA

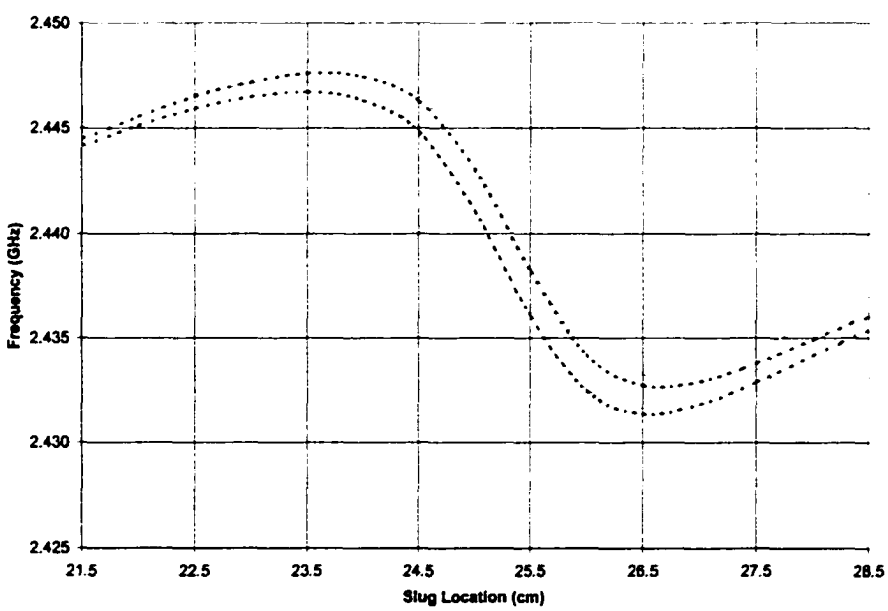

(c) Solid line: I_{anode} = 300 mA, Dashed: I_{anode} = 350 mA

Figure 5.4-37. Locking Frequency Range for a Class III MDA using Power Control. Data shown is for slug 2.

The values of the bandwidths are provided in Figure 5.4-38. The reader may notice that the 300 mA locking bandwidth above does not concur with that shown in Figure 5.4-14. This difference was caused by damage to the magnetron RF caused in the course of extensive heavy-load testing. The slight reshaping of the RF probe resulted in a partially clipped frequency response. This change did not substantially degrade the performance of the magnetron. Details of this change in operating characteristics are provided in Appendix A.4.5.

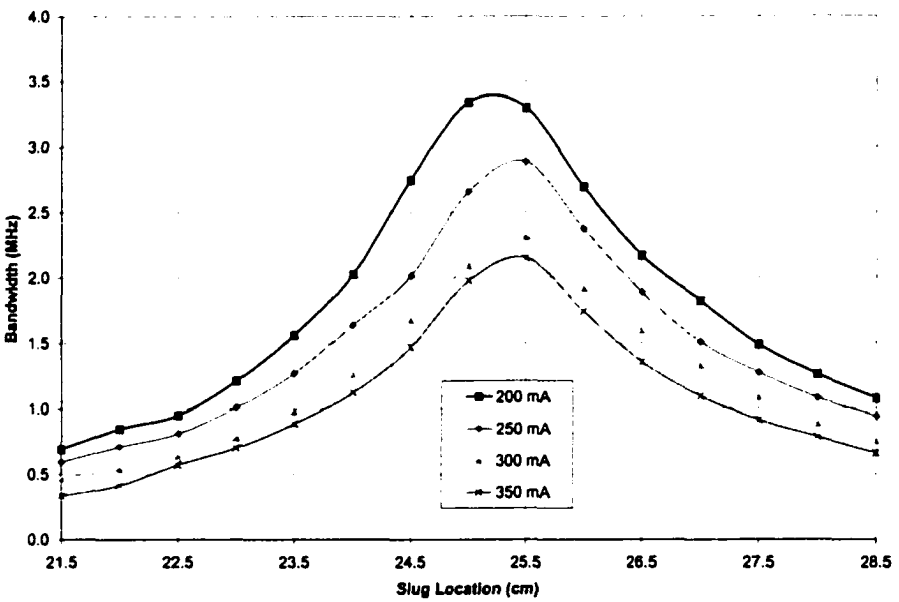

Figure 5.4-38. Locking Bandwidth for a Class III MDA. Data shown for slug 2.

5.5 Class III Closed-Loop MDA Operation

The Class III Closed-Loop (CL) Magnetron Directional Amplifier (MDA) possesses the same capabilities as a Class III OL MDA, but adds a phase-locked loop to automatically control the magnetron's frequency and phase. Output power is affected by the tuning slug position, but is primarily controlled using the DC power supply.

The performance of the magnetron as a function of input power and load impedance has been established at this point. The control inputs discussed so far are sufficient to define its behavior, short of implementing the Class IV amplitude control. The Class III OL MDA data gathered may therefore be considered a baseline for measuring the performance of the CL MDA.

The characterization of the Class III CL MDA entails verifying its operation against this known performance data. The mechanics of the closed-loop operation differ from that of the open-loop configuration, therefore its basic operation is considered first. Then the effects of varying the characteristics of the feedback control loop are briefly considered.

5.5.1 Verification of the Closed-Loop System

The first step in characterizing the Class III CL MDA was to verify its performance against that of the open-loop system. The purpose of this was to demonstrate the operation of the phase control loop and to qualitatively examine the error introduced. In support of this, the following data was collected: (1) output power versus frequency, and (2) phase limit boundaries.

From the preceding sections, a number of results preclude operating the closed-loop system throughout the entire tuning slug range. The efficiency and frequency locking bandwidths both dictate operation in the sink region. Since efficiency in a WPT system is of prime concern, operation elsewhere is highly undesirable. The sink also corresponds to the region of maximum frequency sensitivity. The combined effects of this and the minimal reflected load power provide the best frequency control. As a matter of practicality, the area of interest is further limited to the sink region nearest the magnetron. In a production system, this will provide the smallest and lightest MDA. The reduction of the long line effects may be detrimental to the frequency tuning

sensitivity for certain tuning slugs. However, this may be overcome by a judicious choice of slug sizes.

Output Power versus Frequency. The output power response as a function of frequency was recorded for different input power levels. The data was obtained by sweeping the sink region nearest the magnetron using the signal generator to vary the drive frequency. The results were compared to the data obtained for the OL MDA, shown in Figure 5.5-1.

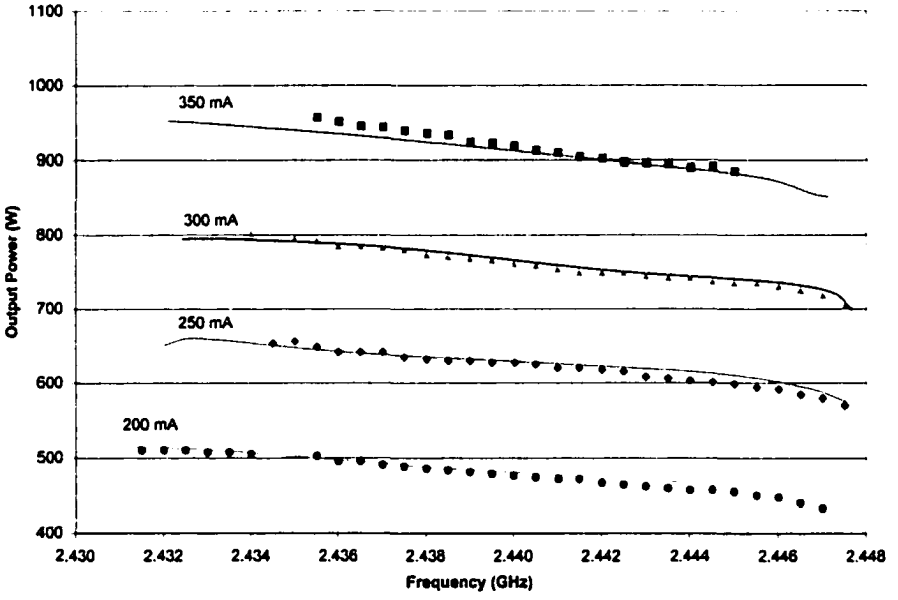

Figure 5.5-1. Comparison of Power versus Frequency for Closed-Loop and Open-Loop Class III MDA. Solid lines indicate possible values from OL operation. Data points indicate locking range obtained for CL operation. Gaps in data due to operator error.

This plot shows that the operation of the closed-loop configuration does in fact follow that predicted by the open-loop system. The open-loop values were plotted for the portion of the sink region corresponding to a slug location from 23.5 cm to 26.5 cm. This range represents all possible operating points within the range, as shown in Figure 5.5-2.

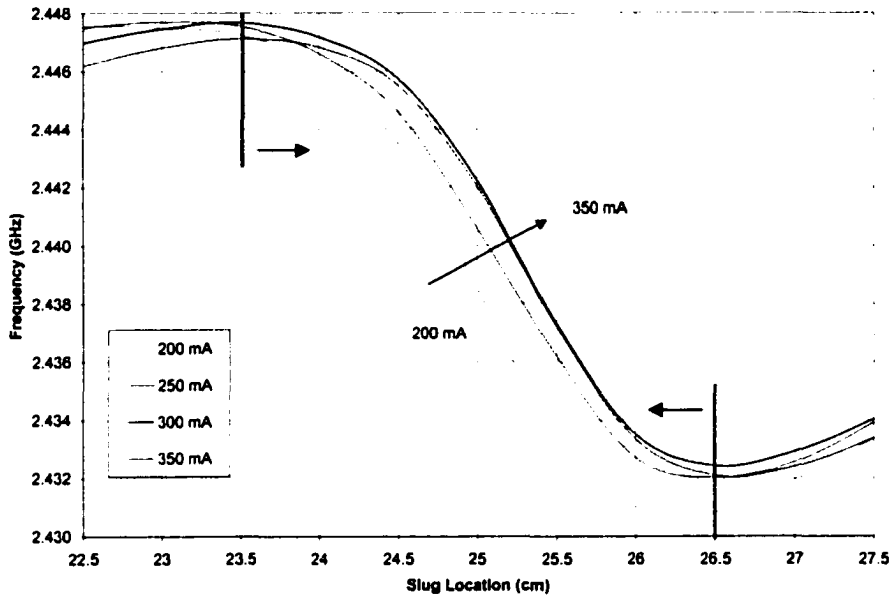

Figure 5.5-2. Linear Portion of Open-Loop Frequency Curves for Class III OL MDA. Arrows show region used for OL/CL comparison.

Not all of the open-loop tuning range is available to the closed-loop operation. The output of the phase comparator changes polarity at the extrema of the frequency curve (limits of the sink region). As the slug location approaches the limit, the slope of the frequency curve begins to roll over. The phase comparator has difficulty discerning the exact value of phase between the injected and output signals. As the slug is pushed further toward the limit, the control loop eventually breaks lock. Therefore, the closed-loop configuration is restricted to operate within a somewhat narrower region.

The closed-loop system in Figure 5.5-1 was capable of sweeping most of the upper frequency range of the sink region (except for the 350 mA case, which broke phase lock prior to going unstable). In comparison, the lower open-loop frequency bounds was not reached by any of the closed-loop power levels. In each case, phase lock was broken prior to the feedback loop going unstable, but could be reacquired by increasing the frequency to within locking limits.

By this time, the hardware configuration had been modified in response to lessons learned and to permit further investigation. The magnetron mounting bracket had been modified to permit better coupling with the waveguide launcher. The new configuration resulted in a wider range of frequencies that could be locked, as shown in Figure 5.5-3. Unfortunately, the only data set taken was for the 300 mA case.

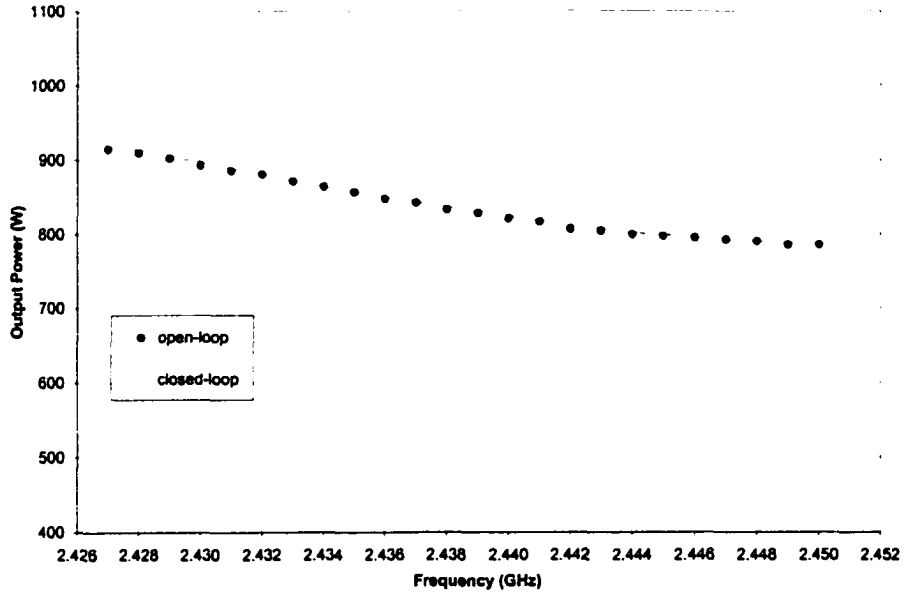

Figure 5.5-3. Power versus Frequency for Closed-Loop and Open-Loop Class III MDA, I_{anode} = 300 mA. Solid lines indicate possible values from OL operation. Data points indicate locking range obtained for CL operation.

Another point of interest regarding Figure 5.5-1 is that the power response of the MDA may fluctuate, especially for high power operation. The 350 mA curve shown in this figure is actually an average for two different data sets. The individual curves are shown in Figure 5.5-4. The upper data set had been taken as the first set of the day and did not fit the output power levels expected. Note that the first three data sets of Figure 5.5-1 had been taken consecutively and performed as expected relative to one another. The second data set for the 350 mA case (bottom most curve in Figure 5.5-4) was taken after allowing the MDA to operate for another two hours after the completion of the first set.

The effects of the thermal environment on power is significant in this case, accounting for an average of ~22 W (2.5%) between data sets.

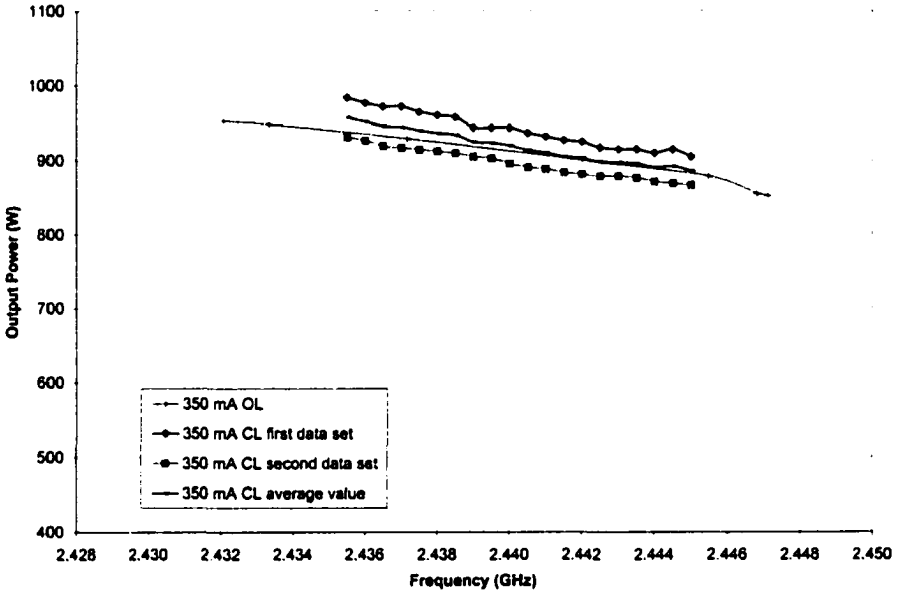

Figure 5.5-4. Power versus Frequency for Closed-Loop and Open-Loop Class III MDA. Demonstrates the effects of mode change between subsequent data sets.

Phase Limit Boundaries. In Section 5.4, the Class III OL MDA was characterized. This included the definition of the frequency locking bandwidth for a given tuning slug, as shown in Figure 5.4-14. The frequency limits describe the maximum and minimum frequency values that the MDA may be driven to for that particular tuning slug and location. These correspond to the phase limits for the frequency locked signal (±90°).

The phase limits for the CL MDA may be defined in a like manner. Instead of defining the limits vertically in terms of changing frequency, they may be defined horizontally in terms of constant frequency. This is shown in Figure 5.5-5.

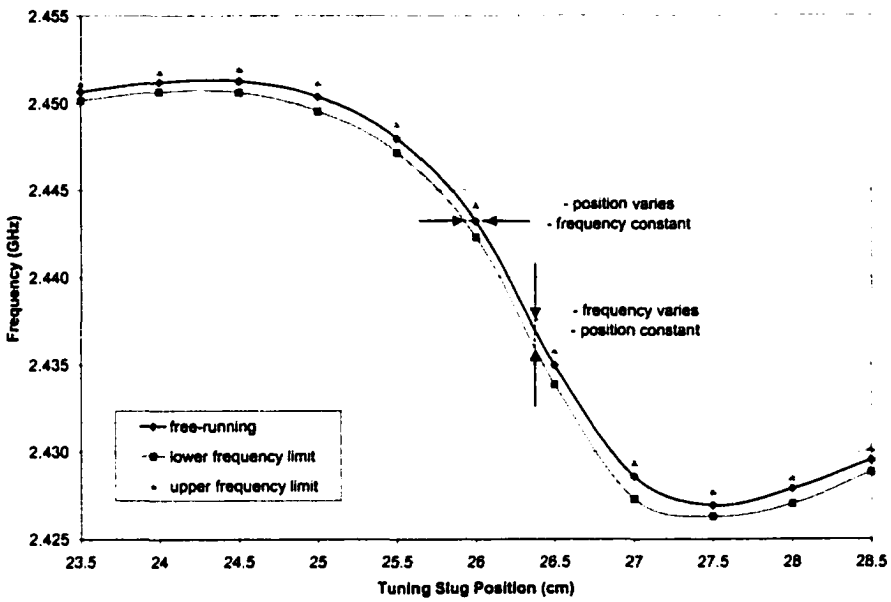

Figure 5.5-5. Phase Boundaries for a Class III MDA. Horizontal limits for CL phase shift. Vertical limits for OL locking bandwidth.

The frequency limit curves form a frequency or phase corridor for the MDA operation. For OL operation, the slug position is fixed and therefore (without changing power) the locking limits may be probed by varying the frequency of the injected signal. For CL operation, a change in the injected frequency results in the slug traveling along the center curve. However, the limits may be evaluated by varying the phase shift between the input and output signals for a particular value of frequency.

In theory, the location of the limits should agree for these two methods. David's equation governing the operation of a frequency-locked amplifier applies equally, regardless of the method used to change the phase between the signals. Therefore, given the phase boundaries either in terms of the frequency limits (OL) or slug position limits (CL), it is possible to predict the other. This is an important point in characterizing the expected behavior of the MDA. Since the magnetron is a nonlinear device dependent upon numerous inputs, and each of these is dependent upon hardware characteristics, it

can be quite difficult to determine a best estimate for performance. Any verification scheme can help minimize the time needed to optimize or troubleshoot the system.

Identifying the anticipated locking bandwidth is a useful exercise, as it directly affects the tuning ability of the MDA. It has also been shown that the efficiency pulling capability for the MDA is related to its locking bandwidth (Section 5.4.2). This process has already benefited the characterization of the UAF Class III MDA. It was used to identify a limitation in the injected signal strength, which was subsequently corrected. The frequency limit curves (OL) and slug position limit curves (CL) for the initial measurements are shown in Figure 5.5-6.

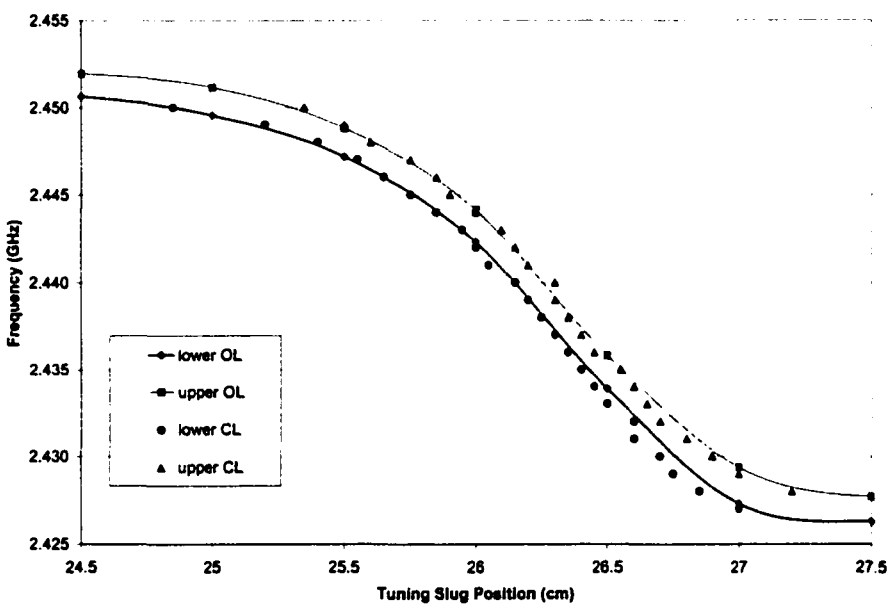

Figure 5.5-6. Initial OL and CL Phase Limits for a Class III MDA. Solid lines indicate OL operation. Data points indicate CL operation. Data is for slug 2.

Comparing the data for the two configurations, the CL results provide somewhat higher bandwidth. Since it has more data points over the range of interest, it is selected as the most likely candidate to model. The predicted frequency data may now be used to

generate a corresponding locking bandwidth curve. This is compared to the actual bandwidth in Figure 5.5-7.

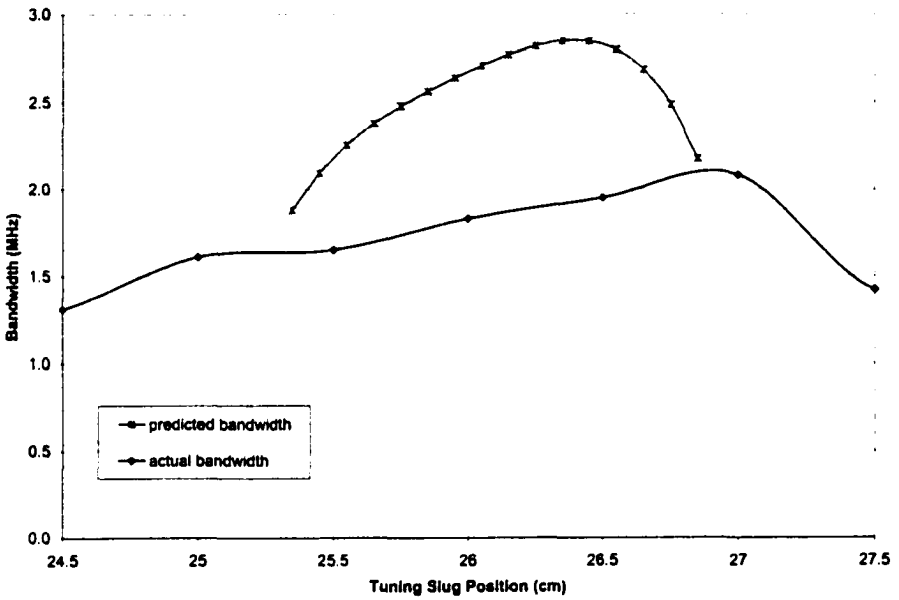

Figure 5.5-7. Comparison of Initial and Predicted Locking Bandwidth for the Class III OL MDA.

As a note, the actual bandwidth shown in this figure appears misshapen compared with that normally seen (see Figure 5.4-14). A portion of this may be due to the granularity of the data taken. However, the bandwidth pattern has also been affected by a number of configuration changes to the MDA. These include adjustments made to the magnetron mounting plate and to the shorting plate location. Either of these may alter the frequency and power characteristics of the MDA. These factors are of interest and are therefore discussed in Appendices A.4.3 and A.4.8.

The predicted bandwidth pattern provides a more likely practical limit to the locking bandwidth. This value was determined by operating the MDA in the CL configuration. The phase boundaries were evaluated by driving the tuning slug position to the edge of

lock for a given frequency. If the CL bandwidth value is to be believed, then some additional factor must impede the effectiveness of the injected reference signal.

Examining the RF injection port reveals two causes for the interference: (1) In the current hardware configuration, RF energy bleeds past the circulators and is coupled through the injection probe to the RF amplifier, and (2) the amplified RF signal being injected is reflected due to impedance mismatches. A schematic showing these signals is provided in Figure 5.5-8. For more details, refer to Figure 3.5-3 and Appendix A.2.

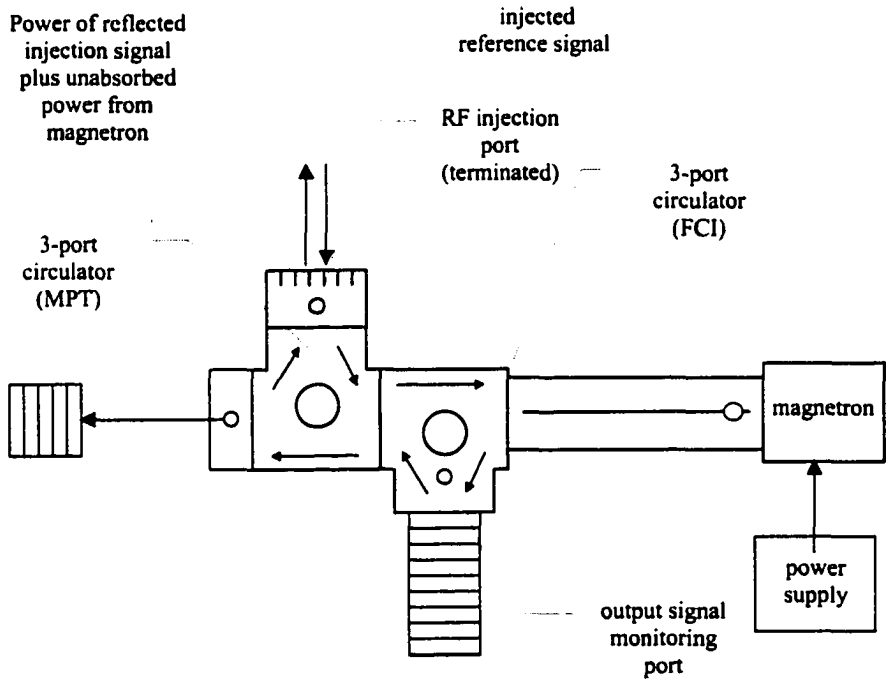

Figure 5.5-8. Injected Reference Signal Degradation by Reflected Power.

The value for the reflected signal measured at the power meter is shown in Figure 5.5-9. This data shows that a significant amount of RF energy interferes with the injected reference signal, especially at the low frequency limit. Some of this is due to the impedance mismatch seen by the injected signal when entering the waveguide. The amount of this contribution may be calculated and compensated for, as described in

Appendix A.2. In addition, it is possible to reduce the impedance mismatch by tuning the injection probe (not done here).

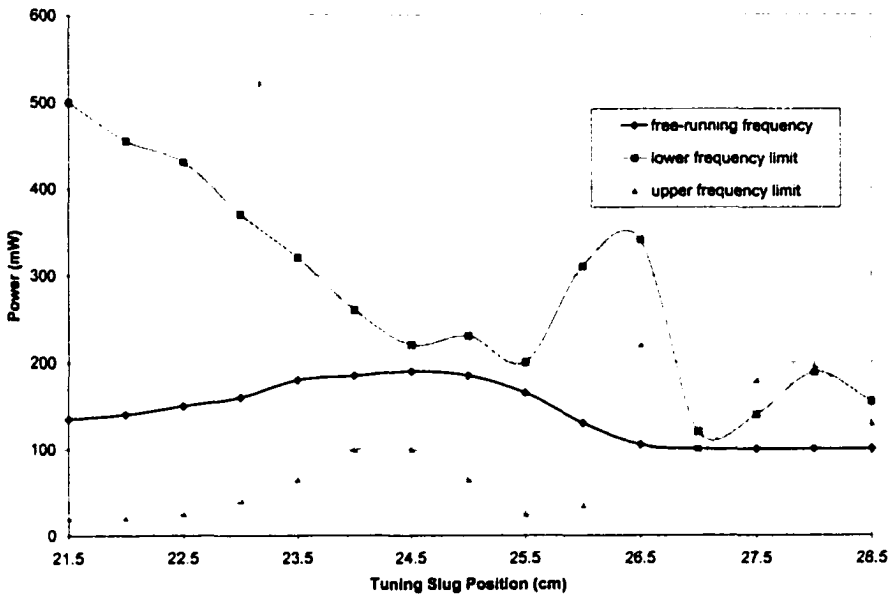

Figure 5.5-9. Power Measured out of Injection Port. Signal composed of reflected power from RF amplifier and bleed-through power from magnetron.

Eliminating the bleed through power from the magnetron requires the addition of a third waveguide circulator. The modified configuration is shown in Figure 5.5-10. The result of the additional circulator was to effectively isolate the injection probe from the unwanted reflected power of the magnetron. Figure 5.5-11 shows the total power at the injection port for the locking BW frequency limits over the sink region. The additional circulator eliminates this signal and greatly reduces the reflected power seen over most of the operating region. It also stabilizes the available injected power to the magnetron over the entire region.

As expected, the reduction in reflected and bleed-through signals at the injection port increases the locking bandwidth, as shown in Figure 5.5-12. The actual bandwidth achieved closely mirrors the predicted value.

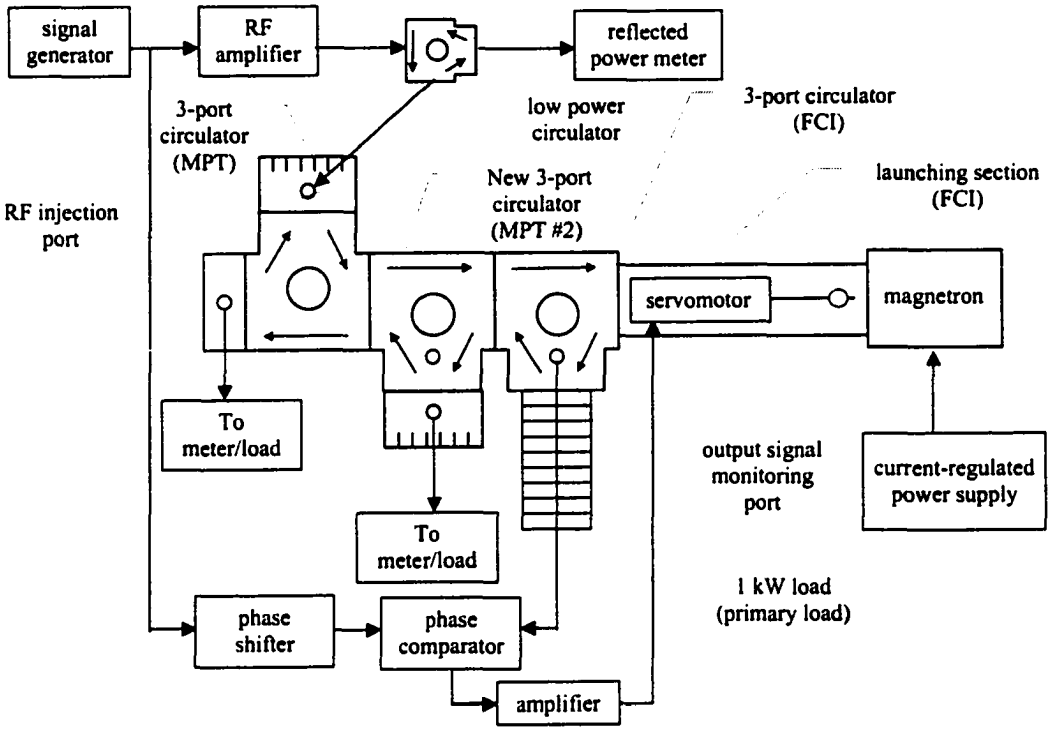

Figure 5.5-10. Modified Hardware Configuration for Class III CL MDA.

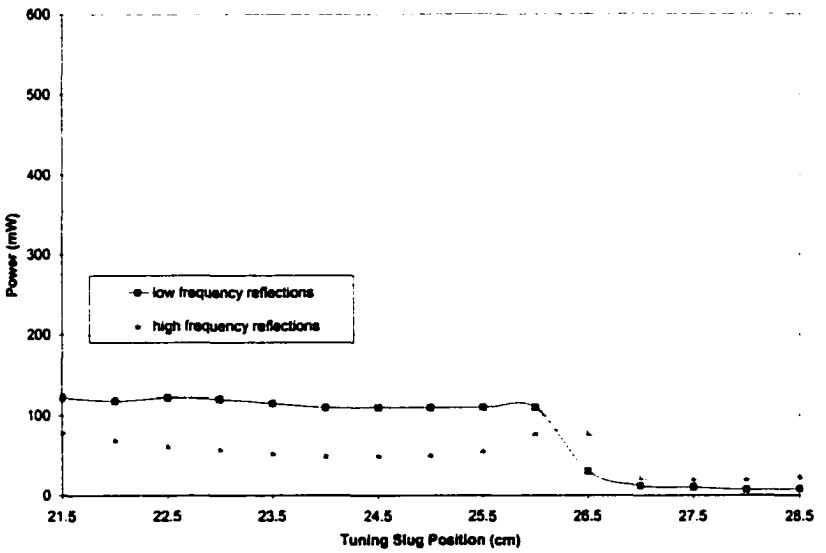

Figure 5.5-11. Effects of Additional Circulator on Total Power Seen at Injection Port. Circulator provides lower reflected power and increased stability over most of the region (compared with Figure 5.5-9).

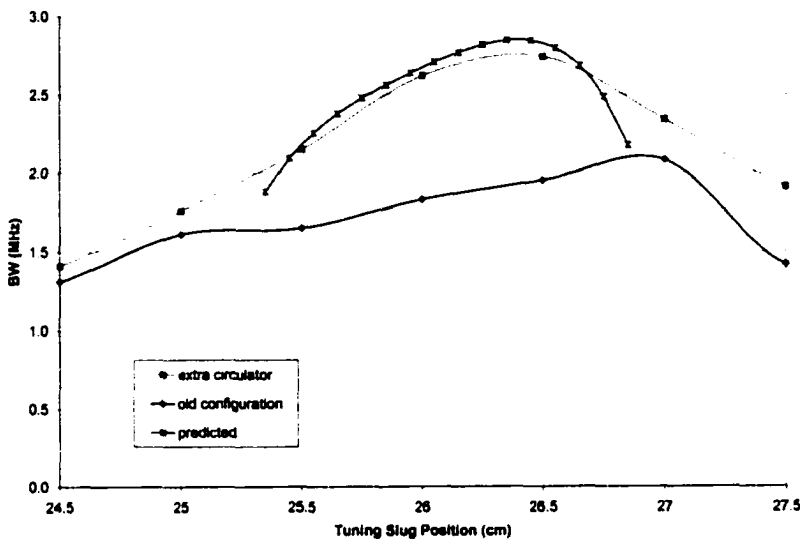

Figure 5.5-12. Effects of Additional Circulator on Locking Bandwidth for the Class III OL MDA.

5.5.2 Effects of Automatic Phase Control

The second portion of this effort was a brief examination of the phase control loop behavior. A full characterization would have included an analysis of: (1) steady state error injected by the control loop, (2) speed of the system, and (3) stability of the system. Unfortunately, time did not permit this to be accomplished.

A qualitative examination of the control loop revealed that the MDA operates satisfactorily for ground-based WPT applications. The slug positioning arrangement described in Section 3.5 affords frequency and phase shifting on the order of a few milliseconds. Component characteristics are provided in Appendices A.2 and A.3. Referring to Figure A.3-1, a servomotor amplifier gain of K_c = 100 provided fast, but stable operation. A gain of 200 resulted in oscillatory behavior of the tuning mechanism associated with marginal stability.

The MDA characterization effort was focused on predicting the limits of operation, which are primarily bounded by the OL characteristics. The Class III CL MDA should behave according to the data presented to this point. Preliminary indications suggest that it does, however much more analysis of the closed-loop system is first needed to adequately quantify its characteristics. Section 8.2 provides recommendations for follow on efforts in this area. The same can be said for the analysis of the Class IV MDA.

6.0 ESPAM

The Electronically-Steerable Phased Array Module (ESPAM) is a single MDA configured as a radiating element in a phased-array for wireless power transmission (WPT). The term ESPAM, coined by Brown, refers to the modular nature of the unit [12]. An ESPAM provides a building block for creating WPT systems that can be specifically tailored to a diverse range of applications.

The concept of operations for the ESPAM is to provide a self-contained radiating unit that may be easily integrated with additional units using a common signal feed and power system. To date, the emphasis has been on characterizing the performance of an individual unit, assessing the sensitivity of its performance to changes in various parameters, and optimizing the functional aspects of its design. Future efforts will shift focus to the form and fit aspects of the ESPAM necessary to make the unit practical for ground and space use.

6.1 ESPAM System Description

Figure 6.1-1 shows the hardware configuration for an ESPAM. It is essentially the same as a MDA, with only slight modifications made to the input and output interfaces. The dummy load used in the MDA is simply replaced by an antenna and some type of impedance matching device, such as a stub-tuner. The input reference signal received by an individual ESPAM unit may require conditioning such as amplitude, phase, or possibly frequency adjustments. This depends largely upon the parameters that may be adjusted for a given application and the scheme used to control the WPT phased array.

Generally, it is assumed that the ESPAM will be comprised of fully functional Class IV MDA units. However, a partially functional ESPAM may be created using any of the different classes of MDA. This situation may arise through equipment shortages or in

designing simplistic systems with very specific capabilities. Though these limited configurations do not provide the full capability of the ESPAM, they are often useful in certain ground-based demonstrations and testing.

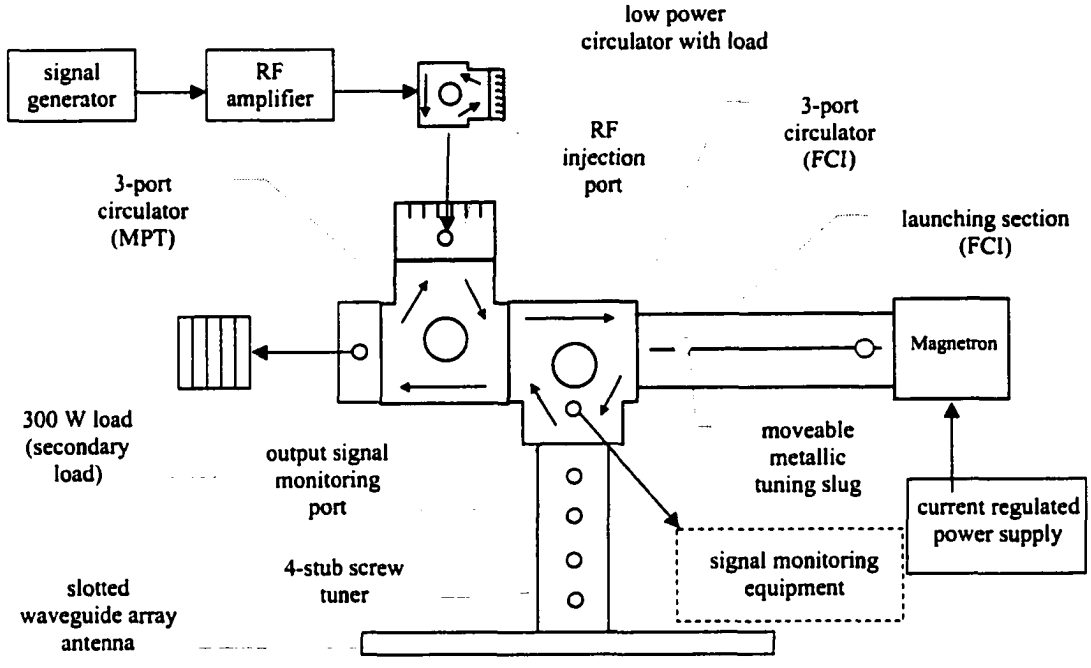

Figure 6.1-1. Physical Configuration of Class III OL ESPAM. Primary load of MDA replaced by SWA and tuning section.

For instance, when a magnetron having the integral electromagnet is not available, a regular microwave oven magnetron may be substituted to create a Class III CL MDA. This configuration provides all the capability of the Class IV MDA, with the drawback that multiple units cannot generally be operated from a common power supply. As another example, Class III OL MDA units may be used to construct a limited ESPAM capable of manually steering a beam of energy.

To avoid ambiguity, the unqualified term 'ESPAM' will only apply to those units comprised of Class IV MDAs. In any other case, the capability of the component MDA

will be identified in its title. For example, an ESPAM consisting of a Class II MDA is termed a Class II ESPAM. The hardware configuration used for the 2-element beam steering demonstration discussed in Section 6.4 consisted of a Class III OL ESPAM and a Class II ESPAM.

Though the antenna may be of any type suitable for a given application, Brown's concept was to use a slotted waveguide array (SWA) for this purpose. A diagram of the SWA is shown in Figure 6.1-2. This antenna may be easily and inexpensively fabricated on a large scale, even in space [13]. For test purposes, two small-scale prototypes were built by Raytheon where Brown worked.

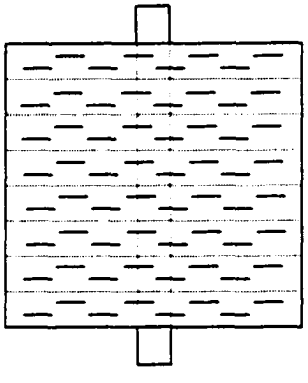

Figure 6.1-2. Prototype Slotted Waveguide Array (SWA).

The prototype SWA consists of a thin aluminum skin with slots cut from the face. The face is fed by eight waveguide sections (shown by the dashed horizontal lines) constructed of the same material. These are in turn fed by a vertical waveguide section. With the dimensions used, this configuration provides an 8 x 8 array of elements with roughly equivalent phases and amplitudes. Dimensions for the slot sizes and spacing are shown in Figure 6.1-3.

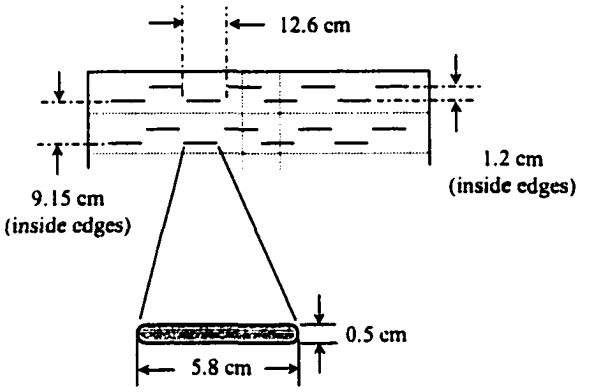

Figure 6.1-3. Measurements of SWA.

6.2 Beam Pattern for Slotted Waveguide Antenna

This section summarizes the results obtained from the beam pattern calculations of the SWA antenna. The detailed development is provided in Appendix A.1.1.

The coordinate system used to analyze the pattern of the SWA is shown in Figure 6.2-1. The angles describing the beamwidths and directions are measured from the antenna boresight (z-axis).

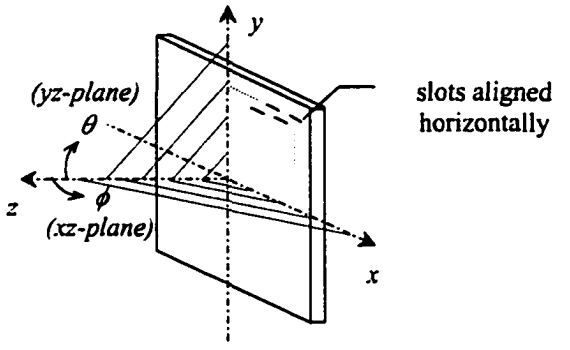

Figure 6.2-1. Geometry for Beam Measurements of Slotted Waveguide Array.

The beam pattern of the 64-element SWA is the product of the pattern factor (geometry of the elements) and the individual element pattern. Therefore, the total electric field may be written as [23]

$$E_{total} = E_{pattern} \cdot E_{slot} \tag{6.2-1}$$

where

E_{total} = resultant E - field pattern
$E_{pattern}$ = pattern factor for the 8 x 8 array
E_{slot} = pattern for a single slot element.

This concept makes it possible to calculate the pattern for the SWA by decomposition of the slot arrangement into that of a single slot element multiplied by an equivalent geometric array of point sources. Graphically, this is represented by Figure 6.2-2.

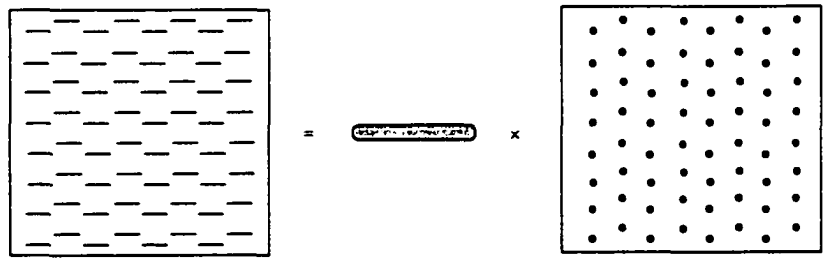

Figure 6.2-2. Graphical Equivalent of Pattern Multiplication for SWA.

The overall pattern factor for the 64-element SWA is calculated to be

$$E(\phi)_{pattern} = \frac{1}{8}\frac{\sin(4\pi\sin\phi)}{\sin(\pi\sin\phi)}\frac{\sin(2.1076\pi\sin\phi)}{\sin(1.0088\pi\sin\phi)}, \tag{6.2-2a}$$

$$E(\theta)_{pattern} = \frac{1}{16}\frac{\sin(8\pi\sin\phi)}{\sin(\pi\sin\phi)}\frac{\sin(0.3540\pi\sin\theta)}{\sin(0.1770\pi\sin\theta)}. \tag{6.2-2b}$$

The normalized slot element pattern (far-field) is given by [23]

$$E_{slot}(\phi) = 1 \tag{6.2-3a}$$

$$E_{slot}(\theta) = \frac{\cos\left(\beta L \cos\theta / 2\right) - \cos\left(\beta L / 2\right)}{\sin\theta} \tag{6.2-3b}$$

where

$$L = \text{slot length } [\lambda]$$

$$\beta = \text{phase constant} = \frac{2\pi}{\lambda}.$$

The total E-field patterns for the 64-element SWA are then

$$E(\phi)_{SWA} = \frac{1}{8}\frac{\sin(4\pi\sin\phi)}{\sin(\pi\sin\phi)}\frac{\sin(2.1076\pi\sin\phi)}{\sin(1.0088\pi\sin\phi)}, \tag{6.2-4a}$$

$$E(\theta)_{SWA} = \frac{1}{16}\frac{\sin(8\pi\sin\phi)}{\sin(\pi\sin\phi)}\frac{\sin(0.3540\pi\sin\theta)}{\sin(0.1770\pi\sin\theta)}\frac{\left[\cos(0.3018\pi\cos\theta) - \cos(0.3018\pi)\right]}{\sin\theta}. \tag{6.2-4b}$$

These calculations were implemented in MATLAB, as described in Appendix A.1.1. Plots of the field patterns are shown in Figure 6.2-3 and 6.2-4.

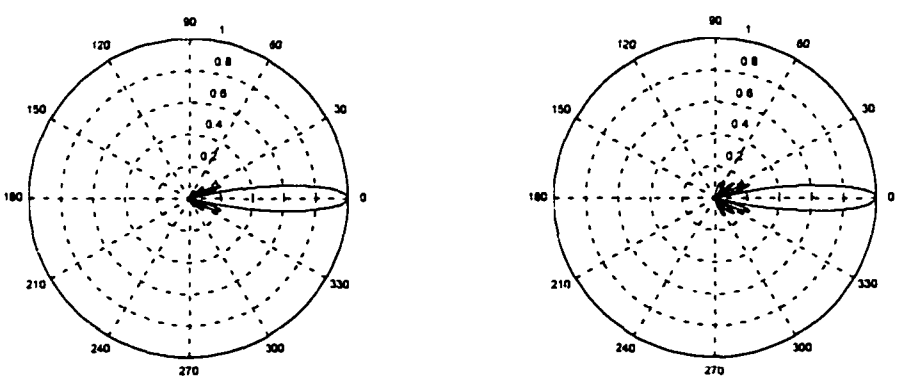

(a) $E(\phi)$ (b) $E(\theta)$

Figure 6.2-3. Polar Plots of E-fields for 64-Element Slotted Waveguide Array.

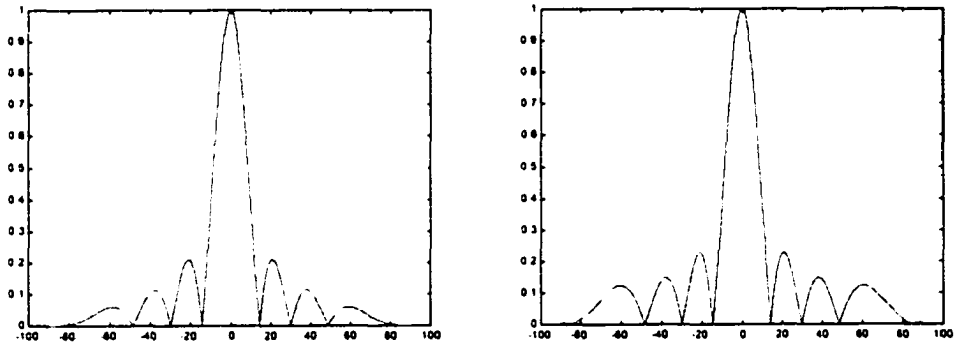

(a) $E(\phi)$ (b) $E(\theta)$

Figure 6.2-4. Fringe Plots of E-fields for 64-Element Slotted Waveguide Array.

The predicted beam pattern yielded a 3-dB beamwidth of 12.8° in each axis. These analytic results compared favorably to the measured beam patterns for the slotted waveguide array, as measured by both Raytheon and NASA JPL [13]. This model is used to predict the resultant beam pattern for multiple ESPAM units in Section 6.3.

6.3 Multiple Element Beam Patterns

ESPAM units may be combined to form phased arrays for WPT applications. These may vary widely in size and sophistication, from a simple 2-element ground-based technology demonstrator to a large commercial system providing power to remote areas. The ESPAMs may even be used as the basis to construct a Solar Power Satellite (SPS), as discussed in Chapter 7.

The same process of pattern factor multiplication used to calculate the single SWA pattern may be extended to predict the resultant beam formed by multiple ESPAM units. From this macro viewpoint, the entire SWA is considered the individual element and the pattern factors are dependent upon the geometry selected. ESPAM units may be configured to form a phased array of any size and shape, as shown in Figure 6.3-1.

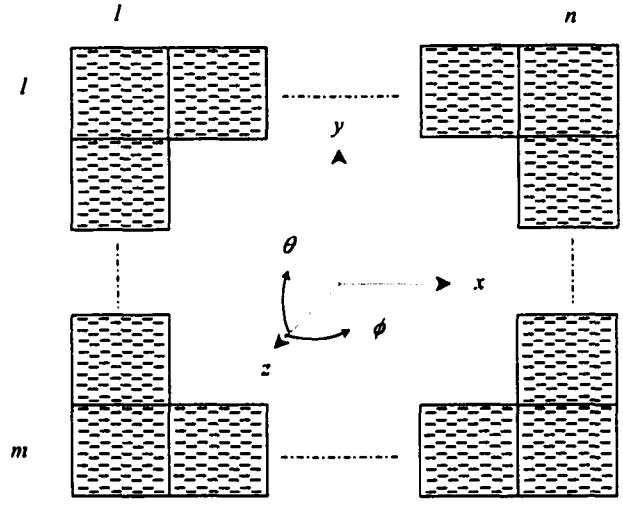

Figure 6.3-1. Rectangular Phased Array of m x n ESPAM Units.

Maintaining the previous coordinate system, the resulting E-field pattern is given by

$$E_{total} = E_{SWA} \cdot E_{pattern} \tag{6.3-1}$$

where

E_{total} = resultant E - field pattern
E_{SWA} = pattern for single SWA element
$E_{pattern}$ = pattern factor.

The normalized pattern factors for the array are described by [23]

$$E_{pattern}(\phi) = \frac{1}{n} \frac{\sin\left(n\psi_h/2\right)}{\sin\left(\psi_h/2\right)} \tag{6.3-2a}$$

$$E_{pattern}(\theta) = \frac{1}{m} \frac{\sin\left(m\psi_v/2\right)}{\sin\left(\psi_v/2\right)} \tag{6.3-2b}$$

where

n = number of units in x - direction (horizontal)

m = number of units in y - direction (vertical)

ψ_h, ψ_v = total phase shift between adjacent horizontal, vertical elements = $d_r \cos\phi + \delta$

d_{rh}, d_{rv} = distance (center - to - center) between horizontal, vertical elements [rad]

ϕ, θ = horizontal, vertical angle from antenna boresight [rad or deg]

δ_h, δ_v = electrical phase shift between horizontal, vertical elements.

The geometry required of the phased array is dependent upon the application. The beamforming portion of the WPT system must satisfy requirements for beamwidth, maximum steering angle, sidelobe levels, and energy density (gain). These drive the number of elements and shape of the array.

As an example, a portable WPT demonstrator may be required to operate within a fairly compact area. It may be required to steer a microwave beam through a rather broad range, say ±30° from the antenna boresight along either axis, with a beamwidth of under 10°. This system would most likely have a relatively low power requirement (say 4 kW), as it may be limited by power available and possibly by transmission levels. The sidelobe levels for this device would generally be of some concern, as it is desirable to minimize human exposure and limit inadvertent RF interference. However, from a power efficiency standpoint, this probably would not be a critical issue. Such an array could easily be constructed with as little as four MDA elements, each driving a low-gain horn antenna (vice the directive SWA antenna).

By comparison, the beam shaping requirements of a SPS at geosynchronous orbit would be much different. This application would require a beamwidth of ~1 arcminute to illuminate the ground receiving site. The received power density would need to be in excess of 150 W/m^2 to be commercially viable (Chapter 7). These tight beamwidth and power density requirements dictate a transmitting array with over 250,000 ESPAM elements. The cost of getting equipment to orbit, demands that the array be made as

small as possible. These competing requirements demand that efficiency be of primary concern in the design. In this scenario, particular attention would be paid to eliminating pattern sidelobes to capitalize on efficiency.

The beam requirements for these or any other phased arrays may be specified in terms of the array geometry. Each parameter in Equation 6.3-2 above has some effect on the resulting beam shape. These will be discussed briefly here in terms of standard antenna performance measures, then examined in-depth in the following subsections.

Beamwidth. The beamwidth of an array is a function of the single element pattern and the maximum separation between elements,

$$BW_{array} \propto \frac{BW_{element}}{nS_{\lambda}} \tag{6.3-3}$$

where

n = number of elements
S_{λ} = element spacing $[\lambda]$.

Therefore, the beamwidth of the main lobe may be decreased by either increasing the number of elements, or by increasing the spacing between them. The effects of varying these parameters are studied in Sections 6.3.2 and 6.3.4.

Gain. The gain of the antenna is a measure of how well the antenna focuses the beam, or how much of the radiated energy is concentrated into the main lobe. This is dependent upon the physical size of the antenna with respect to its operating frequency [23],

$$G = \frac{4\pi}{\lambda^2} A_p \varepsilon_{ap} \tag{6.3-4}$$

where

G = gain of antenna
λ = wavelength [m]
A_p = physical aperture [m^2]
ε_{ap} = aperture efficiency.

For a phased array, the gain of the resultant antenna structure depends upon that portion of the overall area that is occupied by physical elements. This accounts for any empty space that may exist between the elements that does not contribute to the overall power transmitted. The empty space may be a result of extended element spacing or due to failed elements. The impacts of these effects are examined in Sections 6.3.3 and 6.3.5, respectively. The gain is also dependent upon the total number of elements comprising the array (Section 6.3.2).

Sidelobe Levels. Sidelobe levels are closely related to the gain of the phased array. Any energy transmitted must be accounted for within the total beam pattern. As the gain of the phased array is reduced, the sidelobes are thereby increased with respect to the main lobe. Therefore, the sidelobe levels are affected in the same way as the gain by the array geometry (Sections 6.3.2, 6.3.3, and 6.3.5). The sidelobe levels are caused by the intersection of the single element beam pattern and the grating lobe patterns. This forces the location of the resulting pattern nulls and maxima (discussed later).

Beam Steering. The beam steering capabilities of the array are established by the phase shift δ between the elements and by the beam pattern for the individual SWA antenna. The phase shift determines the amount of steering applied to the resultant beam. The single element pattern acts as a filter, limiting the effective amount of steering possible and defining the resultant sidelobe levels. This topic is addressed in Section 6.3.4.

As these performance measures are dependent upon multiple array effects, it is difficult to fully explain them without also examining the array effects in some detail. This is the subject of the remainder of this section.

6.3.1 Sample Calculation of a 2-Element Array

The following sections examine the characteristics of the phased array composed of ESPAM units. The goal is to highlight the sensitivity of the array to variances in its design parameters in Equation 6.3-1, and to identify inherent limitations. Where possible, the effect of varying each parameter is considered separately. Combined effects are examined in the SPS phased array design in Section 7.3.

As a starting point for this effort, a simple 2-element array is analyzed. overall dimensions of the SWA are shown in Figure 6.3-2.

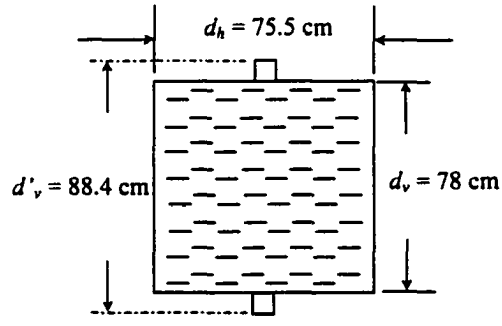

Figure 6.3-2. Overall Dimensions of the SWA.

The physical size of the SWA limits the minimum spacing between elements. For the moment, only horizontal arrays will be considered. (The added complexity of the vertical antenna dimensions will be addressed in Section 7.3.1.) The free space wavelengths at 2.45 GHz is $\lambda = 12.24$ cm. Therefore, the minimum horizontal separation between the centers of adjacent SWA units in terms of wavelengths is $S_{h\lambda} = 6.17\lambda$.

For a 2-element phased array aligned horizontally, the resulting beam may be calculated using pattern multiplication. This process is represented by Figure 6.3-3.

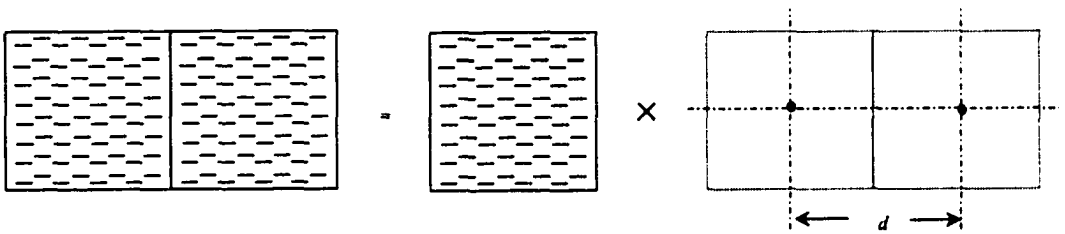

Figure 6.3-3. Beam Pattern Factor Geometry for 2 SWA Elements.

The normalized pattern factor is

$$E_{pattern}(\phi) = \frac{1}{2}\frac{\sin(12.34\pi\sin\phi)}{\sin(6.17\pi\sin\phi)}, \tag{6.3-5a}$$

$$E_{pattern}(\theta) = 1. \tag{6.3-5b}$$

This may be multiplied by the pattern for the single SWA element given in Equation 6.2-4. The resulting beam pattern is

$$E(\phi)_{total} = \frac{1}{16}\frac{\sin(4\pi\sin\phi)}{\sin(\pi\sin\phi)}\frac{\sin(2.1076\pi\sin\phi)}{\sin(1.0088\pi\sin\phi)}\frac{\sin(12.34\pi\sin\phi)}{\sin(6.17\pi\sin\phi)}, \tag{6.3-6a}$$

$$E(\theta)_{total} = \frac{1}{16}\frac{\sin[8\pi(\sin\phi)]}{\sin[\pi(\sin\phi)]}\frac{\sin(0.3540\pi\sin\theta)}{\sin(0.1770\pi\sin\theta)}\frac{[\cos(0.3018\pi\cos\theta)-\cos(0.3018\pi)]}{\sin\theta}. \tag{6.3-6b}$$

Figure 6.3-4 shows a MATLAB plot of the $E(\phi)$ component. The effect of adding the second unit is to collimate the ϕ-pattern, decreasing the overall beamwidth by a factor of ~3 to 4.4°. The θ-pattern is unchanged, as no elements have been added in this direction.

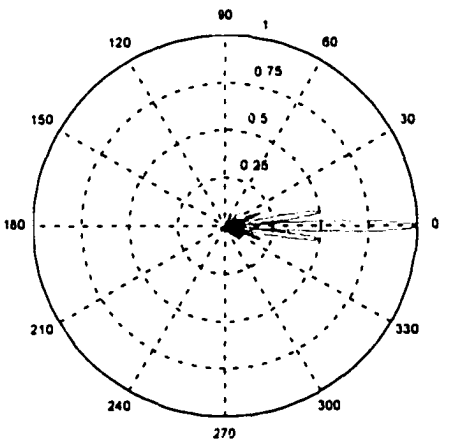

Figure 6.3-4. $E(\phi)$ Pattern for Phased Array of 2x1 SWA Antennas. Antennas mounted adjoining in ϕ-direction, spacing $S_\lambda = 6.17\lambda$, phase shift $\delta = 0$.

Examining the beam patterns associated with the pattern factor components provides insight into the resultant beam shape. The polar beam patterns for these are shown in Figure 6.3-5.

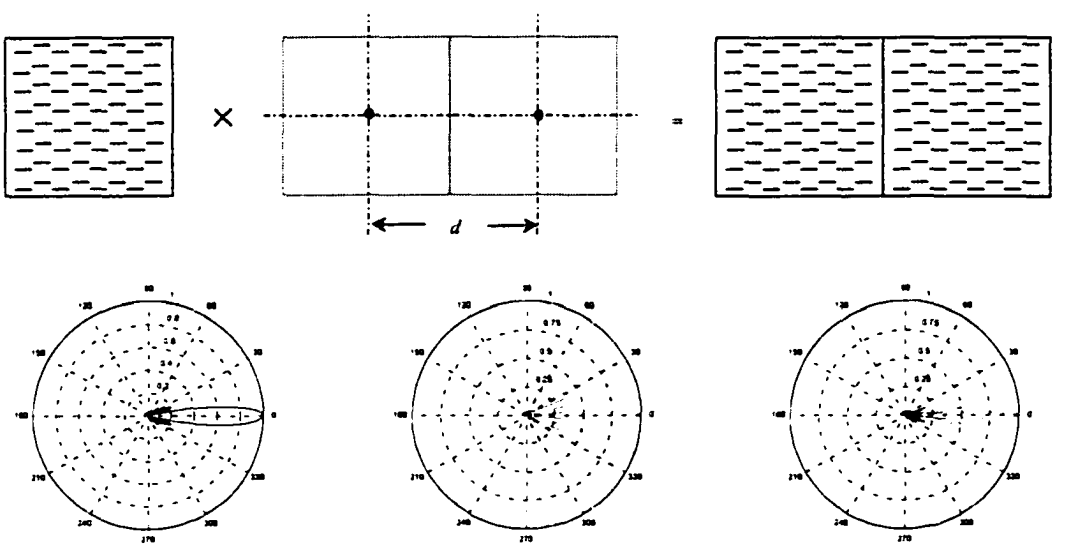

Figure 6.3-5. Beam Pattern Shapes for Pattern Multiplication of Two ESPAM (SWA) Units. Horizontal alignment, spacing $S_\lambda = 6.17\lambda$, phase shift $\delta = 0$.

Another format useful in analyzing the beam patterns is the fringe plot (rectangular beam plot) shown in Figure 6.3-6. The fringe plot expands tight sidelobe areas and provides insight into beam formation not readily apparent using polar plots.

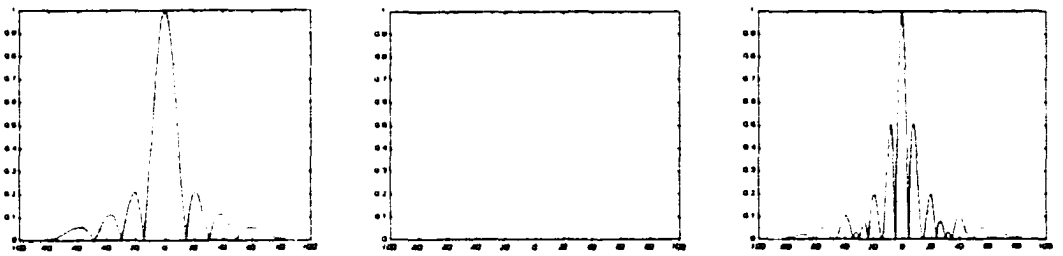

(a) single element pattern (b) pattern factor (c) resultant 2-element beam

Figure 6.3-6. Rectangular Beam Patterns for Pattern Multiplication of Two SWA Antennas. Horizontal alignment, spacing $S_\lambda = 6.17\lambda$, phase shift $\delta = 0$.

The utility of the rectangular plot format is in the decomposition of plots. The patterns may be plotted on the same rectangular plot, as shown in Figure 6.3-7.

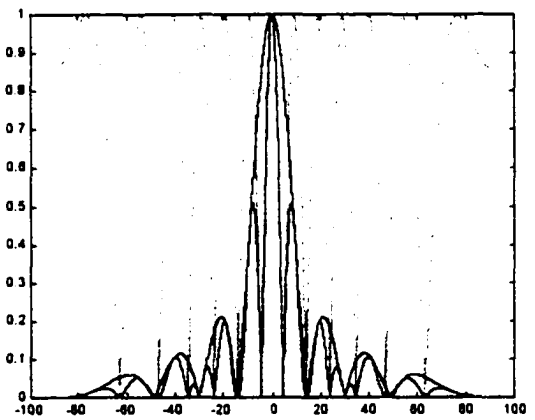

Figure 6.3-7. Pattern Decomposition for 2-Element Array of SWA Antennas. Yellow pattern is due to geometric pattern factor; blue is single element pattern; magenta shows resultant 2-element beam pattern ($S_\lambda = 6.17\lambda$, $\delta = 0$).

In this format, the resultant shape is readily apparent. Nulls in the resultant pattern are forced by nulls in either the single SWA pattern, or by the array factor. Beam maximums occur at the intersection of maximized component patterns.

The pattern factor provides a geometric pattern independent of the physical antenna used. It acts to sample the single element pattern. The single element pattern may be viewed as an envelope limiting the possible values of the resultant pattern. In addition, many other factors that must be considered in the design of large arrays are easily recognized by this graphical technique. This includes the effects of element spacing, missing elements, and beam steering. These will be discussed as encountered in the subsequent sections.

6.3.2 Beamwidth for Multiple SWA Antennas

The number of elements n in the array affects the resultant beam pattern for the phased array given in Equation 6.3-2. This impacts the beam shape by forcing the beamwidth (of all lobes) to a specified value. As a result, the gain and sidelobe levels of the phased array are also affected.

For a long linear array ($n \cdot d_\lambda >> \lambda$), the resulting beamwidth is given by

$$BW_0 \cong \frac{2}{nd_\lambda} \tag{6.3-7}$$

where

BW_0 = total beamwidth (between nulls) [rad]
n = number of sources
d_λ = separation between sources $[\lambda]$.

The half-power (3 dB) beamwidth is related to this by

$$BW_{3dB} \cong \frac{1}{2} BW_0 = \frac{1}{nd_\lambda}. \tag{6.3-8}$$

Because of the principle of pattern multiplication, this same concept holds true for multiple SWA antennas. For an SPS constructed of n ESPAM sections described in Section 6.2, the resulting beamwidth at broadside should be inversely proportional to the number of units,

$$BW_{n\,SWA} \approx \frac{BW_{SWA} d_\lambda}{nS_\lambda} \approx \frac{2BW_{SWA}}{3n}, \tag{6.3-9}$$

where

$$BW_{SWA} \cong 12.8^\circ$$

To test this hypothesis, the calculated 3-dB bandwidth for an n-element SWA array was compared to the predicted values for the SWA array and to a linear array of point sources. The results are shown in Figure 6.3-8.

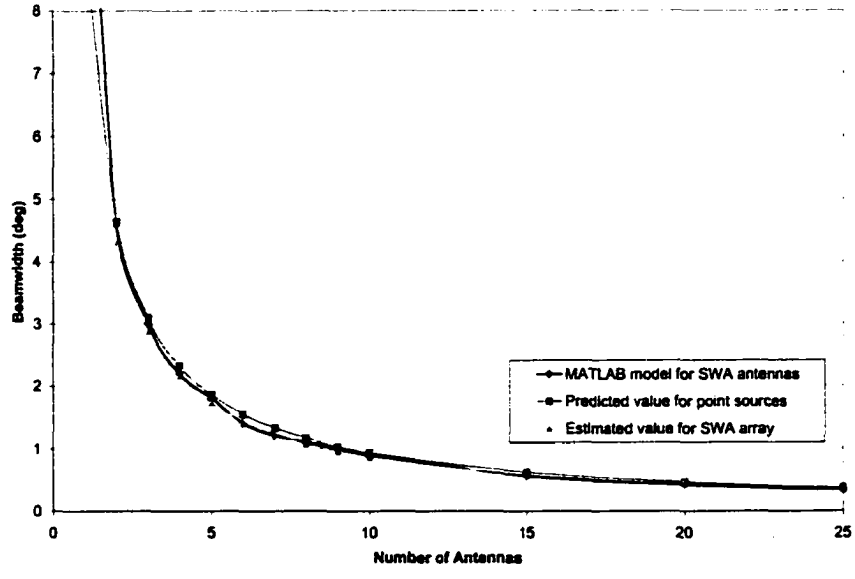

Figure 6.3-8. Resultant 3 dB Beamwidth versus Number of Sources.

This plot shows how the 3-dB beamwidth (broadside) varies with the number of ESPAM units. The plot compares the data from the MATLAB beam pattern model with the predicted beam pattern of a linear array of point sources and the estimated beamwidth for multiple SWA elements using Equation 6.3-9. Note how closely the beamwidth for the linear array of point sources follows the modeled MATLAB data. This is due to the dominating effect of the pattern factor on the resultant beam pattern (Section 7.3).

The shape of the curves argues that the beamwidth of the *n*-element ESPAM will behave as predicted. These curves were compared for calculations ranging from 2 to 1000 units. The measured values from the MATLAB model varied from the theoretical *n*-element linear array by an average of ~9%, compared to only ~6% for the predicted SWA values. Therefore, the Equation 6.3-9 provides a quick means to estimate beamwidth requirements for various size arrays.

The effect of varying the number of elements is demonstrated in the following beam patterns. As seen for the 2-element array example given above, the beamwidth of the array factor lobe is less than that of the single SWA element. As *n* is increased, this lobe quickly decreases, dominating the product of the beams. This narrow main lobe of the array factor then 'samples' the pattern of the SWA antenna. For large *n*, the beamwidth of the resultant pattern is essentially that of the geometric array factor. This explains the high correlation between the beamwidth of a linear array of point sources and that predicted by the array model for high *n* (Figure 6.3-8).

The sidelobes for the pattern factor (PF, or array factor) diminishes in magnitude with increasing *n*, as shown in Figure 6.3-10. The sidelobe levels are much reduced over those for the 2-element pattern seen in Figure 6.3-7.

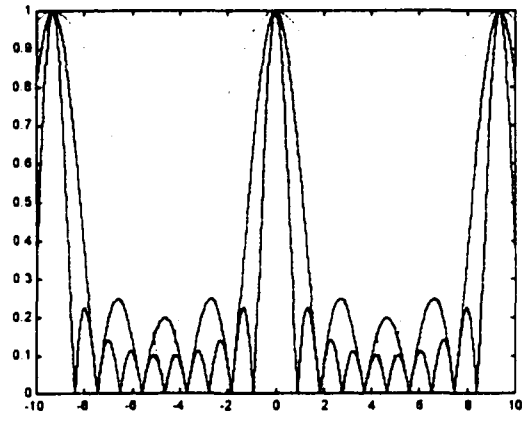

Figure 6.3-9. Expanded Region for Array Factor Patterns of Point Sources, S_λ = 6.17λ. Orange line depicts n = 2: magenta: n = 5, purple: n = 10.

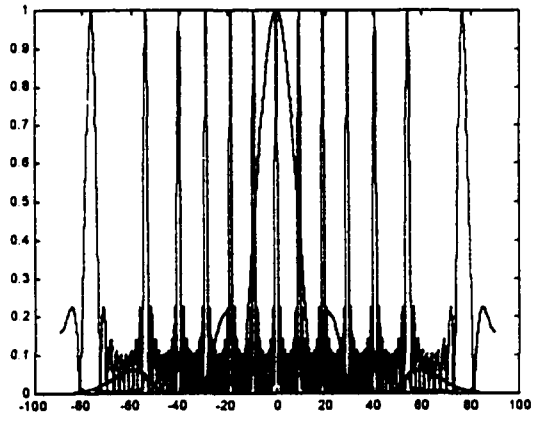

Figure 6.3-10. Resultant Beam for a 10-Element Array of SWA Antennas, S_λ = 4.1λ. Purple line depicts geometric PF for S_λ = 6.17λ; black: single SWA pattern; red: resultant pattern.

Sidelobes of the resultant pattern are further suppressed by corresponding increases in the number of elements, as shown in Figure 6.3-11. This is especially important for very large arrays, such as that proposed for the Solar Power Satellite (SPS) in Chapter 7.

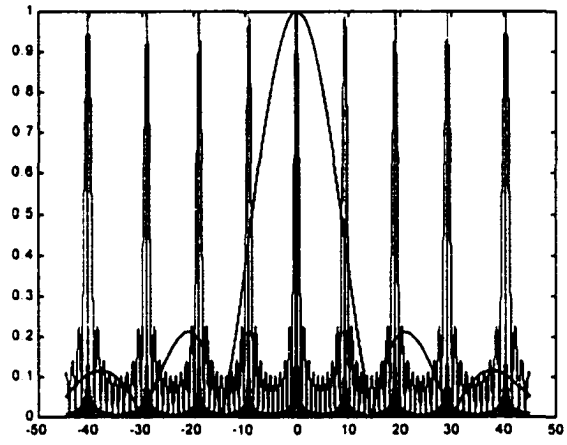

Figure 6.3-11. Comparison of Sidelobes for 100-Element and 10-Element Arrays, $S_\lambda = 6.17\lambda$. Purple (dark) line depicts 10-element PF; orange (light): 100-element PF. Single element pattern (black) and resultant 100-element SWA array pattern (blue) also shown.

6.3.3 Effect of Spacing Variances

The physical spacing S_λ between the SWA elements affects the resultant beam pattern given in Equation 6.3-7. The separation between SWA elements is measured as shown in Figure 6.3-12.

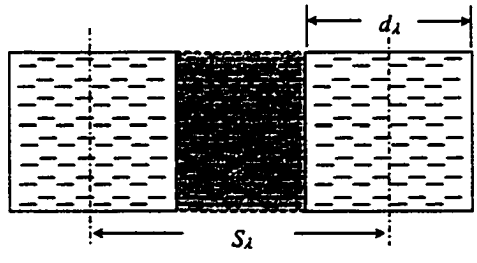

Figure 6.3-12. Separation in SWA Antennas.

As was the case for the number of elements, the element spacing drives the beamwidth of the lobes. It also affects the array gain and sidelobe levels. As the elements are moved

apart, their increased separation provides a larger effective diameter to focus the beam. The beamwidth varies with the spacing according to

$$BW_{3dB} \approx \frac{1}{2S_\lambda} \tag{6.3-10}$$

where

$$S_\lambda = \text{center - to - center distance between elements} [\lambda].$$

The calculated beamwidth for the 2-element horizontal case is shown in Figure 6.3-13. The modeled results from the MATLAB routine are compared with the predicted values from the equation above. The estimate correlates well, except where the separation is small compared with the antenna dimensions. Over the range examined, the predicted value was within an average of 2.4% of the modeled value, with a maximum error of 8.6% occurring at $S_\lambda = 6.17$ ($d_\lambda = 6.17$).

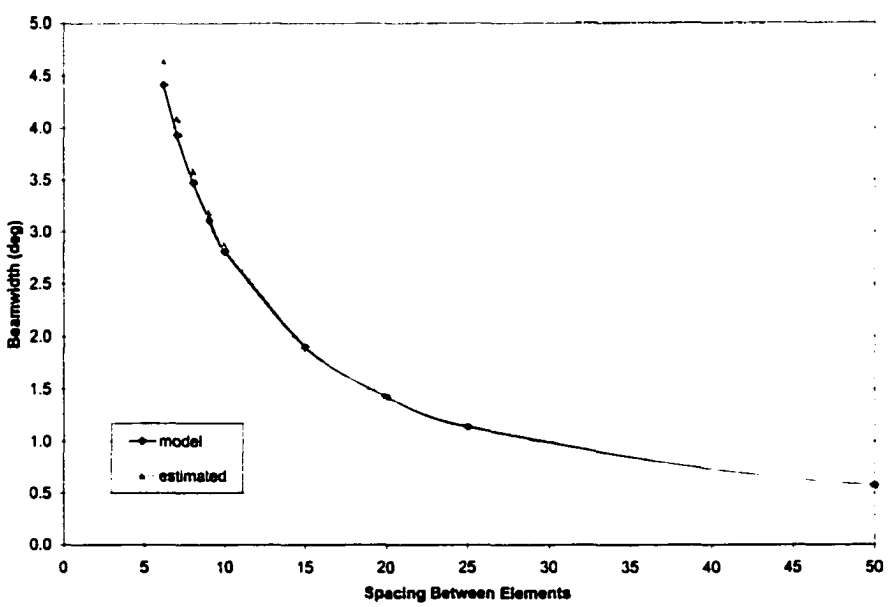

Figure 6.3-13. Effect of Element Spacing on Beamwidth for Multiple SWA Antennas. Broadside condition, 2 elements horizontal.

Element separation also affects the array gain. The gain of the array depends upon the physical area presented by its individual elements. For a phased array, this may be written in terms of the fraction of the geometric pattern occupied,

$$G = \frac{4\pi}{\lambda^2} A_{geometry} \varepsilon_{ap} \tag{6.3-11}$$

where

$$\begin{aligned} G &= \text{gain of antenna} \\ \lambda &= \text{wavelength}\,[\text{m}] \\ A_{geometry} &= \text{geometric aperture}\,[\text{m}^2] \\ \varepsilon_{ap} &= \text{fraction of array occupied (efficiency)}. \end{aligned}$$

For the array in Figure 6.3-12, the gain is

$$A_{geometry} = (S_\lambda + d_\lambda) d_\lambda, \tag{6.3-12}$$

$$\varepsilon_{ap} = \frac{2d_\lambda^2}{(S_\lambda + d_\lambda) d_\lambda} = \frac{2d_\lambda}{(S_\lambda + d_\lambda)}. \tag{6.3-13}$$

Since the array does not present the same physical area as a comparatively sized solid antenna, it cannot provide the same energy density. The element separation effectively diffuses the energy density capacity of the array by introducing grating lobes into the beam pattern. The grating lobes carry energy away in undesired directions, thereby decreasing the gain of the array.

The study of grating lobes is generally associated with the field of interferometry. Though interferometers are instead used to receive low-level radio energy, the beam pattern principles are identical. Here, the parameter limited by the sparse filling of the antenna array is the received signal sensitivity.

As an example, consider the Very Large Array (VLA) in New Mexico. In its maximum baseline configuration of 36 km, the VLA may achieve a resolution of ~0.04 arcseconds,

$$BW \approx \frac{1}{nS_\lambda} = \frac{1}{2(36\,\text{km})} \approx 0.05\,\text{arcsec}$$

However, it only has an equivalent sensitivity of a 130 m solid dish antenna. For a 130 m paraboloidal dish antenna, the physical area is

$$A_p = \pi\left(\frac{d}{2}\right)^2 = \pi\left(\frac{130\,\text{m}}{2}\right)^2 \approx 13{,}273\,\text{m}^2.$$

This is essentially the same as the total area possessed by all (27) of the 25 m antennas comprising the VLA,

$$A_{p_{VLA}} = 27 \cdot \pi\left(\frac{d_{VLA}}{2}\right)^2 = 27 \cdot \pi\left(\frac{25\,\text{m}}{2}\right)^2 \approx 13{,}253\,\text{m}^2.$$

This same effect is seen when transmitting RF energy via the SWA antennas. As the antennas are spread apart, the energy carrying capacity of the main beam is diminished. This is explained graphically by examining the pattern factor of the linear array shown in Figure 6.3-14. Similar to increasing the number of elements, spreading the elements apart decreases the main lobe of the pattern. However, the sidelobes are not attenuated anywhere. Therefore, as the main lobe decreases, sidelobes (grating lobes) move in towards the center of the pattern to 'steal' energy.

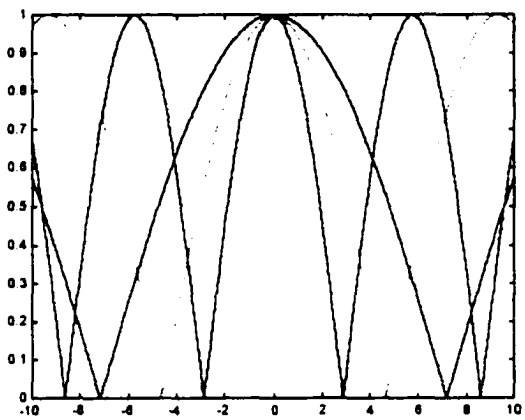

Figure 6.3-14. Expanded Region, Array Factor Patterns for 2-Element Arrays of Point Sources. Orange depicts $S_\lambda = 4\lambda$; magenta: $S_\lambda = 6.17\lambda$; purple: $S_\lambda = 10\lambda$.

The result of this phenomenon upon the SWA phased array is shown in Figure 6.3-15. As the two antennas are further separated, the grating lobes become much more pronounced. The main lobe substantially decreases in width, however, converging grating lobes effectively 'sample' the single element pattern. The magnitude of the grating lobes quickly approaches that of the main lobe and may become indistinguishable.

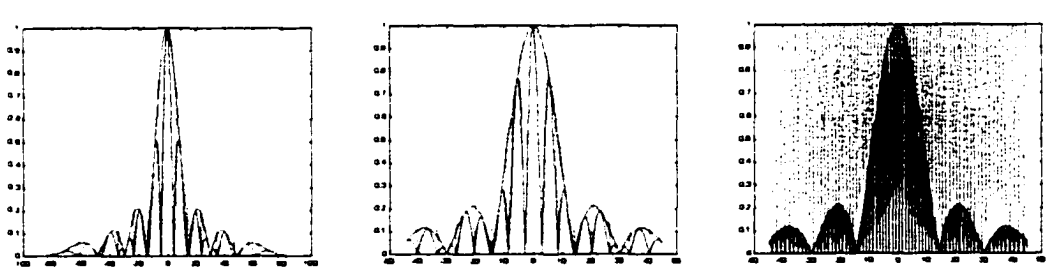

(a) $S_\lambda = 6.17\lambda$ (b) $S_\lambda = 10\lambda$ (c) $S_\lambda = 50\lambda$

Figure 6.3-15. Grating Lobe Progression for Increased Separation of Two SWA Antennas. Each graph shows pattern factor for element separation, the individual SWA pattern, and the resulting beam pattern.

The result is that the average power density throughout the beam envelope is doubled, since two radiating elements are present. However, the intercepted power density will vary according to the width of the receiving array. Narrow arrays might only detect individual beams, losing energy spilled over the edges of the receiving aperture. Wider arrays may capture the desired radiated envelope, but are subject to uneven illumination.

6.3.4 Effect of Phase Shift

Phase shift between elements is used to steer the resultant beam pattern. The direction of the main lobe is important, as are the locations and sizes of side lobes and nulls. The electrical phase shift δ between elements in a phased array affects the resultant pattern of Equation 6.3-2. This may be accomplished electrically by simply inserting an adjustable phase shifting device between the units, as shown in Figure 6.3-16.

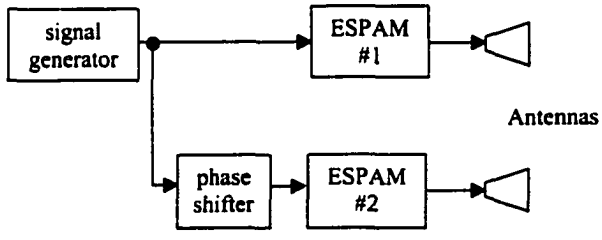

Figure 6.3-16. Simple Arrangement for Single-Axis Beam Steering.

Figure 6.3-17 demonstrates the effect of progressive phase shift on a 2-element array pattern. With the addition of phase shift, one sidelobe begins to gain magnitude and rotates toward the main beam. As this sidelobe increases, the main lobe moves away from the center of the array and decreases in magnitude. At 180° of phase shift (e), their magnitudes are equal and the main lobe has shifted a maximum value of 4°. After this point, the lobes reverse roles — the new main lobe moves toward the center of the array while gaining magnitude. The original pattern is restored at 360°.

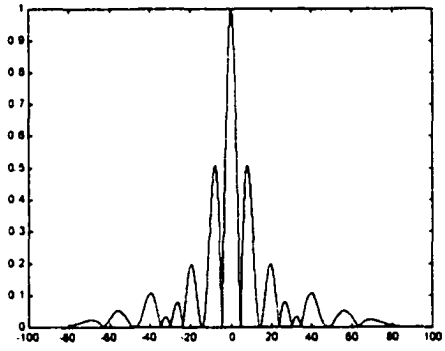

(a) $\delta = 0$ (broadside)

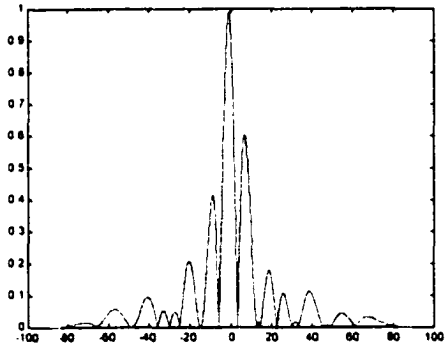

(b) $\delta = 45°$

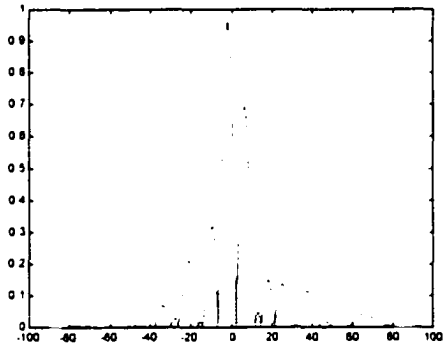

(c) $\delta = 90°$

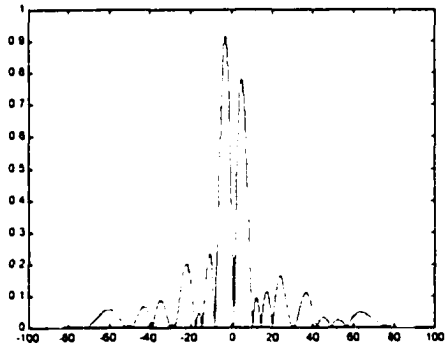

(d) $\delta = 135°$

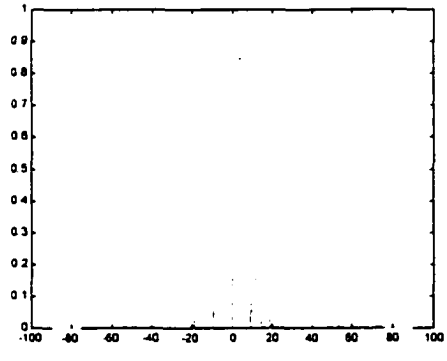

(e) $\delta = 180°$

Figure 6.3-17. Patterns for Phase Shift in 2-Element Phased Array, $S_\lambda = 6.17\lambda$.

It is evident that the total beam steering capability of the dual-unit is relatively small, the resultant beam pattern being dominated by the element pattern of the single SWA. This

is explained by the shapes of the constituent patterns shown in Figure 6.3-18. Because of pattern multiplication, the resulting beam shape is contained within the envelope of the single SWA antenna pattern. The pattern factor shifts with phase, 'sampling' the single SWA element pattern. This limits the maximum beam steering to within ±4.0°. Unfortunately, the pattern yields an equal sized lobe in the opposite direction.

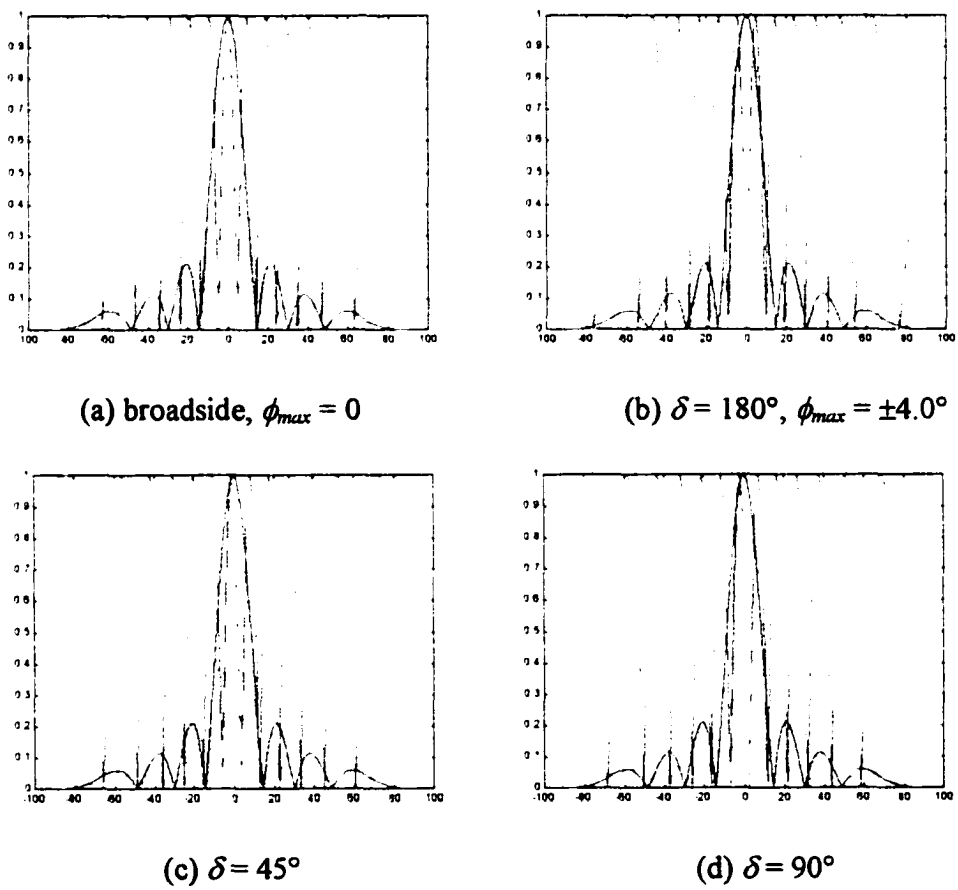

(a) broadside, $\phi_{max} = 0$ (b) $\delta = 180°$, $\phi_{max} = \pm 4.0°$

(c) $\delta = 45°$ (d) $\delta = 90°$

Figure 6.3-18. Pattern Decomposition for 2-Element Array of SWA Antennas. Green line depicts PF for 2-element array at S_λ = 6.17λ; purple: single SWA pattern; orange: resultant pattern.

Consequently, the array must be operated very near broadside. It will have minimal steering capability without significant loss of transmitted power. Increasing the effective

steering range requires using a less directive antenna, expanding the width of the single element envelope in the figure above. However, this will be at the expense of antenna gain. In addition, it must be accompanied by a corresponding reduction of grating lobes (expansion of the pattern factor) if large sidelobes are to be avoided.

6.3.5 Effects of Amplitude Variations

The analysis of the beam patterns so far has assumed that the array consists of constant amplitude sources. This section provides limited, but useful insight into the effects of 'amplitude variations' of elements on the resultant pattern by examining the occurrence of a failed element.

The effect of a failed or missing ESPAM unit on an array may be clearly understood by returning to a linear array of point sources. A diagram of this condition is provided in Figure A.1.2-3. The resultant field seen at some distant point for the entire array is given by Equation A.1.2-2. If the k-th element of the linear array is missing, then the new pattern is then given by Equation A.1.2-36. The effects of missing elements on a sample linear array are shown below in Figure A.1.2-4.

Since it is desired to analyze the effects of a missing element on an array, it is more useful to normalize the pattern factors with respect to the number of elements in the array (before failures). This will yield pattern factors that maintain their proportionality. These patterns are shown in Figure 6.3-19.

The effects on a linear array of ESPAM units may be studied using pattern multiplication. For a 5-element array, the patterns given by corresponding element failures are shown in Figure 6.3-20. The first set of plots compares the effect of the failed element on the array factor. The second set shows the resultant beam pattern.

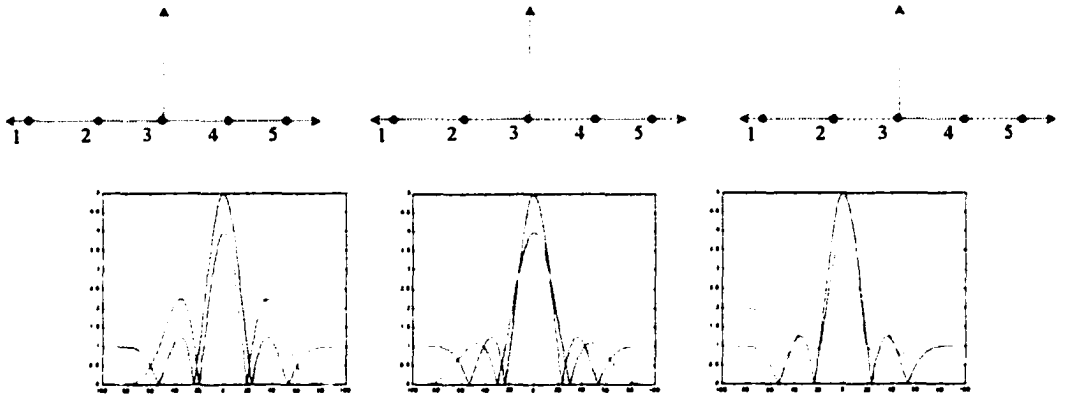

Figure 6.3-19. Effect of Missing Elements on Linear Array of Point Sources. Curves not normalized to emphasize effect on pattern gain.

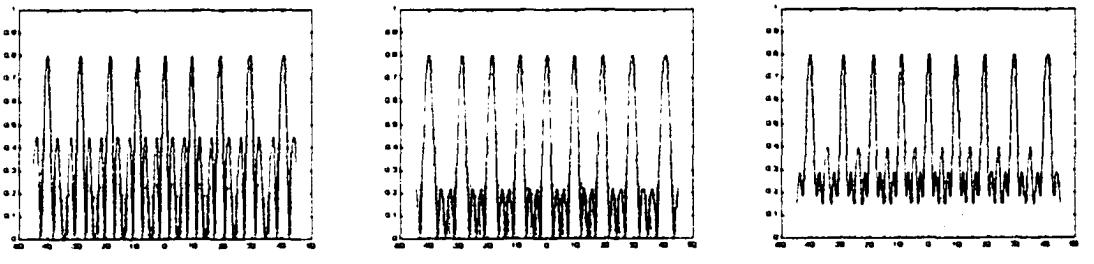

(a) linear array of point sources

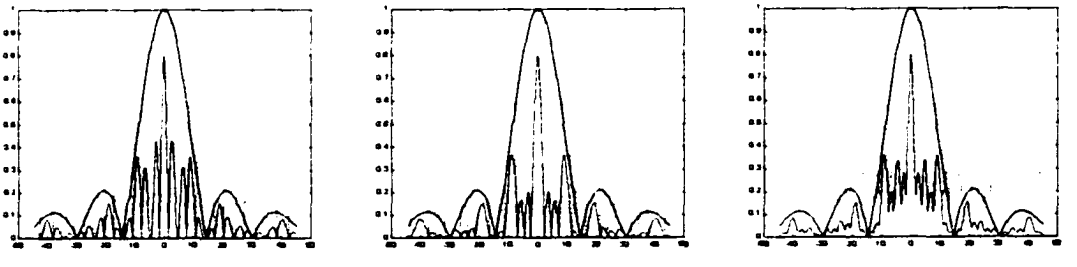

(b) array of SWA antennas

Figure 6.3-20. Effect of Missing Element on 5-Element Array of SWA Antennas. Data shown for $S_\lambda = 6.17\lambda$, $\delta = 0$. Top curve shows pattern factors for all five elements (orange) and one missing element (purple). Bottom curve shows resultant SWA array pattern for missing element (purple).

For the array above, the resultant beam pattern is strongly affected by the location of the failed element. Larger arrays are much less susceptible to the effects of a single element failure. Multiple element failures present a more complex scenario in calculating beam patterns. Up to this point, it has been assumed that the pattern factors for the m x n array are independent. In this case, the total pattern factor may be determined by computing its component factors along orthogonal directions. For example, a complete and symmetric m x n array is shown in Figure 6.3-21.

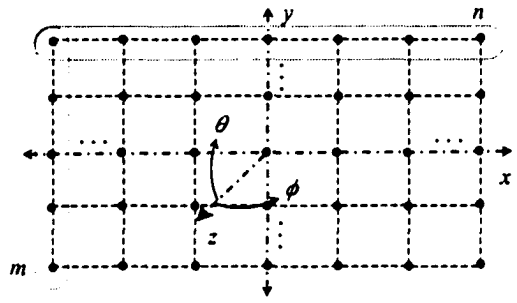

Figure 6.3-21. Rectangular m x n Array of Sources.

The resulting pattern factor is given by

$$E_{PF}(\phi,\theta) = E_{PF}(\phi)\cdot E_{PF}(\theta) = \frac{1}{n}\frac{\sin\left(n\psi_h/2\right)}{\sin\left(\psi_h/2\right)}\cdot\frac{1}{m}\frac{\sin\left(m\psi_v/2\right)}{\sin\left(\psi_v/2\right)}. \qquad (6.3\text{-}14)$$

However, if element failures are introduced into the array, the location of the failures affects the three-dimensional beam pattern. Note that the array in Figure 6.3-22(a) yields the same pattern factors along the axes, and therefore, the same beam shapes along the axes. However, the pattern seen between the axes shown in Figure 6.3-22(b) is much different.

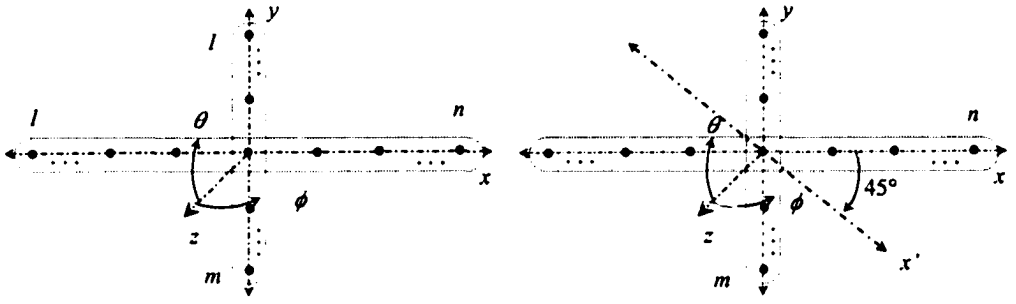

(a) on-axis patterns (b) off-axis patterns

Figure 6.3-22. Equivalent Array of Sources for Patterns in x- and y-directions.

The pattern along the x'-direction has no contributing elements, except at the origin. The resultant beam pattern behaves according to the above equation only along the axes. For exact symmetry of the beam about the z-axis (boresight from antenna), the element pattern must also be perfectly symmetric. This would require proper selection of element placement, amplitude, and phase with respect to the boresight.

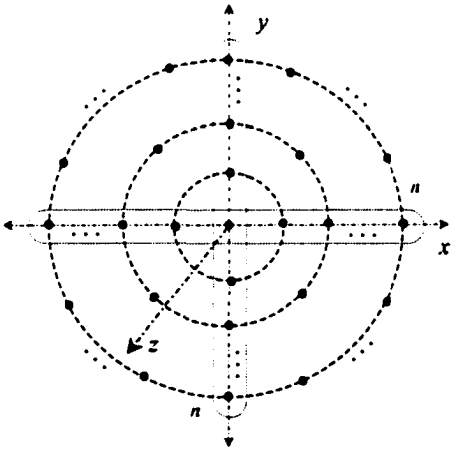

Figure 6.3-23. Circular Array of n-Elements.

The pattern of a circular antenna may be approximated by a rectangular (square) array with clipped corners, as shown below. The elements of the rectangular grid will in general be located in a different location with respect to the center of the array, and will therefore require different driving signals. The beam may be shaped approximately

symmetric with respect to the antenna boresight by judicious selection of amplitude and phase shift for the element location.

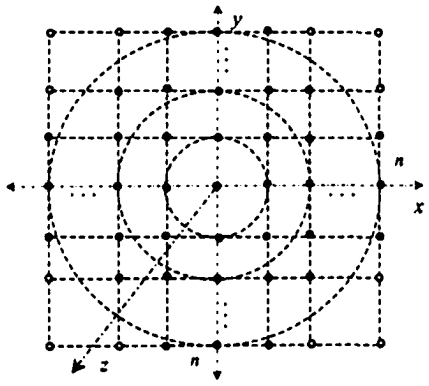

Figure 6.3-24. Square Approximation of *n*-Element Circular Array. Shaded points denote missing sources.

For such an array, the maximum divergence of the beam pattern occurs at the diagonal to the array due to the increased element spacing. Here the spacing is increased by a factor

$$S_{diagonal} = \sqrt{2} \cdot S_{lateral}. \tag{6.3-17}$$

As an example, consider a 5 x 5 array composed of SWA antennas.

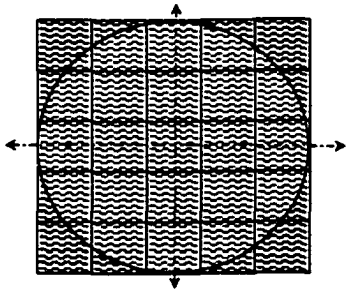

Figure 6.3-25. 5 x 5 Array of SWA Antennas.

For the full array, the diagonal beam pattern is shown below.

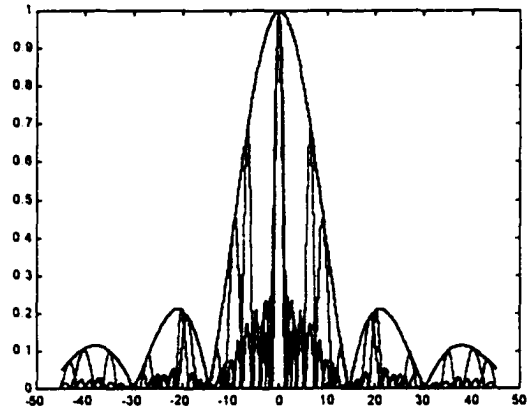

Figure 6.3-26. Axial and Diagonal Beam Patterns for 5-Element Array of SWA Antennas. Blue lines indicate lateral patterns $S_{lateral} = 6.17\lambda$; red depicts diagonal pattern $S_{diagonal} = 8.73\lambda$. Assumes single SWA pattern is symmetric.

As demonstrated in Section 6.3.2, the increased diagonal spacing creates higher side lobes in this direction. Since this sidelobe is caused by the pattern factor sampling the SWA pattern (grating lobe), it will not be eliminated by increasing the array size. However, the width of the lobes will be compressed.

The increased element spacing has reduced the beamwidth of the main lobe from 2.6° to 1.8°. This aspect supports the desire to reduce the array size by clipping the corners. The diagonal elements are thinned to

$$n_{diagonal} = \frac{1}{\sqrt{2}} \cdot n_{lateral}. \tag{6.3-18}$$

Note that this is an approximation for the diagonal spacing, as the lateral measurements of the SWA are 6.17λ and 6.37λ. The approximation yields $S_{diagonal} \approx 8.73\lambda$, instead of the actual value of $S_{diagonal} = 8.87\lambda$. For the purposes of this discussion, the exact value is unimportant.

The resultant pattern is further degraded, as shown in Figure 6.3-27. For the sample 5 x 5 array above, the diagonal is clipped to 3 elements. The array diagonal is not greatly affected by clipping. The dominant beam shape of the SWA antenna effectively suppresses further growth of the sidelobes. For a larger array of SWA elements, the patterns maintain the same characteristic envelope, as shown in Figure 6.3-29.

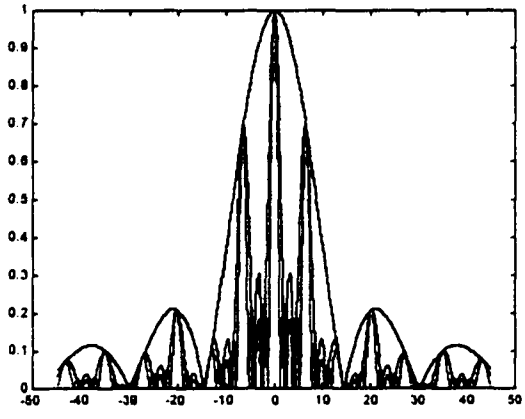

Figure 6.3-27. Comparison of Diagonal Beam Patterns for 5-Element Linear Array, $S_{diagonal}$ = 8.73λ. Blue line depicts diagonal pattern for full array; red denotes clipped diagonal of 3 elements.

Comparing the pattern below with that of Figure 7.3-16 shows that the sidelobe location and magnitude are roughly independent of the number of elements in the array for large *n*. The figure above is not normalized to show both patterns at once and to illustrate the relative magnitudes of the different array shaped. The widths of the sidelobes are compressed with increasing *n* in the same fashion as the main lobe; locations of nulls are forced by either the array factor or the single SWA pattern.

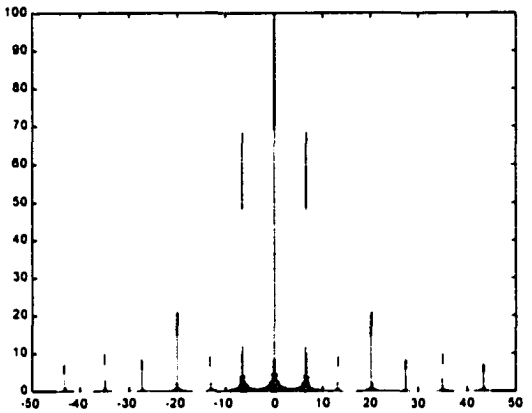

Figure 6.3-28. Diagonal Pattern for 100-Element Array of SWA Antennas, S_λ = 6.17λ. Blue (dark) line shows 100 element diagonal; green (light): 70 elements.

6.4 UAF Beam Steering Demonstration

To verify the operation of multiple ESPAM units, existing components at UAF were utilized to configure a 2-element testbed. The purpose of the testbed was two-fold: (1) to demonstrate that two MDA units could be frequency locked, and (2) to confirm the anticipated beam steering capability using the Slotted Waveguide Array (SWA) antennas.

On 3 June 1998, UAF students steered a WPT energy beam electronically using the testbed. This marked the first time that a phased array composed of ESPAM units was successfully demonstrated. The demonstration established that a multi-unit ESPAM could steer a RF beam and provided rough confirmation of the calculated beam patterns. Participants in this demonstration are listed under the Acknowledgments section.

6.4.1 Description

The configuration selected for the testbed was a 1 x 2 phased array, with the elements horizontally adjacent. A panel consisting of vertical columns of rectenna elements

connected to lights provided a qualitative indication of beamwidth and direction. A conceptual diagram of the testbed layout is shown in Figure 6.4-1.

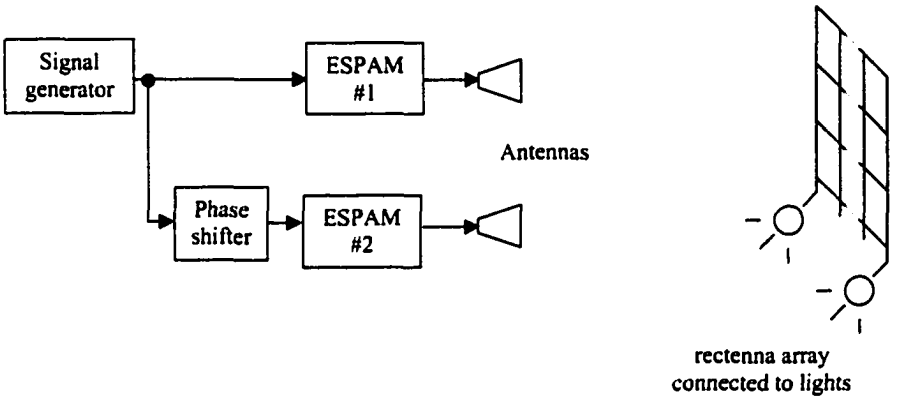

Figure 6.4-1. Conceptual Schematic for Single-Axis Beam Steering Demonstration. MDA units are horizontally adjacent.

This shows the approach generally taken, where some type of signal generator provides a precision reference signal to the elements. A phase shifter then introduces the appropriate amount of phase shift at each radiating element to steer the beam. Large distance separations may require the use of multiple signal generators. These would need to be synchronized to provide the correct phase difference between elements.

However, an alternate method was adopted for the UAF demonstration, shown in Figure 6.4-2. Instead of using a precision signal generator, a portion of the output signal from one unit (the master) was injected into the second unit (slave). A phase shifter located between the two units provided the phase shift necessary to steer the microwave beam.

This approach was selected to demonstrate that one ESPAM unit could provide a signal of sufficient quality for other ESPAMs to track. This capability is important for two reasons. First, it minimizes the amount of expensive support equipment needed, thereby decreasing logistics support and time requirements. In demonstrating the practicality of

simple WPT systems, the benefits of this simply cannot be overstated. Second, it establishes the capability of the MDA as a low-cost, high-power, RF signal generator/amplifier in its own right. This application may further reduce equipment costs by replacing expensive, lower-gain RF amplifiers currently used. In addition, cascading MDA units could provide an even higher power RF source.

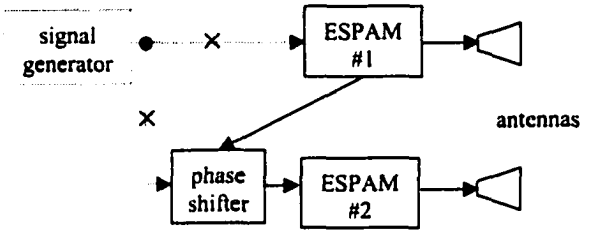

Figure 6.4-2. Modified Reference Signal Source for Dual-Unit Demonstration.

6.4.2 Physical Configuration

The physical configuration used for the demonstration is shown in Figure 6.4-3. The two ESPAM units were mounted on a cart and positioned roughly 12 feet from the rectenna array. The ESPAM on the left was designated the master unit, consisting of a Class III OL MDA mated with one of the SWA antennas via a 4-stub tuner. The master was frequency-tuned using a reactance tuning slug, as described Section 3.3.

A portion of the master output signal was used as the reference signal for the slave ESPAM unit (right). This signal was routed through a manual rotary-type phase shifter to provide the beam steering capability. The signal then was amplified prior to injecting it into the slave unit (as the master output signal probe was of a low-power design).

The slave unit consisted simply of a Class II MDA connected to the other SWA antenna. Control of this unit was limited to output power and frequency adjustments made via the power supply (see Section 3.2). In addition, a small amount of influence was possible by

varying the injected power and frequency. A second circulator was added to isolate the injected signal from reflected/coupled power.

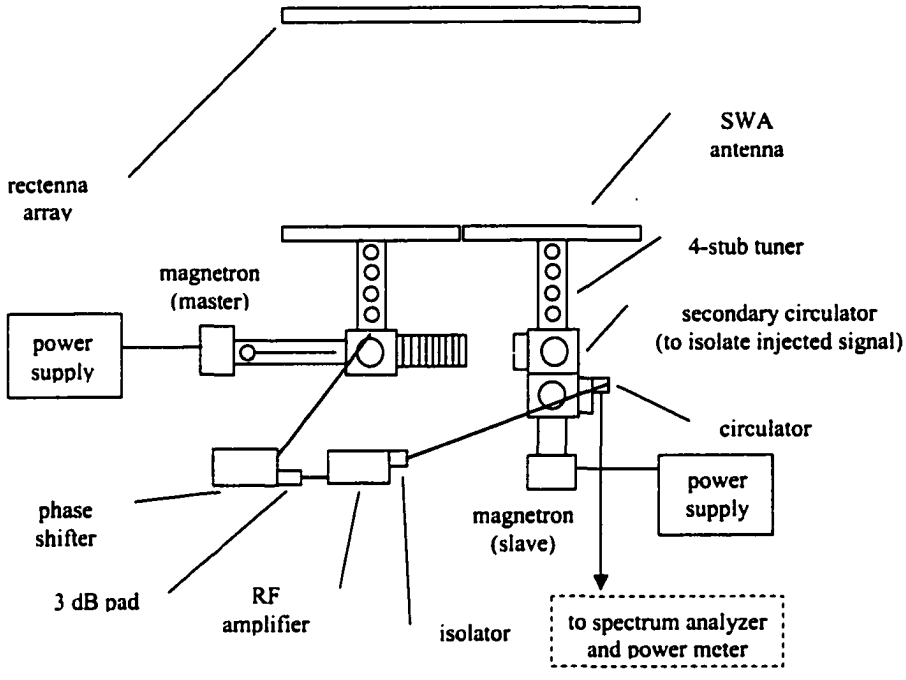

Figure 6.4-3. Physical Configuration of ESPAM Units for UAF Beam Steering Demonstration.

A rectenna array was used to provide an indication of transmitted beam shape and steering. The rectenna (*rec*tifying an*tenna*) element converts the incident RF energy to DC electricity. This consists of a dipole antenna, a power rectifying diode, and capacitor. A diagram for a typical rectenna element is shown in Figure 6.4-4. Detailed information concerning its construction and operating characteristics is available in [13].

Columns of rectenna elements were connected to 12 VDC automotive bulbs. These were separated by 6.5", providing an angular resolution of ~2.5° at 12 feet from the ESPAM transmitting antennas.

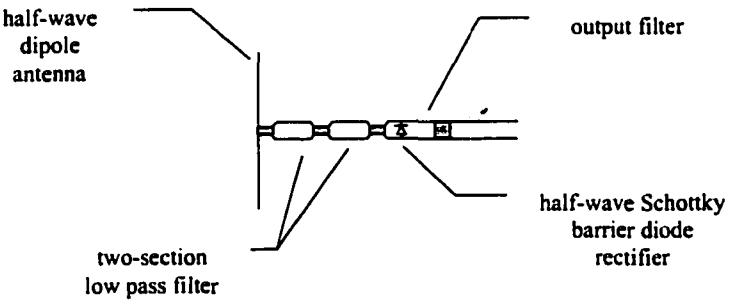

Figure 6.4-4. Rectenna Element Diagram.

The layout of the array used for the demonstration is shown in the figure below.

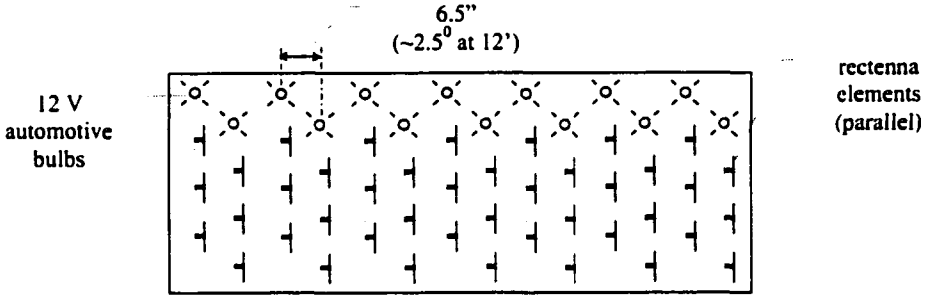

Figure 6.4-5. Rectenna Indicator Panel Layout.

The hardware configuration also included portable test equipment to monitor the ESPAM operation and provide trouble-shooting assistance. The test equipment cart consisted of a spectrum analyzer, power meter, multimeter, and plotter.

6.4.3 Procedure

Individual beam patterns for each unit were measured to be about 15 degrees, quite close to the predicted values (Section 6.3). The beam patterns and signal strength were first roughly estimated using the rectenna indicator, shown in Figure 6.4-4. They were then verified by a more sensitive hand-held power indicator (12 elements with one bulb).

Prior to frequency locking, the ESPAM units operated independently, as indicated by two separate beam patterns. Frequency of operation of the master ESPAM was about 2.42 GHz; the slave at about 2.56 GHz. The next step was to drive the master to a frequency within the locking range of the slave unit. This was accomplished by inserting an appropriately sized tuning slug in the launching section of the master ESPAM.

Tuning slug #3 (5/8" DIA x ¾") was used to drive the master ESPAM (Class III OL) to a frequency within the locking range of the slave unit. The two units were locked at 2.453 GHz and manually steered via the rotary phase shifter. The 360° of electrical phase shift steered the beam through an angle of approximately ±4°.

6.4.4 Results

Although this was intended to be a qualitative demonstration, we were able to collect approximate performance data. Columns of rectenna elements were located at roughly 2.5° increments (at a distance of 12' from the antennas), with each column connected to a 12 VDC automotive bulb. By noting the relative illumination of the bulbs, we were able to measure the resultant beam direction and beamwidth. The data favorably corresponded to the predicted behavior from Section 6.3, though the measurements were made in the near field region (~4 m, versus ~40 m for the Fraunhofer region).

The measured pattern demonstrated the same general behavior as the predicted shapes, as shown in Figure 6.4-6. The broadside condition corresponded with a beam centered on the rectenna array, while a phase shift of 180° from this point resulted in a dual-beam pattern. The beam directions and widths also correlated pretty well, within the limitations of the measurements made.

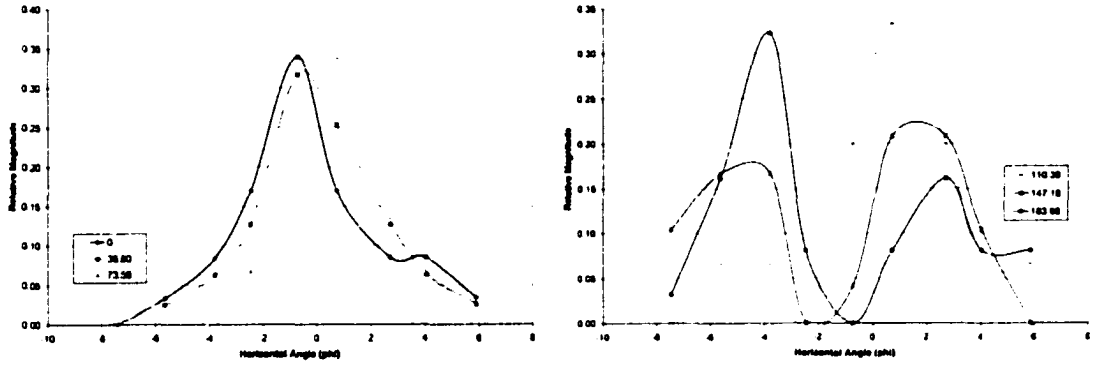

(a) measured beam near broadside (b) measured beam near $\delta = 180°$

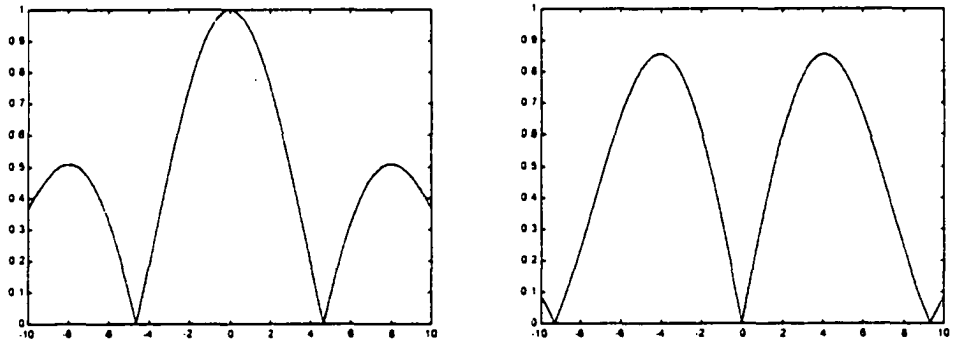

(a) predicted beam near broadside (b) predicted beam near $\delta = 180°$

Figure 6.4-6. Comparison of Actual and Predicted Beam Patterns for Dual-Unit Demonstration. SWA antennas mounted horizontally adjoining, $S_\lambda = 6.17\lambda$.

The rectenna array was not instrumented with a power measurement device. Therefore, the beam intensity measurements were limited to a comparative visual estimate. Also limiting the measurements was the angular resolution of the rectenna elements. This was decreased by operating closer to the ESPAM units than had been anticipated due to power limitations.

6.4.5 Problems Encountered

Power Limitations. The demonstration revealed the criticality of ensuring adequate power availability for the ESPAM units. This impacted the demonstration in two ways.

First, the amount of utility power necessary to operate both ESPAMs stressed the capabilities of the test site. Initially, both power supplies were operated from the same service outlet using long extension cords. The two units could not operate simultaneously, with the master causing the slave to cutout repeatedly. This was indicated by a dimming, then eventual cutoff of the slave rectenna panel lights. In addition, the slave power supply would fail to provide the necessary current. We attempted to run the two units simultaneously numerous times, varying the startup sequence and power levels. However, whenever the master was brought up to the same power output level as the slave, the slave would inevitably falter and drop out.

The problem demanded a separate source of power for each unit. Since the number of electrical service outlets in the test location was limited, it was not possible to power the second unit from the local grid without incurring excessive line losses. The situation was finally remedied by powering one ESPAM with a portable 3.5 kW generator. From a logistical perspective, both of these facts are of significance.

Second, the amount of power required to adequately illuminate the automotive bulbs stressed our input power capabilities. Contributing factors were (1) the design of the receiving array (bulb power requirements and rectenna element spacing), (2) location of the sun during long Alaskan summer days, and (3) input power limitations imposed. Though the power supplied to the ESPAM units was sufficient for operation, each unit was still power-limited. Because of the long extension cord required to reach the utility outlet (slave), and the power factor of the generator (master), each power supply was limited to approximately 230 mA DC available.

To balance the bulb power requirements with beam steering indications, we located the ESPAM units about 12 feet from the rectenna array. This was approximately 1/3 shorter than anticipated, causing the angular resolution of the rectenna array to be less than had been originally intended.

Load Reflections. At initial power up, differences in the loads seen by each magnetron prevented the units from frequency locking. This was evidenced by a lack of steering ability, and the persistence of two distinct beam shapes in the measured pattern. Analyzing the master MDA output indicated that excessive reflections from the load drowned out the desired magnetron signal (to be injected into the slave MDA). Plots of this signal showed 2 separate frequency components were present—the desired narrowband magnetron frequency and a wideband reflected signal.

Much of the unwanted reflections seen at the master ESPAM were eliminated by tuning the load. This was accomplished by adjusting the 4-stub tuner between the waveguide and the antenna. Using both the spectrum analyzer and a power meter, the unwanted spectral content was minimized at the master ESPAM output port. In addition, the reflected power from the load seen at the slave MDA was used as a second means of maximizing the master power output.

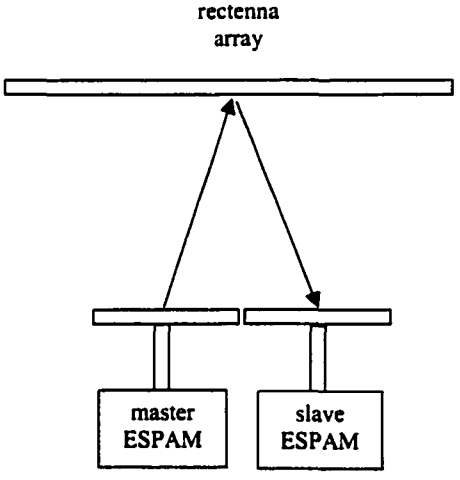

Figure 6.4-7. Feedback Path of RF Energy Reflected to Slave ESPAM.

This process was repeated to impedance match the antenna of the slave unit. Re-tuning the antennas for the new load environment yielded much improved results. Previous

measurements had indicated approximately 15 W reflected at the input probe — now it was reduced to ~4 W. However, this still was not enough, as the reflected power still dominated the injected signal (1 W).

To further isolate the magnetron from reflected power, another waveguide circulator was introduced between the injection point and the antenna. With the extra circulator added and the slave MDA again re-tuned, the reflected signal was lowered to an acceptable level (~40 mW).

6.4.6 Summary

We achieved a frequency-locked system and manually steered the resulting beam. The results were received with much enthusiasm from members of the WPT community. This proof of concept has taken WPT a small, but important step toward viability.

Frequency locking was accomplished without the use of an external frequency source. We demonstrated that the MDA output could be used as a RF source for other units. This could provide a very low-cost, high-power RF amplifier (or even source) for certain applications.

The demonstration showed the 2-element ESPAM phased array to not only be possible, but practical and robust. Items of significance include: (1) A frequency separation of 14 MHz was overcome by tuning a single ESPAM unit. The tuning slug performance was predicted using Figure 5.4-8. (2) The units were locked in a noisy environment, with excessive power reflected from the equipment and surroundings. (3) One unit was powered by a portable generator. (4) The entire demonstration was housed on three equipment carts, with setup of the units requiring under 15 minutes (assuming waveguide components assembled and no adjustment of the 4-stub tuners necessary).

7.0 Performance Requirements for SPS

This chapter briefly addresses antenna beamwidth and pointing requirements for a conceptual Solar Power Satellite (SPS) located in Geostationary Earth Orbit (GEO). It also provides a comparison of beam steering requirements between GEO and low earth orbit (LEO) configurations. Conceptual antenna designs are provided for these beam forming requirements based upon the ESPAM modules described in Chapter 6.

7.1 System Description

This section recommends the GEO orbital configuration to be used for the final SPS. It provides a set of design considerations used in selecting the orbit, and the physical layout of the transmitting antenna. These may be of benefit in designing interim LEO solutions designed to satisfy special needs, or as technology demonstrators for SPS.

7.1.1 General Design Considerations

The basis for selecting any potential SPS configuration is that the overall system must meet certain general requirements. These may be boiled down to a set of rather simplistic, but important goals: satisfies a specific need, is cheap, simple, safe, reliable, and long-lasting. The choice of whether the SPS is designed for a LEO or GEO has a large impact on these factors.

Most importantly, the system must have a clearly defined purpose. A specific program objective might be to "provide 25 GW of near-continuous (95%) solar energy directly to five predetermined sites in North America within 30° north latitude by the year 2020." This particular objective would certainly drive the SPS in to a different implementation than would one to "provide 1 GW of near-continuous (95%) solar energy directly to one predetermined site in Alaska by the year 2020."

Support requirements also have strong implications for the design of the system. For example, the desires for a simple, reliable, and long-lasting system seem to drive the SPS design to a GEO implementation. However, the lack of a suitable transportation system currently prohibits this, both financially and environmentally. On the other hand, the LEO approach provides easier access to orbit, but requires a huge investment in system complexity for its operation and maintenance.

The SPS initiative is a massive effort that will be developed over the course of many years. As technology advances and applications are found suitable of its maturity, many SPS ventures will be undertaken by entities with different goals and resources. Some of these will invest their interests in the large efforts associated with a GEO-based network. Others will desire to provide smaller amounts of power to high latitude locations.

Regardless of the final orbital configuration chosen, certain aspects of a SPS system must be proven to meet the requirements listed above. The system must be cost-efficient to use — it should provide a clear improvement in energy costs over alternative solutions, either now or within some foreseeable time frame. For the system to be cost effective, it also must be low maintenance and have an extended lifetime or be easy to replace. It must be safe and not adversely affect the environment in any way.

Within the constraints of this paper, it is not possible to address all the tradeoffs necessary in designing a SPS system. The purpose of this section was merely to touch lightly on some of the design considerations, and to lay the groundwork for the study accomplished in the remainder of this chapter. For an in-depth study of this topic, the reader is referred to [1], [2], and [24].

7.1.2 Proposed Orbital Configuration — Geostationary Earth Orbit

Following the rationale from the previous section, it is first necessary to identify the purpose of the proposed SPS system. It is assumed that this massive space effort will be accomplished incrementally over time, gaining the support of the scientific and economic communities. Though some of this will likely be done in LEO, it is probable that some testing will occur on smaller initial capability systems located at GEO. It is also understood that some portion of a total SPS system will eventually incorporate GEO satellites to provide a baseline power capability. These factors considered, the system analyzed here is based upon a standard GEO configuration proposed by others [2]. The reason for this decision becomes evident when analyzing the orbital effects on the design of the SPS provided in Section 7.1.4.

For the purpose of this discussion, it is assumed that the SPS is located in a geosynchronous orbit. Initially, the satellite will be fixed in a geostationary orbit (inclination $i = 0$) and the ground rectenna array located directly on the equator. Then the effects of varying the latitude of the rectenna array and inclination of the orbit will be addressed. A diagram illustrating the general concept is shown in Figure 7.1-1.

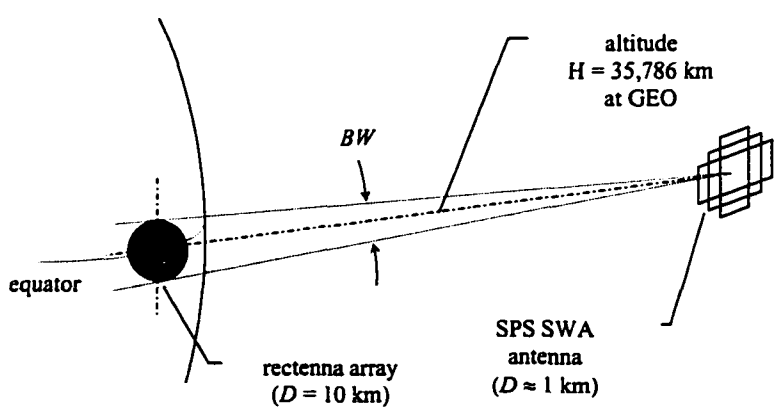

Figure 7.1-1. Conceptual Diagram of GEO SPS, Receiving Array at Equator.

The SPS is located in a geostationary orbit directly above the equator. The altitude of the orbit provides a period of 24 hours, matching the rotation of the earth. This configuration provides a nearly continuous supply of power. The satellite is eclipsed from the sun less than 1% of the time (maximum of 72 minutes/day for roughly three weeks during spring and fall equinoxes). The orbital geometry of the GEO configuration is shown below.

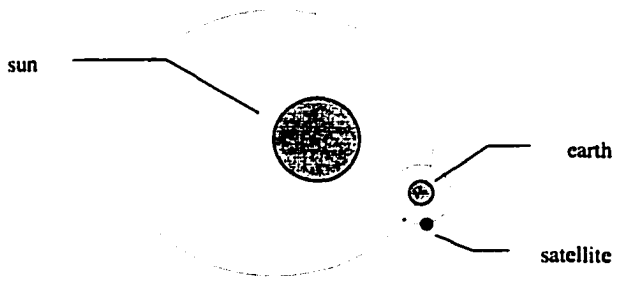

Figure 7.1-2. Orbital Geometry for the GEO SPS.

For the configuration shown, it is assumed that the solar collecting arrays of the SPS always face the sun. In addition, the angular orientation of the radiating slotted antenna array must be fixed with respect to the target. Though the solar arrays are massive, they require very little realignment to meet the necessary rotation rate of once per year. The daily rotation of the slotted arrays places somewhat more demand on the attitude control subsystem, as these arrays are also quite large (1 km diameter).

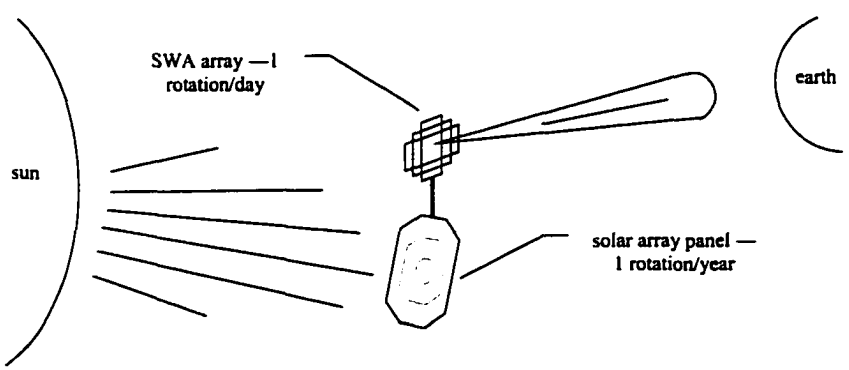

Figure 7.1-3. Array Pointing Considerations for SPS.

The choice of the GEO system for the final arrangement is based upon the relative simplicity of design. The primary disadvantages of this scheme are the height of the orbit and the corresponding large transmitting antenna required for this height. Since the beam subtended by a receiving site from this distance is small, the antenna must have a high gain (and therefore be large at this wavelength). In addition, to provide a reasonable power density at the receiver, the solar arrays must also be very large. Both of these factors drive up the cost per satellite enormously. On the positive side, this single SPS may provide very high power levels for years with only minimal stationkeeping.

7.1.3 Alternate Orbital Configurations

In contrast to GEO, a low earth orbit (LEO) configuration would have the advantage of requiring much less fuel to orbit, but would significantly increase the tracking requirements for the solar and radiating arrays (typical period of 90 minutes). In addition, an individual satellite would be eclipsed from the sun during a significant portion of its orbit. These requirements would greatly increase the complexity of the overall system, affecting the attitude determination and control system of each satellite, dynamic beam steering, integration with ground receiving arrays, load leveling at power grids, and storage of excess for use at night or during peak hours.

Due to the increased complexity required of a LEO configuration, it is debatable whether this arrangement would be used for large-scale power production. It seems more likely that its use will be economically and politically restricted to special use situations, such providing power to high latitude locations. However, this will probably be a necessary step in the proof-of-concept before ultimately building a large GEO-based system. A detailed comparison of orbital requirements is provided in Section 7.1.4.

Another possibility is to put SPS units in solar orbits near the earth. These satellites would orbit the sun, rather than the earth, as shown in Figure 7.1-4. This configuration would provide a constant source of power, but would have the disadvantage of rotating with respect to our ground reference frame. Therefore, the beam would have to be dynamically steered and enabled as receiving arrays rotated under its field of view.

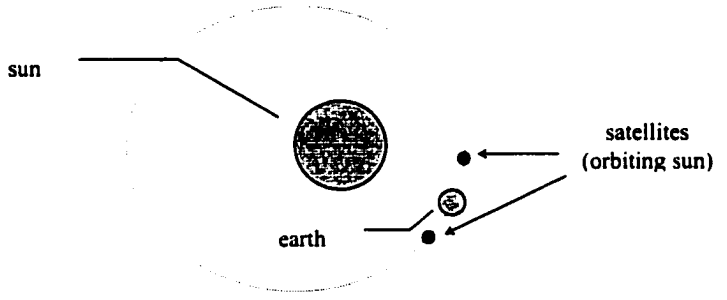

Figure 7.1-4. Schematic for Heliocentric SPS.

In addition, such a system would require even tighter beam steering due to the increased distance. Perhaps most significant would be the increased cost of fielding such a system, as it would require the most fuel and size. These drawbacks render the scheme impractical for the foreseeable future.

7.1.4 Orbit Comparison

This section compares the effects of orbit altitude selection on the SPS design. For the analysis, orbit altitudes from 200 km through geosynchronous are examined. For the basis of this discussion, the satellite is considered to be in a prograde (easterly) equatorial orbit. This orbit is assumed to be perfectly equatorial and circular: inclination $i = 0$, and eccentricity $e = 0$. A diagram of the orbital configuration is the same as shown in Figure 7.1-1, but with a variable altitude H.

It is desired that the beamwidth of the transmitted energy exactly fill the receiving array. When the satellite is directly overhead, this beamwidth is given by

$$BW_{required} = 2\tan^{-1}\left(\frac{D_{receiver}}{2H}\right). \qquad (7.1\text{-}1)$$

The required beamwidth decreases rapidly with increasing altitude, from over 2.5° at 200 km to under 1 arcmin at geosynchronous orbit. A graph of the relation is shown below.

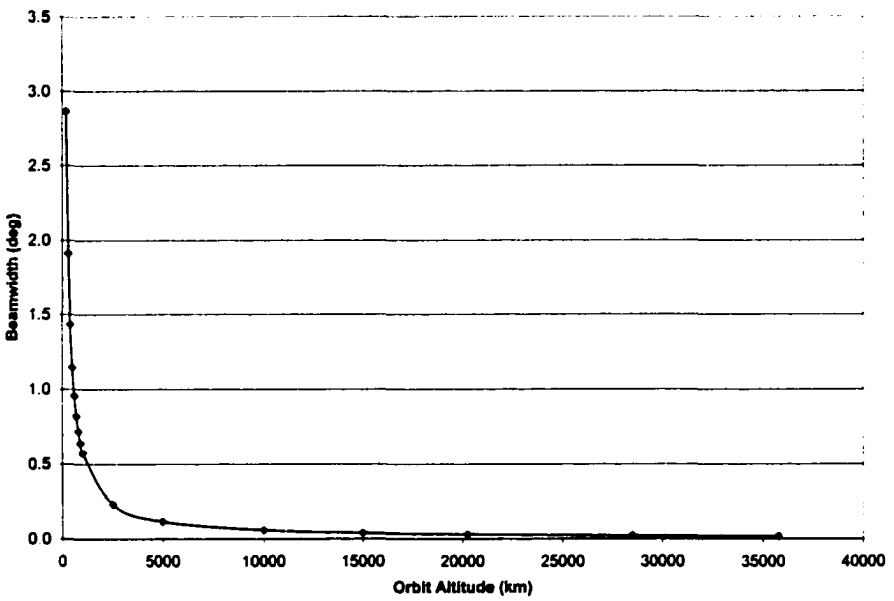

Figure 7.1-5. SPS Beamwidth to Fill 10 km Receiving Array.

For any arrangement other than a true geostationary orbit, the satellite will rotate with respect to the earth's surface. Therefore the calculated beamwidth is valid only for the moment that the satellite passes directly overhead the receiving station. As the satellite approaches and departs the receiver, the longitudinal footprint of the beam from the satellite is lengthened. To counteract this, the longitudinal width of the receiving array must be extended, as shown in Figure 7.1-6. This situation is equivalent to that of the offset receiving site for the GEO configuration discussed in detail in Section 7.2.

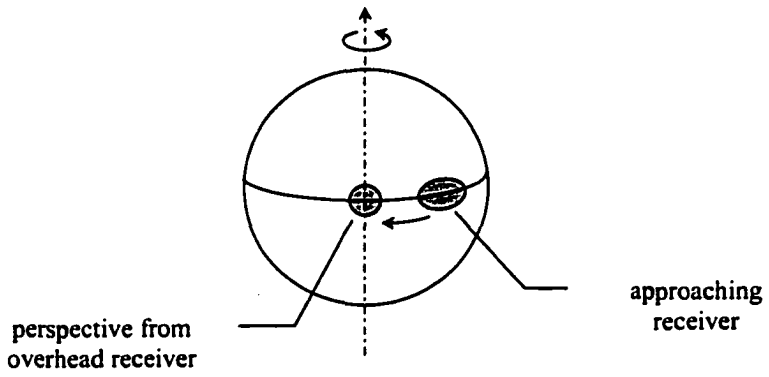

Figure 7.1-6. Effects of Angular Offset on Sizing for Receiving Site.

After the required beamwidth for the orbit altitude is determined, the number of ESPAM units n necessary to achieve this beamwidth may be calculated. Rearranging Equation 6.3-9 yields

$$n \approx \frac{2BW_{SWA}}{3BW_{required}}, \tag{7.1-2}$$

where

$BW_{SWA} = 12.8^{\circ}$ (beamwidth for single SWA)
$BW_{required}$ = beamwidth required for given altitude.

This produces a linear relationship between the number of elements and the altitude, providing a handy means for estimating the number of elements required for the array. The estimated results are accurate to within ~2.5% at 533 elements, as 520 elements are actually required to achieve the 57.67 arcsec beamwidth for the geostationary orbit.

With the number of axial elements n determined, the total array size may be computed. Assuming a simple rectangular (square) configuration, the total number of elements N required to form the array is shown in Figure 7.1-7. This represents the area and mass of

the transmitting antenna that must be delivered to orbit. Therefore, minimizing the number of elements is of importance.

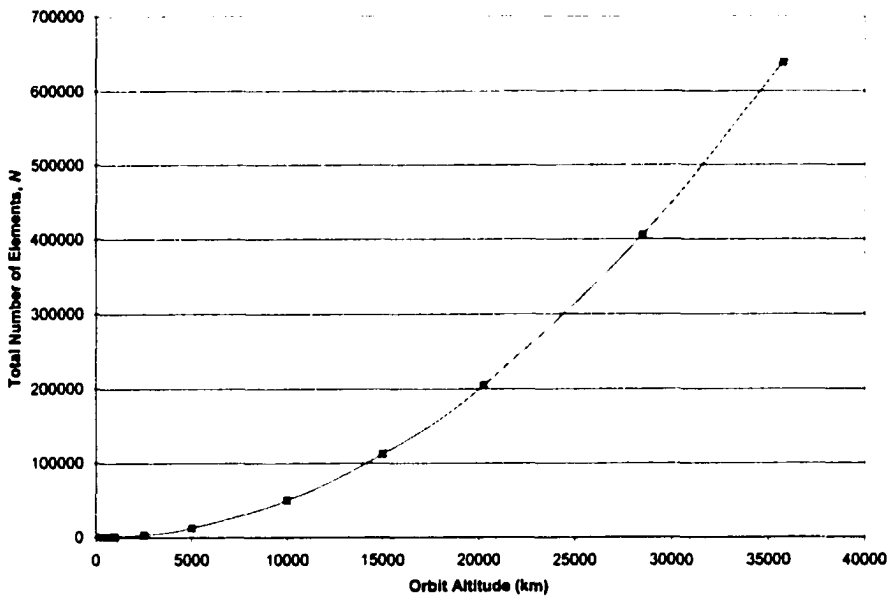

Figure 7.1-7. Total Number of Elements for SPS Array.

As previously mentioned, if a satellite is not directly over the receiving array, then the beam pattern is affected. This causes the beam to be spread downfield from the satellite, requiring the beam or receiving array be adapted to this wider pattern. It may also force the satellite to electronically steer the beam in the direction of the array, if not mechanically pointed in that direction. This causes the formation of sidelobes that decrease the efficiency of the transmitted beam (Section 7.3).

Adding to this is the complication induced when the satellite and the receiving array are in relative motion. This is the case for any satellite altitude, with the exception of the geostationary case. For an equatorial orbit, this relative motion is described by the difference in rotational velocity of the satellite and the earth [4],

$$\Delta\omega = \omega_{satellite} - \omega_{earth} = \frac{1\,\text{rev}}{P} - \omega_{earth}. \tag{7.1-3}$$

The period P of the satellite's orbit is shown in Figure 7.1-8. This is calculated using

$$P = 2\pi\sqrt{\frac{a^3}{\mu}}, \tag{7.1-4}$$

where

$$P = \text{period of orbit}\,[\text{sec}]$$
$$a = \text{semi-major axis}\,[\text{km}]$$
$$\mu = \text{gravitational parameter}\left[\frac{\text{km}^3}{\text{sec}^2}\right].$$

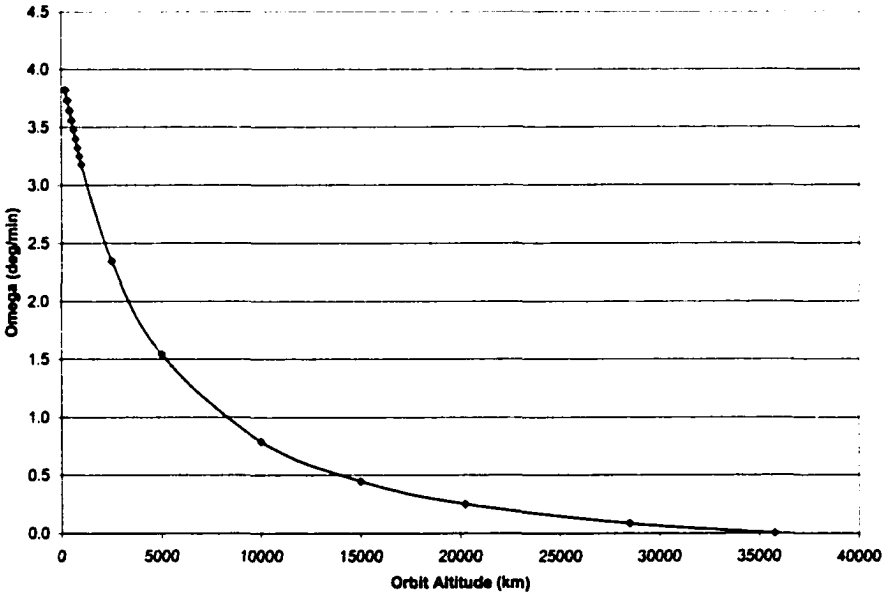

Figure 7.1-8. Relative Angular Velocity for the Equatorial SPS.

This data can be directly translated as the slew rate requirements for the satellite. When the satellite comes within the designated transmission range of a ground receiver, the energy is downlinked to the array. As the satellite passes through this transmission range, the signal is continuously steered towards the receiver. This presents a slew rate

for the satellite and for the ground station (assuming it controls the transmission) that exceeds 3° per minute. LEO orbits are also limited by the decreased visibility of the ground site.

Fuel requirements are also very different for the LEO and GEO satellites. The LEO orbits do not require as much ΔV to attain, but require constant adjustment to overcome drag and other effects. Expenditure of fuel to maintain the orbit is called *stationkeeping.* A performance chart quantifying the stationkeeping ΔV requirements as a function of orbit altitude is shown in Figure 7.1-9 [25].

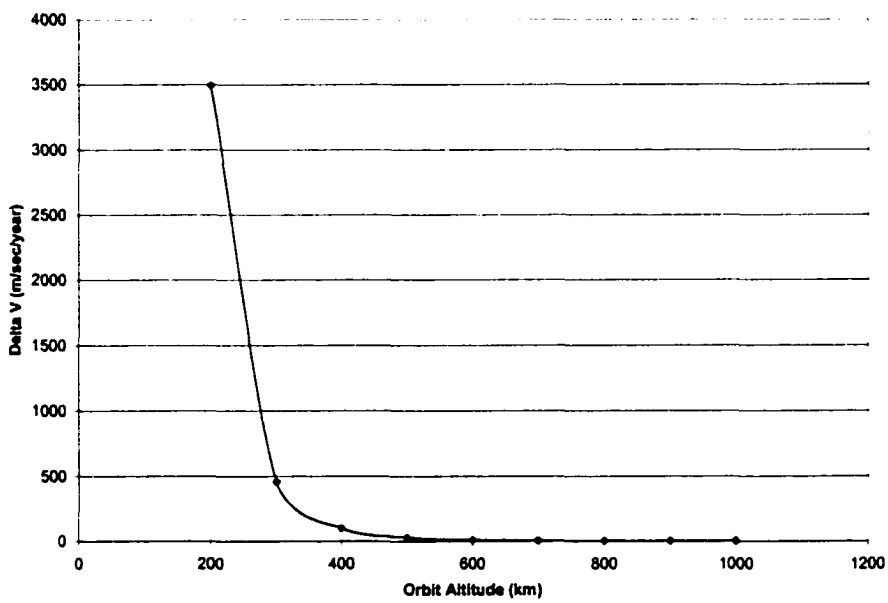

Figure 7.1-9. Delta V Orbit Maintenance Requirements.

Due to the amount of drag present at altitudes below 300 km, maintaining these orbits for any sustained amount of time is untenable. Raising the orbital altitude to 400 km greatly decreases these effects. Compared to LEO configurations, the GEO orbit offers almost negligible resistance.

However, the cost of getting the satellite to GEO is much higher. The amount of energy needed to get the satellite into its final orbit is the sum of its launch velocity requirements and the final orbit size. A simplified diagram showing these components is given in Figure 7.1-10.

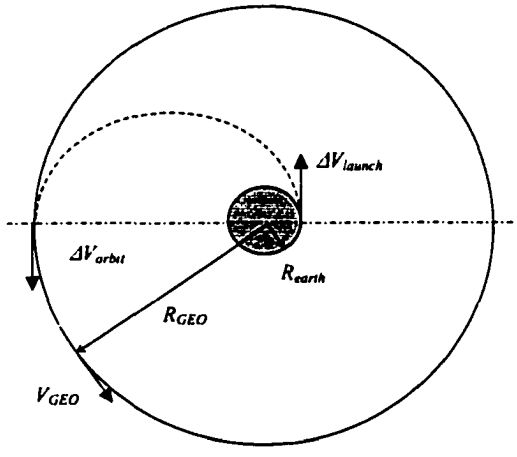

Figure 7.1-10. Transfer Orbit to Final Orbit [4].

The total change in velocity ΔV required to attain the orbit is given by

$$\Delta V_{total} = \Delta V_{orbit} + \Delta V_{launch} \tag{7.1-5}$$

where

$$\Delta V_{launch} = V_{transfer}\Big|_{earth} - V_{earth} + \Delta V_{losses} \tag{7.1-6}$$

$$\Delta V_{losses} \approx 1000\ \mathrm{m \cdot sec^{-1}}$$

$$V_{earth} = 465.1\ \mathrm{m \cdot sec^{-1}}.$$

The velocity change required at earth to enter the transfer orbit is given by

$$V_{transfer}\Big|_{earth} = \sqrt{2\left(\frac{\mu}{R_{earth}} + \varepsilon_{transfer}\right)}. \tag{7.1-7}$$

The specific mechanical energy of the transfer orbit ε is related to the orbit size:

$$\varepsilon_{transfer} = \frac{\mu}{2a_{transfer}}, \tag{7.1-8}$$

$$a_{transfer} = \frac{R_{earth} + R_{orbit}}{2}. \tag{7.1-9}$$

Likewise, the velocity change required to enter the final circular orbit is

$$\Delta V_{orbit} = V_{orbit} - V_{transfer}\Big|_{orbit}, \tag{7.1-10}$$

$$V_{transfer}\Big|_{orbit} = \sqrt{2\left(\frac{\mu}{R_{orbit}} + \varepsilon_{transfer}\right)}, \tag{7.1-11}$$

$$V_{orbit} = \sqrt{\frac{\mu}{R_{orbit}}}. \tag{7.1-12}$$

Figure 7.1-11 summarizes the total ΔV required to attain the possible SPS orbits. This shows that the GEO orbit requires roughly twice the ΔV to attain than does the LEO orbit. Factoring in the large size of the GEO SPS (roughly 400 m diameter) shows that fielding this array would be a daunting task.

The power required of the transmitting array elements will now be calculated. As an initial assumption for the problem, it was assumed that the array size for a given orbit would be the minimum needed to satisfy its beamwidth requirements. This provides a limit to the number of array elements at a specific orbit altitude. This may be a somewhat inaccurate construct, but provides a first-cut scaling tool to account for drag and other orbital perturbations that are amplified for low earth orbits.

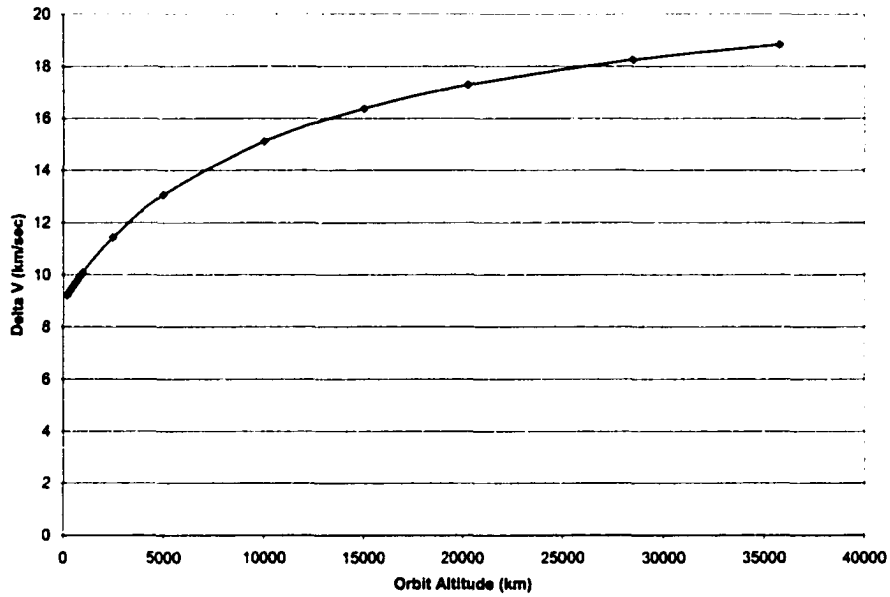

Figure 7.1-11. Delta V Required to Establish Orbit.

For the SPS to be cost effective, it should produce at least as much energy density at the receiving array as would be produced by an equal amount of ground-based solar cells. Assuming that approximately 1000 W/m^2 reach the surface of the earth and the ground site is exposed to the sun for only ½ of the day, this yields a figure of roughly 500 W/m^2. If the solar array is considered to be ε_{solar} = 30% efficient (a liberal estimate), then the power produced on the ground may reach 150 W/m^2. By working backwards from this, the amount of power to be supplied by the SPS may be calculated.

The power density at the receiving site is dependent upon the power transmitted from the SPS. This is given by Friis' transmission formula [23],

$$S_r = \frac{P_r}{A_r} = \frac{P_t A_t}{R^2 \lambda^2}(1 - L_a) \tag{7.1-14}$$

where

$$S_r = \text{received power density}\left[\frac{\text{W}}{\text{m}^2}\right]$$
$$P_r, P_t = \text{power received, transmitted}\,[\text{W}]$$
$$A_r, A_t = \text{area of receiver, transmitter}\,[\text{m}^2]$$
$$R = \text{distance travelled}\,[\text{m}] = H$$
$$\lambda = \text{wavelength of signal}\,[\text{m}]$$
$$L_a = \text{atmospheric loss.}$$

The atmospheric losses encountered for the GEO SPS illuminating a ground receiver site directly beneath it are almost negligible. For a frequency of 2.45 GHz, the normalized value for atmospheric attenuation is [26]

$$\frac{L_a}{\ell} = 0.001\,\frac{\text{dB}}{\text{km}}. \qquad (7.1\text{-}15)$$

If the maximum altitude of the earth's atmosphere is roughly 50 miles (~80 km), then the attenuation would have to be less than 0.08 dB. However, since the atmospheric density decreases with altitude, the attenuation is actually much less than this amount. The value for the attenuation has been determined to be $L_a \approx 0.035$ dB = 1.01% [25].

Therefore, only about 1% if the power transmitted to the equatorial site will be lost. As a point of comparison, this value has been predicted to be a maximum of 2% for fair weather; 13% attenuation for the worst weather conditions [2]. Because of the relative uncertainties for the exact transmitting and receiving conversion efficiencies, this value may easily be absorbed and therefore is not considered further.

Equation 7.1-14 provides the maximum power density received at the center of the rectenna array. This value tapers off to the edge of the receiving array, where its value should be minimal. If the receiver captured all of the energy, then the value would be zero outside the bounds of the array. However, this is not the case for the actual array.

The power calculations here assume that the 3-dB beamwidth is captured within the array bounds, with the residual spilling over the edges. This is done to minimize the power variation within the receiving antenna, thereby reducing the amount of rectenna elements necessary. (The receiving array would be surrounded by a safety zone to protect personnel from power outside of the pattern.)

In this configuration, the power would vary from its maximum level at the center of the array to ½ that amount at its edges. The average power of the array may be approximated by 75% of the maximum. The calculation may be further simplified by assuming that the sidelobe levels for a large array are negligible. (Figure 7.3-8 shows that the sidelobes for the SWA will in fact need to be suppressed in some fashion.) Since the atmospheric attenuation is very low, it may then be assumed that all power transmitted from the SPS is received at the rectenna array.

Assuming a rectenna efficiency of $\varepsilon_{rectenna} = 70\%$, the total amount of power that must be received at the rectenna array is $P_r = 16.83$ GW. Assuming no losses due to attenuation or sidelobes, this is equivalent to the power transmitted from the SPS. For a magnetron efficiency of $\varepsilon_{magnetron} = 70\%$, the total power transmitted is $P_t = 2.40$ GW. This value is divided by the total number of array elements N to obtain the normalized power required of each ESPAM. The results of this calculation are shown in Figure 7.1-12.

Because of the scale of the numbers, the minimum orbit altitude shown is 5000 km. The power required of each ESPAM decreases logarithmically, dropping to to 84.7 kW per ESPAM for an array size of 530 x 530 elements. Increasing the size lessens the required power and provides some beam shaping margin should elements fail.

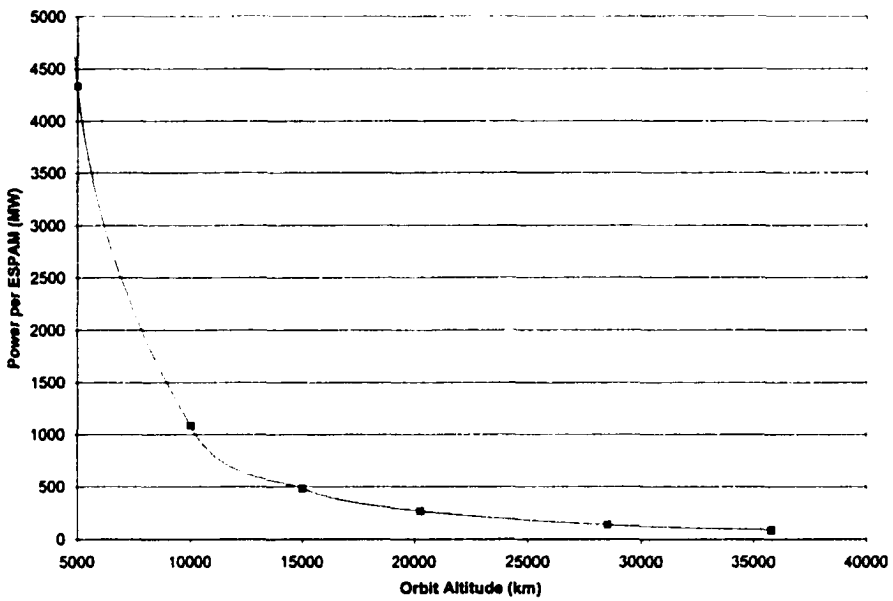

Figure 7.1-12. Power per ESPAM Required to Illuminate 10 km Receiving Array with 150 W/m^2 Usable Power.

The power per ESPAM for varying sizes of GEO arrays is shown in Figure 7.1-13.

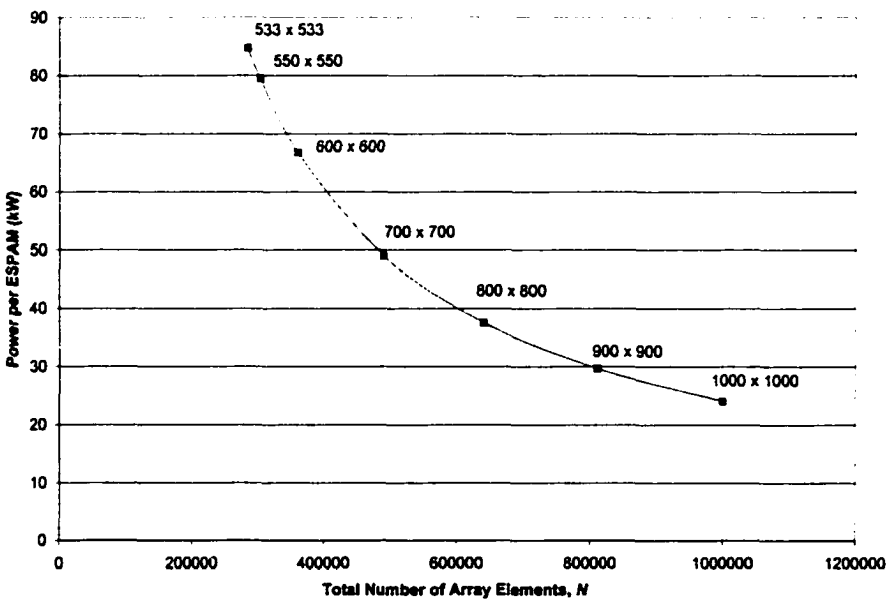

Figure 7.1-13. Power Density for SPS with Performance Margin Added.

The power requirement for the SPS is met by a 550 x 550 array of ESPAMs, each powered by a 80 kW magnetrons (could be implemented using three 30 kW magnetrons). This yields a power density of 216 W/m^2 (151 W/m^2 after conversion to DC).

Orbit choice must also consider the impacts of solar eclipses. These limit the duty cycle of the SPS, and thereby reduce the power output capacity. The maximum length of the solar eclipse may be estimated as [25]

$$TE = \frac{2\rho}{360\,\text{deg}} P \tag{7.1-16}$$

where the earth angle subtended by the satellite ρ is given by Equation 7.2-2. The total amount of time eclipsed during one day is then

$$TE_{day} = TE \cdot n_{eclipse}. \tag{7.1-17}$$

The maximum eclipse time per day as a function of altitude is plotted in Figure 7.1-14. This may be plotted as a percentage of total time available for power generation, as shown in Figure 7.1-15. Note that these are maximum times and do not account for seasonal changes in the orbital geometry. For example, the GEO satellite is eclipsed 72 min/day, but for only (2)-3week periods at the spring and fall equinoxes. This increases the duty cycle to roughly 99% availability [2].

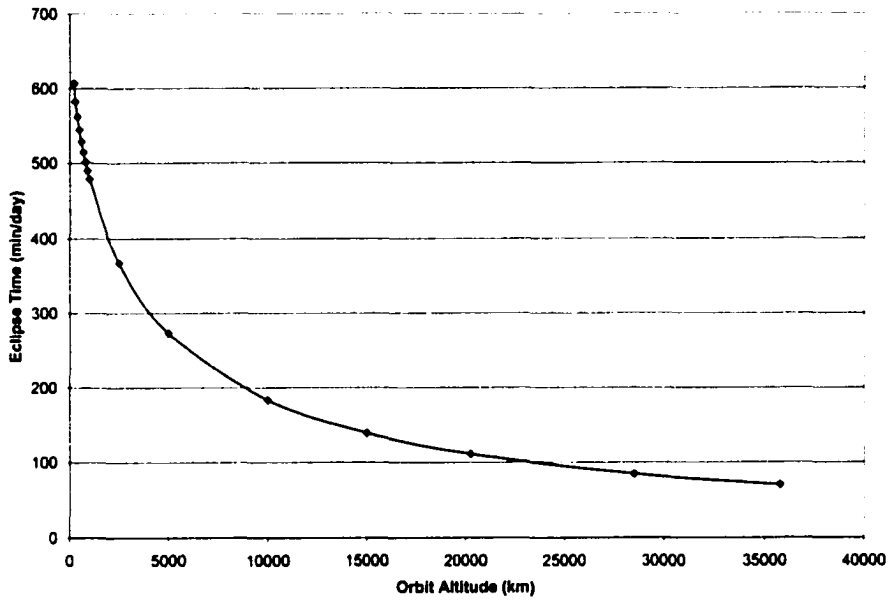

Figure 7.1-14. Maximum Eclipse Time per Day for SPS Orbits.

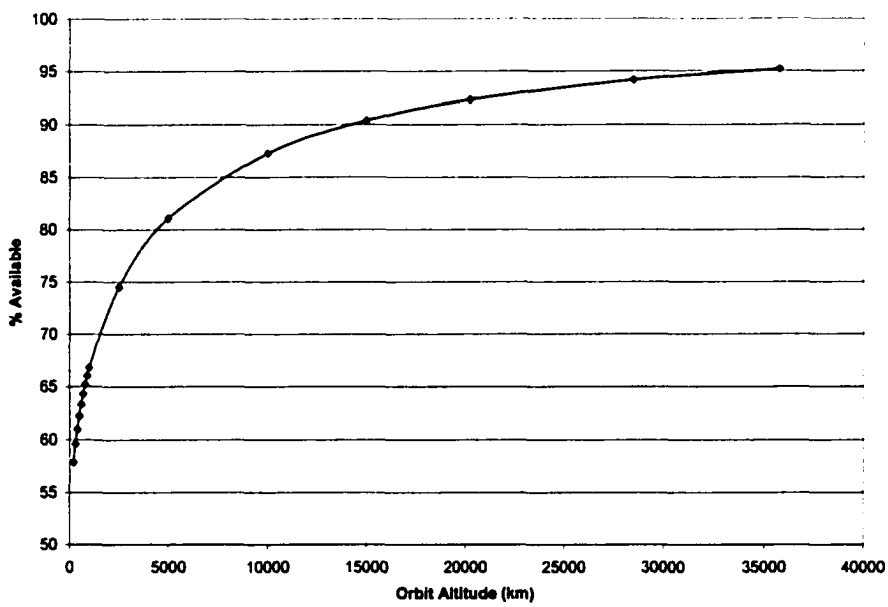

Figure 7.1-15. Percentage of Duty Cycle Available.

Table 7.1-1 summarizes some of the significant performance requirements driven by the differences in the LEO and GEO orbits. This is only meant to provide rough

performance estimates. The data provided assumes the ground receiving site configuration shown in Figure 7.1-1.

Table 7.1-1 Summary of Orbital Effects on SPS Design.

	LEO 1	LEO 2	GEO
Orbit Altitude	300 km	1000 km	35,768 km
Beamwidth to fill 10 km receiver	1.9097 deg	3.44 arcmin	57.67 arcsec
Number of ESPAM units for beamwidth	5 x 5	15 x 15	533 x 533
Slew Rate	0.0621 deg/sec	0.0529 deg/sec	-
ΔV to Orbit	9.34 km/sec	10.10 km/sec	18.83 km/sec
ΔV for Stationkeeping [25]	4.56E+02 m/sec/year	1.22E-01 m/sec/year	-
Orbit Period	90.52 min	105.12 min	24 hrs
Maximum Eclipse	36.59 min	34.93 min	69.40 min
Maximum Eclipse Time	582.09 min/day	478.57 min/day	69.40 min/day
Power required of each ESPAM for 150 W/m^2 at receiver, $\varepsilon_{magnetron} = \varepsilon_{rectenna} = 70\%$	962 MW each	107 MW each	84.7 kW

The power density at the receiver below is the maximum value at the center of the array, and tapers off to ½ the value at the edge of the receiving site. The power data presented also assumes no loss to sidelobes.

Comparing the orbits demonstrates the relative merits of the GEO configuration. With the exception of the ΔV to orbit, the GEO orbit provides exceptional advantages over the

LEO. The eclipse time and beam steering requirements are considerably relaxed for the GEO orbit, since the relative position of the satellite is essentially fixed. It is acknowledged that the beamwidth requirements for the GEO orbit are tight for this altitude. This will introduce some beam steering requirements to counteract the effects of orbit perturbations.

Power calculations assume that a 80 kW magnetron will power each ESPAM unit. The array size given assumes a minimum size necessary to focus the beam to fit within the receiving array. Nothing precludes using a larger transmitting array for the lower altitude orbits, other than the increased drag on the satellite and the torsional forces that would be experienced. In fact, the transmitting array would have to be larger to provide the necessary beamwidth when not directly overhead the array.

In any event, due to the increased complexity required of a LEO configuration, it is debatable as to whether this arrangement would be used for large-scale power production. It seems more likely that its use will be economically and politically restricted to special use situations, such providing power to high latitude locations. However, it will almost certainly be a necessary step in the proof-of-concept before ultimately building a large GEO-based system.

7.2 Orbital Requirements of GEO SPS

This section examines the performance requirements of the SPS in a geosynchronous (GEO) orbit. It provides the reference frame for calculating the necessary beamwidth and steering for the SPS when in an ideal geostationary orbit. It also highlights the astrodynamics principles necessary to analyze the motion of the satellite when accounting for imperfections in the orbit.

7.2.1 Ideal Geostationary Orbit

Suppose a circular rectenna array with a diameter of 10 km is located at the equator directly beneath an SPS satellite in a geostationary orbit, as shown in Figure 7.1-1. The orbit is assumed to be ideal, being perfectly circular (eccentricity $e = 0$) and lying in the equatorial plane (inclination $i = 0$).

For proper operation of the system, the beam should exactly fill the receiving array. This will provide the most even power distribution across the array, and prevent overspill of the beam. To satisfy this condition, the beamwidth required is

$$BW_{required} = 2\tan^{-1}\left(\frac{D/2}{H}\right). \qquad (7.2\text{-}1)$$

At geosynchronous orbit, this yields a value of $BW_{required} = 57.67$ arcsec. However, this beamwidth is valid only for the ideal case — any offset or relative motion between the satellite and ground receiver will cause the beam to spill over the array edge. This is not a likely scenario, even for the idealized orbit. Geographic, economic, and political considerations will require most ground receiver sites be located some distance from the equator.

Extending the analysis to the case of an offset ground site becomes more complex. This requires the definition of a geocentric (earth-centered) coordinate system, as shown in Figure 7.2-1.

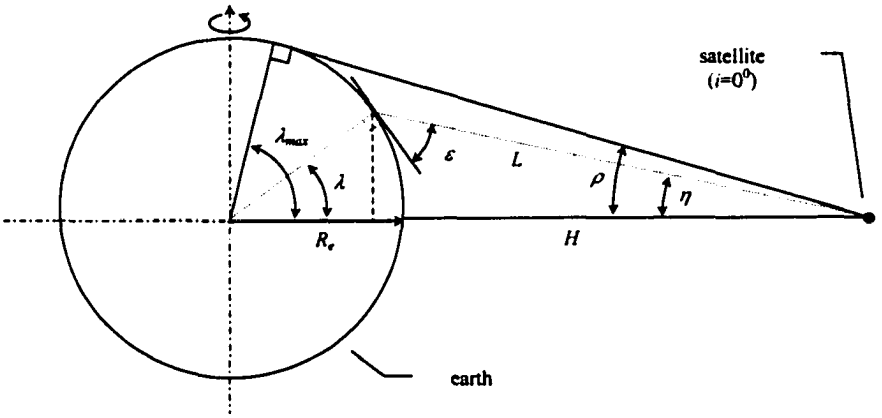

Figure 7.2-1. Earth Angular Geometry for SPS [25].

The parameters of interest are:

R_e = radius of earth = 6378 km
H = altitude of satellite = 35,786 km
L = slant range to target
η = angle from nadir
λ = latitude of target
ρ = grazing angle (defines boundary of footprint)
λ_{max} = maximum latitude seen by satellite
ε = satellite elevation angle.

The curvature of the earth limits the maximum offset between the satellite and the ground receiver. At extremely high latitudes, the site is blocked by the horizon. The limiting value of latitude λ_{max} may be found by

$$\sin\rho = \cos\lambda_{max} = \frac{R_e}{R_e + H}. \tag{7.2-2}$$

For a GEO SPS system, the maximum angle subtended by the earth (grazing angle) is calculated to be $\rho = 8.7°$. Translating this angle to the earth centered coordinates, the maximum site latitude is $\lambda_{max} = \pm 81.3°$.

Any location between these latitudes can theoretically see the satellite, with the same exclusion zones measured longitudinally. The footprint of earth seen by the satellite is shown in Figure 7.2-2.

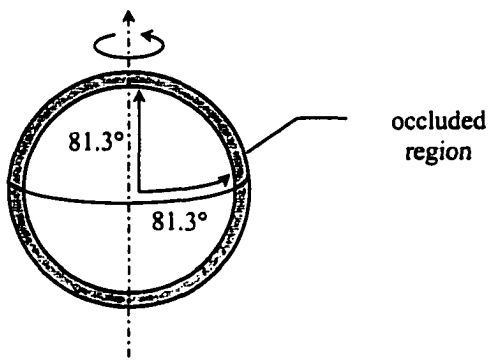

Figure 7.2-2. Portion of Earth Visible from a Geostationary Satellite.

The gray ring depicts the region of the earth occluded from view by the horizon due to the proximity of the satellite. This is the theoretical maximum that may be achieved. However, physical factors reduce the site location even further. At the higher latitudes, terrain features can obstruct the line-of-sight path. In addition, the curvature of the earth causes an apparent beam spreading in the 'downfield' direction, similar to the stretching of a shadow. This requires either elongating the receiving array, or tilting it in the direction of the satellite. Either of these can be a costly prospect, making large site displacements impractical.

To examine the magnitude of these effects, assume that a receiving site is located at 40° N latitude directly in line with the satellite longitudinally, as shown in Figure 7.2-3. Since the objects are aligned longitudinally, the beamwidth in this direction is only slightly affected by the increased distance to the array. The majority of the increase results in the latitudinal dimensions of the receiving array to account for the curvature of the earth.

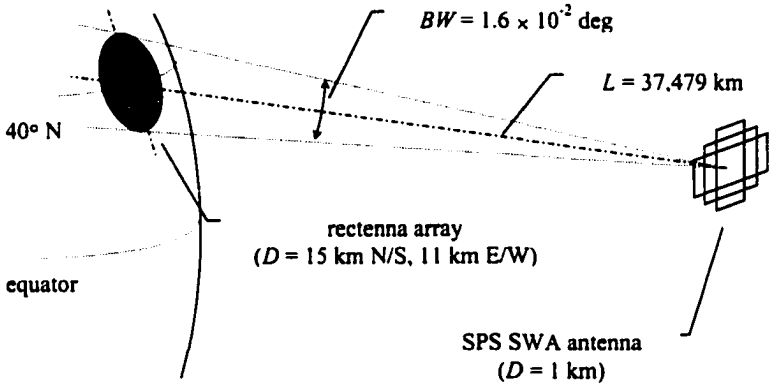

Figure 7.2-3. GEO SPS, Receiving Array at 40° N Latitude.

Because of the offset, the satellite must steer the beam at an angle η to intercept the site. This is called the nadir angle η, defined as

$$\tan\eta = \frac{\sin\rho\sin\lambda}{1-\sin\rho\cos\lambda}. \tag{7.2-3}$$

For a site latitude of 40° N, this yields a nadir angle of $\eta = 6.3°$. The latitudinal (N/S) dimension of the array must be lengthened by an amount ΔD to account for the offset. First, the new slant range L from the satellite to the ground site is found using

$$R_e \sin\lambda = L\sin\eta. \tag{7.2-4}$$

For a site located at 40° N, the slant range L is calculated to be 37,479 km. This increased distance results in a slightly increased longitudinal (E/W) footprint,

$$D_{longitude} = 2L\tan\left(\frac{BW}{2}\right). \tag{7.2-5}$$

The new slant range yields a modified longitudinal footprint of $D_{longitude}$ = 10.479 km. Next, the latitudinal stretching of the pattern due to the curvature of the earth is calculated using

$$\Delta D = \frac{D_{adjusted}}{\cos\varepsilon}, \tag{7.2-6}$$

$$\cos\varepsilon = \frac{\sin\eta}{\sin\rho}. \tag{7.2-7}$$

The satellite elevation angle ε is calculated to be 43.68°, which leads to an adjusted downfield beam width of $D_{latitude}$ = 14.943 km.

The resulting array is stretched into an elliptical shape with the major axis (N/S) approximately 15 km, adding almost 50% to its original length. The minor axis is less affected, being increased by only about 5%. The total impact is to increase area of roughly 60% over that required by the aligned array. Following the same procedure, the receiving array shape for any latitude may be calculated, as shown in Figure 7.2-4. The calculations are truncated at 50°, as the latitudinal dimension of the array grows as a third order polynomial, making receiving arrays at higher latitudes impractical.

Plotting the array dimension data in terms of area shows that the array must *double* in ground space when offset by just 47° offset, as shown in Figure 7.2-5. This has the effect of halving the incident power density, bringing it far below the design goals of 150 W/m^2 stated in Section 7.1. For the GEO SPS configuration under consideration, this renders high latitude sites impractical. Therefore, it will therefore be assumed that the maximum latitude of the ground site will not exceed the cited example of 40°.

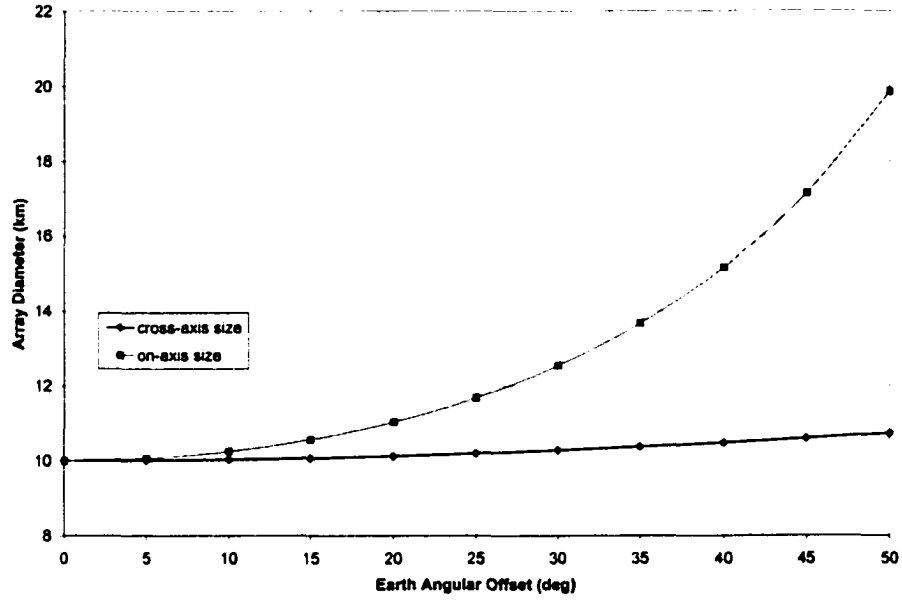

Figure 7.2-4. Effects of Ground Site Offset on Array Size.

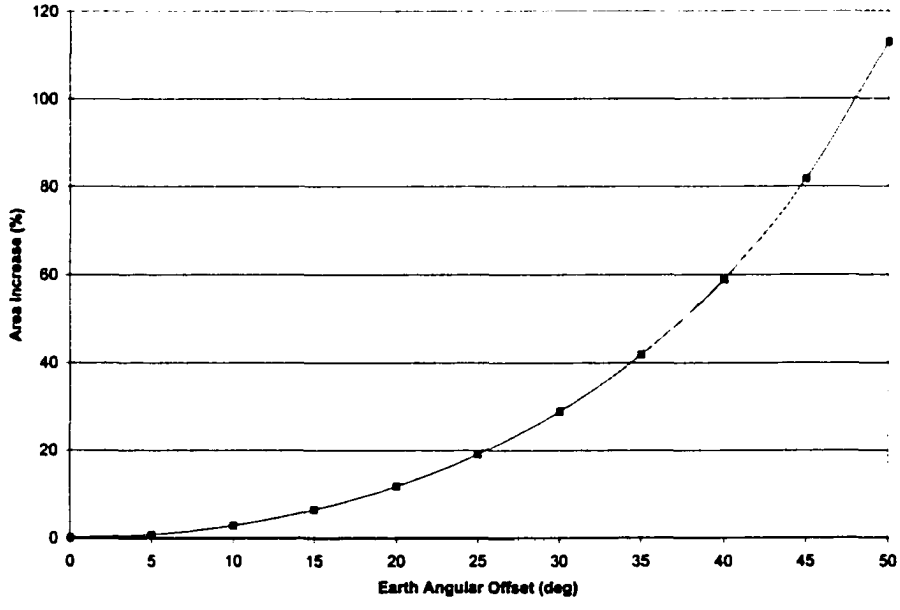

Figure 7.2-5. Effects of Ground Site Offset on Array Area Requirements.

The same calculations used above may be applied to longitudinal offsets, or in any combination thereof. Shifting the relative longitude will cause a corresponding

latitudinal (E/W) stretching of the pattern. The effects of latitudinal and longitudinal offsets for a geostationary satellite are summarized in Figure 7.2-6.

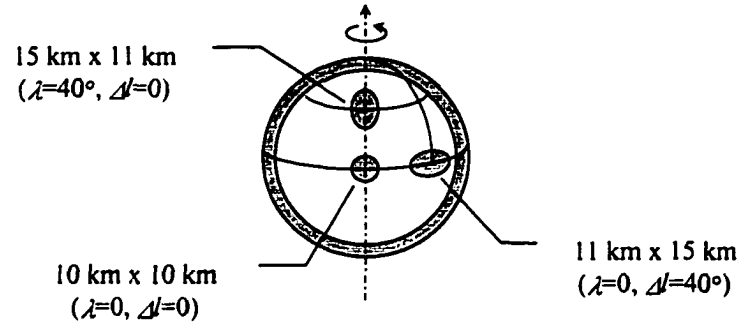

Figure 7.2-6. Effects of Angular Offset on Sizing for Receiving Site.

In addition to the simple geometric effects presented thus far, the orientation of the rectenna elements at the receiving site must be adjusted to provide maximum conversion efficiency. Another factor to be considered is the increased path loss caused by the higher latitudes. All of these technical factors combine, driving the rationale for sites to be located as near the equator as possible. These must be balanced with other technical, economic and political factors that argue for providing the receiving array nearby.

7.2.2 Geosynchronous Orbit.

So far in the discussion, the satellite has been limited to a perfectly circular equatorial orbit. Though many geosynchronous satellites are placed in near-perfect orbits, this is merely a mathematical construct — the perfect geostationary orbit does not exist. A satellite's orbit may be considered geostationary only if it is *relatively* stationary for the application intended. This depends upon the satellite performance capability, such as directivity of the satellite/ground antennas and precision of the satellite attitude determination and control subsystem (ADACS). For some satellites and applications, a particular orbit may be considered geostationary. For others, this may not be the case.

To establish the requirements of a geostationary orbit for the SPS, it is necessary to quantify the motion of the satellite permitted for its beamforming capabilities (steering and beamwidth). The beamforming requirements for the static case have already been discussed in this section. The capabilities of the SPS to provide this beam are examined in Section 7.3. What remains to explore is the effect of motion upon these requirements.

Removing the constraints of the ideal geostationary orbit permits the orbit eccentricity e and inclination i to be varied. This introduces relative motion between the satellite and the ground receiver.

Eccentricity Effects. The eccentricity of the orbit describes the amount by which it deviates from a perfect circle. This affects the distance between the satellite and the earth at any point in its orbit, which in-turn creates a change in ground speed between the satellite and receiver. A diagram describing the orbital geometry of the problem is provided in Figure 7.2-7.

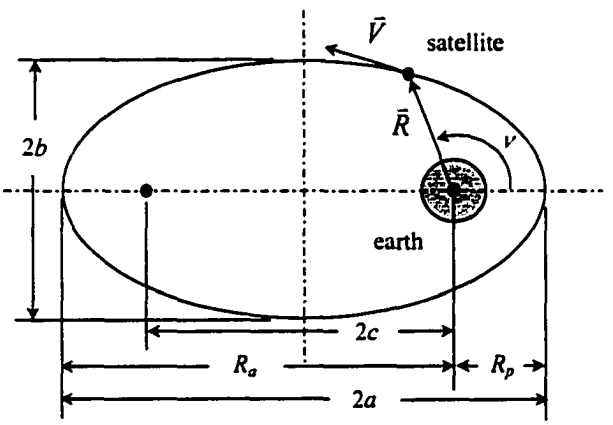

Figure 7.2-7. Geometry for General Elliptical Orbit [4].

In general, the flight path of the satellite orbiting the earth is described by an ellipse. The speed of the satellite varies along the flight path is inversely proportional to its radial distance to the earth according to

$$V_{satellite} = \sqrt{2\left(\frac{\mu}{R} + \varepsilon\right)}. \tag{7.2-8}$$

The specific mechanical energy of the orbit ε is

$$\varepsilon = \frac{-\mu}{2a}, \tag{7.2-9}$$

where

$$V_{satellite} = \text{satellite velocity}\left[\frac{\text{km}}{\text{sec}}\right]$$
$$R = \text{radius from center of earth to satellite}\,[\text{km}]$$
$$\varepsilon = \text{specific mechanical energy}\left[\frac{\text{km}^2}{\text{sec}^2}\right]$$
$$\mu = \text{gravitational parameter}\left[\frac{\text{km}^3}{\text{sec}^2}\right]$$
$$a = \text{semi - major axis of satellite orbit}\,[\text{km}].$$

Therefore, the satellite's velocity is fastest when it passes closest to the earth (periapsis) and slowest when furthest from the earth (apoapsis), as illustrated in Figure 7.2-8.

R_a = radius of apoapsis (furthest distance)
R_p = radius of periapsis (closest approach)

Shaded areas depict the portion of the orbit traversed within a certain span of time. Kepler's second law states that equal areas of an orbit are swept out in equal times. By selecting the pie shapes so that their areas are roughly equivalent, the relative speeds of the satellite become apparent.

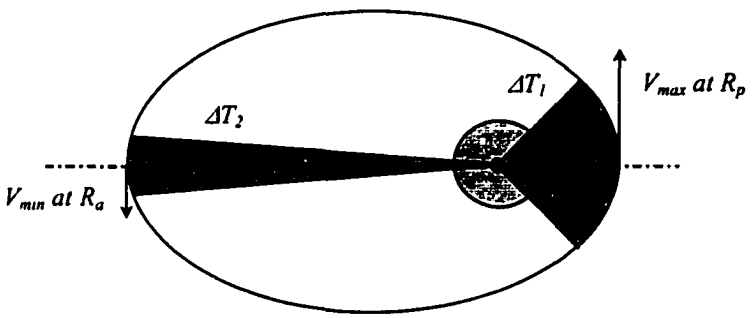

Figure 7.2-8. Relationship Between Orbit Shape and Satellite Velocity.

The satellite's speed continually changes between these points, varying with the distance from the earth. This distance is given by the polar equation for a conic section,

$$R = \frac{a(1-e^2)}{1+e\cos\upsilon} \tag{7.2-10}$$

where

e = eccentricity of orbit
υ = angle of true anomaly.

The orbit eccentricity may be found using

$$e = \frac{c}{a} = \frac{R_a - R_p}{R_a + R_p}. \tag{7.2-11}$$

To calculate the satellite velocity, it is first necessary to determine the gravitational parameter for the central body (in this case, earth). This quantity is a constant for any celestial body and is dependent upon its mass. For the earth, this would be

$$\mu_{earth} = Gm_{earth}, \tag{7.2-12}$$

where

$$G = \text{universal gravitational constant} = 6.6726\times10^{-11}\left[\frac{\text{N}\cdot\text{m}^2}{\text{kg}^2}\right]$$

$$m_{earth} = \text{mass of earth} = 5.9742\times10^{24}\ [\text{kg}].$$

Therefore, the gravitational parameter for the earth is $\mu_{earth} = 3.985\cdot10^5\ \text{km}^3\cdot\text{sec}^{-2}$.

The trace of the satellite's path over the earth is called its *ground track* and is caused by the rotation of the earth with respect to the satellite. The groundtrack of a GEO satellite due to orbit eccentricity is shown in Figure 7.2-9. The trace of the satellite oscillates about a central location over a 24 hour period.

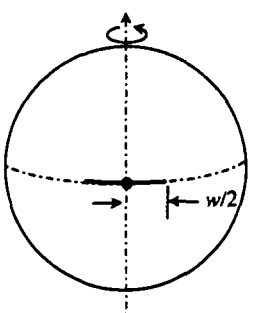

Figure 7.2-9. Periodic Motion of GEO Satellite Due to Orbit Eccentricity.

The magnitude of the oscillation is given by [25]

$$\omega_{ecc} = \pm\left(\frac{360\ \text{deg}}{\pi}\right)e. \tag{7.2-13}$$

where

h = half - height (latitudinal) of ground track pattern
ω = half - width (longitudinal) of ground track pattern
i = inclination of orbit
e = eccentricity of orbit.

The impact of this effect depends upon the magnitude of the oscillation versus the beamwidth of signals transmitted between the satellite and ground site. It is generally desired to provide stationary ground antennas and to eliminate or minimize the satellite steering requirements. Some typical values of orbit eccentricity for geosynchronous satellites are shown in Table 7.2-1.

Table 7.2-1. Typical Values of Orbit Eccentricity and Inclination [27].

Satellite	Eccentricity	Inclination (deg)
MORELOS 2	0.0002099	0.4727
SPACENET 1	0.0002218	2.3769
SBS 5	0.0002484	0.0088
DSCS III - 1	0.0003549	6.8774
SPACENET 3R	0.0003616	0.0089
INTELSAT 505	0.0005021	7.2002
FLTSATCOM 4	0.0006198	12.1356
TDRS - 1	0.0017480	10.2660
NATO 3D	0.0017599	5.6714

The ground track oscillation for these orbits is shown in Figure 7.2-10. The relationship is linear with orbit eccentricity. For the GEO SPS, the tight beamwidth imposed on the microwave beam makes the orbit sensitive to the exact value of eccentricity. A beamwidth of 57.67 arcsec is required to exactly fill the 10 km receiving array. In comparison, an eccentricity of only $e_{IBW} = 0.0001390$ will produce a groundtrack (error in steering) equaling this value. An orbit having a comparable eccentricity appears to be obtainable, but still must be augmented by a beamsteering capability to cancel the induced position error.

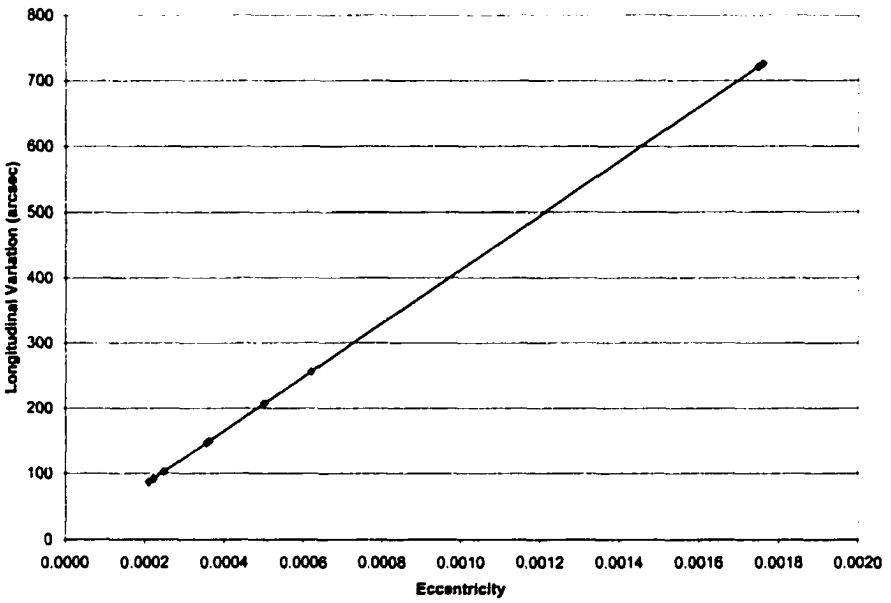

Figure 7.2-10. Eccentricity Effects on Satellite Ground Track.

Figure 7.2-10 shows how the steering for the SPS would be affected by slackening the eccentricity. For the case of the non-offset ($\eta = 0$) ground receiver, the relation between the orbit eccentricity and the required beamsteering is given by

$$\alpha_{eccentricity} = \pm\frac{\omega_{ecc}}{2} = \pm\left(\frac{180\,\text{deg}}{\pi}\right)e. \qquad (7.2\text{-}14)$$

If the satellite and ground site are offset, the steering angle must be resolved into latitudinal and longitudinal components. In Section 7.3, it is shown that the steering angle adversely affects the beam pattern. Therefore, it is desirable to minimize the required steering angle for the SPS.

Another consideration is the required *slewrate* of the steered microwave beam, which is also affected by the eccentricity of the orbit. The maximum slew rate is defined by the greatest difference in the satellite's ground speed versus that of the receiving site. For

the nominal orbit values in Table 7.2-1, the maximum slew rates are shown in Figure 7.2-11. These values are reached at perigee.

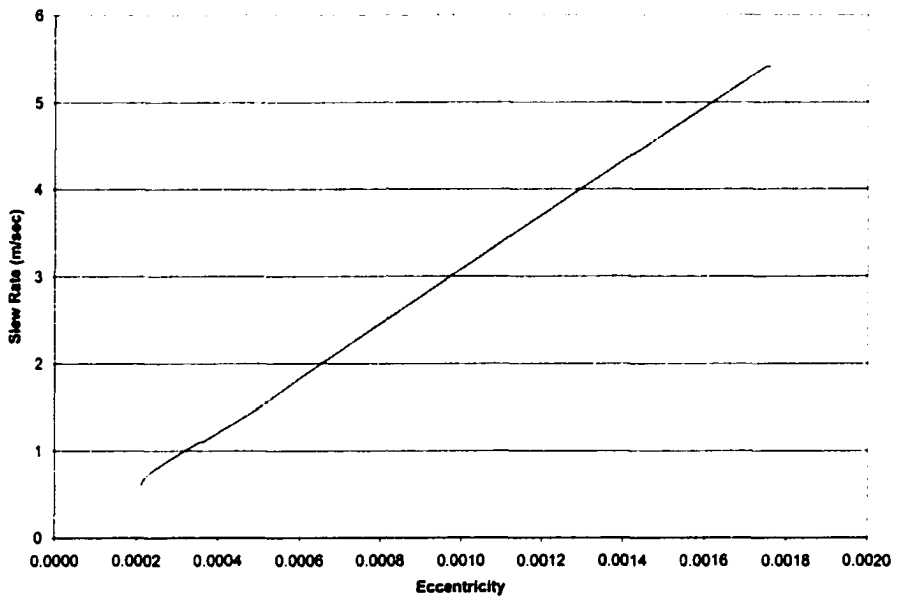

Figure 7.2-11. SPS Maximum Slew Rate versus Eccentricity for Nominal Orbits.

The speed of the groundtrack varies with the satellite's position along its orbit (Figure 7.2-8). Endpoints of the trace correspond to two points of the orbit where the satellite velocity matches that of the earth. For a prograde satellite, the $L \rightarrow R$ segment (CCW from above) corresponds with the orbit near perigee. This portion of the groundtrack will therefore be traced out faster than the $R \leftarrow L$ (CW) segment, with the difference in ground speeds being proportional to the eccentricity of the orbit.

Though the primary orbit under consideration is a GEO orbit, this effect would be significant in any highly elliptical orbits designed to provide maximum coverage of a particular hemisphere (such as the Russian Molniya orbit). Such orbits may be used in SPS technology demonstrations for a variety of reasons. The elliptical orbit provides certain advantages to the circular orbit. By slowing the satellite down over the desired earth location, the beamsteering and slew rate requirements may be loosened.

Finally, note that the *beamwidth* projected on the ground also varies due to the orbit eccentricity. For orbits circular orbits, this effect is minimal (~±1.6 m variance for e = 0.000139 using a beamwidth of 57.67 arcsec) and therefore should not be of concern. For more elliptical orbits, the change in footprint becomes significant. Table 7.2-2 gives the projected beam width variance for some values of eccentricity (not accounting for lateral displacement effects).

Table 7.2-2. Variance in Projected Beam Width Due to Orbit Eccentricity.

Eccentricity	*beam variance*
0.002	23.6 m
0.005	58.9 m
0.010	117.8 m
0.020	235.7 m
0.050	58.92 m
0.100	1178.3 m

Inclination Effects. Inclination describes the orientation of the orbital plane with respect to the equatorial plane of the earth, as shown in Figure 7.2-12.

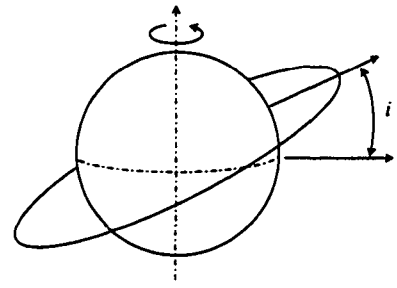

Figure 7.2-12. Measurement of Orbit Inclination.

Introduction of this factor makes analysis of the satellite ground track more complicated. A satellite in an inclined orbit cannot remain over a constant earth position, since the two rotate about different axes. Over a 24-hour period, the trace of the satellite appears to 'walk' up and down the earth with respect to a central location on the equator. This provides a similar groundtrack to that for the eccentricity shown in Figure 7.2-9, but rotated by 90°. Momentarily disregarding the varying groundspeed induced by earth latitude, the groundtrack would appear as shown below.

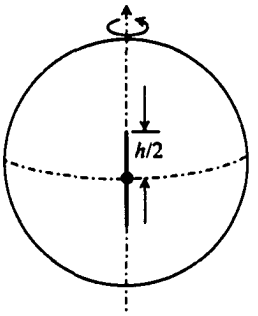

Figure 7.2-13. Periodic Motion of GEO Satellite Due to Orbit Inclination. Differential rotation rate due to earth latitude neglected.

The satellite's groundtrack is also affected by the differential in groundspeed seen at any latitude. Every point on earth rotates with a certain tangential velocity due to the earth's rotation, except the poles. This is generally referred to as *launch site velocity*, as it can provide some assistance in getting the payload into space (depending upon the desired launch direction and the location of the site). However, this velocity must also be accounted for when designing a satellite with a particular ground target.

Since the earth rotates at approximately 24 hrs/day, and its equatorial radius is roughly 6378 km, then its equatorial velocity is

$$V_{equator} = \omega_{earth} R_{earth} \approx 465 \frac{\text{m}}{\text{sec}}. \qquad (7.2\text{-}15a)$$

Therefore, the easterly travel of any point on the earth is given by

$$V_{site} = 465 \cos \lambda_{site} \left[\frac{\text{m}}{\text{sec}} \right] (\text{east}). \qquad (7.2\text{-}15b)$$

The resulting groundtrack pattern appears as a *figure-8*, as shown in Figure 7.2-14.

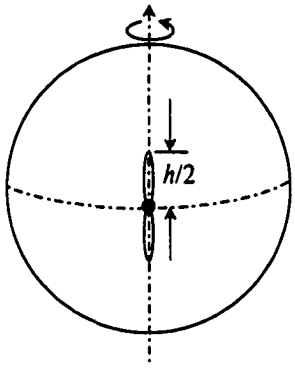

Figure 7.2-14. Ground Track of GEO Satellite Due to Orbit Inclination.

The value of the longitudinal oscillation is given by

$$h_{inc} = \pm i, \qquad (7.2\text{-}16)$$

$$\omega_{inc} = \tan^{-1}\left[\frac{1}{2} \left(\sqrt{\sec i} - \sqrt{\cos i} \right) \right]. \qquad (7.2\text{-}17)$$

The impact of this effect again depends upon the magnitude of the oscillation versus the beamwidth of signals in question. Typical values of orbit inclination for the same geosynchronous satellites are shown in Table 7.2-1. The impact of inclination over this range of values is plotted in Figure 7.2-15.

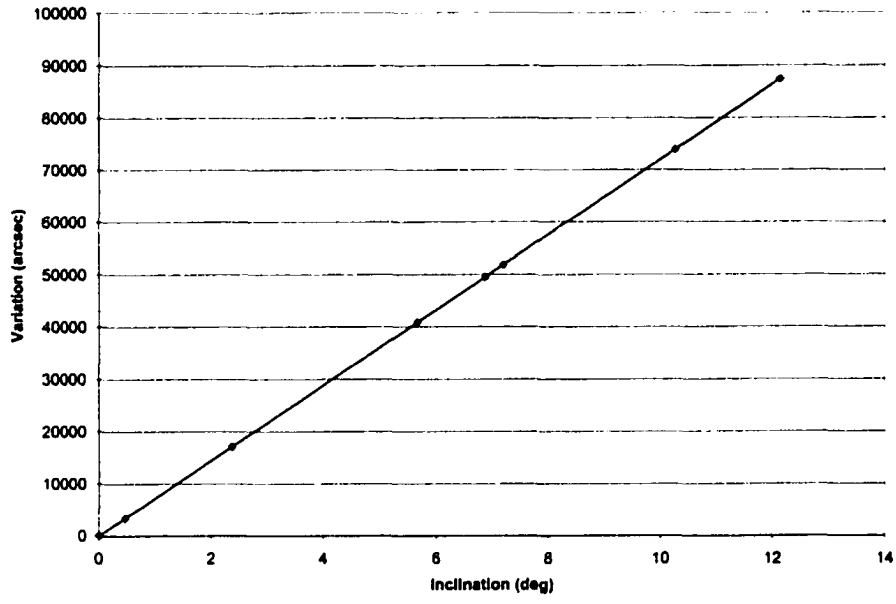

(a) latitudinal variation

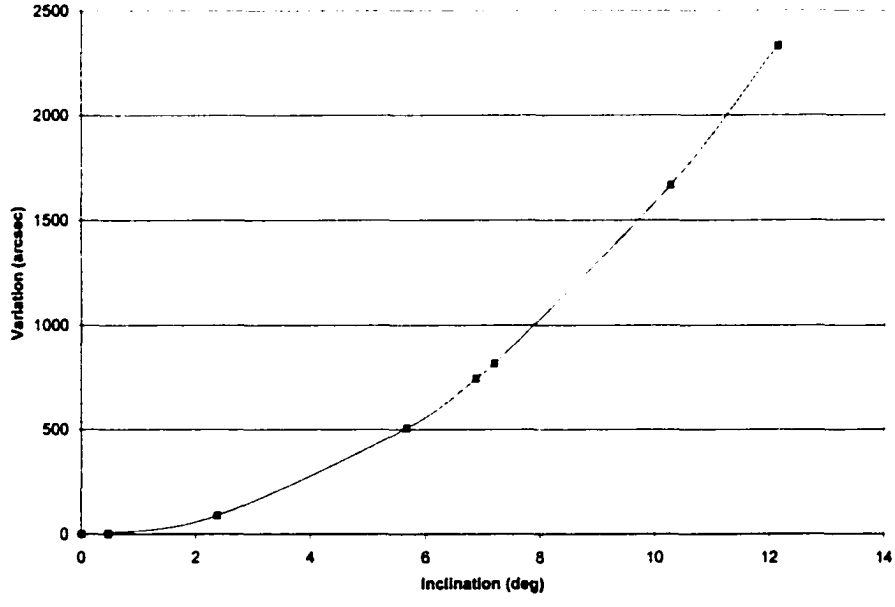

(b) longitudinal variation

Figure 7.2-15. Inclination Effects on Satellite Ground Track.

Analysis of the SPS requirements is the same as for the eccentricity effects. The parameters of concern are the maximum steering angle, slew rate, and spreading effects of the beam at the receiving site.

To compensate for orbit inclination, the beam must be capable of steering an equal amount

$$\alpha_{inclination\ latitude} = \pm\frac{h}{2} = \pm i\,, \tag{7.2-18}$$

$$\alpha_{inclination\ longitude} = \pm\frac{\omega_{inc}}{2} = \pm\frac{1}{2}\tan^{-1}\left[\frac{1}{2}\left(\sqrt{\sec i} - \sqrt{\cos i}\right)\right]. \tag{7.2-19}$$

The inclination effects on beamsteering are significant. Examining the figure above shows that the latitudinal effects of the orbit inclination dominate. Since the latitudinal displacement equals the orbit inclination, the beam is completely displaced by an inclination greater than i_{IBW} = 57.67 arcsec. In comparison, the same longitudinal offset would require an inclination of 1.915°, and therefore is not considered a limiting factor. This is supported by an examination of the two charts in Figure 7.2-16.

The required slew rate is determined by resolving the differential velocities into components. Since the latitudinal value of angular displacement dominates, the overall slew rate requirement is approximated by this velocity component. This is given by

$$\dot{\alpha}_{inclination} \approx R_{satellite}\frac{i}{12\ \text{hrs}}. \tag{7.2-20}$$

Slew rate requirements corresponding to the nominal GEO values given earlier are shown in Figure 7.2-17.

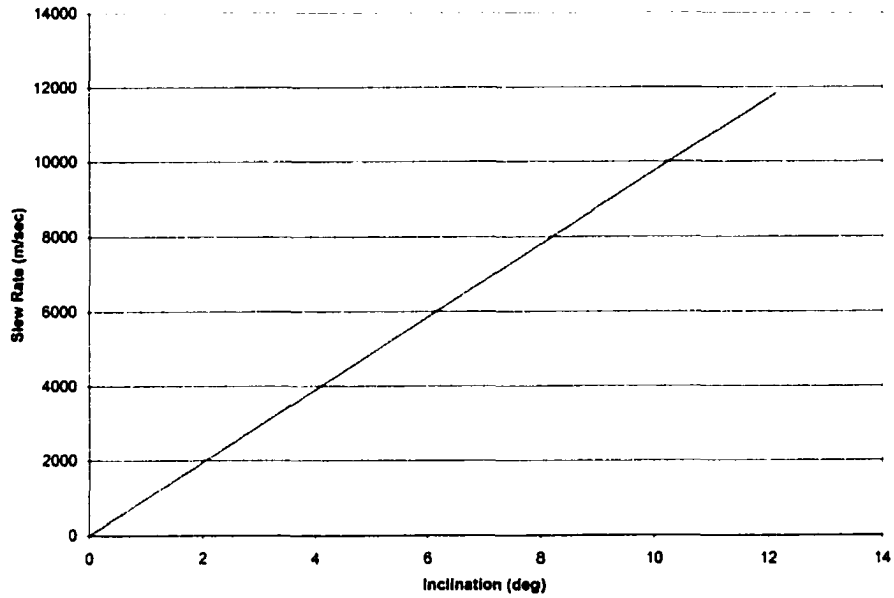

Figure 7.2-16. SPS Maximum Slew Rate versus Inclination for Nominal Orbits.

The beamwidth projected on the ground varies with inclination, due to the lateral separation between the satellite and ground site. The offset affects both the width of the beam, as well as the angle of incidence on the site. This is essentially the same problem encountered in Section 7.2-1, except here the satellite is offset vice the ground site. Therefore, the results in Figure 7.2-6 apply to this situation as well.

Combined Effects of Orbit Eccentricity and Inclination. The combined effects of multiple orbit anomalies quickly complicates SPS performance requirements. Providing a detailed analysis of the orbit effects would require introduction of other factors, such as orbit perturbations. Modeling these effects would be best accomplished with an appropriate astrodynamics utility, such as Satellite Toolkit. However, a quick look at the combined effects of eccentricity and inclination is beneficial in understanding some of these. The actual groundtrack for the satellite is a combination of both the orbit inclination and eccentricity. The resulting pattern may either trace out a racetrack or figure-8, depending upon the dominant factor involved, as shown below.

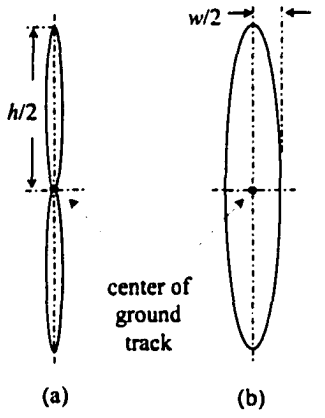

Figure 7.2-17. Daily Periodic Motion of Geosynchronous Satellite about Ground Point. Groundtrack dominated by (a) inclination; (b) by eccentricity.

These effects must be considered when determining the necessary beam steering capability for the SPS. For instance, if a US satellite were launched from Kennedy Space Center (28.5° N), then the minimum inclination directly achievable for the orbit would also be 28.5°. If the orbit were not adjusted, the ground track of the GEO satellite would appear as shown in Figure 7.2-18.

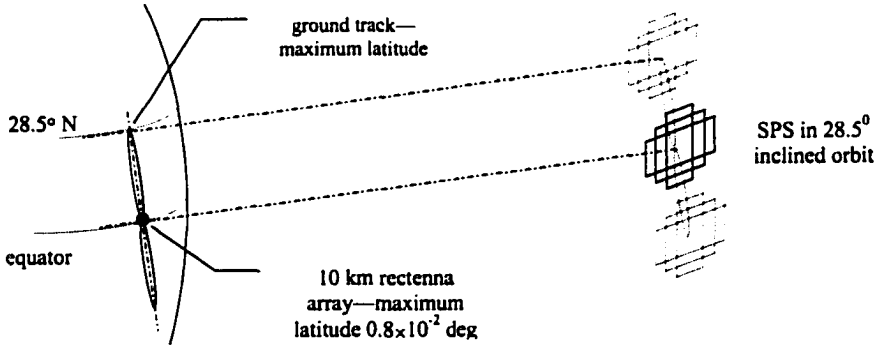

Figure 7.2-18. Effect of Orbit Inclination on Beam Steering for GEO SPS.

This would require a rigorous beam steering capability, with the beam direction varying by 57° over a 24-hour period. It would also require an elongated footprint of the beam in the N/S direction. Alternately, the elongated beamwidth may be counterbalanced by real-

time adjustment of the latitudinal beamwidth. This situation may be rectified, either by an orbital plane change (expensive), or by launching directly from an equatorial site.

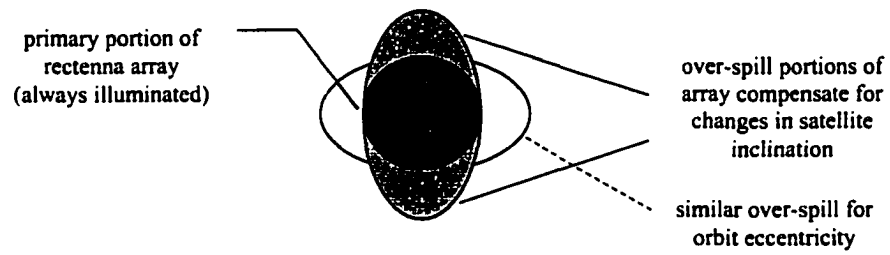

Figure 7.2-19. Effects of Satellite Inclination on Rectenna Array Shape. Assumes beam is dynamically directed to array center.

The tight beamwidth requirements of the SPS dictate stringent control of the power beam to exactly fill the rectenna array. This control will necessarily possess components of orbit station keeping, as well as a dynamic beam steering capability. To minimize these effects, and thereby simplify the SPS design and maximize its efficiency, the SPS orbit should be selected as nearly geostationary as possible.

Satellites in non-geostationary orbits will require additional beam forming/steering capability to function efficiently and safely. These orbits should be selected as the best compromise satisfying mission requirements, considering satellite loiter time and ΔV requirements to achieve and maintain the orbit.

7.3 Beam Pattern Calculations for GEO SPS

This section develops the size and shape of the SPS array satisfying the orbital requirements outlined in Section 7.2.

The beamwidth required to exactly illuminate a receiving array of 10 km diameter from a geostationary orbit was found to be $BW_{required}$ = 57.67 arcsec. It is desired to find the

minimum number of ESPAM units required to achieve this beamwidth. This will yield the minimum size for a satellite meeting the beam steering requirements. We will initially assume a simple rectangular pattern, as shown in Figure 6.3-1.

Calculating the expected number of ESPAM units n to achieve the required beamwidth,

$$BW_{n\,SWA} \approx \frac{2BW_{SWA}}{3n}. \tag{7.3-1}$$

Therefore, the SPS will require roughly $n \approx 533$ ESPAM units to meet the beamwidth. This estimate was verified by examining the resultant beamwidth of the MATLAB model in the neighborhood. The same analysis may be performed for the ESPAM units aligned vertically. Since the physical construction of the SWA antennas differs in the vertical direction, the minimum spacing is increased to ~7.22λ (Figure 6.3-2). The resulting data for both axes is shown in Table 7.3-1.

Table 7.3-1. Beamwidth for SPS Elements.

Horizontal elements $S_{h\lambda} = 6.17\lambda$	Beamwidth (arcsec)
500	59.40
510	58.68
520	57.24
530	56.52

Vertical elements $S_{v\lambda} = 7.22\lambda$	Beamwidth (arcsec)
430	59.40
440	57.96
450	56.52
460	55.08

If this were taken to be the minimum number of ESPAM units necessary to achieve the desired beamwidth, then the dimensions of the SPS could be reduced to:

$$D_h = (530 \text{ units})\left(\frac{0.7565 \text{ m}}{\text{unit}}\right) \approx 400 \text{ m}, \tag{7.3-2a}$$

$$D_v = (450 \text{ units})\left(\frac{0.8841 \text{ m}}{\text{unit}}\right) \approx 400 \text{ m}. \tag{7.3-2b}$$

This is less than the proposed value for the SPS. For a simple rectangular array, this would correspond to a reduction in area/weight of

$$\Delta A(\%) = \frac{A_{original} - A_{revised}}{A_{original}} \times 100\% = 84\%. \tag{7.3-3}$$

This is a substantial reduction of size in the transmitting array. The number of elements will be finalized later in the design, according to the desired safety factor for the beam width and the power level for each magnetron. However, these preliminary results show that the beamwidth will not be the limiting case for the SPS design.

The resultant broadside beam patterns for the array are shown in Figure 7.3-1. The horizontal array yields a desirable beam pattern with very low sidelobes, about 10% the level of the main lobe (or -20 dB down). The vertical pattern produces a somewhat less pleasing pattern, with sidelobes on the order of 25% (-12 dB).

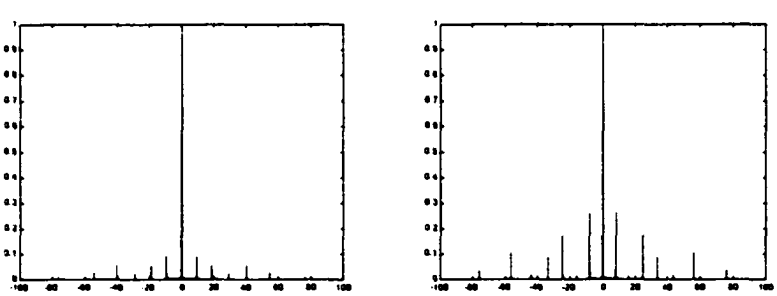

(a) horizontal pattern, $S_\lambda = 6.17\lambda$ (b) vertical pattern, $S_\lambda = 7.22\lambda$

Figure 7.3-1. Beam Patterns for 530 x 450 Element Array of SWA Antennas.

It is important to note that the above calculations are for ideal conditions and include no margin for error. Therefore, they represent an optimized size of the SPS transmitting array. Sources of error include: spacing variances, phase variances, and amplitude variances. These will be briefly examined in the following sections.

7.3.1 Effect of Spacing Variances

Variable element spacing may be forced upon the SPS transmitting array in some situations. This may be required for a number of practical reasons, including structural considerations (rigidity, thermal expansion), placement of other satellite components (cooling, communications), or even fabrication techniques. The end result is a break in the pattern of radiating slot elements. For this condition, the beamwidth is given as

$$BW_{3dB} = \frac{1}{n}\left(\frac{1}{S_\lambda + d_\lambda}\right) \approx \frac{1}{nS_\lambda} \tag{7.3-4}$$

where

d_λ = dimension of antenna face $[\lambda]$
S_λ = center - to - center distance between elements $[\lambda]$.

This relationship may be approximated as linear for small changes in the product $n(S_\lambda+d_\lambda)$. Figure 7.3-2 shows the effect of relatively small spacing variances on the minimum sized SPS (530 x 450 elements). In the range of interest of 57.67 arcseconds, beamwidth is a linear function of spacing. Spacing changes of 0.1λ produce beamwidth changes of roughly 1 arcsec. For larger changes in element spacing, the beamwidth varies logarithmically, as shown in Figure 6.3-13.

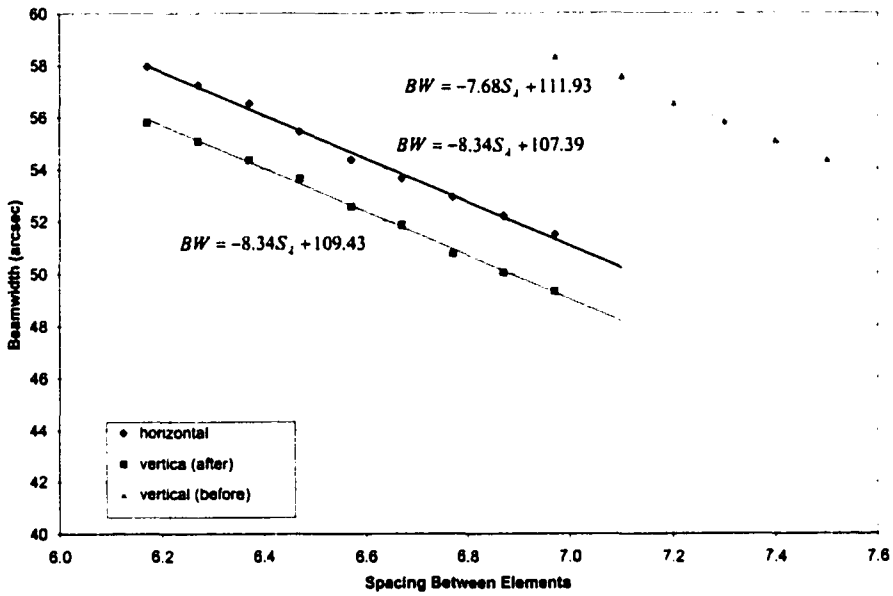

Figure 7.3-2. Effect of Element Spacing on Beamwidth for Minimum SPS Antenna Array. Broadside condition, 530 elements horizontal, old vertical: 450 elements, new vertical: 510 elements.

Two sets of data are provided for the vertical sizing of the SPS – one assuming that the vertical feeds on the SWA may be altered to diminish the size, and one maintaining the existing configuration (Figure 6.3-2). The curve shown for the existing vertical dimension is offset from the others due to the length of the vertical waveguide stubs.

7.3.2 Effect of Phase Variances

The cumulative effects of the sidelobe behavior for the minimum sized SPS are shown in Figure 7.3-3. These plots demonstrate how the sidelobes increase for the SPS beam pattern as it is electronically steered.

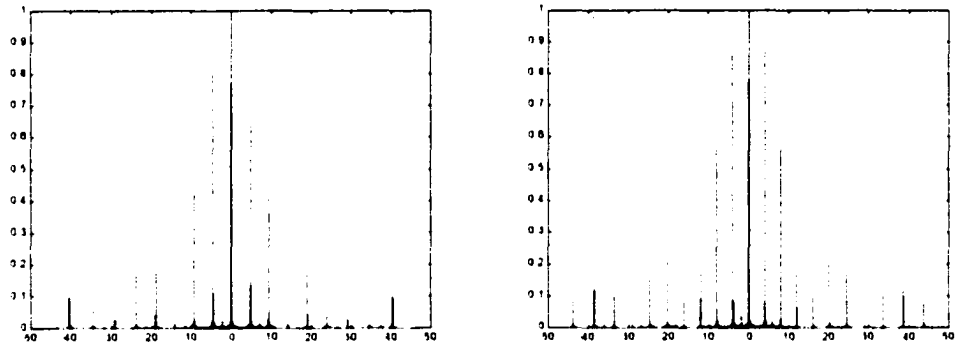

(a) horizontal elements, $S_\lambda = 6.17\lambda$ (b) vertical elements, $S_\lambda = 7.22\lambda$

Figure 7.3-3. Patterns for 530 x 450 Elements SWA Antennas. Blue lines depict no phase shift; orange: 90° shift; red: 180° shift.

A comparison of the patterns reveals that the closer horizontal spacing performs better. The sidelobes are relatively high for either configuration, but are about 15% less for the tighter spacing. The horizontal pattern develops maximum sidelobes of ~40% at broadside, versus ~55% for the vertical pattern. The same relative behavior is noted for operation at $\delta = 90°$. The increased spacing has a mixed effect on the array performance at $\delta = 180°$ -- the maximum steering angle is decreased, but the lobe level is higher.

Therefore, the beam pattern may be generally improved by reducing the vertical element spacing. This requires altering the existing SWA to eliminate or offset the extended sections of vertical waveguide protruding from the antennas (Figure 6.3-2). The minimum spacing that may be achieved is then decreased to

$$d_{\lambda v} = (78.0\,\text{cm})\left(\frac{\lambda}{12.24\,\text{cm}}\right) = 6.37\lambda.$$

Allowing some spacing for mounting, the vertical spacing is set to the same value as for the horizontal ($S_{v\lambda} = S_{h\lambda} = 6.4\lambda$). This should yield a resultant vertical pattern close to that obtained for the horizontal. Plots using the new spacing are given in Figure 7.3-4.

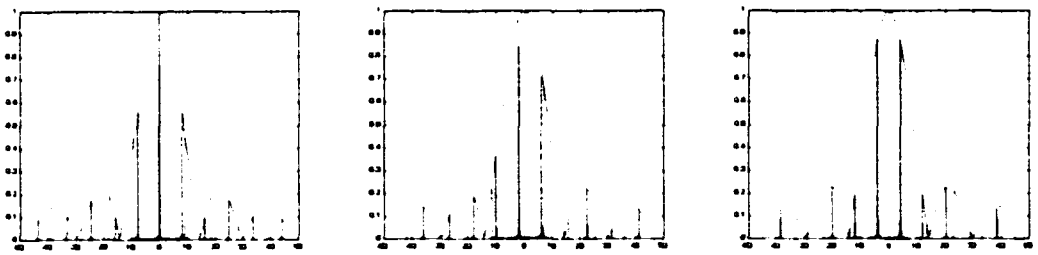

(a) broadside (b) 90° phase shift (c) 180° phase shift

Figure 7.3-4. Comparison of Element Spacing for 500 SWA Elements. Orange lines depict 6.17λ; purple: 6.4λ; green: envelope for single SWA.

With the exception of the $\delta = 180°$ case, the sidelobes were suppressed. This is caused by adjusting the array factor to sample the SWA pattern at more efficient locations (Section 6.3.2). It is noted that the resultant 'sampled' pattern for either value of element separation does not yield the magnitude that might be expected, for other than the broadside condition. This is caused by a destructive cancellation of the pattern factor when a phase shift is added, more noticeable for large n, as shown in Figure 7.3-5.

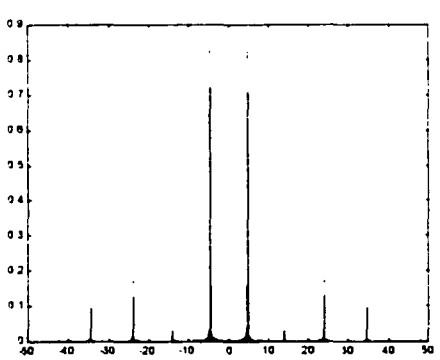

Figure 7.3-5. Pattern Factor for Linear Array of Point Sources, $S = 4.1\lambda$, $\delta = 180°$. Purple lines depict $n = 390$; orange: $n = 780$; black: $n = 1560$ elements.

The pattern factor is also affected by element spacing for the phase-shifted array. Overlaying the pattern factors on the beam pattern for the single SWA antenna shows the

sampling levels possible. Assuming the SPS will operate at or near the broadside condition, the overall beam pattern has been significantly improved. It does require that the additional 80 elements be added to maintain the desired beamwidth focus. For the reminder of the discussion, the SPS antenna structure will therefore be assumed to be a 530 x 530 element array.

The area of the new rectangular array is then given by

$$A_{array} = D_h \cdot D_v , \tag{7.3-2}$$

where

$$D_v = (530 \text{ units})\left(\frac{0.78 \text{ m}}{\text{unit}}\right) = 413.4 \text{ m} . \tag{7.3-3}$$

The new area for the array is relatively unchanged at $A_{array} = 1.658 \cdot 10^5$ m^2.

The maximum phase shift needed for this structure will now be calculated. From Section 7.2.1, the maximum angle required for a geostationary satellite to subtend any point on the earth was given as $\rho = 8.7°$. This corresponded to a maximum site latitude of $\lambda_{max} = \pm 81.3°$. However, fielding the 10 km diameter receiving array at this location would not be practical because of the angle of incidence of the satellite beam with the earth. This would require the receiving array be essentially mounted vertically with respect to the ground to intercept adequate microwave energy. For practicality, the site locations will therefore be limited to within $\pm 40^0$ of nadir.

This then reduces the beam steering requirements to $\eta \approx 6.3°$ (Equation 7.2-3). For the 530 x 530 element array, a maximum beam steering angle $\eta_{max} = 4.0°$ for either axis is possible at a phase shift of $\delta = 180°$. The overall beam patterns for the broadside and $\delta = 180°$ conditions are shown in Figure 7.3-7. An expanded view of the 2-element case is provided in Figure 6.4-6.

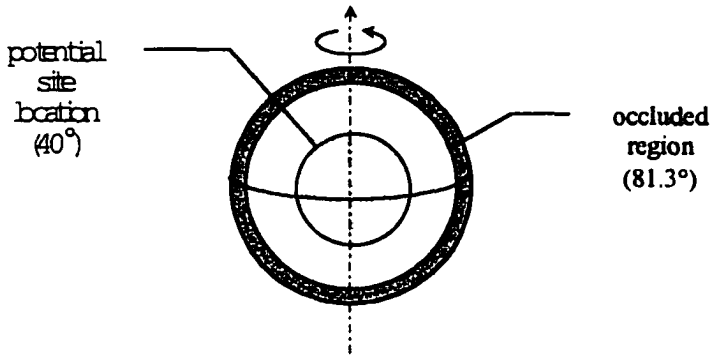

Figure 7.3-6. Potential Receiving Site Locations for a Geostationary SPS.

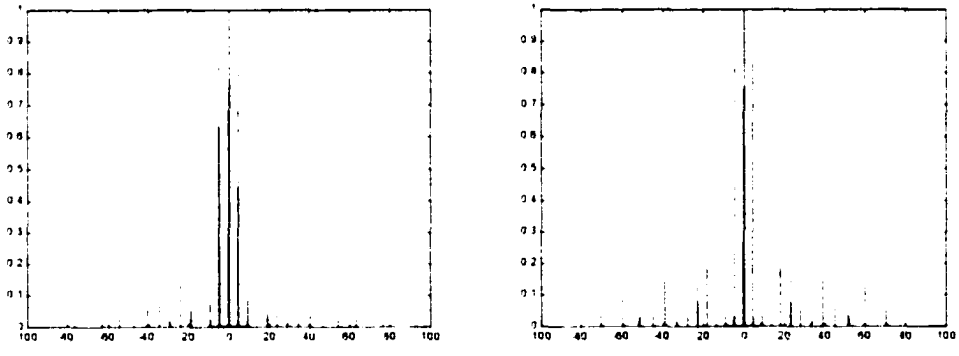

(a) horizontal (b) vertical

Figure 7.3-7. Maximum Beam Steering for 780-Element Array of SWA Antennas, $S_h = S_v = 6.4\lambda$. Broadside patterns shown in blue, $\delta = 180°$ in red.

Unfortunately, the maximum steering requirement of the SPS (6.3°) exceeds its electronic steering capability (4°). In addition, steering the beam electronically causes significant sidelobes. Therefore, the SPS should be steered mechanically when possible, with small dynamic corrections made with the electronic steering ability. A more robust electronic steering capability will require some means to null the present sidelobes. These may also be minimized by optimizing the beam shape, either by using an amplitude distribution for the elements (as in a binomial distribution) or by reducing the size of the SWA elements.

7.3.3 Effect of Amplitude Variances

The existing beam model is currently limited, providing the ability to account only for failed elements. The emphasis of a rigorous study should be to predict the effects of element failures on the resultant beam. Determining the minimum acceptable beamwidth and sidelobe levels is a first step essential in this analysis. The minimum array size may then be selected by assuming an element failure rate and probability for failure in a given array location. The subject of sparse arrays would require a detailed study in itself. However some very rough estimates for beam degradation are provided here.

A related factor which must be considered is the diagonal beamwidth of the array. It is desirable to minimize the elements needed to just barely fill the 10 km receiving array. The diagonal beam pattern for the SPS array depends upon the physical shape selected. Assuming a square 530 x 530 array, then the number of elements along the diagonal and their spacing is

$$n_{diagonal} = \frac{n_{lateral}}{\sqrt{2}} \approx 375, \tag{7.3-4}$$

$$S_{diagonal} = \sqrt{2} \cdot S_{lateral} \approx 9.05\lambda. \tag{7.3-5}$$

Therefore, the beamwidth of the diagonal is given by

$$BW_{diagonal} \approx BW_{lateral} \cdot \frac{n_{diagonal}}{n_{lateral}} \cdot \frac{S_{diagonal}}{S_{lateral}} = BW_{lateral}. \tag{7.3-6}$$

The patterns for the lateral and diagonal directions are compared in Figure 7.3-8. The two patterns are defined by the intersection of the array factors and the single SWA antenna pattern. The array factor for the diagonal element spacing causes substantially

higher sidelobes than for the lateral beam. Both have a magnitude of unity normal to the antenna boresight.

Clipping the corners of the array reduces the number of diagonal elements to 375. Since the number of elements is sufficiently large, there is no substantial difference in the normalized beam patterns between the clipped and full diagonal arrays. The resulting (non-normalized) beam plots are shown in Figure 7.3-9.

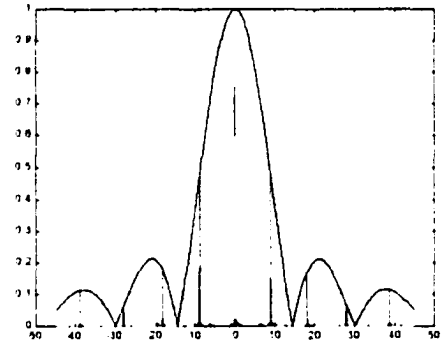

Figure 7.3-8. Comparison of Diagonal and Lateral Beam Patterns at Broadside. Purple lines represent lateral pattern; magenta: diagonal pattern. The main lobe of the lateral pattern is obscured by that of the diagonal.

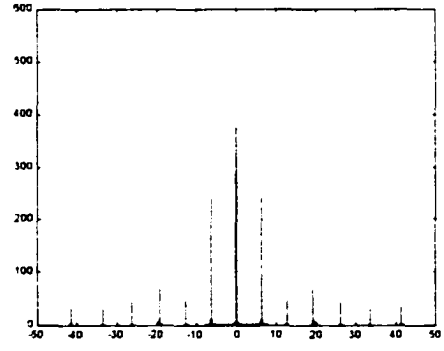

Figure 7.3-9. Comparison of Diagonal Beam Patterns for Full and Clipped Configurations. Orange lines depict full diagonal; purple: clipped diagonal.

From the perspective of reducing the total sidelobe level, clipping the corners of the array provides a better beam pattern, since the magnitude is less. A conceptual sketch of the array is shown in Figure 7.3-10.

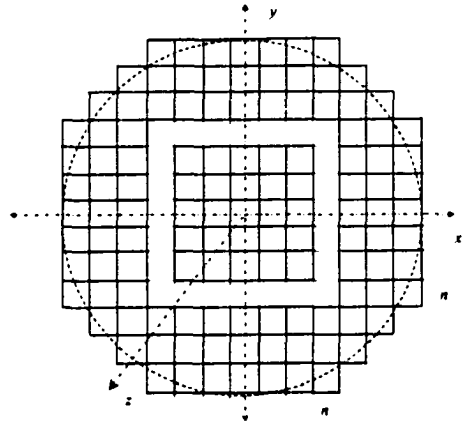

Figure 7.3-10. Circular Array Composed of Rectangular SWA Antennas.

This would permit an additional reduction in size for the antenna. The approximate size is given by the equation for the area of an ellipse,

$$A = \pi ab \tag{7.3-7}$$

where

a = semi - major axis
b = semi - minor axis.

When clipping the corners of a square array, this may be calculated by

$$k = n^2 \frac{\pi}{4} \tag{7.3-8}$$

where

n^2 = total number of elements in the rectangular (square) array

k = number of elements in circular array

$\frac{\pi}{4}$ = array clipping factor.

Therefore, the area of the array is calculated to be $A_{array} = 1.302 \cdot 10^5$ m^2. This provides a savings over the rectangular array of

$$\Delta A(\%) = \frac{A_{\text{rectangular}} - A_{\text{clipped}}}{A_{\text{rectangular}}} \times 100\% = 21.4\%.$$

With the above qualifications, the clipped array of SWA antennas could provide an adequate transmitting platform for the SPS mission outlined. However, some method must be identified to suppress the sidelobes predicted to occur across the diagonal. In addition, the array must be operated in a near broadside condition to avoid significant signal loss to sidelobes.

8.0 Conclusions

Section 8.1 summarizes the key results of the dissertation. Suggestions for follow-on research are discussed in Section 8.2.

8.1 Summary of Results

8.1.1 MDA

The major contribution from this effort was the characterization of the Magnetron Directional Amplifier (MDA). This study provided the first verification of Brown's results, and went well past that in many regards. To appreciate the key aspects of the research presented here, it is necessary to review Brown's research.

Brown defined the MDA classes and briefly quantified the performance of each. His work provided an initial baseline against which future investigations could be measured. However, the main emphasis of his work was on furthering the field of wireless power transmission (WPT) by demonstrating the effectiveness of the MDA. Brown's focus was on providing a capability that would satisfy a need — in this case, the need for a cleaner and cheaper energy source. To that end, he concentrated on characterizing the performance of one hardware configuration taken to its logical conclusion. Brown was intimately aware of the requirements of WPT applications, as he had pioneered many of these initiatives. His MDA configuration satisfied these requirements and served as a proof of concept for WPT. His continuing interests then focused on convincing others of the practicality and necessity of such a system.

The research conducted for the UAF characterization effort differed somewhat in emphasis. Since the groundwork had already been laid showing the MDA to be possible, the focus shifted to quantifying how well the MDA might be made to operate. To realize

the maximum performance potential for the MDA, it would be necessary to dissect its performance. An optimal capability would have to be the result of maximizing each contributing factor. The tactic taken was to trace Brown's initial steps. Starting with the basic components needed to operate the magnetron, each incremental capability was examined in detail. This provided a measure of the MDA's performance limitations and the relative effects of each factor. The discoveries of this investigation, its shortcomings, and recommended follow-on efforts are summarized throughout this chapter.

8.1.1.1 Magnetron Performance

The first objective of the study was to configure a magnetron operating into a dummy load and observe its behavior. The significant results obtained from examining the magnetron operation include: (1) measurement of the magnetron startup and cool-down times, (2) correlation of the MDA output power and operating frequency with magnetron temperature, and (3) characterization of moding behavior for several magnetrons.

The MDA characterization effort began by correlating the output power to the operating temperature of magnetron and load. This demonstrated the effects of temperature on the frequency and power output of the MDA. Maintaining a constant power level and frequency for each radiating element is essential to the operation of a phased array. Therefore, it was critical to understand how these parameters varied during the startup sequence of the MDA. This data would be needed to determine the warmup time required by an array prior to phase locking. It would also be used to analyze the effects of a single element dropout.

Of particular interest was the tendency some magnetrons displayed during the warmup cycle to mode. Moding describes the magnetron's sometimes abrupt change of output power and operating frequency in response to changes in its environment (input power or load). These effects are documented in Section 5.1 and Appendix A.4.6. This behavior

could preclude proper steering of a phased array particularly during the startup period. To determine the likelihood of this would require an analysis of the possible beam patterns formed during startup.

8.1.1.2 Class I MDA

The significant results obtained from examining the Class I MDA include: (1) locking bandwidth versus the injected power level, (2) verification of David's equation for a frequency-locked amplifier, and (3) effects of the injected frequency on output power.

The locking bandwidth of the MDA was shown to be a function of the injected signal power for a given operating power level. Below the threshold, the injected signal is overcome by reflected power within the waveguide. This sets a limit to the maximum effective gain of the MDA that may be obtained through the use of signal injection. The locking limit was shown to follow David's equation governing the operation of a frequency-locked amplifier. This provides an experimental means to determine the external quality factor Q_E of the MDA.

The output power of the MDA was seen to vary with the injected signal frequency. The output power fluctuated by ~5% across the operating range. This result was not previously identified and would be important to the overall efficiency of a WPT system. The power variance is explained by the change in load impedance caused when the signal pulls the MDA through its sink region. The effects of the injected signal are similar to that caused by a tuning slug, as shown in Figure 5.2-5. This affirms the nature of the two tuning methods to be the same, thereby providing an explanation of Brown's tuning slug in terms of David's equation for the injected signal. This is a useful analogy that helps explain the frequency stability of the non-injected Class III MDA, such as was used in the UAF beam steering demonstration (Section 6.4).

8.1.1.3 Class II MDA

The MDA characterization effort examined the effects of power control alone, and in conjunction with the injected signal. The significant results obtained from examining the Class II MDA include: (1) frequency pushing characteristics of the MDA, (2) linearity of the MDA as DC → RF converter, (3) efficiency of the MDA throughout operating range, (4) dependency upon power supplies, (5) correlation of output power and temperature, (6) phase shift ranges attainable, and (7) locking bandwidth versus system gain.

The DC input power provided a straightforward means to control the MDA output power. This would be set in accordance with the requirements of the WPT application, with an emphasis on operating efficiency. The MDA proved to be linear in its conversion of DC to RF power, making it an attractive choice as a high-power RF generator. The frequency response of various magnetrons to power control was not as well-behaved. These differed substantially, but depending upon the other performance requirements, might be overcome by use of an appropriately sized tuning slug (Class III MDA).

While power conversion was almost linear, some variances were noted. These were traced to the *V-I* characteristic curves of the power supplies. As happened more than once during this effort, detailed experimental observations were eventually borne out by supporting theory. The power variances are explained by the impedance characteristics of the power supply and the load. The magnetron operating point is selected by the intersection of the electronic admittance and the load admittance curves, as shown in Figure 5.4-3. Irregularities in the *V-I* curves can cause moding to occur. The shape of these admittance curves may be used to explain a number of other behaviors noted which are addressed later in the discussion.

The ability to vary the relative power levels of the injected signal and magnetron output provided a valuable analysis tool into the behavior of the MDA. The locking bandwidth

of the injected signal was found to be a function of the gain of the MDA (ratio of output to injected powers). This behavior provided the key to understanding that reflected power internal to the waveguide interfered with the signal lock. Recognition of this fact led to hardware modifications designed to improve the impedance matching between waveguide sections, and from the injected signal probe into the guide. This resulted in improved locking bandwidths. Application of these principles made it possible to successfully frequency-lock the two ESPAM units in the UAF beam steering demonstration (Sections 6.4 and 8.1.2).

8.1.1.4 Class III OL MDA

Investigation of the Class III OL MDA provided much information regarding its inner workings. The information learned from this effort defines the performance envelope of the MDA. The significant results obtained from examining the Class III MDA include: (1) effects of the tuning slug on frequency and power, (2) quantified response for different size slugs, for efficiency, frequency range, stability, and stress on magnetron, (3) prediction of response verified, and (4) comparison of relative effects of slug, injected signal, and power control on MDA.

The primary investigation of the Class III MDA involved the effects of the tuning slug on output power and operating frequency. The slugs provided an exceptionally large range of MDA responses. The MDA efficiency was varied up to 74.5% from its no-slug efficiency of 50.8%. The operating frequency was tuned over a range of 42.3 MHz at 2.442 GHz, for a fractional bandwidth of 1.7%. The ability of the MDA to overcome a large frequency offset was confirmed in the UAF beam steering demonstration, where one ESPAM was shifted by 14 MHz to provide frequency locking between the units.

The response of the MDA to the different sized tuning slugs was shown to be predictable. Both the frequency and output power were directly proportional to the size of the slugs,

as shown in Figures 5.4-8 and 5.4-9. The slugs formed families of lines with constant diameters and lengths. This made it possible to predict the MDA response for a given slug size. In fact, this was the method used to select the size of slugs 13 – 16 (defined in Table 3.4-1). These curves provide the WPT engineer a means to select the appropriate size tuning slug for a given application.

The tuning slug has two primary functions: (1) to pull the operating frequency of the magnetron to a desired value, and (2) to provide an improved impedance match, thereby maximizing power transmitted and frequency locking bandwidth. Slug choice is made by first examining the characteristics of the constituent loads and magnetrons. Off-the-shelf magnetrons will typically display similar performance characteristics; however, these can vary with time and usage. Loads may also vary, causing different operating frequencies.

Selection of an appropriate sized tuning slug is essentially a tradeoff between system sensitivity and stability. The Rieke diagram for the MDA, along with the Smith chart impedance curves provides a useful means to estimate system performance and speed design (Figure A.4.1-7). Large slugs pass nearest the sink, producing great changes in operating frequency and output power for very little change in position. With proper control, the closed-loop system (Class III CL or Class IV MDA) may provide stable operation in this desirable region.

During the characterization effort, it was found that operation of the MDA deep within the sink region requires careful control of the slug position. The large slugs may damage the magnetron in some situations. This can lead to catastrophic failure of the magnetron and/or DC power supply, or to a more gradual deformation of the magnetron RF probe over time. An explanation of the general behavior causing this is offered in Appendices A.4.5 and A.4.6.

The Class III MDA provided a means to compare the relative tuning effects of the tuning slug, input power control, and the injected signal. In the case of the Class III OL MDA, a combination of the first two is generally required to achieve an operating point within a given locus. Fine tuning of the MDA is accomplished through the injected reference signal. For the Class IV MDA, feedback paths provide the means to stabilize the input power and slug position at optimum points.

In addition to the performance measurements made on the Class III MDA, a number of behaviors were observed that provide valuable insight into the magnetron's characteristics: (1) the resonant peak efficiency behavior observed for some load impedances, (2) the mismatched line behavior describing the MDA frequency response, (3) the long line effects upon the MDA behavior in sink regions, (4) several types of moding, (5) and temperature dependencies associated with the waveguide load.

The behavior of the MDA with the air-cooled load provided a resonant peak power condition when using larger tuning slugs. The response of the MDA is shown in Figures 5.4-4 and 5.4-5. This phenomenon was investigated thoroughly, spanning months of effort and launching a number of other studies (Appendices A.4.1 – A.4.8). The resonant behavior was real and could be verified by the load temperature (Section 5.4.2.1). This behavior can be explained by the using the tuning slug to drive the magnetron deep within its sink region. Brown's MDA configuration would not have noticed this behavior because of its larger waveguide size with respect to the tuning slug used. The data presented in Appendix A.4.8 describes how the location of the shorting plate affects the MDA operation. Figure A.4.8-16 shows the formation of the resonant behavior as the shorting plate drives the magnetron further into its sink region. The behavior of certain resonant load conditions is validated by theory [15].

A number of other phenomena were observed during the MDA characterization which were previously unknown or unexplained. One of these was moding of the magnetron,

where the MDA output jumps instantaneously between different power and frequency points. The magnetron operating point is defined by the intersection of the electronic admittance and load admittance curves. As either of these controls is varied, the curves change shape, forcing the operating point to shift. Moding occurs when the intersection of the curves is broken and the magnetron must reestablish oscillation at a new operating point. This phenomenon explains a number of quirks observed in the MDA behavior, such as: (1) frequency discontinuities encountered in the sink region for large tuning slugs, (2) resonant efficiency behavior discussed above, (3) day-to-day differences in power data of 2 – 3% which were previously attributed to instrumentation errors, and (4) instability of operating points with changing component temperature. Each of these behaviors is important in optimizing the performance of the MDA. A detailed discussion of this subject is presented in Appendix A.4.6.

Another phenomenon investigated in the UAF MDA was that of long-line effects. This is manifested by an increased slope of the frequency versus tuning slug position response in the sink regions when the slug is further from the magnetron (Section 5.2.1). This behavior is more apparent with larger tuning slugs, where the slope may become a discontinuity (moding) at some multiple of the guide half-wavelength. This can cause the MDA to be inoperable for some configurations. Long-line effects are explained by the dispersive transmission quality of the guide. Higher frequencies have a shorter guide wavelength, and therefore change the slope of the frequency curve between successive transition regions (sink). The location of this discontinuity can vary, depending upon the direction of approach. This condition is known as hysteresis. This behavior was observed in the UAF MDA, and later supported by theory [15].

In general, the response of the MDA to the presence of the tuning slug may be described by the magnetron's operation into a mismatched transmission line. The amount of frequency pulling is directly related to the amount of susceptance provided by the tuning

slug, which is related to its size. The impedance (or admittance) of the load defines the MDA performance.

A MATLAB plotting routine for the Rieke diagram was developed as a graphical analysis tool for this characterization effort. It plots the load impedance associated with contours of constant power and frequency for the magnetron. Some examples of this are shown in Appendix A.4.1. The Rieke diagram is helpful because it shows the effects of load impedance changes in terms of electrical distance from the magnetron. The shape of the contours and location of impedance data points identifies the location of the sink region. This helps predict the effect of an impedance change on the MDA based upon the location of the tuning slug.

During the characterization effort, a number of partial models describing the performance of the Class III OL MDA were developed. This includes the circuit model shown in Section 4.2. This model was pieced together in the initial stages of the effort using various sources and was later validated by the other theoretical models [15]. Another useful model describing the interaction of the injected reference signal in terms of impedance was provided in David's work [11]. This was adapted to explain the tuning provided by Brown's tuning slug arrangement, and for a number of other signals incident on the magnetron probe. Yet another performance model was developed showing the interrelations between impedance, operating power, and component temperature when selecting an operating point. This is shown in Figure 5.3-7.

It must be emphasized that these tools are not fully developed, in that a full analytic model of the MDA does not yet exist. However, the conceptual models are useful in explaining the MDA behavior.

For example, the load admittance curves and impedance data used for the Rieke diagram are limited by the method used to measure the data (Appendix A.4.1). The exact value of

the load impedance, and therefore the shape of the Rieke curves, cannot be accurately depicted without a measurement probe of the same shape as the magnetron. However, the trend data provided in the plots is still valuable in understanding the effects of the tuning slugs upon the MDA.

The models obtained from this effort are incomplete. Many of the parameters needed to complete the analytic model may only be estimated through detailed knowledge of the construction of the specific magnetron under test. In addition, performance measurements of 'identical' magnetrons may yield substantially different results, where even slight changes in the load may affect the MDA performance substantially when operating near the sink region. Even slight differences in the magnetron construction may also cause the same large performance variations. These differences can ultimately be accounted for with a model of high enough resolution. However, the conceptual models developed so far are still of use in explaining the MDA performance.

8.1.1.5 Class III CL MDA

The primary investigation of the Class III CL system involved researching the operating limits. The CL theoretical performance is bounded by that which may be obtained by the OL system. Its performance is further limited by characteristics of the phase control loop hardware. The significant results obtained from this examination include: (1) maximum locking bandwidth and (2) power versus frequency data.

The CL locking bandwidth is determined by the slope of OL frequency response for a given slug size. The upper and lower bounds for the locking bandwidth found for the OL configuration correspond to the phase limits for CL operation, as illustrated in Figure 5.5-6. Since the slug location may be correlated to either the frequency or phase boundary, this provides a means to compare their performance. This check may be used to optimize the MDA performance. In one hardware configuration, the frequency and phase limits

differed substantially. An analysis of the hardware revealed that reflected power internal to the waveguide was interfering with its locking capability. By further isolating the injected signal, the predicted bandwidth was restored.

The characterization effort also focused on verifying the portion of the sink regions that would provide stable operation. This depends primarily upon the slope of the frequency curves. Small slugs provide less tuning range, as well as a shallow slope. The slope of these curves rounds over near its maxima, further limiting the useful range of slug motion. Larger slugs provide more tuning range and crisper cusps near the maxima, but may be driven over the cusps because of the inertia of the slug tuning mechanism.

8.1.1.6 Overall Effects on Magnetron

In addition to the effects attributed to a particular MDA configuration, some overall behaviors were noted concerning the operation of the magnetron. One major set of data concerned the effects of other load components on MDA operation, such as the shorting plate location, magnetron coupling, and waveguide size. The other body of data addresses comparisons of magnetron behavior when coupled with different hardware. This includes operating different magnetrons in same MDA (the same magnetron models with different usage histories and the same models just 'out-of-the-box'), and operating the same magnetron in different MDA configurations.

The various hardware configurations examined during this effort provided unique insight into the behavior of the magnetron. The magnetron launching section provided by FCI permitted the shorting plate location to be adjusted with respect to the magnetron. This method of tuning provides strong influence over the behavior of the MDA. Proper positioning of the plate allows the magnetron to be operated deep within the sink region. Small changes in its location can dramatically affect the character of the MDA. This

capability made it possible to see the formation of the important resonant load condition discussed above. Details of this investigation are provided in Appendix A.4.8.

Another factor influencing the MDA operation is the coupling of the magnetron to the load. Coupling is affected by many aspects of the waveguide cavity geometry, but is maximized when the magnetron RF antenna is centered within the waveguide. A slight variation in probe depth was shown to have significant impact on the MDA operation. Brown also employed a screw-type tuner opposite the magnetron probe to maximize the coupling. Results of this investigation are provided in Appendix A.4.3.

A more subtle, but important factor influencing the MDA behavior is that of waveguide size. The waveguide acts as a highpass circuit for the RF energy and has its own *RLC* characteristics which contribute to the overall load placed on the magnetron. During the characterization effort, a number of moding behaviors were observed that pointed to a high sensitivity of the magnetron to the load. Some of this may be attributed to the waveguide size used for this effort. The UAF MDA was constructed of WR-284 waveguide components, whereas Brown's configuration used a slightly larger size guide. The sensitivity of operating magnetrons at 2.45 GHz into this size medium is known, and calls for care in machining practices [28]. Temperature variances caused by changes in output power affect the waveguide size. These in turn may cause the impedance fluctuations needed to initiate the mode shifts observed. A discussion of the effects of waveguide size is given in Appendix A.4.2.

In light of the sensitivity demonstrated by the MDA to changes in load impedance, it is not unexpected that different magnetrons would behave somewhat differently in a set configuration. However, the magnitude of these differences was surprising. Comparison of three Samsung 2M181 (the model used primarily in this effort) magnetrons yielded substantially different results, as shown in Figures A.4.4-1 and A.4.4-2. The usage history of the three units has not been tracked, and therefore some differences might be

expected. However, an evaluation of four new National 2M107A-605 magnetrons also produced significantly different responses. In this case, some of the magnetrons would not even operate in the current MDA configuration, while others performed fine. The results of this comparison are provided in Appendix A.4.6. This data seems to indicate that relatively small variances in magnetron construction may cause large differences in performance.

Another factor to investigate was how a single magnetron would perform in the two MDA configurations. This was accomplished by comparing Brown's results versus the performance of his magnetron in the UAF MDA. This showed that the magnetron retained the same basic performance characteristics (slope of power versus frequency curves in the sink region). The difference in the frequency tuning range was explained by the size of the tuning slugs used. These results provide support that the magnetrons are indeed different from one another.

8.1.2 ESPAM

As part of the characterization effort, the MDA was configured to radiate the output power. The dummy load was replaced with the slotted waveguide array (SWA) antenna described in Section 6.1. This configuration of the MDA is referred to as the Electronic Steerable Phased Array Module (ESPAM). Two of the ESPAM units were frequency locked to create a 2-element phased array. The 2-element array was used to demonstrate that a microwave beam could be steered electronically. Details of the demonstration are provided in Section 6.4.

Several aspects of the demonstration are significant, not only to the phased array operation, but also to the performance of the MDA itself: (1) this was the first-ever operation of a phased array using the MDA/ESPAM, (2) circumstances provided an

excellent opportunity to showcase the 'ruggedness' and versatility of the MDA, and (3) the MDA was shown to be an acceptable RF generator for cascaded operation.

This demonstration marked the first time that the MDA had been used in this fashion. The MDA had been used by Brown for years to demonstrate the feasibility of wireless power transmission (WPT), but had never been used to form a phased array. The demonstration showed that the MDA could fulfill its intended purpose, and that it was capable of operating under non-ideal conditions. The RF beam was used to illuminate a panel of bulbs fed by vertical columns of rectenna elements. The resultant beam was steered through ±4° corresponding to 360° of electrical phase shift. The observed pattern matched that predicted by the model, which was also developed for this effort (Sections 6.2 and 6.3).

The ESPAM proved to be quite capable and practical in accomplishing this task. The entire frequency separation of 14 MHz was overcome with a single Class III ESPAM. The other unit had only a Class II capability (injected signal and power control). In addition, both units were power limited due to the utility power available. It is significant that one unit was powered by a portable generator, though the power factor limited its output.

A final significant fact is that no reference signal was provided to the two ESPAM units. Instead, one unit served as a master, providing a portion of its output signal to frequency-lock the slave. This substantially reduces the equipment required of a portable WPT demonstration, making it easier to illustrate the practicality of the MDA/ESPAM. Such simplifications may dramatically increase the chances of acceptance of this technology and the concept of WPT. In addition, the MDA established itself as a capable RF generator in its own right. This use of the MDA could prove valuable as a high power RF source to feed a higher-power MDA or for other applications.

8.1.3 SPS

Part of the overall effort has been to define the beam shaping requirements for a solar power satellite (SPS) composed of ESPAM units. This is considered the ultimate application of the MDA. The study investigated orbit selection, ground site locations, and power requirements for one 'standard' baseline system used to analyze potential SPS candidates [2]. The orbit selected was that of a geostationary orbit. Impacts of nonzero orbit eccentricity and inclination were presented as part of the analysis. The design proposed reduces the standard SPS transmitting array from 1 km diameter to under 800 km, for an area savings of 84%. Using a rectangular 550 x 550 array of ESPAM units with 80 kW magnetrons, the SPS would transmit 16.9 GW and provide an energy density of 215 W/m^2 in the 10 km diameter receiving dish. Assuming a 70% efficient magnetron and 70% efficient rectenna array, then one SPS and receiver pair should provide 12.8 GW of power. Information on the orbit selection and SPS design is provided in Chapter 7 and Appendices 3.1 and 3.2.

8.1.4 Synopsis of MDA Results

One of the major questions to be answered from this effort is: *How well can MDA performance be predicted?* It has been shown that the relative performance of a particular MDA configuration may be predicted with regards to the tuning slug size and location, and the injected signal. In addition, limited models have been developed to help analyze the MDA behavior, though these are largely empirical in nature. Since the MDA seems to be very sensitive to load changes and magnetron changes, this makes a total prediction of a generic magnetron's behavior in the MDA unlikely. However, by first measuring some aspects of the MDA performance, it appears that it may be extrapolated using the models available.

The other question of interest is: *How suitable is the MDA for WPT applications, particularly the SPS?* The MDA provides an exceptional frequency tuning range with very high conversion efficiencies possible. It has demonstrated itself to be physically rugged and practical. More analysis is needed to investigate its behavior, particularly for (1) Class IV operation and (2) operation in a vacuum. However, the MDA appears to be well-suited for ground-based WPT applications.

8.2 Recommendations for Follow-on Research

8.2.1 MDA

Class IV MDA Analysis. The Class IV MDA capability was never attained during the initial effort. Therefore, the entire characterization of the amplitude control system has yet to be accomplished. It is expected that the Class IV MDA will behave quite similarly to the Class III CL configuration. The perceived benefit of this endeavor is to demonstrate that multiple MDA/ESPAM units may be operated form a single power supply. Eliminating the need for a current-regulated supply should also substantially drive down the cost of fielding an array.

Closed-Loop Stability/Sensitivity Analysis. The model of the magnetron phase control loop depends upon the slug position, and on the injected signal frequency and power as dynamic inputs. The model performs a table lookup of the slug position to determine the magnetron operating frequency, output power, and external quality factor. These inputs, together with the injected signal frequency and power, are necessary for calculating the phase shift of the output signal.

Output Spectral Content Characterization. To date, the effort of characterizing the MDA has focused on determining the rough effects of tuning the magnetron using input power and load impedance changes. The load impedance is a function of many parameters,

including slug size and position, shorting plate location, magnetron coupling, the injected reference signal, and the inherent impedance characterizations of the waveguide and load components. All of these factors, and the output probe characteristics, affect the spectral content of the measured output signal.

A full characterization of the MDA output spectrum should be made to catalog the effects of each parameter above. This should be done for both the MDA and ESPAM configurations, as each output method introduces its own effects on the signal. The ESPAM must be studied using the SWA antenna to determine its affect in generating harmonics. The MDA should also be examined, as it shows some promise as a high-power RF amplifier/generator in its own right.

8.2.2 Beam Pattern Model

The general goals for follow-on efforts are to reduce pattern sidelobes and increase beamsteering. The beam pattern calculated for the Slotted Waveguide Array (SWA) antenna provided a good first-cut at modeling the actual pattern. However, the model has a number of shortcomings that limits its usefulness.

SWA Element Pattern. The beam shape of single SWA pattern has only been calculated for the horizontal and vertical directions. The rotated beam shape has not been determined. The diagonal spacing of elements distorts the beam pattern, increasing sidelobe levels. The maximum divergence from the calculated pattern should occur at 45° to the axis. It is desirable to provide a higher resolution model of the pattern, with the beamwidth calculated for a number of angular offsets from the axes.

Multiple Element Patterns. The predicted array patterns suffer from the same limitation as does the single element model. The pattern factor calculations are accomplished only along the horizontal and vertical axes, and for the 45° diagonal case. Compounding this

are the off-axis errors introduced by the single element pattern calculations. Therefore, to provide a more accurate model, the beamwidth should be computed as a function of angle about the boresight.

Amplitude Distribution. The current model only implements a uniform current distribution for the multiple element patterns. To minimize sidelobe levels, an actual array would likely make use of a binomial or Tchebysheff distribution.

Fill Factors. The current model only permits constant (x- or y-direction) adjustments in spacing and phase between elements. For the SPS project, this may not be a valid assumption. Instead, the SPS may be comprised of some type of sparsely populated array, consisting of multiple satellites or array sections.

Element alignment. The current model assumes all elements are perfectly aligned, with no offsets in the plane of the antenna and no rotation of elements. This is not likely for a large structure exposed to wind or thermal loading.

SWA Element Size. In the existing model, the SWA size is fixed to that of the two prototype antennas. It would be useful to study the effects of the size of the array on sidelobe levels and beamsteering capability.

Display Types. The current model is limited to providing 2-D plots of the beam patterns. The pattern computation improvements outlined above would benefit from an enhanced 3-D pattern display.

In addition, future efforts should include the examination of different size SWA antennas, as well as other less directive antenna types.

8.2.3 Multiple Unit ESPAM Testbed

Measurement of Radiated Patterns. It would be beneficial to compare the expected far-field antenna patterns with the actual patterns. This would validate the software models used and uncover anomalies in the antennas. The proposed enhancements to the testbed will make this possible for single elements, and for small arrays. In addition to the existing SWA antennas, this could be done for other promising antenna types.

Demonstration of 4-Element Array. The next step in showcasing the viability of WPT is to complete a dual-axis technology demonstrator. The real test of the practicality of this technology (other than efficiency and controllability) is how portable the array may be made. This drives a number of other requirements, any of which could potentially become a show-stopper for a successful demonstration.

-- Setup time. Should require a minimum amount of time to setup and teardown.
-- Space. Should require a minimum amount of space to operate.
-- Packaging. Should minimize space and weight for transportation.
-- Rugged. Components should be sturdy, somewhat weather resistant.
-- Power. Should minimize power requirements, arrange for support at site.
-- Test equipment. Should minimize, arrange for support at site.
-- Easy to operate. Should require minimal training, include O&M manuals.

Appendix A.1 Beam Pattern Calculations for the Slotted Waveguide Array

This appendix contains the beam pattern calculations for a single element slotted waveguide array (SWA). Section A.1.1 contains the calculations specific to the single SWA pattern discussed in Chapter 6. Section A.1.2 provides the supporting pattern factor equations used in this calculation, which are also applied to the calculation of multiple element SWA patterns examined in Chapters 6 and 7.

A.1.1 SWA Beam Pattern Calculations

This section provides an approximate means to analytically predict the beam pattern of the slotted waveguide array (SWA). The resulting beam pattern is used for multi-unit beam pattern calculations. The SWA is a 64-element array of slots fed by waveguide sections, as shown in Figure A.1.1-1.

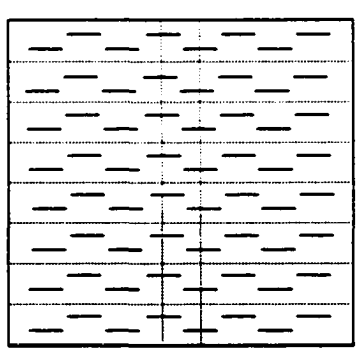

Figure A.1.1-1. 64-Element Slotted Waveguide Array (SWA).

The element spacing for the array is shown in Figure A.1.1-2.

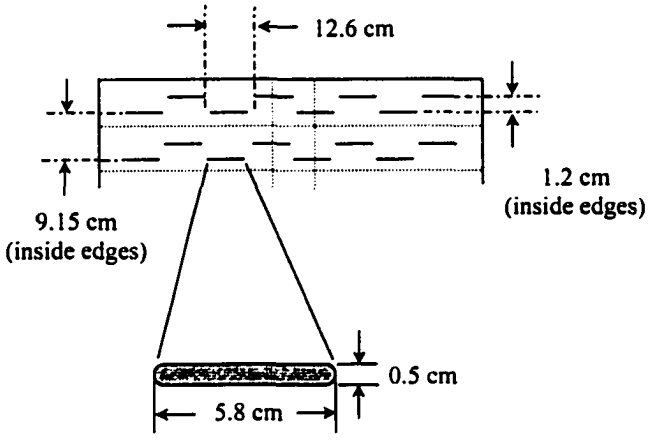

Figure A.1.1-2. Measurements of SWA.

The basis for calculating the beam pattern of the SWA is the principle of pattern multiplication. This states that the overall beam pattern resulting from an array of like radiating elements is the product of the pattern factor (geometry of the elements) and the individual element pattern. The total electric field pattern is given by [23]

$$E_{total} = E_{pattern} \cdot E_{slot} \qquad \text{(A.1.1-1)}$$

where

E_{total} = resultant E - field pattern
$E_{pattern}$ = pattern factor for 8 x 8 array
E_{slot} = pattern for single slot element.

Graphically, this process may be represented by the following diagram.

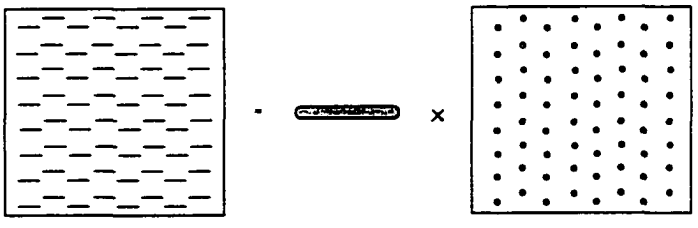

Figure A.1.1-3. Graphical Equivalent of Pattern Multiplication for SWA.

The coordinate system used to calculate the pattern is shown in Figure A.1.1-4. The angles describing the beamwidths and directions are measured from the antenna boresight, shown by the z-axis below.

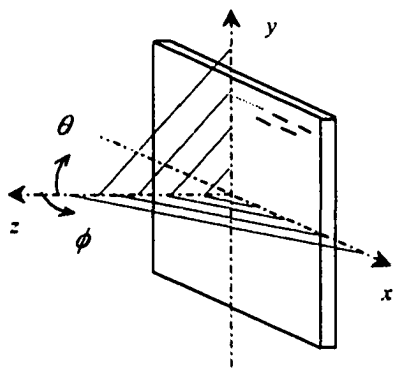

Figure A.1.1-4. Geometry of Beam Measurements for Slotted Waveguide Array.

The electric field generated by a slot element is caused by the capacitive effect of charge buildup across the gap. The slots are oriented horizontally, as shown in Figure A.1.1-5.

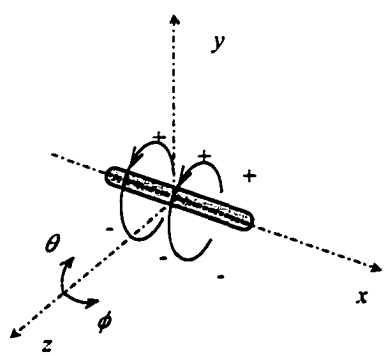

Figure A.1.1-5. Electric Field Generated by Charge across Slot Gap.

For a slot of length L, the resulting field pattern components are given by [23]

$$E_{slot}(\theta) = \frac{\cos\left(\beta L \cos\theta/2\right) - \cos\left(\beta L/2\right)}{\sin\theta} \qquad \text{(A.1.1-2a)}$$

$$E_{slot}(\phi) = 1. \qquad \text{(A.1.1-2b)}$$

where

$$\beta = \text{phase constant} = \frac{2\pi}{\lambda}\left[\frac{\text{rad}}{\text{s}}\right].$$

The beam pattern calculations used in this analysis do not account for mutual resistance due to the element spacing. For the element separations shown in Figure A.1.1-10, the free space horizontal spacing is $d_{h\lambda} \approx 0.75\lambda$ and is $d_{v\lambda} \approx 0.13\lambda$. For the echelon configuration shown, the mutual resistance between these would be $z_m \approx$ -3.7 Ω, compared to an element self-impedance of z_s = 73.1 Ω. Therefore, the mutual impedance effect is estimated to be less than 5% and is considered further.

Now the pattern factor for the 64-element slotted waveguide array may be determined. The overall pattern factor may be written as the product of its contributing factors, which allows the computation to be broken into intermediate steps. First is the determination of the equivalent pattern factor for each horizontal strip of four point sources. This simplifies the original pattern factor into the following components.

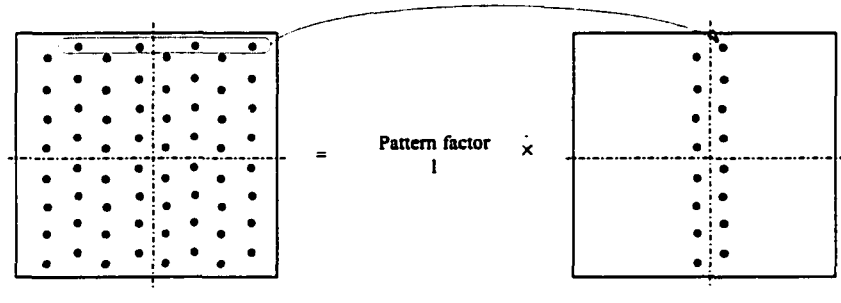

Figure A.1.1-6. Equivalent Pattern Factor for First Simplification.

It is necessary to find the field pattern for linear arrays of point sources multiple times in determining the overall SWA pattern. Therefore, it is beneficial to include the problem geometry and results here. Suppose there exists a linear array of n isotropic point sources, as shown in Figure A.1.1-7.

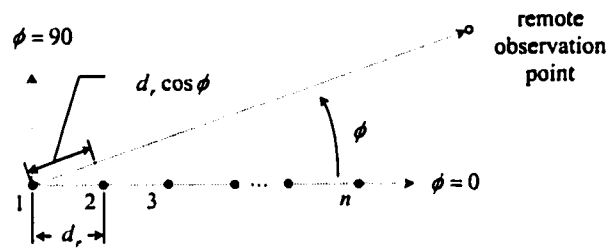

Figure A.1.1-7. Linear Array of n Isotropic Point Sources [23].

It can be shown that the pattern resulting from this array of point sources is given by

$$E_{array} = \frac{1}{n} \frac{\sin\left(n\psi/2\right)}{\sin\left(\psi/2\right)}, \qquad \text{(A.1.1-1)}$$

where

E = amplitude of point sources
ψ = total phase shift between adjacent sources
n = number of sources.

The total phase shift between elements is defined to be

$$\psi = d_r \cos\phi + \delta \qquad \text{(A.1.1-2)}$$

where

$d_r \cos\phi$ = physical distance
δ = electrical phase shift.

Further details on this derivation are provided in Appendix A.1.2.

This result may now be applied to the SWA calculation. However, before the pattern factor can be calculated, we desire to first verify the assumption that the slots radiate at an equal phase. From Figure A.1.1-2, the center-to-center physical distance between slot elements is d_h = 18.4 cm. To find this distance in radians, it is necessary to calculate the wavelength of the radiated signal within the guide [22],

$$\lambda_g = \frac{\lambda_0}{\sqrt{1-\left(\frac{f_c}{f_0}\right)^2}} = \frac{\lambda_0}{\sqrt{1-\left(\frac{\lambda_0}{\lambda_c}\right)^2}} \qquad \text{(A.1.1-3)}$$

where

λ_g = wavelength in guide
λ_0 = wavelength in free space
λ_c = guide cutoff wavelength
f_c = guide cutoff frequency
f_0 = operating frequency.

The cutoff frequency of the guide may be found by

$$f_c = \frac{c}{\lambda_c} \qquad \text{(A.1.1-4)}$$

where

c = speed of light in free space = $3 \cdot 10^8 \left[\frac{\text{m}}{\text{sec}}\right]$
λ_c = cutoff wavelength of guide.

The cutoff wavelength of the guide is given by

$$\lambda_c = \frac{2a}{m} \qquad \text{(A.1.1-5)}$$

where

a = guide major (inner) dimension
m = mode number = 1 (TE_{10} mode).

For the eight horizontal feed sections of the SWA, the guide width is 3.25". Therefore, the guide cutoff wavelength is λ_{ch} = 16.51 cm. The guide wavelength for the eight horizontal sections is λ_{gh} = 18.24 cm. Comparing this with the value of 18.4 cm measured verifies that the slots will yield roughly equal phases.

The pattern factor for the linear arrays of four horizontal slots may now be calculated. Substituting the values $d_{rh} = 2\pi$, $\delta = 0$, and $n = 4$ into Equation A.1.1-6 yields a pattern factor of

$$E_{PF1} = \frac{1}{4}\frac{\sin\left[4\pi\left(\cos\phi_{array}\right)\right]}{\sin\left[\pi\left(\cos\phi_{array}\right)\right]}. \qquad \text{(A.1.1-6)}$$

However, this equation must be modified to account for the different coordinate system used for the SWA beam pattern, which measures the angle from the broadside direction. In terms of the SWA coordinate system,

$$\phi = \phi_{SWA} = \phi_{array} - 90^0. \qquad \text{(A.1.1-7)}$$

This pattern factor applies only to the ϕ-direction; the field in the θ-direction is unaffected. Therefore, the components are given by

$$E_{PF1}(\phi) = \frac{1}{4}\frac{\sin(4\pi\sin\phi)}{\sin(\pi\sin\phi)} \qquad \text{(A.1.1-8a)}$$

$$E_{PF1}(\theta) = 1. \qquad \text{(A.1.1-8b)}$$

Next, the pattern factor for the resulting columns of sources is found.

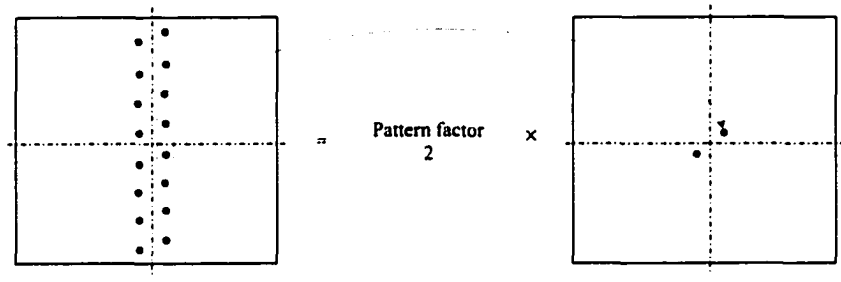

Figure A.1.1-8. Equivalent Pattern Factor for Second Simplification.

Again, we wish to verify the assertion that the phase from each 'effective' source is equal. To do this, it is necessary to find the guide wavelength of the vertical guide section feeding the horizontal guide sections. For the vertical section, the width is measured to be 3 1/8". Its cutoff wavelength is then λ_{cv} = 15.875 cm, yielding a guide wavelength of λ_{gv} = 19.22 cm. The center-to-center vertical spacing between slots is measured to be d_v = 10.15 cm. Therefore, the effective sources are located at approximately ½ the guide wavelength, yielding roughly equal phases.

The second pattern factor may now be calculated. Substituting in the values of $d_{rv} = 2\pi$, $\delta = 0$, and $n = 4$ into Equation A.1.1-6 yields a pattern factor of

$$E_{PF2} = \frac{1}{8}\frac{\sin(8\pi\cos\phi_{array})}{\sin(\pi\cos\phi_{array})}. \qquad \text{(A.1.1-9)}$$

Again, this pattern must be put in terms of the SWA coordinate system. The resulting pattern components are given by

$$E_{PF2}(\phi)=1 \tag{A.1.1-10a}$$

$$E_{PF2}(\theta)=\frac{1}{8}\frac{\sin(8\pi\sin\theta)}{\sin(\pi\sin\theta)}. \tag{A.1.1-10b}$$

Finally, the complete pattern factor may be computed.

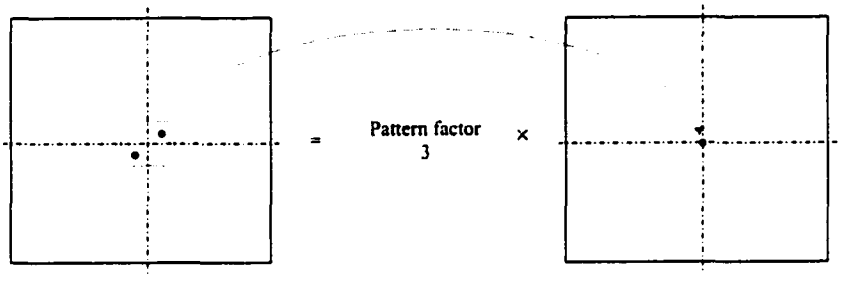

Figure A.1.1-9. Equivalent Pattern Factor for Final Simplification.

This calculation is the most complicated, if accounting for the rotational effect on the beam pattern caused by the offset of the constituent sources. Doing so requires breaking the patterns of the constituent sources into components along the new axes, performing the pattern factor calculation, then transforming the resultant beam patterns back to the original reference frame. Figure A.1.1-10 gives the coordinate system for the transformation.

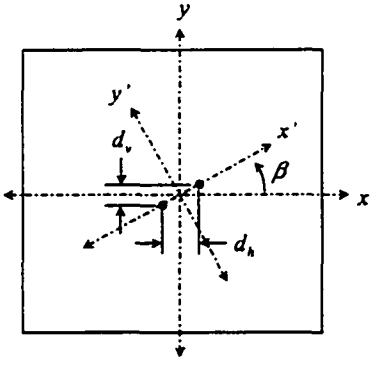

Figure A.1.1-10. Coordinate Transformation for Calculating Final Pattern Factor.

The horizontal and vertical separations of the two elements are

$$d_h = 9.2\,\text{cm} \rightarrow d_{h\lambda} = 0.5044\lambda_{gh} \rightarrow d_{hr} = 2.0176\pi\,\text{rad} \qquad \text{(A.1.1-11a)}$$

$$d_v = 1.7\,\text{cm} \rightarrow d_{v\lambda} = 0.0885\lambda_{gv} \rightarrow d_{vr} = 0.3540\pi\,\text{rad}. \qquad \text{(A.1.1-11b)}$$

The separation along the x'-axis is

$$d_\lambda = \sqrt{(0.5044\lambda)^2 + (0.0885\lambda)^2} = 0.5121\lambda \qquad \text{(A.1.1-12a)}$$

$$d_r = (0.5121\lambda)\left(\frac{2\pi}{\lambda_g/2}\right) = 1.0242 \cdot 2\pi\,\text{rad}. \qquad \text{(A.1.1-12b)}$$

The angle of the coordinate transformation is

$$\beta = \tan^{-1}\left(\frac{1.7}{9.2}\right) = 10.47^\circ. \qquad \text{(A.1.1-13)}$$

Therefore, the effective sources are located at approximately ½ the guide wavelength, yielding roughly equal phases. Substituting the values d_r = 2.047π rad and n = 4 into Equation A.1.1-6, the pattern factor is

$$E_{PF} = \frac{1}{2}\frac{\sin(2.0484\pi\sin\phi')}{\sin(1.0242\pi\sin\phi')}. \qquad \text{(A.1.1-14)}$$

This pattern factor applies only to the ϕ'-direction; the field in the θ'-direction is unaffected. Therefore, the components of the pattern factor are

$$E_{PF}(\phi') = \frac{1}{2}\frac{\sin(2.0484\pi\sin\phi')}{\sin(1.0242\pi\sin\phi')} \qquad \text{(A.1.1-15a)}$$

$$E_{PF}(\theta') = 1. \qquad \text{(A.1.1-15b)}$$

To complete the process, this pattern factor must be transformed back to the original coordinate system. Graphically, this process appears as shown in Figure A.1.1-11.

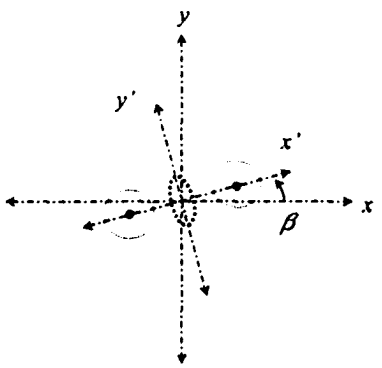

Figure A.1.1-11. Graphical Analysis of Final Pattern Factor.

Since the component elements lie along the x'-axis, the resultant main lobe is roughly halved in this direction (shown in bold). The pattern in the direction of the y'-axis is unaffected. This assumes that the element patterns were symmetric to start with. The resultant beam may then be resolved into its original x and y components.

Fortunately, using the principle of superposition, the problem may be rearranged to ease the pattern factor calculation. Instead of solving for the pattern and then resolving it into components, the elements are first resolved into x- and y- components. What results are two sets of equivalent components, one along each axis.

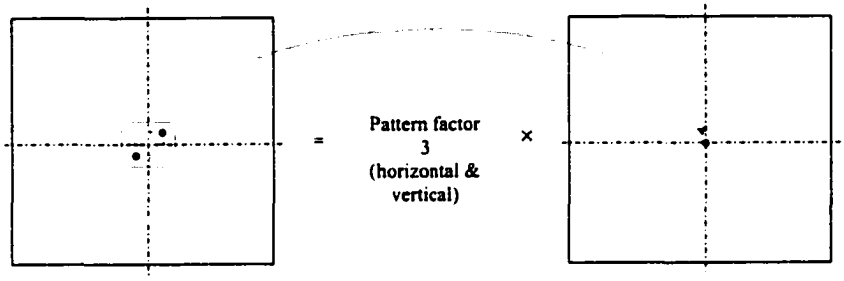

Figure A.1.1-12. Equivalent Sources for Calculating Final Pattern Factor.

The pattern factor components are solved

$$E(\phi)_{PF3} = \frac{1}{n_h}\frac{\sin\left(n_h\psi_h/2\right)}{\sin\left(\psi_h/2\right)} \qquad \text{(A.1.1-16a)}$$

$$E(\theta)_{PF3} = \frac{1}{n_v}\frac{\sin\left(n_v\psi_v/2\right)}{\sin\left(\psi_v/2\right)} \qquad \text{(A.1.1-16b)}$$

where

$$\psi_h = d_{rh}\sin\phi = 2.0176\pi\sin\phi$$
$$\psi_v = d_{rv}\sin\theta = 0.3540\pi\sin\theta$$
$$n_h = n_v = 2.$$

Therefore, the final pattern factor is

$$E(\phi)_{PF3} = \frac{1}{2}\frac{\sin(2.1076\pi\sin\phi)}{\sin(1.0088\pi\sin\phi)} \qquad \text{(A.1.1-17a)}$$

$$E(\theta)_{PF3} = \frac{1}{2}\frac{\sin(0.3540\pi\sin\theta)}{\sin(0.1770\pi\sin\theta)}. \qquad \text{(A.1.1-17b)}$$

The resulting total pattern factor for the 64-element array is the product

$$E_{pattern} = E_{PF1} \cdot E_{PF2} \cdot E_{PF3} \tag{A.1.1-18}$$

which may be resolved into its components

$$E(\phi)_{pattern} = E(\phi)_{PF1} \cdot E(\phi)_{PF2} \cdot E(\phi)_{PF3} \tag{A.1.1-19a}$$

$$E(\theta)_{pattern} = E(\theta)_{PF1} \cdot E(\theta)_{PF2} \cdot E(\theta)_{PF3}. \tag{A.1.1-19b}$$

The final pattern factor components are given by

$$E(\phi)_{pattern} = \frac{1}{8} \frac{\sin(4\pi \sin\phi)}{\sin(\pi \sin\phi)} \frac{\sin(2.1076\pi \sin\phi)}{\sin(1.0088\pi \sin\phi)} \tag{A.1.1-20a}$$

$$E(\theta)_{pattern} = \frac{1}{16} \frac{\sin[8\pi(\sin\theta)]}{\sin[\pi(\sin\theta)]} \frac{\sin(0.3540\pi \sin\theta)}{\sin(0.1770\pi \sin\theta)}. \tag{A.1.1-20b}$$

Recall that the individual slot pattern is given by Equation A.1.1-2. Substituting the values for the slot length in wavelengths,

$$\beta L = \left(\frac{2\pi}{\lambda_{gv}}\right)(5.8\,\text{cm})\left(\frac{\lambda_{gv}}{19.22\,\text{cm}}\right) = 0.6035\pi\ \text{rad}. \tag{A.1.1-21}$$

The slot pattern is then given by

$$E_{slot}(\theta) = \frac{\cos(0.3018\pi\cos\theta) - \cos(0.3018\pi)}{\sin\theta}. \tag{A.1.1-22}$$

Therefore, the total pattern for the 64-element SWA is given by

$$E(\phi)_{SWA} = \frac{1}{8}\frac{\sin(4\pi\sin\phi)}{\sin(\pi\sin\phi)}\frac{\sin(2.1076\pi\sin\phi)}{\sin(1.0088\pi\sin\phi)} \qquad \text{(A.1.1-23a)}$$

$$E(\theta)_{SWA} = \frac{1}{16}\frac{\sin(8\pi\sin\theta)}{\sin(\pi\sin\theta)}\frac{\sin(0.3540\pi\sin\theta)}{\sin(0.1770\pi\sin\theta)}\frac{[\cos(0.3018\pi\cos\theta)-\cos(0.3018\pi)]}{\sin\theta}. \qquad \text{(A.1.1-23b)}$$

This yields the following E-field plots (generated by MATLAB).

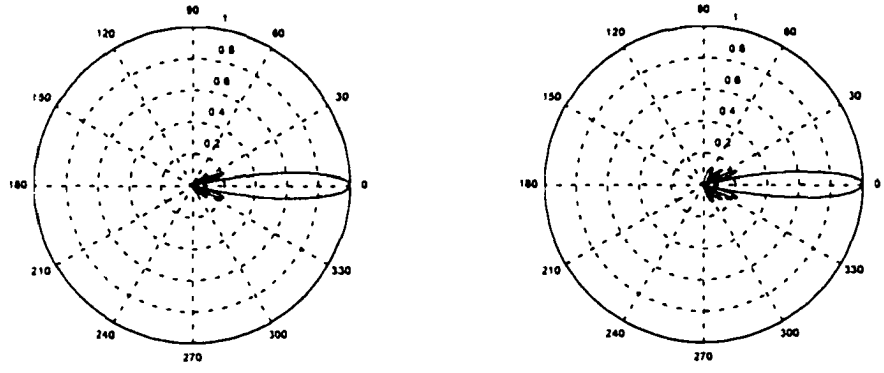

Figure A.1.1-13. Polar Plots of E-field Components for 64-Element SWA.

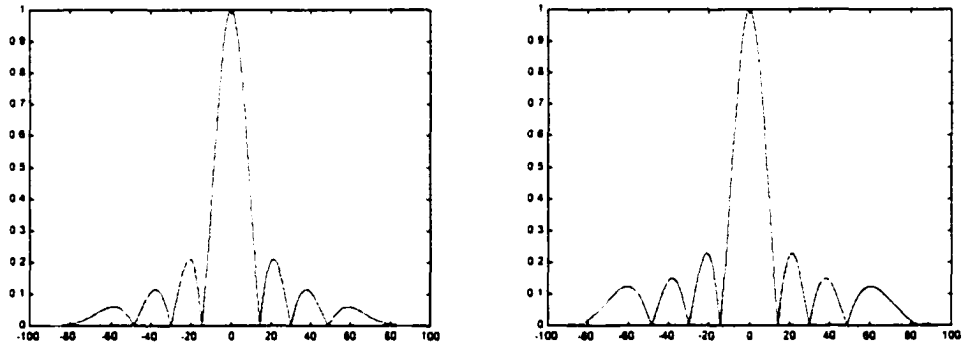

Figure A.1.1-14. Fringe Plots of E-field Components for 64-Element SWA.

A.1.2 Pattern Factor Calculations for Linear Arrays

This section is provided in support of the SWA beam pattern calculations in Appendix A.1.1. It gives the calculations for the pattern factors used in pattern multiplication, including pattern shapes, beam null locations, and effects of missing elements. These equations are used in the calculation of the beam pattern for multiple SWA elements.

Beam Pattern. Suppose there exists a linear array of n isotropic point sources as shown in Figure A.1.2-1.

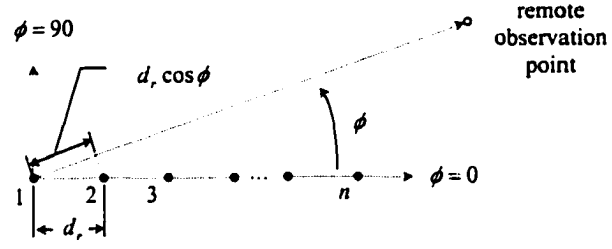

Figure A.1.2-1. Linear Array of n Isotropic Point Sources [23].

The resultant electric field seen at the remote observation point is a sum of the contributions from each point source,

$$E_{total} = E_1 + E_2 + E_3 + \cdots + E_n . \qquad \text{(A.1.2-1)}$$

Assuming that the sources are of equal amplitude and have a linear phase shift between them, this may be rewritten as

$$E_{total} = E\left(1 + e^{j\psi} + e^{j2\psi} + \cdots + e^{j(n-1)\psi}\right) \qquad \text{(A.1.2-2)}$$

where

E = amplitude of point sources
ψ = total phase shift between adjacent sources
n = number of point sources.

The total phase between adjacent sources results from the physical spacing (as seen by the observer) and the electrical phase shift induced. If the observation point is distant compared to the spacing of the sources, then the total phase shift seen is

$$\psi = d_r \cos\phi + \delta \tag{A.1.2-3}$$

where

$d_r \cos\phi$ = physical distance
δ = electrical phase shift.

Multiplying Equation A.1.2-2 by the quantity $e^{j\psi}$ yields

$$E_{total}e^{j\psi} = E\left(e^{j\psi} + e^{j2\psi} + \cdots + e^{jn\psi}\right). \tag{A.1.2-4}$$

Subtracting the result from Equation A.1.2-2 yields

$$E_{total} - E_{total}e^{j\psi} = E\left(1 + e^{j\psi} + e^{j2\psi} + \cdots + e^{j(n-1)\psi}\right) - E\left(e^{j\psi} + e^{j2\psi} + \cdots + e^{jn\psi}\right). \tag{A.1.2-5}$$

This may be factored to obtain

$$E_{total}\left(1 - e^{j\psi}\right) = E\left(1 - e^{jn\psi}\right). \tag{A.1.2-6}$$

Then the total electric field due to the linear array is given by

$$E_{total} = E\frac{\left(1 - e^{jn\psi}\right)}{\left(1 - e^{j\psi}\right)}. \tag{A.1.2-7}$$

Employing trigonometric substitutions, the total electric field is given by

$$E_{total} = E\frac{e^{jn\psi/2}}{e^{j\psi/2}}\frac{\left(e^{jn\psi/2} - e^{-jn\psi/2}\right)}{\left(e^{j\psi/2} - e^{-j\psi/2}\right)}. \qquad \text{(A.1.2-8)}$$

Writing this in terms of the sine function,

$$E_{total} = Ee^{j\left(n-1/2\right)\psi}\frac{\sin\left(n\psi/2\right)}{\sin\left(\psi/2\right)}. \qquad \text{(A.1.2-9)}$$

This may be further simplified by centering the resultant beam pattern at the midpoint of the linear array,

$$E_{total} = E\frac{\sin\left(n\psi/2\right)}{\sin\left(\psi/2\right)}. \qquad \text{(A.1.2-10)}$$

Normalizing the field by its maximum value results in the pattern factor for the linear array,

$$E_{array} = \frac{1}{n}\frac{\sin\left(n\psi/2\right)}{\sin\left(\psi/2\right)}. \qquad \text{(A.1.2-11)}$$

Null Directions and Beamwidth. The pattern nulls occur where the E-field magnitude is zero,

$$E_{total} = E\frac{\left(1-e^{jn\psi}\right)}{\left(1-e^{j\psi}\right)} = 0. \qquad \text{(A.1.2-12)}$$

Assuming the denominator is non-zero, then this condition occurs at

$$e^{jn\psi} = 1, \qquad \text{(A.1.2-13)}$$

which requires that

$$n\psi = \pm 2k\pi \qquad \text{(A.1.2-14)}$$

where $k = (1, 2, 3, ...)$. Equating this with the definition for the total phase between sources,

$$\psi = d_r \cos\phi_0 + \delta = \pm\frac{2k\pi}{n}. \qquad \text{(A.1.2-15)}$$

Solving for the angle of the null,

$$\phi_0 = \cos^{-1}\left[\frac{1}{d_r}\left(\pm\frac{2k\pi}{n} - \delta\right)\right][\text{rad}]. \qquad \text{(A.1.2-16)}$$

When working with two-dimensional arrays, beam patterns are usually measured from the boresight of the antenna (perpendicular to the face at the center). Therefore, the complementary angle γ for the linear array is defined as shown in Figure A.1.2-2.

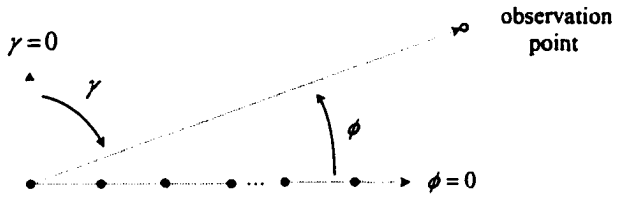

Figure A.1.2-2. Angle Definitions for Linear Array of Point Sources.

In terms of this new angle, the null directions are given by

$$\gamma_0 = \sin^{-1}\left[\frac{1}{d_r}\left(\pm\frac{2k\pi}{n} - \delta\right)\right][\text{rad}]. \qquad \text{(A.1.2-17)}$$

The total main lobe beamwidth between the nulls is defined as

$$BW = 2|\gamma_0|[\text{rad}]. \qquad \text{(A.1.2-18)}$$

These equations may be simplified for some special cases. For the broadside condition $(\delta = 0)$,

$$\gamma_0 = \sin^{-1}\left(\pm\frac{k}{nd_\lambda}\right). \qquad \text{(A.1.2-19)}$$

If the array is long $(nd_\lambda >> k)$, this may be approximated as

$$\gamma_0 \approx \pm\frac{k}{nd_\lambda}. \qquad \text{(A.1.2-20)}$$

The bandwidth is defined as twice the null angle, therefore

$$BW = \frac{2k}{nd_\lambda}. \tag{A.1.2-21}$$

For the main lobe $(k = 1)$, these are further reduced to

$$\gamma_0 \approx \pm\frac{1}{nd_\lambda}, \tag{A.1.2-22}$$

$$BW = \frac{2}{nd_\lambda}. \tag{A.1.2-23}$$

For the endfire condition $(\delta = -d_r)$, the null angle calculation requires some additional trigonometric manipulations.

$$d_r \cos\phi_0 + \delta = \pm\frac{2k\pi}{n} = d_r \cos\phi_0 - d_r \tag{A.1.2-24}$$

$$\therefore 1 - \cos\phi_0 = \mp\frac{k}{nd_\lambda}. \tag{A.1.2-25}$$

Making use of the half-angle formula,

$$\sin^2 A = \frac{1}{2}(1 - \cos 2A). \tag{A.1.2-26}$$

Substituting into this form yields

$$\sin^2\frac{\phi_0}{2} = \frac{1}{2}(1 - \cos\phi_0) = \mp\frac{k}{2nd_\lambda}. \tag{A.1.2-27}$$

Therefore, the null angle is

$$\phi_0 = 2\sin^{-1}\left(\sqrt{\mp\frac{k}{2nd_\lambda}}\right). \qquad \text{(A.1.2-28)}$$

Writing this in terms of the usual boresight angle yields

$$\gamma_0 = \frac{\pi}{2} - \phi_0 = \frac{\pi}{2} - 2\sin^{-1}\left(\sqrt{\mp\frac{k}{2nd_\lambda}}\right)[\text{rad}]. \qquad \text{(A.1.2-29)}$$

If the array is long $(nd_\lambda >> k)$, this may be approximated as

$$\gamma_0 = \frac{\pi}{2} - \sqrt{\mp\frac{2k}{nd_\lambda}}\,[\text{rad}]. \qquad \text{(A.1.2-30)}$$

For the main lobe $(k = 1)$, this is further reduced to

$$\gamma_0 = \frac{\pi}{2} - \sqrt{\mp\frac{2}{nd_\lambda}}\,[\text{rad}], \qquad \text{(A.1.2-31)}$$

$$BW = 2\sqrt{\mp\frac{2}{nd_\lambda}}\,[\text{rad}]. \qquad \text{(A.1.2-32)}$$

Effects of Missing Sources. Assume that the k-th element of the linear array is now missing, as shown in Figure A.1.2-3.

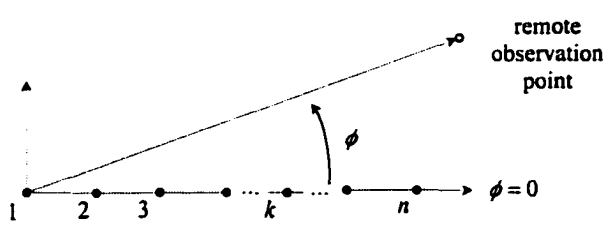

Figure A.1.2-3. Linear Array with k-th Element Missing.

Recall that the total E-field seen at a remote observation point is given by Equation A.1.2-2. Explicitly showing the component of the k-th term, the total field is

$$E_{total} = E\left(1 + e^{j\psi} + e^{j2\psi} + \cdots + e^{jk\psi} + \cdots + e^{j(n-1)\psi}\right). \qquad \text{(A.1.2-33)}$$

As before, multiplying equation by the quantity $e^{j\psi}$ yields

$$E_{total}e^{j\psi} = E\left(e^{j\psi} + e^{j2\psi} + \cdots + e^{j(k+1)\psi} + \cdots + e^{jn\psi}\right). \qquad \text{(A.1.2-34)}$$

Subtracting the equations yields

$$E_{total}\left(1 - e^{j\psi}\right) = E\left(1 - e^{jn\psi}\right) + Ee^{jk\psi}\left(e^{j\psi} - 1\right). \qquad \text{(A.1.2-35)}$$

Then the total electric field due to the linear array is given by

$$E_{total} = E\frac{\left(1 - e^{jn\psi}\right)}{\left(1 - e^{j\psi}\right)} - Ee^{jk\psi}. \qquad \text{(A.1.2-36)}$$

In terms of the sine function, the field is

$$E_{total} = Ee^{j\left(n-1/2\right)\psi}\frac{\sin\left(n\psi/2\right)}{\sin\left(\psi/2\right)} - Ee^{jk\psi}. \qquad \text{(A.1.2-37)}$$

This form demonstrates clearly the affect of the missing source on the beam pattern. Referencing the beam to the center of the array and normalizing yields

$$E_{array} = \frac{1}{n}\left[\frac{\sin\left(n\psi/2\right)}{\sin\left(\psi/2\right)} - e^{j\left(k-\frac{n+1}{2}\right)\psi}\right]. \qquad \text{(A.1.2-38)}$$

Alternatively, the pattern may be calculated by summing the individual contributions from each radiating element,

$$E_{array} = \frac{1}{n}\sum_{k=1}^{n} e^{j\left(k-\frac{n+1}{2}\right)\psi} = \frac{1}{n}\sum_{k=-\frac{n}{2}}^{\frac{n}{2}} Ee^{jk\psi}. \qquad \text{(A.1.2-39)}$$

The effects of missing elements on a sample linear array are shown in Figure A.1.2-4.

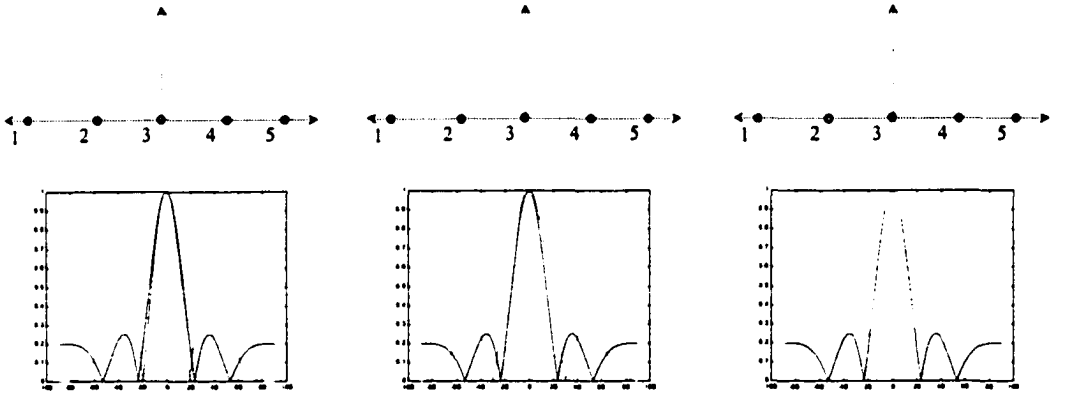

Figure A.1.2-4. Effect of Missing Elements on Linear Array of Point Sources. Blue curves show n = 5 case, other curves show beam pattern with missing element in shaded location above ($d_i = 0.5\lambda$, $\delta = 0$) [23].

Appendix A.2 Equipment Characteristics

This appendix outlines the physical hardware characteristics of the MDA support equipment. This includes details of the configuration and performance of the MDA instrumentation, the phase control loop, and the DC power supplies.

A.2.1 Reference Signal Injection Equipment

The reference signal injection components include a vector signal generator, an RF amplifier, a manual rotary-type phase shifter, a phase comparator (double balanced mixer), and various other components needed to plumb the system and monitor signals. These components are all imperfect hardware items, subject to the physical design constraints discussed in this section. A detailed diagram of these is shown below.

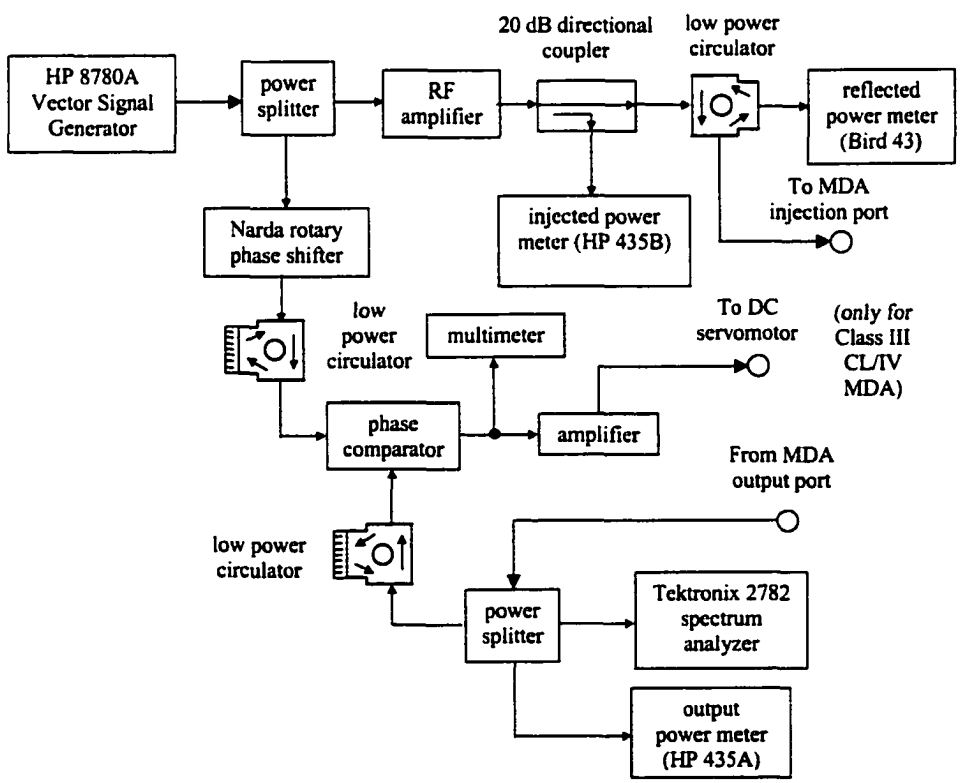

Figure A.2-1. Reference Signal Injection Components.

The reference signal from the HP 8780A vector signal generator is split into two streams. The portion of the signal to be injected into the MDA is first amplified up to 1.6 W maximum. It is then sampled using the 20 dB directional coupler and the HP 435B power meter before being injected into the MDA. A low-power coaxial circulator protects the RF amplifier output from reflected power due to the coax-to-waveguide impedance mismatch.

The second half of the split reference signal is routed through the phase control circuitry. The signal is first manually shifted via a Narda rotary-type phase shifter. The shifted signal is then passed to the phase comparator implemented by a double-balanced mixer. Note that both input channels to the comparator must be protected from bleed-through. This is accomplished via the low power circulators shown at the mixer inputs. The comparator generates a low-level voltage signal that is proportional to the phase difference of the inputs. The phase error signal is then amplified to drive a DC servomotor, which positions the tuning slug at the appropriate location to meet the desired frequency or phase condition. A diagram showing the slug positioning mechanism is provided at Figure 3.5-4.

The primary RF amplifier used was a Mini-Circuits ZHL-42, which is limited to ~+32 dBm output. This power restriction somewhat limited our capability to test certain aspects of the performance of the MDA, such as the phase locking limits for the Class I/II/III OL MDA configurations. In addition, the amplifier's output varies somewhat over the operating frequency band, as shown in Figure A.2-2.

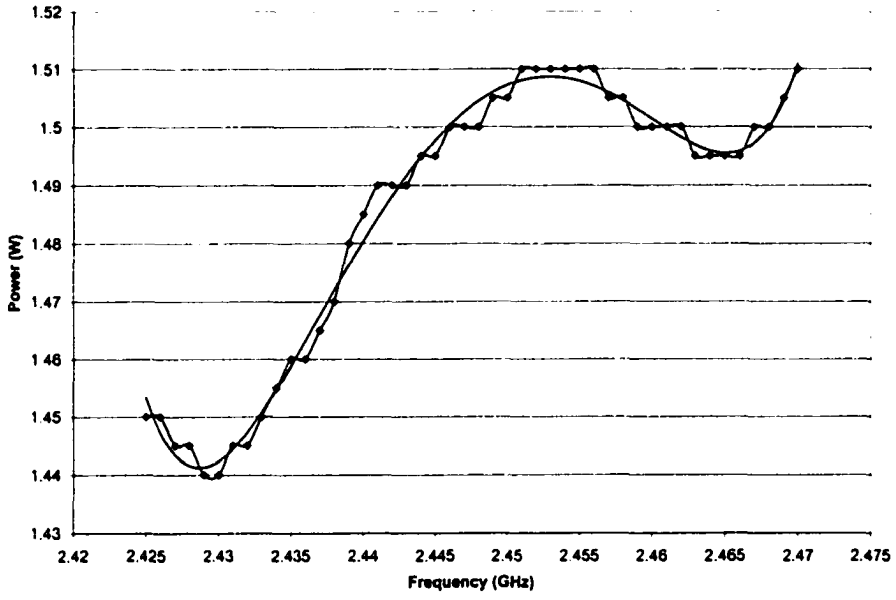

Figure A.2-2. RF Amplifier Characteristics over Operating Frequency Range.

Additional power level fluctuations are caused by the frequency characteristics of the other signal injection components, such as the injection probe. The situation may be further complicated by high frequency capacitive effects of component junctions. The overall behavior of these components in tandem may not be obvious. Therefore, care should be exercised in assuming performance characteristics. When possible, it is best to measure the actual behavior of the components used as subassemblies.

The actual power of the injected reference signal transmitted into the waveguide was calculated by measuring the input power (HP 435B) and the reflected power (Bird 43). This yielded the injected power figure shown in Figure A.2-3.

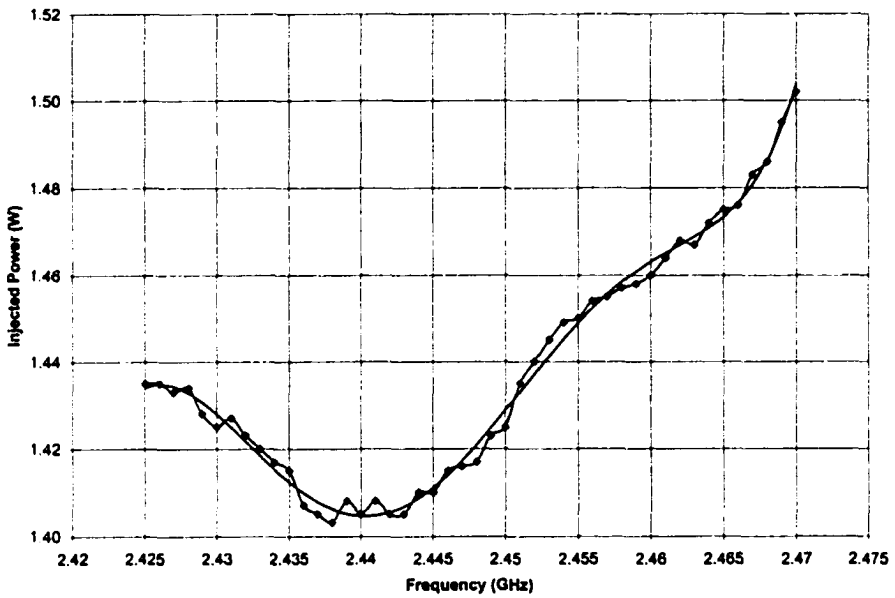

Figure A.2-3. Injected Power Entering Waveguide versus Frequency.

This data was also used to calculate general transmission coefficient data for any input power level, as shown in Figure A.2-4.

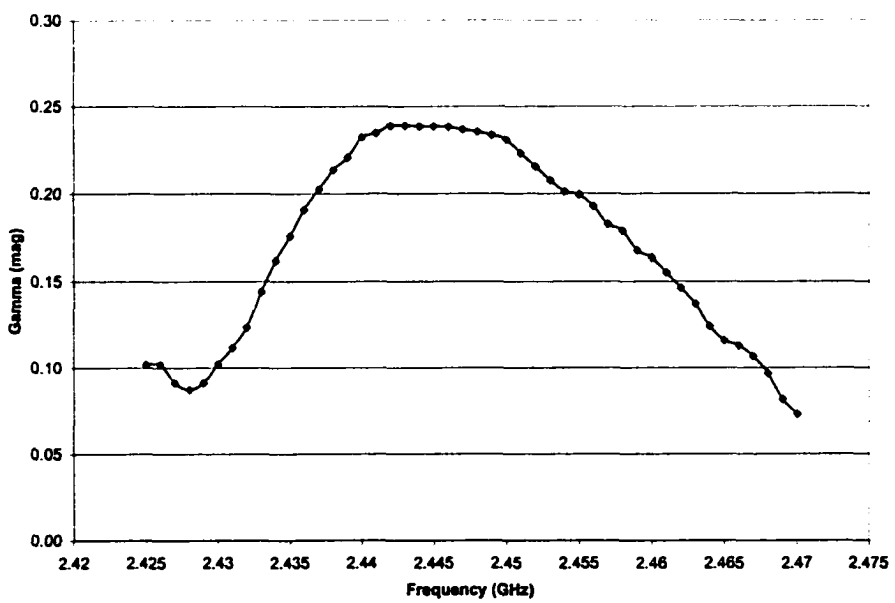

Figure A.2-4. Reflection Coefficient for Signal Injection Subassembly.

This can potentially impact the frequency locking bandwidth of the MDA. If not accounted for, these power variations can result in erroneous BW calculations, or cause adverse system performance. This frequency dependency can limit the operation of the MDA, requiring higher injected signals to function properly. The impact of this may be minimized in future configurations by matching the injection probe to the load.

A.2.2 Instrumentation Resolution

Instrumentation resolution accounted for some errors in measurements. These may be attributed to the output power meters, DC power supplies, and frequency measurement equipment.

The output power levels were measured using the HP 435A power meter. The output power level ΔP_{output} was limited by the meter scale resolution ΔP_{meter},

$$\Delta P_o = K_{probe} K_{splitter} \Delta P_{meter} \tag{A.2-1}$$

where

K_{probe} = signal attenuation due to output probe = 51.52 dB

$K_{splitter}$ = signal attenuation due to power splitter = 5.28 dB.

The meter resolution was limited to ΔP_{meter} = 0.005 mW causing an uncertainty in the output power of ΔP_{output} = 2.393 W. This calculation does not include errors due to equipment calibration. These are considered to be roughly constant across the operating range used, and therefore are not of concern in making relative measurements.

The scale resolutions for the DC power supplies induced some error in the efficiency measurements. The uncertainty in input power ΔP_{DC} is given by

$$\Delta P_{DC} = \Delta V \cdot \Delta I \qquad \text{(A.2-2)}$$

where

ΔV = voltage scale resolution = 0.01 kV
ΔI = current scale resolution = 1 mA.

This correlates to an input power resolution of ΔP_{DC} = 0.01 W. This calculation does not include errors due to equipment calibration. These are addressed in the following section.

Frequency measurements were made with the Tektronix 2782 Spectrum Analyzer. These readings were not limited generally limited by resolution available, but rather by scales selected for particular data sets. The effects of any resolution limitations caused by this are discussed where necessary in the discussion of results (primarily Chapter 5).

A.2.3 DC Power Supply Characteristics

The magnetron operating point is a function of both the load impedance and the input power, as shown in Figures 3.1-2 and 5.4-3. Therefore, to accurately characterize the behavior of the MDA, it was also necessary to baseline the performance of the current-regulated power supplies used. To do this, each power supply was connected to an identical test load — a Class II MDA described in Section 3.3. The voltage provided to the MDA was measured as a function of current.

It was noted that the power supply operation was slightly affected by the MDA temperature. Therefore, after each new current setting was established, the system was allowed to stabilize for 10 minutes between data point. The leads of the power supply were switched, and the process was repeated. Operation was essentially independent of the sense of the leads. The results of the *V-I* characterization are shown in Figure A.2-5.

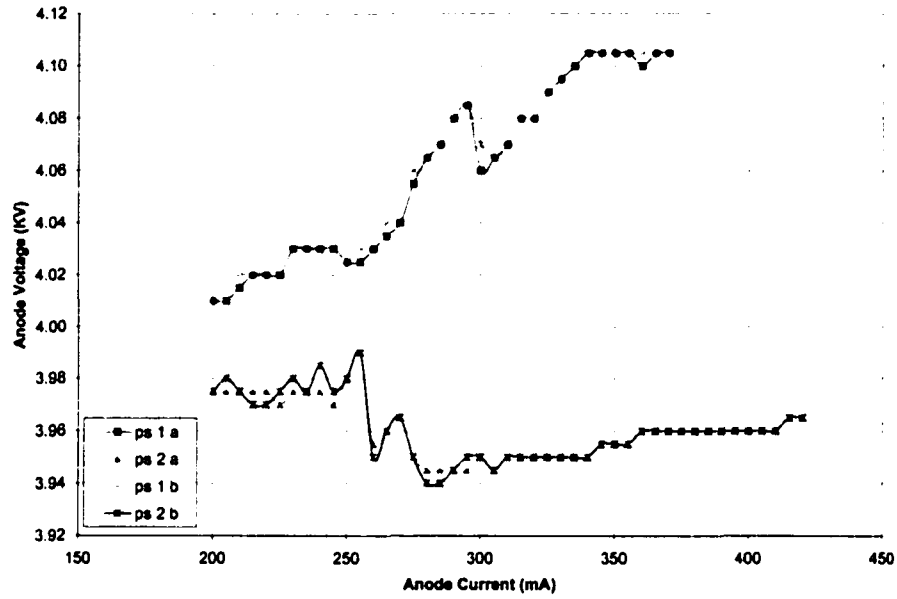

Figure A.2-5. DC Power Supply *V-I* Characteristics.

It was noted that power supply #2 (provided by Bill Brown) was stiffer than our original unit, as it provided less change in voltage for a change in current demand. This is particularly evident for the region of operation around 300 mA, where power supply #1 displays nonlinear behavior. Comparison revealed a difference in calibration between the units.

The magnetron provides a fairly linear conversion of DC power into RF power, as shown in Figure A.2-6. The difference in waveforms further highlight the calibration difference between the units (attributed to power supply #2).

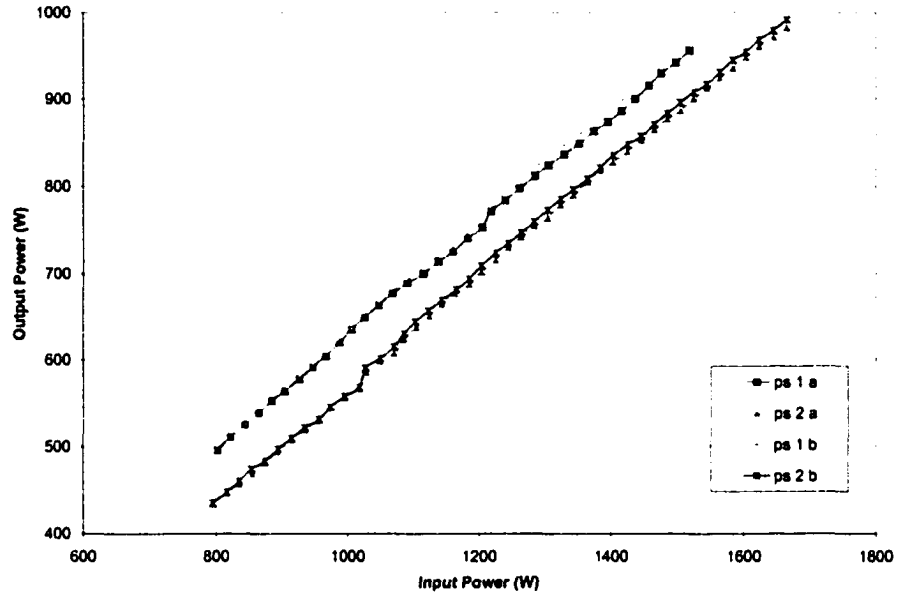

Figure A.2-6. Output Power versus Input Power for Current Regulated Power Supplies Driving a Class II MDA.

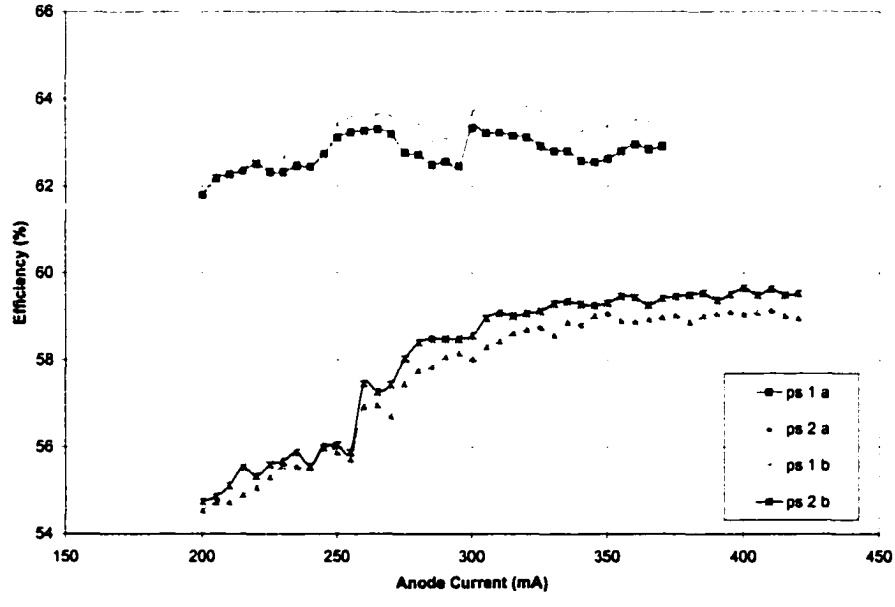

Figure A.2-7. Efficiency versus Anode Current for Current Regulated Power Supplies Driving a Class II MDA.

The power supply efficiency curves are shown in Figure A.2-7. Both power supplies both show a slight increase in magnetron efficiency at higher input power levels. The difference between the two power supplies creates an error of ~8% at lower frequencies and narrows to ~4% at higher ones.

The frequency curves for the power supplies is shown in Figure A.2-8. This shows that the frequency of operation is relatively independent of the power supply used.

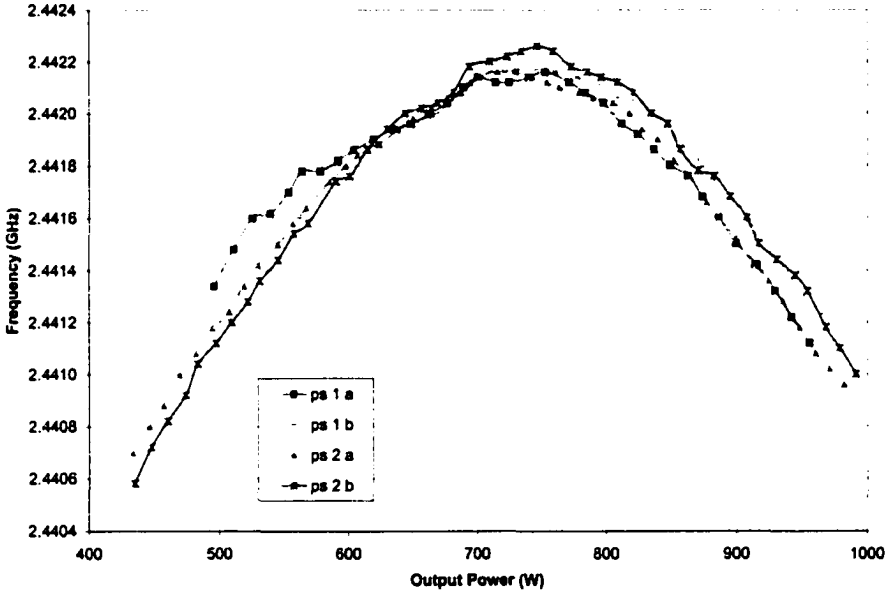

Figure A.2-8. Frequency versus Output Power for Current-Regulated Power Supplies Driving a Class II MDA.

Magnetron case temperature versus anode current for the power supplies is shown in Figure A.2-9. Case temperature for the magnetron is linear with output power. Slight variations can be seen in the average slopes for the two power supplies. These result in a temperature differential of ~4% at high output operation, corresponding to previous efficiency calculations. The difference in efficiencies between the two units is believed to be primarily due to the current readings of power supply #2. The 4% error seen at high power operation would correlate to ΔI_{error} = 12 mA at 300 mA.

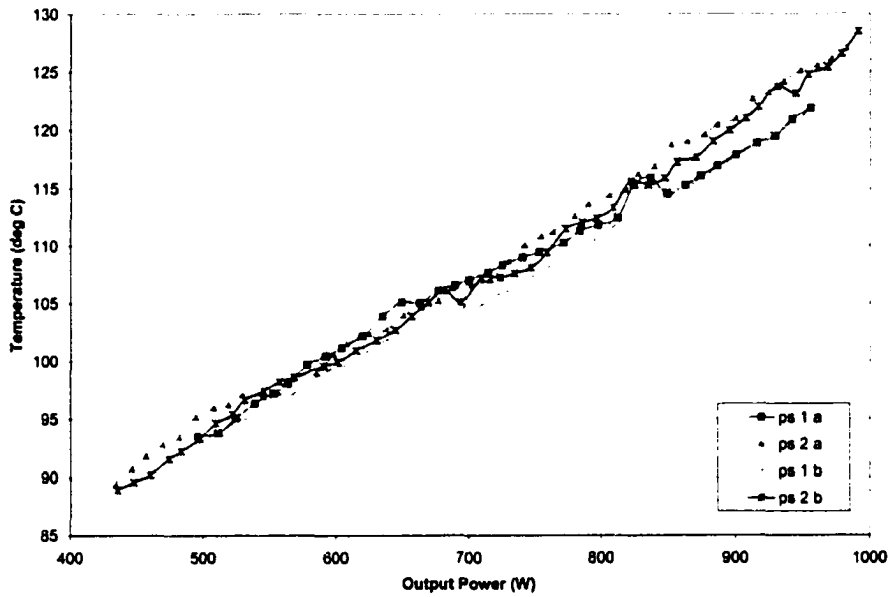

Figure A.2-9. Magnetron Case Temperature versus Output Power for Current-Regulated Power Supplies Driving a Class II OL MDA.

Additional information regarding the influence of the power supplies is provided in Section 5.2.

Appendix A.3 Controls Model

This appendix provides the modeling accomplished for the Class III CL and Class IV MDA. This effort was not completed, but is provided as a record of the work. The information contained here provides a starting point for future efforts and is beneficial in understanding the overall operation of the MDA.

An overall block diagram describing the operation of the Class IV MDA is given below.

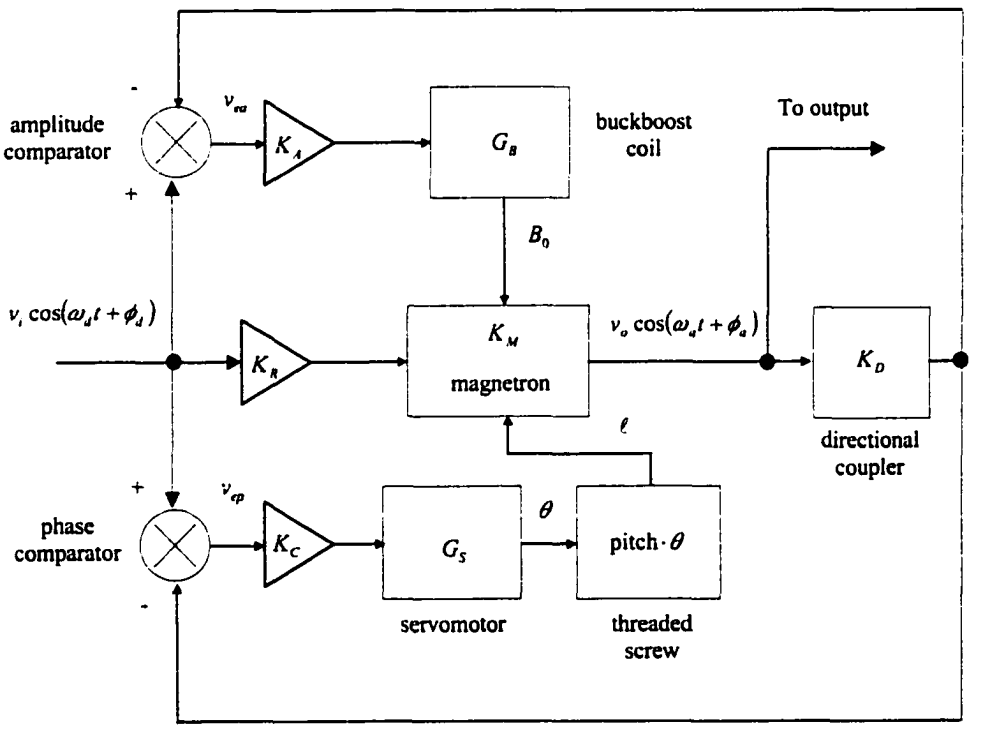

Figure A.3-1. Control Block Diagram for Class IV MDA.

The following definitions apply:

$v_i \cos(\omega_d t + \phi_d)$ = input signal with desired amplitude, frequency, and phase
$v_o \cos(\omega_a t + \phi_a)$ = output signal with actual amplitude, frequency, and phase
G_S = servomotor transfer function
G_B = buckboost coil transfer function
K_R = gain of RF amplifier = 30 [dB]*
K_M = gain of magnetron =~ 30 [dB]
K_C = gain of servomotor amplifier = 20 [dB]
K_A = gain of buckboost coil amplifier = __ [dB]
K_D = gain of directional coupler = -20 [dB]
v_{ep} = error signal for phase control [V]
v_{ea} = error signal for amplitude control [V].

*The gain of the RF amplifier is actually a function of frequency, accounting for the physical characteristics of the amplifier and the capacitive effects of the connecting components at high frequency. Additional details are provided in Appendix A.7.

Phase Control Loop. Examining the components of the phase-locked loop, the first is the phase comparator. This may be modeled by the symbol

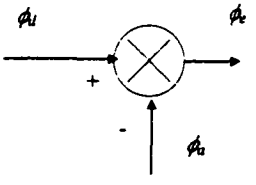

and is described by the function

$$\phi_e = \phi_d - \phi_l. \qquad \text{(A.3-1)}$$

Since the phase comparator is implemented with a double-balanced mixer, the output signal is a voltage. Assuming that the phase comparator is independent of small changes in signal amplitude,

$$v_{ep} = \phi_e . \tag{A.3-2}$$

The next component to be modeled is the servomotor amplifier. The gain for the amplifier is the parameter being analyzed. It is desired to determine the range of suitable values to optimize the performance of the phase-lock loop (typical experimental values are 100 to 200).

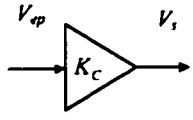

The transfer function for the amplifier is given by

$$K_c = \frac{V_s}{V_{ep}} . \tag{A.3-3}$$

The DC servomotor is the next component in the loop.

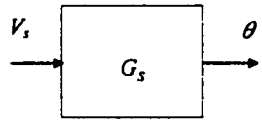

Its transfer function is approximated by the third order model:

$$G_S = \frac{\theta(s)}{V_s(s)} = \frac{1/K_B}{s\left(1 + \frac{J_T}{\left(K_B K_T / R_T\right)} s\right)\left(1 + \frac{L_M}{R_T} s\right)} \tag{A.3-4}$$

where

$\theta(s)$ = servomotor output position [rad]

$V(s)$ = servomotor input voltage [V]

K_B = back - EMF constant = $3.1 \cdot 10^{-2} \left[\frac{\text{V}}{\text{rad/sec}}\right]$

K_T = torque sensitivity constant = $4.5 \left[\frac{\text{oz} \cdot \text{in}}{\text{amp}}\right]$

J_T = total moment of inertia = $1.3 \cdot 10^{-4}$ [oz · in · sec^2]

L_M = armature inductance = 10^{-3} [H]

R_T = total circuit resistance = 17.1 [Ω]

The circuit resistance is a combination of the motor and source resistances,

$$R_T = R_M + R_S \tag{A.3-5}$$

where

R_M = motor resistance = 16.7 [Ω]

R_S = source resistance = 1 [Ω].

Substituting these values into the transfer function yields

$$G_S(s) = \frac{3.4615 \cdot 10^7}{s(s + 60.6258)(s + 17{,}700)}. \tag{A.3-6}$$

The next component modeled is the mechanical linkage converting the servomotor rotation into linear translation of the tuning slug.

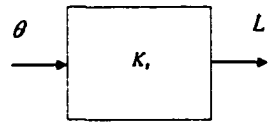

The transfer function of the linear actuator using a 32 threads per inch rod is given by

$$K_s = \frac{L}{\theta} = 1.2633 \times 10^{-2} \left[\frac{\text{cm}}{\text{rad}}\right]. \qquad \text{(A.3-6)}$$

The last component of the phase control loop is the magnetron. The action of this input is seen as a change in the impedance to the magnetron. The magnetron must therefore alter its operating frequency and power because of the change in impedance. The equations governing this result from balancing the imaginary and real components of the load admittance with the driving electronic admittance of the magnetron (Equations A.8-63 and A.8-74). Unfortunately, these parameters may only be determined through intimate knowledge of the design of the magnetron. Alternately, some may be estimated empirically through observation of the magnetron's behavior. This is the general approach, and the one taken here.

The magnetron may be modeled as shown in Figure A.3-2.

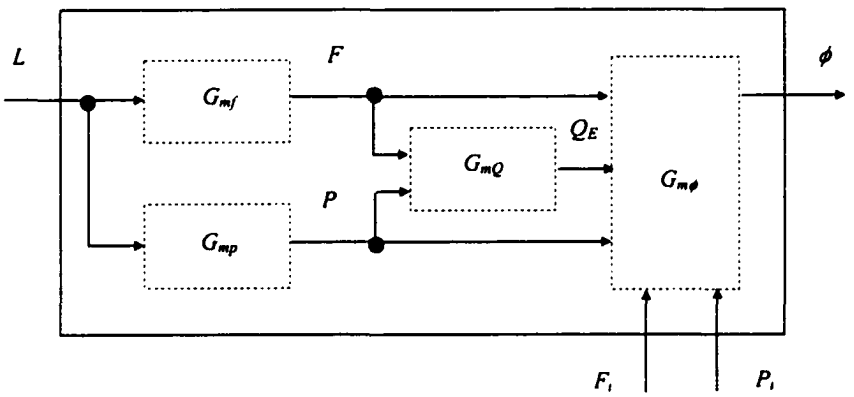

Figure A.3-2. Magnetron Control of Output Signal Phase.

The transfer function G_{mf} is obtained by examining the MDA's frequency response for a particular tuning slug in the sink region. The empirical results for the MDA with slug 2 (Table 3.4-1) are provided in Figure A.3-3.

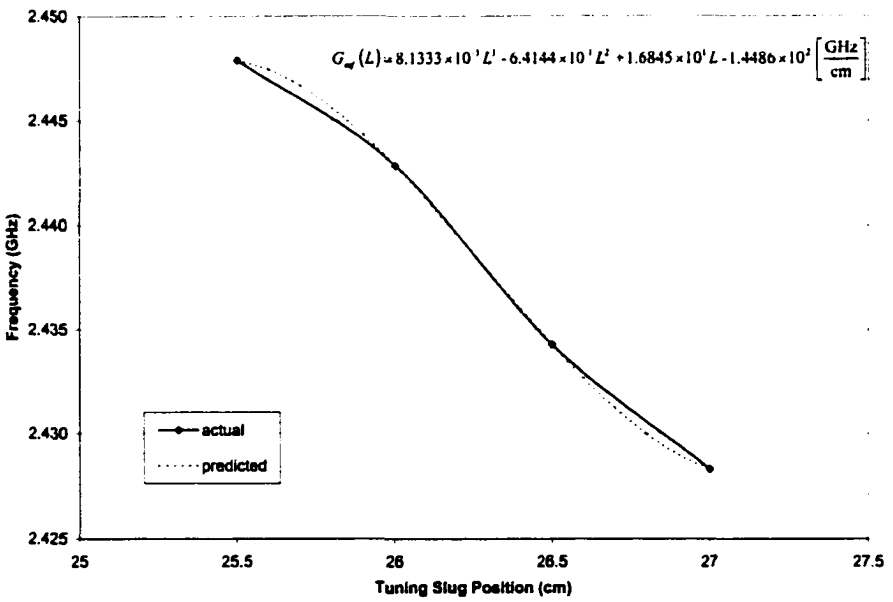

Figure A.3-3. MDA Frequency in Sink Region.

This data may be modeled by

$$G_{mf}(L) = 8.1333\times10^{-3}L^3 - 6.4144\times10^{-1}L^2 + 1.6845\times10^{1}L - 1.4486\times10^{2}\left[\frac{\text{GHz}}{\text{cm}}\right]. \quad \text{(A.3-7)}$$

The transfer function G_{mp} is given by the MDA's power response for the same tuning slug. The corresponding data is shown in Figure A.3-4. The power curve is described by the function (accounting for attenuation in sampling)

$$\begin{aligned} G_{mp}(L) &= 4.7863\times10^{5}\left(-8.00\times10^{-2}L^3 + 6.36L^2 - 1.68\times10^{2}L + 1.49\times10^{3}\right) \\ &= -3.829\times10^{4}L^3 + 3.044\times10^{6}L^2 - 8.041\times10^{7}L + 7.132\times10^{8}\left[\frac{\text{W}}{\text{cm}}\right]. \end{aligned} \quad \text{(A.3-8)}$$

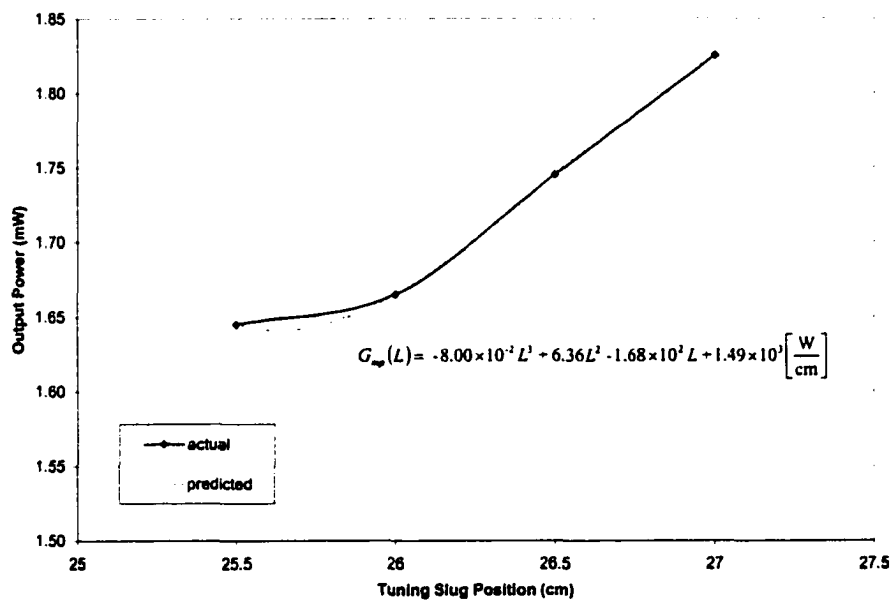

Figure A.3-4. MDA Output Power in Sink Region (sampled level).

The third transfer function of the magnetron model relates the relative frequencies and power levels of the input and output signals to the output signal phase. This function is given by David's equation [11],

$$\phi = \sin^{-1}\left[\frac{(f - f_I)}{f} \cdot Q_E \cdot \sqrt{\frac{P_O}{P_I}}\right] \qquad \text{(A.3-9)}$$

where

ϕ = phase shift between input and output of amplifier
f = free running frequency of the magnetron
f_I = frequency of the drive source
P_I = power input from the driver
P_O = power out of the directional amplifier
Q_E = external Q of the magnetron.

Since the input signal power and frequency are measured quantities, the only remaining parameter to be calculated is the external quality factor. This can be found by examining the frequency locking bandwidth over the sink region for the given tuning slug.

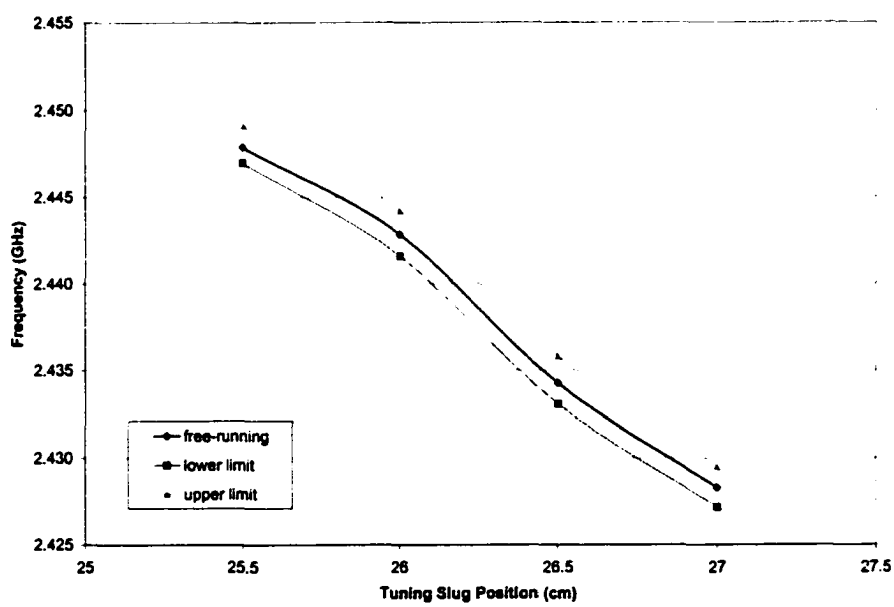

Figure A.3-5. MDA Frequency Locking Limits in Sink Region.

This yields the locking bandwidth curve shown below.

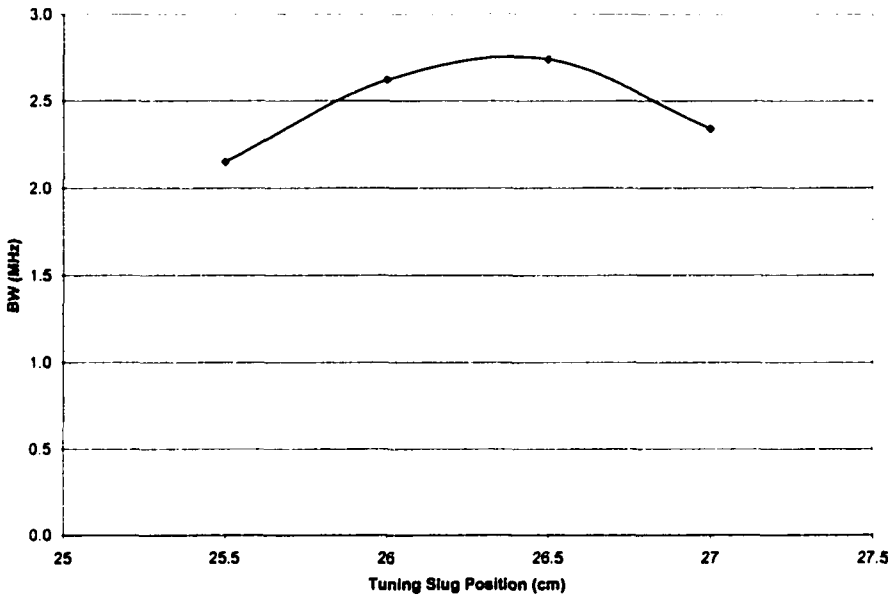

Figure A.3-6. MDA Locking Bandwidth in Sink Region.

Equation A.3-9 may be solved for the external quality factor (section 4.1),

$$Q_E = \frac{2f}{BW}\sqrt{\frac{P_i}{P_o}} \qquad \text{(A.3-10)}$$

where BW = locking bandwidth .

For the preceding data, the quality factor curve is shown in Figure A.3-7. The transfer function for Q_E is defined by

$$G_Q(L) = 2.9193\times10^{1}L^2 - 1.5418\times10^{3}L + 2.0433\times10^{4}\left[\frac{1}{\text{cm}}\right]. \qquad \text{(A.3-11)}$$

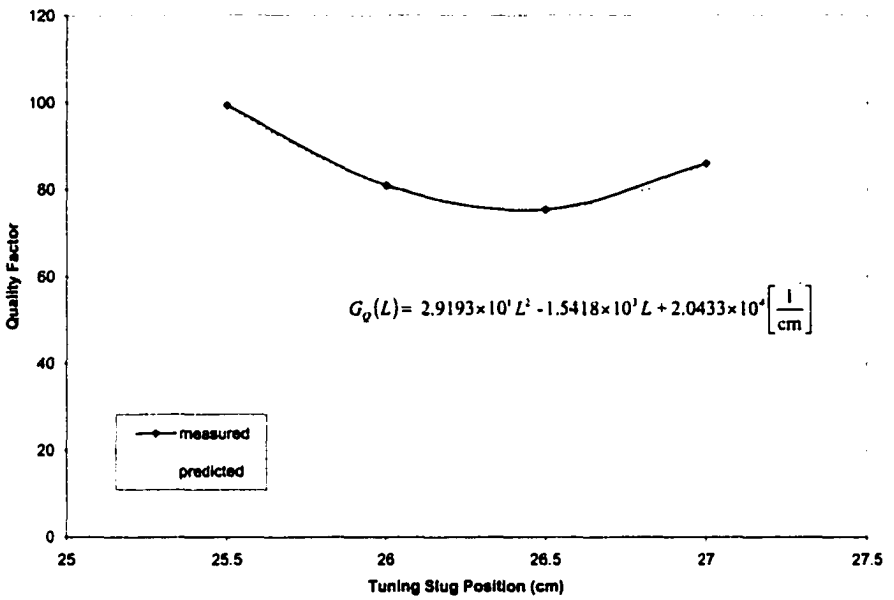

Figure A.3-7. External Quality Factor in Sink Region.

Since Q_E may also be put in terms of the tuning slug position, an alternate model for the magnetron may be constructed, shown in Figure A.3-8.

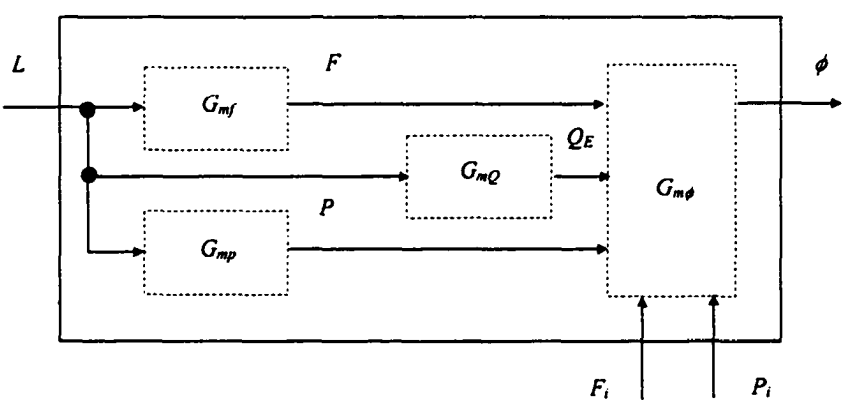

Figure A.3-8. Alternate Model for Magnetron Control of Output Signal Phase.

Finally, the output phase may be calculated from Equation A.3-9. Since this is a multiple input function, no simple transfer function may be written for these intermediate variables (F_o, P_o, and Q_E). However, each of these may be written in terms of the tuning

slug position, L. Therefore, the output phase may be written as the following transfer function,

$$\frac{\phi_a}{L} = \sin^{-1}\left[\frac{(f - f_u)}{f} \cdot Q_E \cdot \sqrt{\frac{P_o}{P_i}}\right]. \qquad \text{(A.3-12)}$$

The previously identified intermediate variables may be treated as inputs (calculated as shown above or by lookup table). Then the block diagram for the magnetron is as follows.

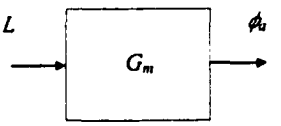

This finishes the feed-forward components of the control loop. The feedback path may simply modeled as unity, since the output signal levels do not affect the phase (assumed that the phase comparator is independent of small changes in signal amplitude).

The resulting control block diagram for the phase-locked loop is shown in Figure A.3-9.

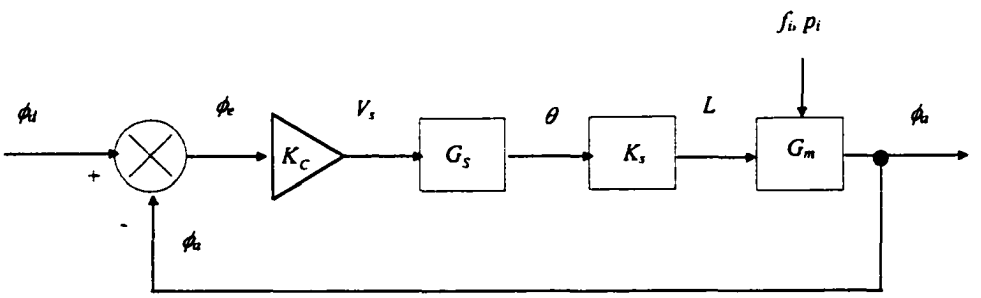

Figure A.3-9. Control Block Diagram for Phased-Lock Loop.

The overall transfer function is given by

$$\frac{\phi_a(s)}{\phi_d(s)} = \frac{K_c G_s K_s G_m}{1 + K_c G_s K_s G_m}. \tag{A.3-13}$$

Substituting the equations for each component yields

$$K_c G_s K_s G_m = (K_c)\left[\frac{3.4615 \cdot 10^7}{s(s+60.6258)(s+17{,}700)}\right]\left(1.2633 \times 10^{-2}\ \frac{\text{cm}}{\text{rad}}\right)\left(\sin^{-1}\left[\frac{(f - f_u)}{f} \cdot Q_E \cdot \sqrt{\frac{P_o}{P_i}}\right]\right). \tag{A.3-14}$$

This equation is difficult to model analytically because of its dependency on the input frequency and power. These are modeled as disturbances in the diagram above. The system response may be solved numerically over a small interval. The solution is not provided here.

Since the magnetron's reaction to a change in load or power is much faster than the time response of the servomotor (microseconds versus milliseconds), the magnetron may be viewed as providing an instantaneous response. Therefore, it will not significantly affect the time response of the closed loop. In light of this fact, it is somewhat beneficial to examine the response of the servomotor and amplifier.

The root locus plot for the servomotor and amplifier is shown in Figure A.3-10.

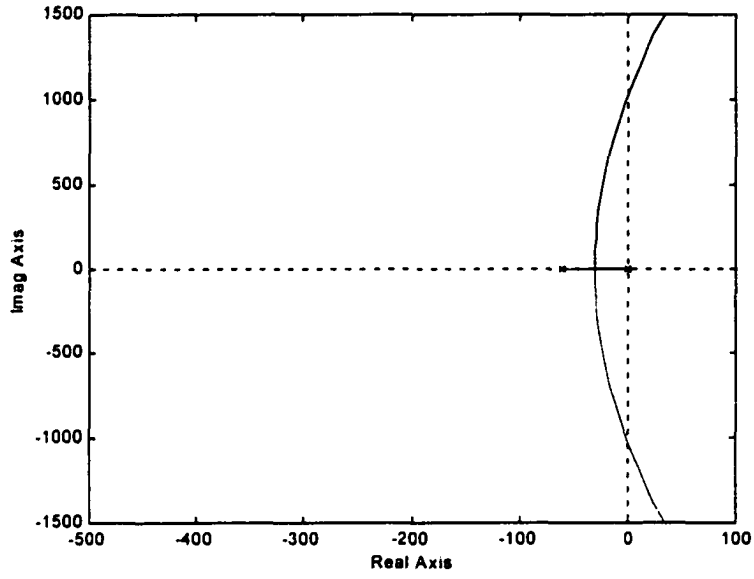

Figure A.3-10. Root Locus for Phase Control Loop.

From experimental results, it is known that the phase control loop becomes marginally stable at an amplifier gain $K_c = 200$. This is evidenced by a rapid oscillatory behavior of the tuning slug mechanism. This corresponds to the location where the root locus branches cross the imaginary axis.

Appendix A.4 Supplemental Analysis of MDA Performance

A.4.1 Load Impedance Tools

This section discusses the tools used to analyze the MDA load impedance. It provides the measurement techniques necessary to arrive at the load impedance data, and the general significance of the graphical tools.

To determine the operating characteristics of the magnetron, its power and frequency are measured for numerous load impedance values. This data may then be plotted in curves that define the magnetron performance graphically. One common type of curve used for this purpose is the Rieke diagram. To construct a Rieke diagram, the load impedance (reflection coefficient) data is first measured and plotted on a Smith chart. Then contours of constant frequency and output power are overlayed on these data points [19], [20].

A.4.1.1 Measurement of Load Impedance Using a Coax/Waveguide Adapter

Most of the load impedance measurements made during the effort used a coax/waveguide adapter to emulate the magnetron probe. For these sets, the shorting plate location was considered to be constant. Therefore, the coax/waveguide adapter could at least provide a rough estimate of the impedance seen by the magnetron. Later, the effects of moving the shorting plate were examined. This required a new method of measuring the impedance data, which is addressed in Section A.4.2.

To measure the load impedance, the load subassembly of the MDA was connected to the HP 8753 network analyzer. The magnetron and launching section were replaced by a coax-to-waveguide adapter and a section of slotted waveguide, shown in Figure A.4.1-1. Reflection coefficient data was measured for all load configurations used to characterize

the MDA performance. The load was varied by moving each of 16 different tuning slugs in increments of 0.5 cm along the slotted waveguide section.

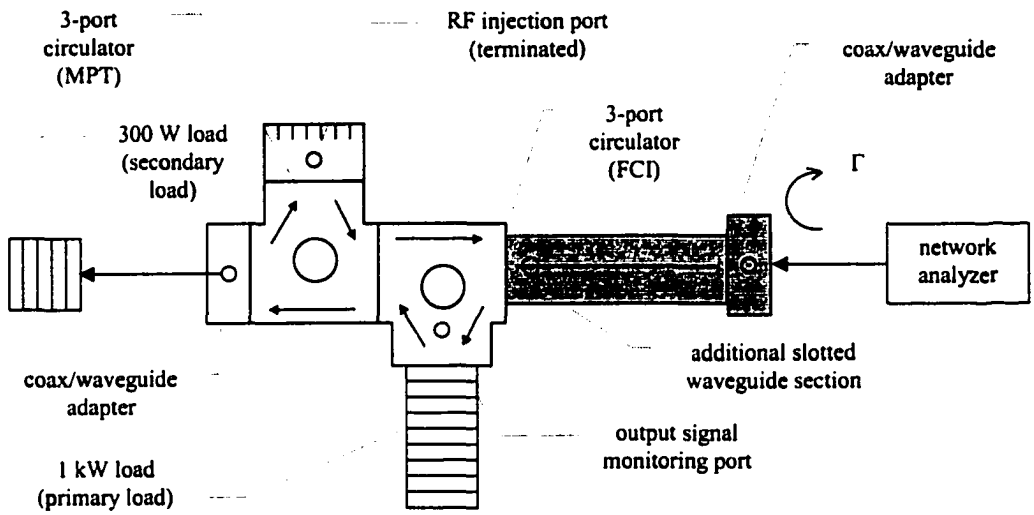

Figure A.4.1-1. Hardware Configuration for MDA Load Impedance Measurements. Note comparison to Class III MDA configuration in Figure 3-4.3.

Each set of measurements was dependent upon the relative location of the tuning slug. To correlate the data, it was necessary to provide a common frame of reference between the configurations. The diagram in Figure A.4.1-2 shows both configurations.

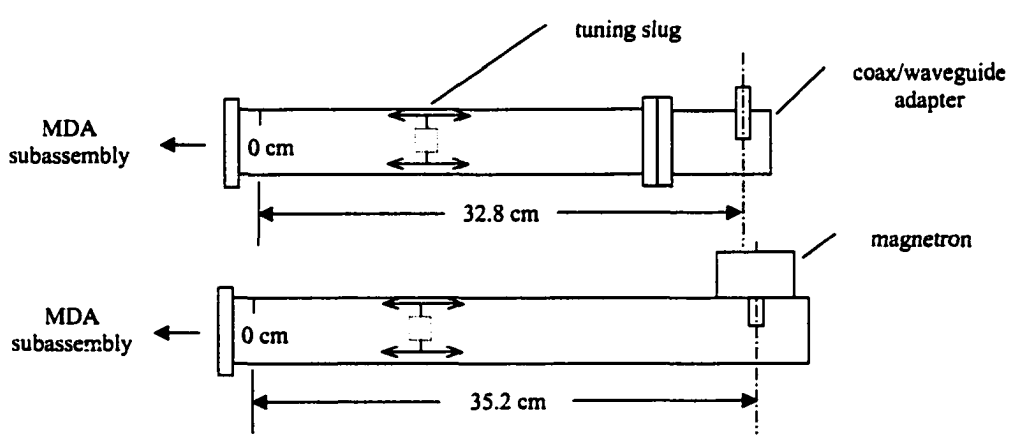

Figure A.4.1-2. Physical Offset in Distances to Tuning Slug.

These two configurations provided a difference in distance from the probes to the tuning slug that had to be corrected prior to entering the reflection coefficient lookup table. This distance was found to be approximately 2.4 cm. In addition, the load impedance is also a function of frequency, as shown in Figure A.4.1-3. To plot the correct value of impedance on the Smith chart, it first had to be correlated to the operating frequency of the magnetron for the same slug location.

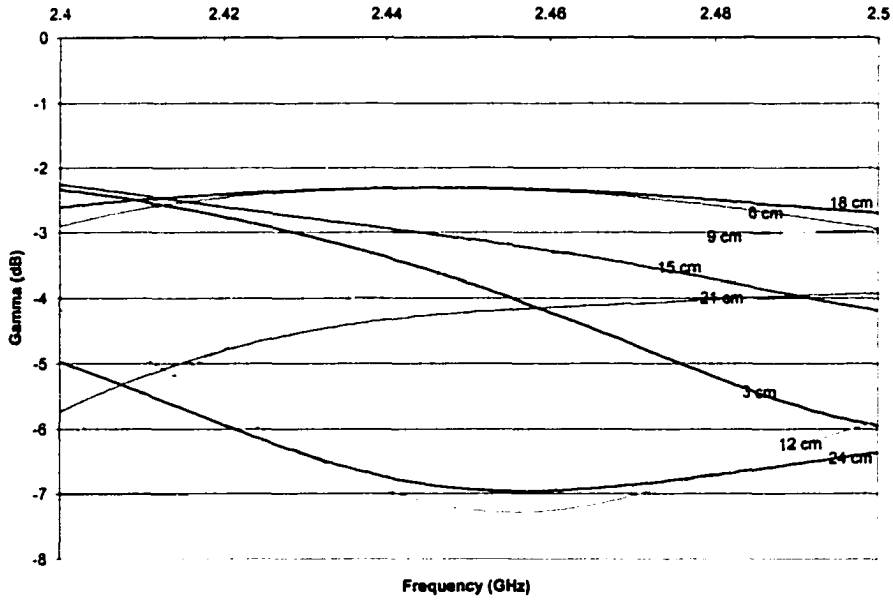

Figure A.4.1-3. Reflection Coefficient of MDA Load versus Frequency. Data shown for slug 2 at various locations.

These measurements were substantiated by comparing the measured MDA load impedance to the expected transverse impedance values given in Equation A.4.2-1. The impedance waveform corresponding to the offset roughly matches that of the theoretical transverse impedance. Plotting the normalized transverse impedance corresponding to the slug location yields the curves in Figure A.4.1-4.

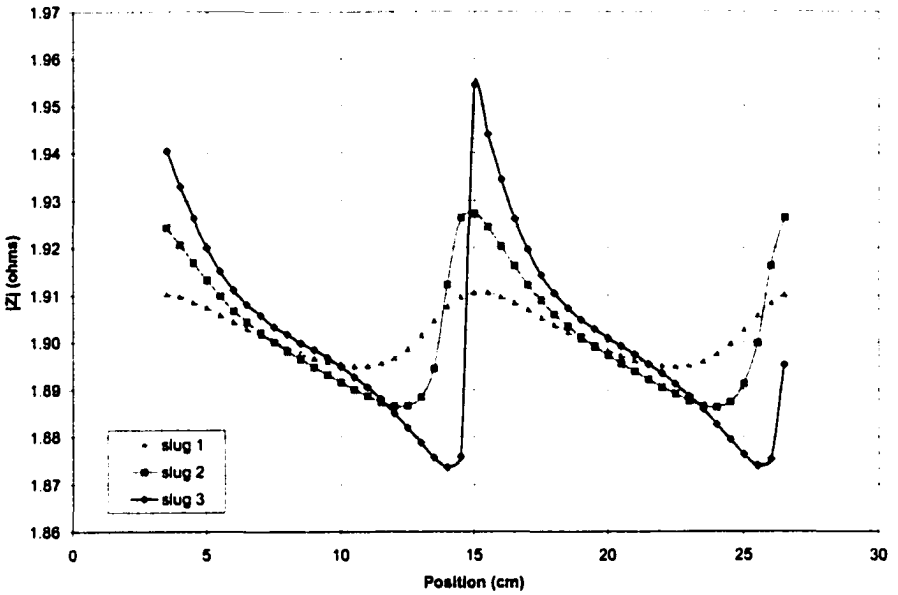

Figure A.4.1-4. Theoretical Transverse Impedance versus Tuning Slug Position.

Each point corresponds to the value of waveguide transverse impedance for the MDA frequency at that point. These curves were then compared to the impedance curves corresponding to the reflection coefficient data measured by the configuration in Figure A.4.1-1. This data was converted to a load impedance using the equation

$$z_L = \frac{1+\Gamma}{1-\Gamma} \qquad \text{(A.4.1-1)}$$

where

z_L = normalized load impedance
Γ = reflection coefficient (complex).

The resulting load impedance curves are shown in Figure A.4.1-5. The two waveforms do not match as closely as would be desired, since the transverse impedance is calculated for an unobstructed waveguide. The tuning slug alters the apparent cross-section of the guide and therefore will result in a distorted waveform. However, the similarity of the two patterns gives an indication that the slug is located in roughly the correct position.

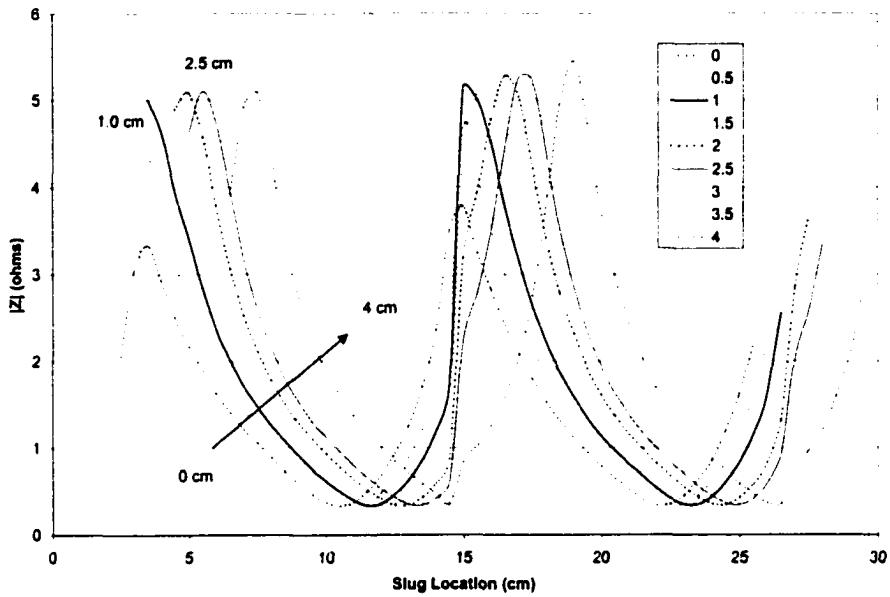

Figure A.4.1-5. Effect of Distance Corrections for Impedance Measurements. An offset of 2.5 cm corresponds to actual separation; 1.0 cm yields the most correct waveform.

A.4.1.2 Rieke Diagram

Having measured the 'correct' load reflection coefficient, this may be plotted on the Smith chart. The set of points from each tuning slug may be combined to show the general characteristics of the magnetron and load, such as the general location of the 'sink' (region of no oscillation). The entire set of load impedances tested for the MDA is shown in Figure A.4.1-6.

The impedance data by itself provides some insight into the effects of the tuning slug on the MDA performance. The pattern of points for each slug forms a circle on the Smith chart, repeating every ½ guide wavelength (~11.5 cm at 2.45 GHz). The relative spacing of the points identifies areas having stronger influence on the magnetron behavior. This

region is referred to as the sink of the Rieke Diagram. This corresponds to the 'steep' frequency transition region discussed in Chapter 5.

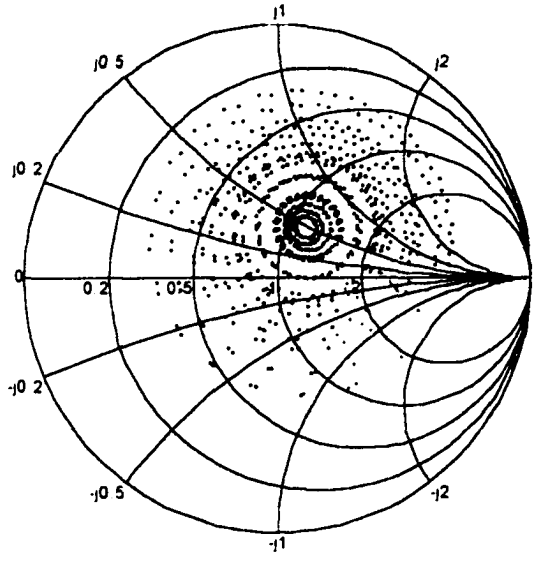

Figure A.4.1-6. Set of all MDA Load Impedances. Light blue points indicate general region of 'sink' for Rieke diagram.

The Rieke diagram is then constructed by tracing out contours of constant frequency and power. Constant frequency contours roughly parallel reactance lines of the Smith chart, while power contours generally parallel resistance lines. A sample Rieke diagram obtained for the Class III OL MDA is shown in Figure A.4.1-7.

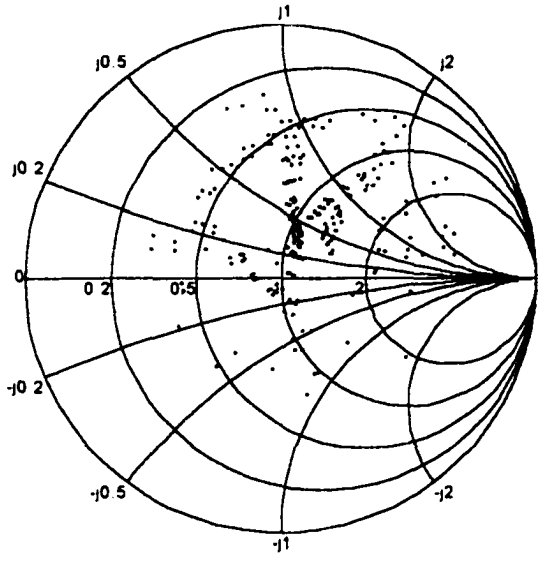

Figure A.4.1-7. Rieke Diagram for MDA. (Magenta: frequency contours, 5 MHz intervals; Blue: output power, 120 W intervals)

For distinct frequency and power contours, more data points (load conditions) are needed, especially in the region of the sink. However, an alternate form of the Rieke diagram may be constructed showing the data plotted in continuous bands. In this case, the data is presented using separate plots for the frequency and power data, as shown in Figures A.4.1.8 and A.4.1-9.

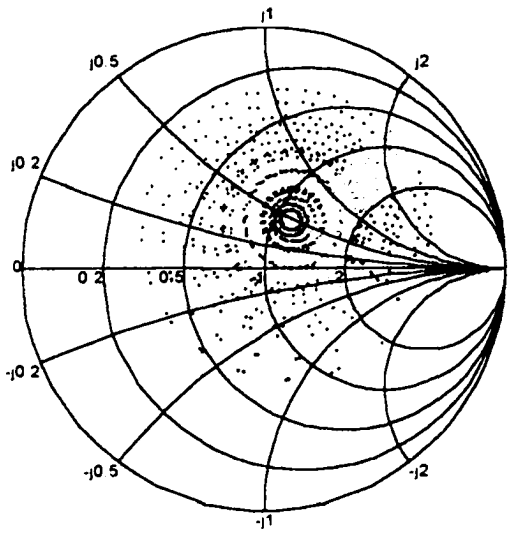

Figure A.4.1-8. MDA Operating Frequency Bands. Bands are 5 MHz wide, beginning at 2.42 GHz (black → magenta → ... → black).

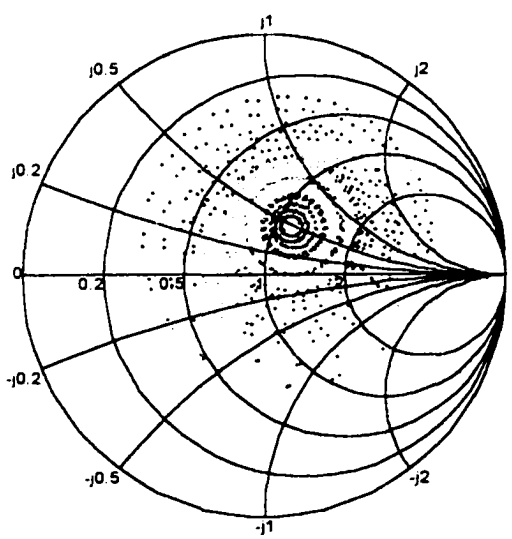

Figure A.4.1-9. MDA Output Power Bands. Bands are 0.1 mW wide, beginning at 0.8 mW (black → ... → orange). Corresponding output power levels are bands of ~50W, beginning at 380W.

Of interest is the effect of different sized tuning slugs on the behavior of the magnetron. Figure A.4.1-10 shows an overlay of tuning slug positions displayed as radial pinwheel lines on the Smith chart.

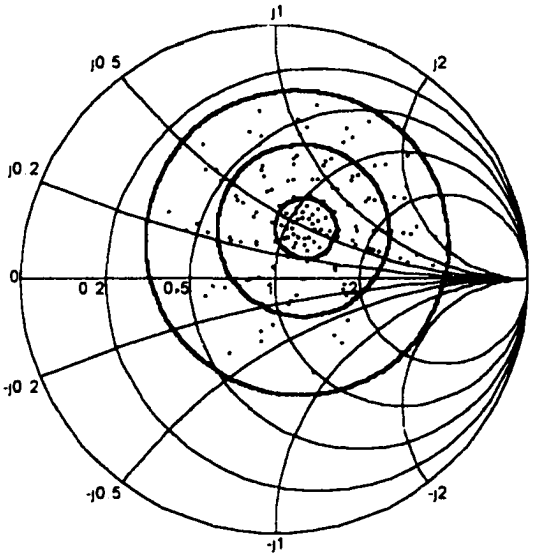

Figure A.4.1-10. Lines of Constant Slug Size and Location for the MDA. Radial lines indicate relative slug position; circles show possible impedance values for MDA load with different slugs.

Red lines indicate the approximate bounds on the sink region. Concentric circles trace all possible impedance values for the MDA load as the slugs move through a distance of $\lambda/2$. The intersection of the radial position lines and the circular impedance traces define points of operation for each slug. In the sink region, a given slug position change produces a disproportionately high change in the operating frequency and output power.

The motion of the tuning slugs along the trace lines helps explain the performance characteristics of the magnetron. Below is a curve showing MDA power output as a function of tuning slug position for three different slug sizes. Low power output (efficiency) regions, such as 8 – 10 cm correspond to poor impedance matching regions

on the Smith chart, whereas high efficiency regions correspond to good impedance conjugate matching regions (sink) of the Smith chart.

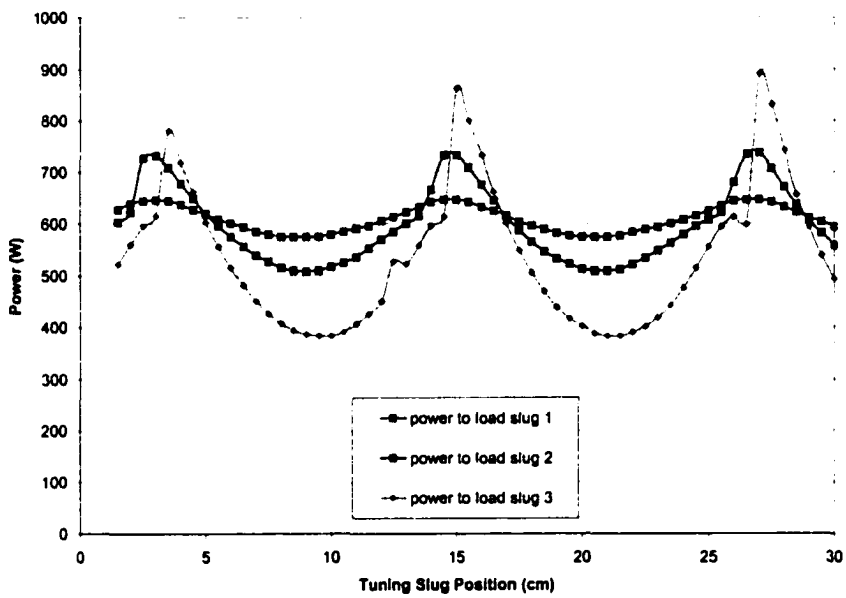

Figure A.4.1-11. Output Power versus Tuning Slug Position.

The sink regions and low efficiency regions are highlighted on the Smith chart in Figure A.4.1-12. Slug motion along the low efficiency region produces relatively little change in the MDA operating point. The same amount of slug travel in the sink region produces larger impedance changes. This is further exaggerated by the nature of the sink region in Figure A.4.1-8. A given amount of impedance change (shown as motion along the slug trace) provides a much larger change in the MDA response.

Likewise, the operating frequency of the MDA may be explained using the Rieke diagram. Smaller slugs gradually traverse the lines of constant frequency — the slope is somewhat steeper nearer the sink, but still relatively gentle. Larger tuning slugs cut across numerous frequency contours in the sink region, providing dramatic change in operating frequency for relatively little slug movement. The corresponding frequency response for the Class III MDA is given in Figure A.4.1-13.

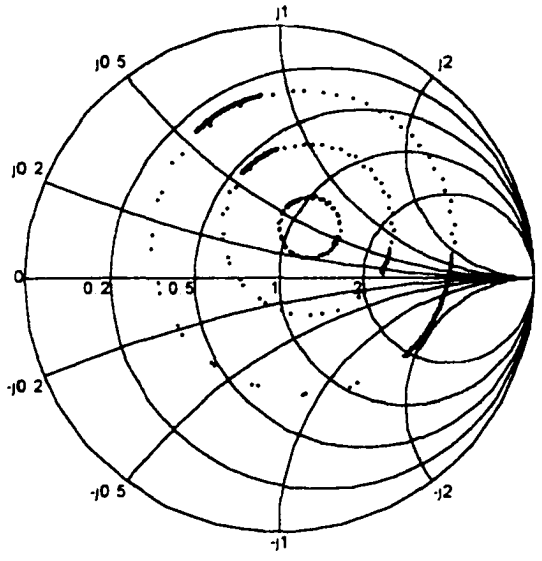

Figure A.4.1-12. Efficiency Regions for the MDA. Red regions indicate high power efficiencies; magenta denotes low efficiency regions. Larger tuning slugs (larger circles) provide more swing in efficiency.

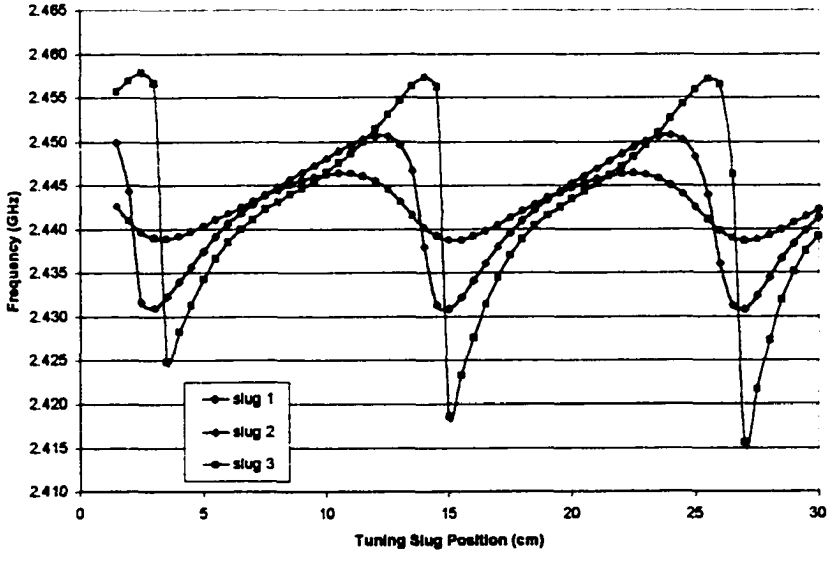

Figure A.4.1-13. Operating Frequency versus Tuning Slug Position. Larger slugs provide more frequency range and a steeper transition region.

The Rieke diagram may be put in rectangular format, as shown in Figure A.4.1-14. The efficiency is plotted as a function of frequency for all data points using four different sized tuning slugs. Slug 1 is relatively small from a reactance point of view, and therefore, affects the efficiency very little. The no-slug operating point is located at the centroid of the loop (f = 2.443 GHz, ε = 50.8%).

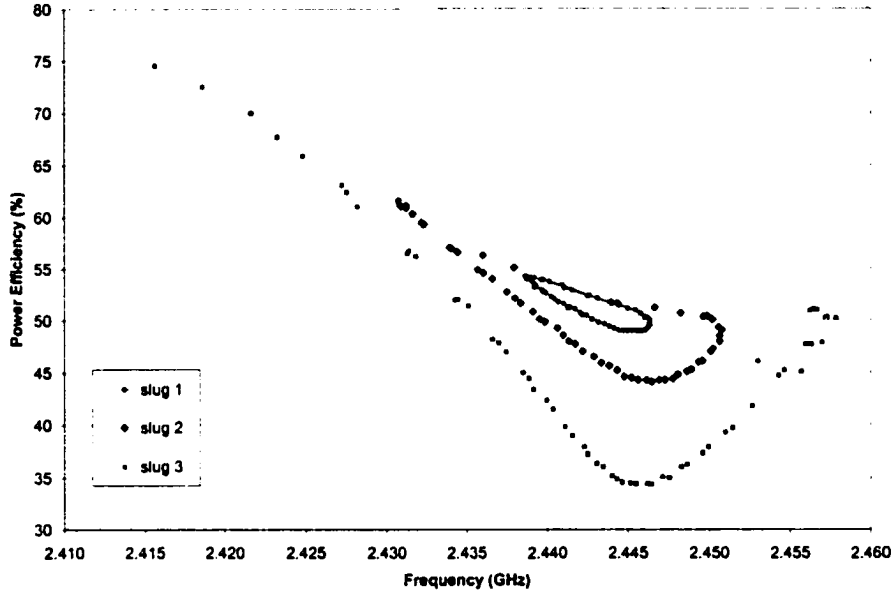

Figure A.4.1-14. Efficiency as a Function of Operating Frequency for a Class III MDA. Larger slugs provide a wider range of tuning.

As the slugs increase in size, the efficiency pattern becomes distorted. More of the operating points are eventually pulled down to lower operating efficiencies. However, the data points occupying the upper region of the curves do not extend directly upwards. Instead, these points are stretched across a comparatively large frequency range, forming a boundary. This boundary represents the sink region of the Rieke diagram.

Sparseness of the high efficiency data points on the 'handle' (sink) can be viewed as a relative measure of stability. Points located near the top of the handle are difficult to

achieve, requiring heavy loading of the magnetron and precise control. A tuning slug a that is sufficiently large for the waveguide will eventually exceed the magnetron's ability to operate. High temperatures associated with the low efficiency region may damage the magnetron RF probe. Alternately, operation in the very high efficiency region may cause destruction of the magnetron or the DC power supply.

A.4.1.3 Impedance Measurements Using Modified Magnetron Probe

Later in the characterization effort, it was desired to examine the influence of the shorting plate position on the operation of the MDA. Therefore, the coax/waveguide adapter could no longer be used. Instead, a test probe emulating the magnetron RF probe was fabricated. This was constructed by cannibalizing one of the Samsung magnetrons (S/N 5237). The probe attaches to the waveguide at the magnetron mounting plate. A diagram of its construction is shown in Figure A.4.1-15.

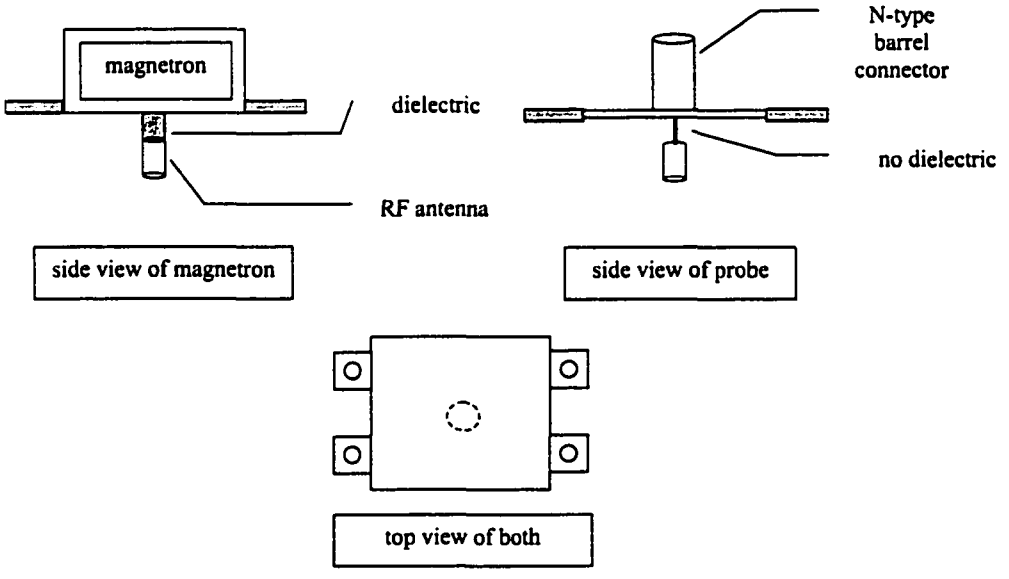

Figure A.4.1-15. Impedance Probe Schematic.

The network analyzer was attached to the probe to measure the impedance of the MDA from the magnetron's perspective. For each location of the shorting plate, the tuning slug was moved throughout its normal range, taking an impedance measurement at each point. The test configuration used is shown in Figure A.4.1-16.

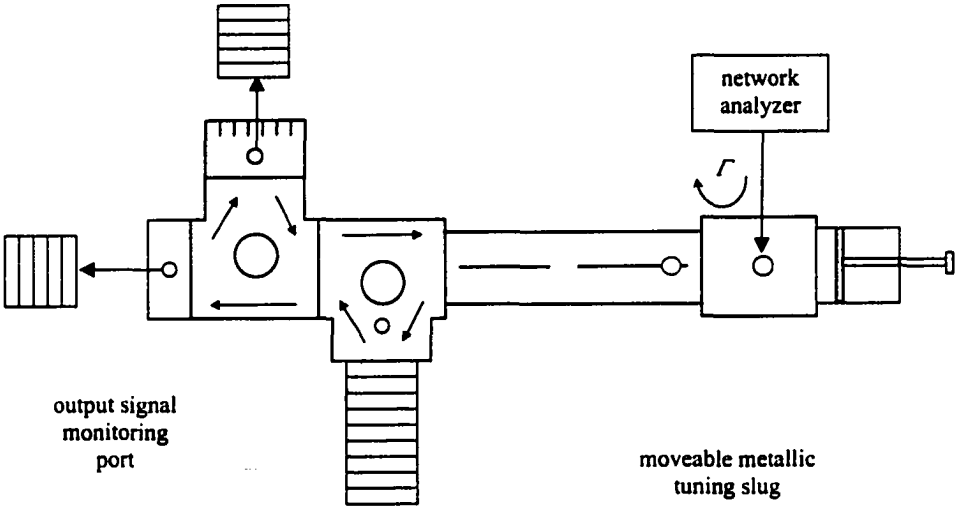

Figure A.4.1-16. Impedance Measurement Test Configuration.

This data was then plotted on the Smith Chart shown in Figure A.4.1-17. To show the difference between the measurements using this homemade probe versus the previous coax/waveguide adapter method, the plots for two slugs are given for each. As can be seen above, the two probes yield quite different patterns. The coax/waveguide adapter couples more of the RF energy, and therefore provides larger patterns. The homemade probe couples relatively little energy in comparison. The coax/waveguide adapter also shows the sink region being located toward the bottom right of the graph, whereas the homemade probe shows this in the upper left portion of the circles.

For precise measurements, it is necessary to utilize a probe with the same antenna shape as the magnetron being tested. The probe must also be tuned and calibrated according to specifications. However, much may be learned by studying the relative influences of the

shorting plate and tuning slug. This may be accomplished with a simple probe such as was shown in Figure A.4.1-15.

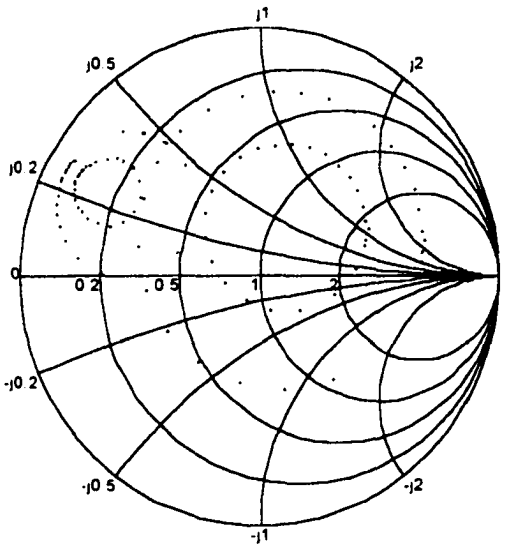

Figure A.4.1-17. Comparison of MDA Impedance Traces for Two Different Probes. Blue circles taken by previous coax/waveguide adapter; red circles resulting from new magnetron type probe. Both sets show data for slugs 2 (inner) and 3 (outer).

The probe measured the impedance of the MDA as a function of both shorting plate location and tuning slug position. A plot showing the combined effects is provided below. The analysis of these effects is provided in Appendix A.4.8.

With the graphical tools developed, the MDA performance may be analyzed in terms of the Smith chart. Analysis of each class of MDA is provided in the appropriate sections of Chapter 5.

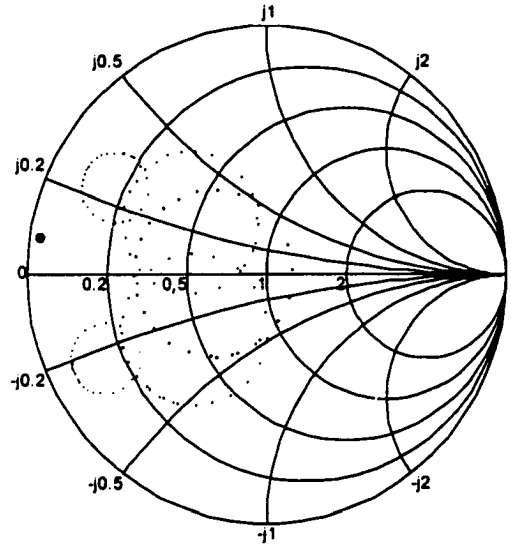

Figure A.4.1-18. Effect of Shorting Plate and Slug on a Class III MDA. View of impedance circles for slug 2 from magnetron probe.

A.4.2 Waveguide Size

This section discusses the effect of waveguide size on the operation of the MDA. The interaction of the magnetron and the load is complex, where the load includes everything that affects the total impedance seen at the output of the magnetron RF probe. This includes the primary load, tuning slug size and location, injected reference signal, and the waveguide component characteristics. The waveguide size itself affects the impedance of the load.

The transverse impedance inside the waveguide may be defined in terms of the guide size and the operating frequency. The normalized impedance for the TE_{10} mode is calculated by the equation [22]

$$z_T = \frac{1}{\sqrt{1-\left(\frac{f_c}{f}\right)^2}} = \frac{1}{\sqrt{1-\left(\frac{\lambda}{\lambda_c}\right)^2}} = \frac{1}{\sqrt{1-\left(\frac{\lambda}{2a}\right)^2}}, \qquad \text{(A.4.2-1)}$$

where

z_T = normalized ransverse impedance
f_c, λ_c = cutoff frequency, wavelength
f, λ = operating frequency, wavelength
a = major interior dimension of the waveguide.

The geometry for the interior of the waveguide is shown in the diagram below.

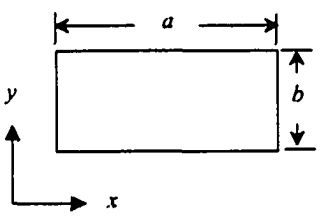

Figure A.4.2-1. Geometry for Waveguide Interior.

The present MDA configuration at UAF uses WR-284 waveguide, which was designed for operation in the 2.6 – 3.95 GHz frequency band. Although this size is convenient from a space/weight perspective, it is not ideally suited for the 2.4 – 2.5 GHz ISM band. The transverse impedance for this size waveguide is shown in Figure A.4.2-2.

The WR-284 waveguide (top curve) displays a substantial impedance change over the ISM band. The next two larger waveguide sizes are included for comparison purposes. The center curve shows the impedance for WR-340 waveguide, which is designed for the 2.2 – 3.3 GHz range. The bottom curve is the impedance response for WR-430, which is intended for use at 1.7 – 2.6 GHz.

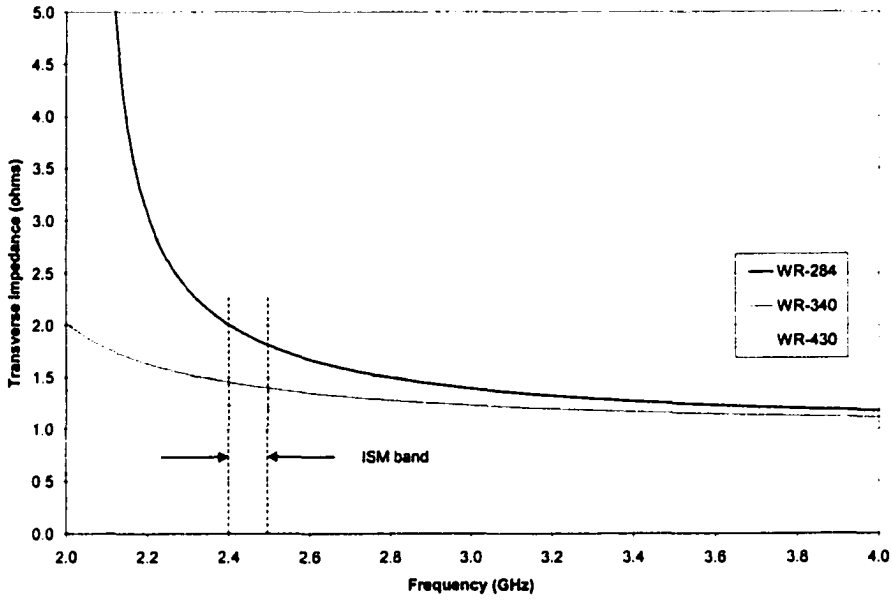

Figure A.4.2-2. Transverse Impedance for Standard Waveguides at 2 – 4 GHz.

The effect of the waveguide size came into question because of large performance differences between William Brown's MDA configuration and our own. Upon investigation, it was determined that the waveguide used in the two hardware configurations varied slightly in size. The interior dimensions of the actual waveguide varied from the standard sizes shown above. UAF's waveguide is essentially WR-284; Brown's had been homemade and was nearer in size to WR-340. The measurements and associated cutoff frequencies for all the sizes are shown in Table A.4.2-1.

Table A.4.2-1. Waveguide Interior Dimensions.

	WR-284	WR-340	WR-430	Brown	UAF
a (in)	2.84	3.40	4.30	3.248	2.815
b (in)	1.34	1.70	2.15	1.575	1.299
f_c (GHz)	2.079	1.737	1.373	1.818	2.098

The calculated values of transverse impedance for each waveguide across the 2.4 – 2.5 GHz ISM band are plotted in Figure A.4.2-3. For this frequency range, the impedance curves may be approximated as straight lines.

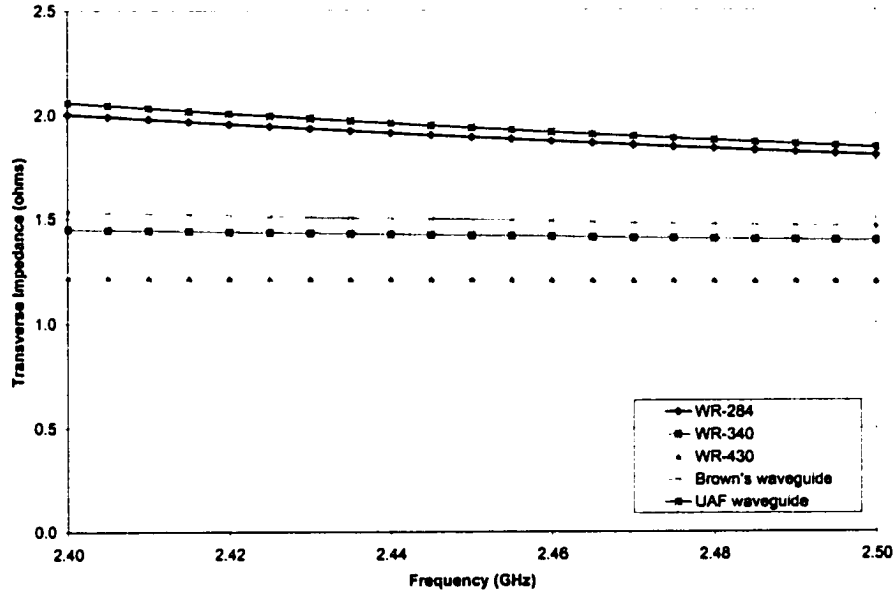

Figure A.4.2-3. Transverse Impedance for Different Size Waveguides at 2.4 – 2.5 GHz.

The impedance variance across the ISM band was then calculated for each of the waveguide sizes, using the formula

$$\Delta z(\%) = \frac{z_{2.5\,\mathrm{GHz}} - z_{2.4\,\mathrm{GHz}}}{z_{2.45\,\mathrm{GHz}}}. \qquad \text{(A.4.2-2)}$$

The resulting values for each waveguide are shown in Table A.4.2-2. The difference in impedances across the band helps to explain the different output power for the two configurations, since output power varies with the MDA load impedance.

Table A.4.2-2. Impedance Variance Across the ISM Band.

	$Z_{2.4\ GHz}$ (Ω)	$Z_{2.45\ GHz}$ (Ω)	$Z_{2.5\ GHz}$ (Ω)	ΔZ (%)
WR-284	2.003	1.891	1.801	10.65
WR-340	1.449	1.418	1.390	4.14
WR-430	1.219	1.208	1.197	1.87
MPTS	1.532	1.492	1.457	**5.03**
UAF	2.059	1.936	1.839	**11.38**

The above analysis is only based upon the theoretical load impedance presented by the waveguide. As mentioned, the accuracy of this is limited by introducing the tuning slug into the waveguide. It is also limited by only examining the magnitude of the impedance. In reality, the phase of the impedance also plays a large role in determining the power and frequency of the MDA.

The total load presented to the magnetron in the Class III MDA is chiefly composed of the primary load and a tuning slug. Figure A.4.2-4 shows a Smith chart with the possible load impedance values for 16 different sized tuning slugs measured at various positions along the waveguide. A total of 752 load impedance values were measured.

The centroid of the concentric circles represents the impedance of the primary load without a tuning slug. The offset from the center is caused by operating at a frequency of 2.45 GHz in the WR-284 waveguide. Though the ISM band is above the cutoff frequency of 2.078 GHz, the waveguide does not provide an optimum impedance match. To illustrate, Figure A.4.2-5 shows a plot of load impedance versus frequency for WR-284 waveguide using a precision matched load.

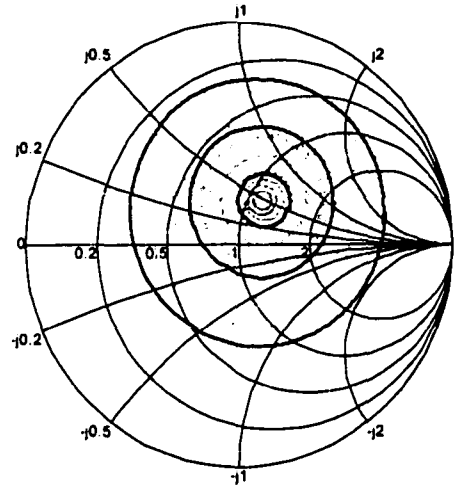

Figure A.4.2-4. Load Impedances for Class III MDA. Data shown for WR-284 waveguide at 2.45 GHz. Circles trace all possible values of load impedance for slugs 1 – 3. Slug 1 data shown in center.

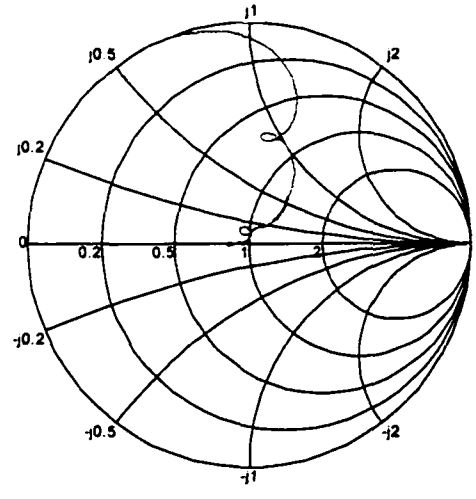

Figure A.4.2-5. Load Impedance versus Frequency for WR-284 with Precision Load. As the frequency is increased above cutoff, the load impedance curve begins to spiral inward toward a more nearly matched load condition. The darkened portion of the trace represents impedances at 2.4 – 2.5 GHz.

The MDA load subassembly presents similar impedance characteristics. Figure A.4.2-6 is a plot of load impedance versus frequency for the MDA load. This plot shows the no-slug impedance of the MDA load at the center of the slug traces.

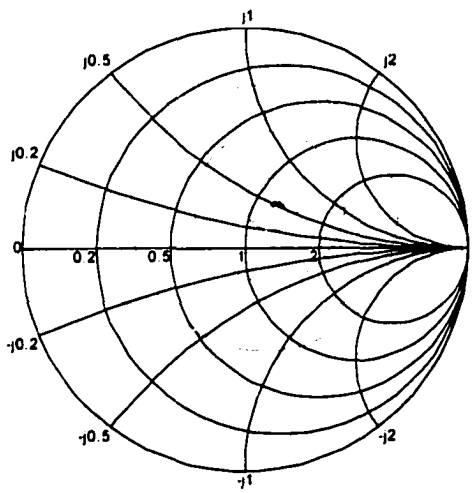

Figure A.4.2-6. Load Impedance for MDA Subassembly. Looped trace at center shows load impedance for ISM band (no slug). Circular traces show total impedance seen by magnetron for slugs 1 – 3.

Following this rationale, it should be possible to center the slug traces by utilizing a waveguide size which provides a better impedance match in the ISM band, such as WR-340 or WR-430, or by operating at a frequency where this waveguide is better matched to the load. As the frequency is increased from 2.45 GHz towards 4.0 GHz, the slug traces should migrate about the corresponding no-slug load impedance for that frequency. Results of the investigation are shown in Figure A.4.2-7.

Slug impedances traced a closed path about the no-slug point for that frequency. When operating at frequencies where the no-slug point is near the center of the Smith chart, the traces formed nearly concentric circles about the point, as shown in Figure A.4.2-7(b).

Figure A.4.2-7(a) shows that operating at frequencies near the edge of the chart exaggerated the path deformation.

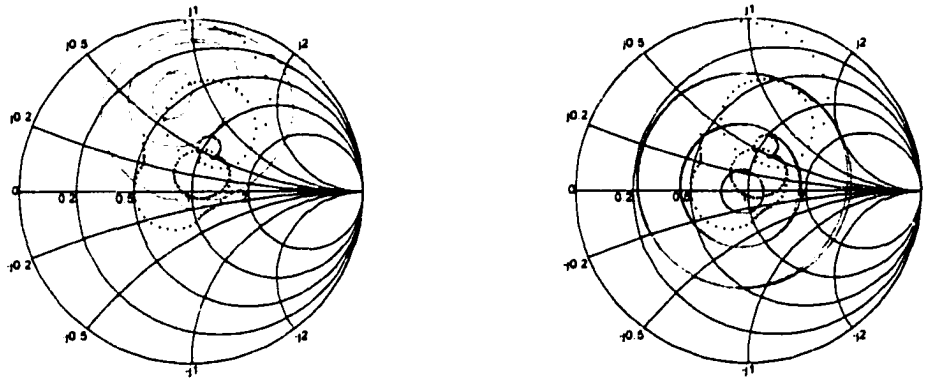

(a) f = 2.2 GHz (b) f = 2.6 GHz

Figure A.4.2-7. Traces of Slugs 1 – 3 for Different Frequencies. Load impedance without a slug from 2.1 – 2.9 GHz is shown by the dotted line. Slug traces at 2.2 GHz are compressed by boundary of Smith chart. Traces at 2.6 GHz are nearly concentric and show the no-slug load to be matched (at center).

The characteristics of the MDA operating with WR-340 waveguide may be estimated by examining the higher frequency response of WR-284. Figure A.4.2-8 shows the no-slug impedance of the MDA as a function of frequency. This plot shows that the impedance is better behaved in the vicinity of 2.6 GHz. The resonant loop appearing in the ISM band has been removed. It is believed that operation of the MDA using WR-340 waveguide will likewise produce more predictable results.

It must be stated that the above impedance analysis is subject to certain limitations. First, it is assumed that the measured impedance may reasonably approximate that seen by the magnetron. This has been shown to be roughly true (Appendix A.4.1), but not within a specified accuracy. To accurately measure the impedance, a probe closely emulating the

characteristics of the actual magnetron RF probe is required. This would provide the added capability to examine the effects of the shorting plate position (Appendix A.4.8).

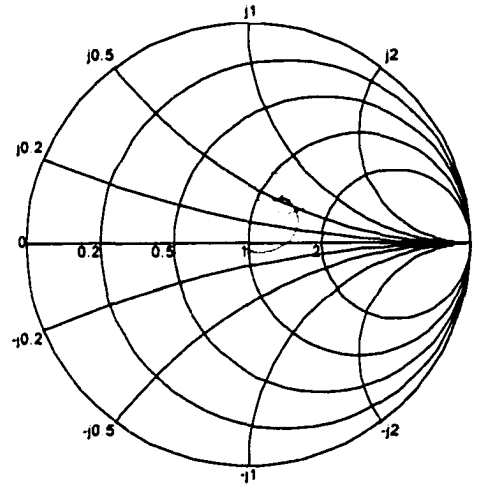

Figure A.4.2-8. MDA No-Slug Load Impedance for 2.3 – 2.6 GHz. Darkened portion of trace shows impedance in ISM band. Lighter portions show impedances in the 2.2 – 2.3 GHz and 2.5 – 2.6 GHz bands. Point located nearest center of chart corresponds to 2.6 GHz.

The recommended choice of waveguide size depends upon many factors. On the positive side, WR-284 is smaller and lighter than WR-340 (18% by weight). This can add up to substantial cost saving on large-scale projects. It will also generally be less expensive to purchase waveguide lengths at this size. These factors are quite important in demonstrating the viability of the WPT systems.

Some performance gain should be possible by upgrading to WR-340 waveguide. It has been shown that the transverse impedance of the smaller WR-284 varies more across the ISM band. This will result in more variation of the power output. However, it is not entirely clear how the tuning slug affects the overall impedance. The slug obviously provides a better conjugate match to the magnetron and may therefore dwarf the effects

of the waveguide size. Yet, the overall impedance does appear to be affected by the offset from the center of the Smith chart. It seems that both components may play a significant role in optimizing the MDA performance.

It is also known that WR-284 is more temperamental in applications at this frequency. The variation in size of the waveguide can affect system performance, and therefore must be closely scrutinized for high-power applications [28]. The sensitivity of the impedance to the waveguide dimensions amplifies the effects of thermal loading. Small changes in the expansion of the waveguide can therefore provide rather large power fluctuations. In this way, the waveguide provides a tight bandpass filter (it is an *RLC* circuit). This thermal loading appears to be responsible for a good deal of the moding behaviors seen in the MDA operation. A larger waveguide size would provide a more forgiving bandpass characteristic.

The larger waveguide would provide better power stability across the frequency range, but may prevent the magnetron from running at peak efficiency. A large tuning slug may have be required to achieve the same efficiency results, which will tend to destabilize the power response.

One aspect of the waveguide size that may be readily characterized is the power loss to surface resistance in the guide. The formula for the copper losses is given as [22]

$$\alpha_c = \frac{R_s}{b\eta\sqrt{1-\left(f_c/f\right)^2}}\left[1+\frac{2b}{a}\left(\frac{f_c}{f}\right)^2\right] \qquad \text{(A.4.2-3)}$$

where

α_c = attenuation $[\text{nepers} \cdot \text{m}^{-1}]$
R_s = surface resistivity $[\Omega]$
a, b = major, minor dimensions of waveguide $[\text{m}]$
η = impedance of free space $\approx 377\ \Omega$
f_c = cutoff frequency in guide $[\text{Hz}]$
f = operating frequency $[\text{Hz}]$.

For copper WR-284 waveguide operating 2.45 GHz, the value for the attenuation is $\alpha_c|_{\text{WR-284}} = 1.968 \cdot 10^{-3}$ nepers$\cdot$m^2. For the WR-340 waveguide, the attenuation had dropped to $\alpha_c|_{\text{WR-340}} = 1.294 \cdot 10^{-3}$ nepers$\cdot$m^2. For short runs, the attenuation is negligible. However, the calculation shows that the WR-340 waveguide absorbs less energy, and therefore is not as susceptible to fluctuations.

This section has attempted to compare the relative performance of WR-284 and WR-340 waveguide to ascertain whether the larger size would benefit the MDA performance. This is hard to predict without testing the proposed configuration. Developing an analytical model to predict the MDA power output and frequency versus the tuning slug is difficult, as the magnetron is a nonlinear device. Predicting the MDA performance based upon impedance measurements has not yet been successful either. Precision probes are needed to obtain impedance data similar to that seen by the magnetron RF probe. In light of the unique characteristics observed over this characterization effort, it seems prudent to construct an MDA of WR-340 components and test it.

A.4.3 Probe Depth

This section describes the effect of changing the magnetron coupling to the waveguide, which may be altered by varying the depth of the RF probe in the waveguide.

During the course of characterizing the MDA, the primary magnetron used for the task was damaged (Samsung 2M181 S/N 5194). The damage sustained was a gradual erosion

of the RF probe antenna due to low-level arcing. The effects of this are discussed in Appendix A.4.5. Four new generic magnetrons were purchased to (1) increase the inventory should this unit fail, and to (2) provide a sample of performance variation for new magnetrons. However, getting these units to operate with the MDA hardware configuration proved troublesome. This launched an investigation into the methods for coupling the magnetron to the waveguide, which included adjusting the probe depth and locating the shorting plate. The details of the shorting plate characterization are given in Appendix A.4.8.

As a result of this effort, the probe depth was found to affect the operation of all of the magnetrons. The coupling of the magnetron to the waveguide is maximized when the RF antenna is centered within the guide. A diagram of this is shown in Figure A.4.3-1.

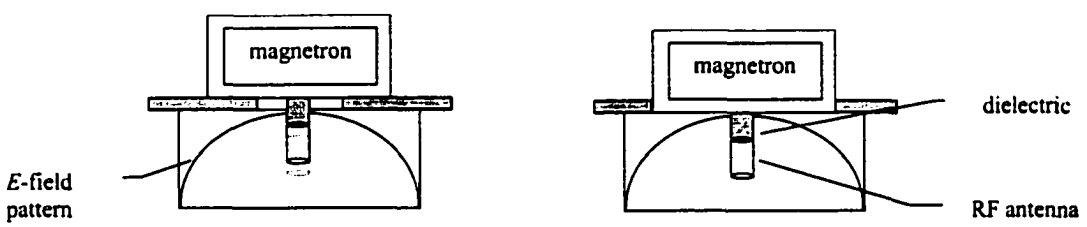

(a) previous position (b) corrected

Figure A.4.3-1. Magnetron Probe in Waveguide.

It was determined that the original fan/magnetron mounting plate kept the magnetron probe from being centered. The plate was therefore modified to alleviate this condition.

The probe depth had a strong effect upon the magnetron operation. Centering the probe restored the magnetron's tuning range to a value exceeding that prior to the damage. A history of the frequency response for the MDA is shown in Figure A.4.3-2.

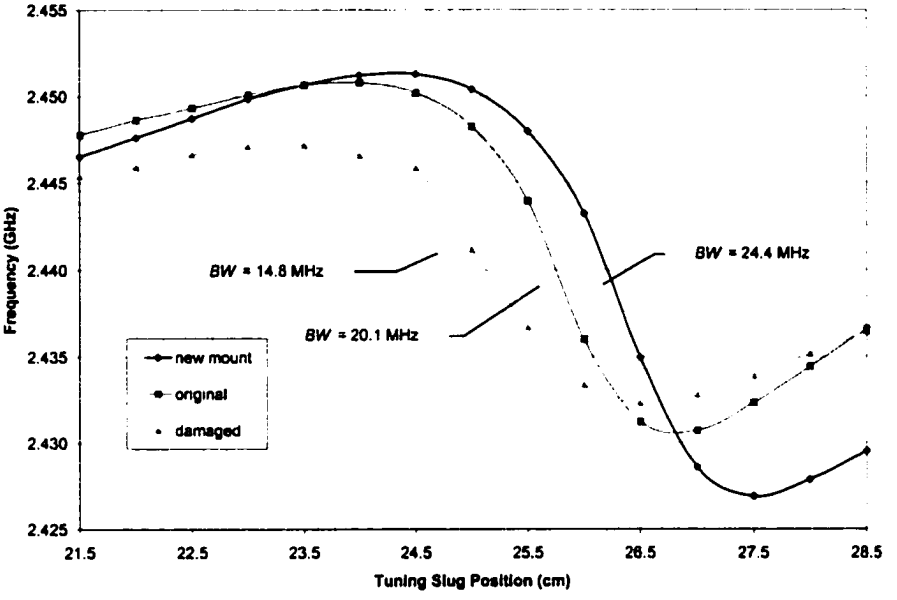

Figure A.4.3-2. Samsung 2M181 S/N 5194 Frequency Performance History. Data shown for I_{anode} = 300 mA, slug 2.

The original magnetron configuration provided a bandwidth of 20.1 MHz for slug 2 at 300 mA (performance for all 16 slugs is summarized in Figure 5.4-10). When the damage to the magnetron was recognized, this amount had been reduced approximately by 25% to a value of 14.8 MHz. By properly adjusting the probe depth, however, even more frequency pulling was regained. This effect increased the bandwidth by almost 65% to a value of 24.4 MHz (over 20% overall gain).

Because of the linear nature of the frequency curves in Figure 5.4-8, these values should scale accordingly to account for the increased coupling. For example, the new tuning range of slug 1 would be

$$\Delta f_{max} \approx 1.2(7.7\ \text{MHz}) = 9.2\ \text{MHz}.$$

The new pulling range for slug 16 would be

$$\Delta f_{max} \approx 1.2(29.9\,\text{MHz}) = 35.9\,\text{MHz}.$$

This slug is now approaching the value of tuning provided originally by slug 3. Since it is believed that slug 3 was responsible for the damage to the magnetron, caution is suggested when using either of these slugs.

It is not surprising to find that increasing the magnetron coupling to the waveguide also increases its power output and efficiency. Decreasing the resistance of the interface permits the RF energy to flow more freely. The comparative efficiency responses are shown in Figure A.4.3-3. Of particular interest is the improved efficiency that occurred with the damage to the RF probe. The deformation ironically provides a better impedance match than did the original antenna. The efficiency response is further improved by the probe depth adjustment. The overall gain from the original configuration to the existing one is ~11% efficiency.

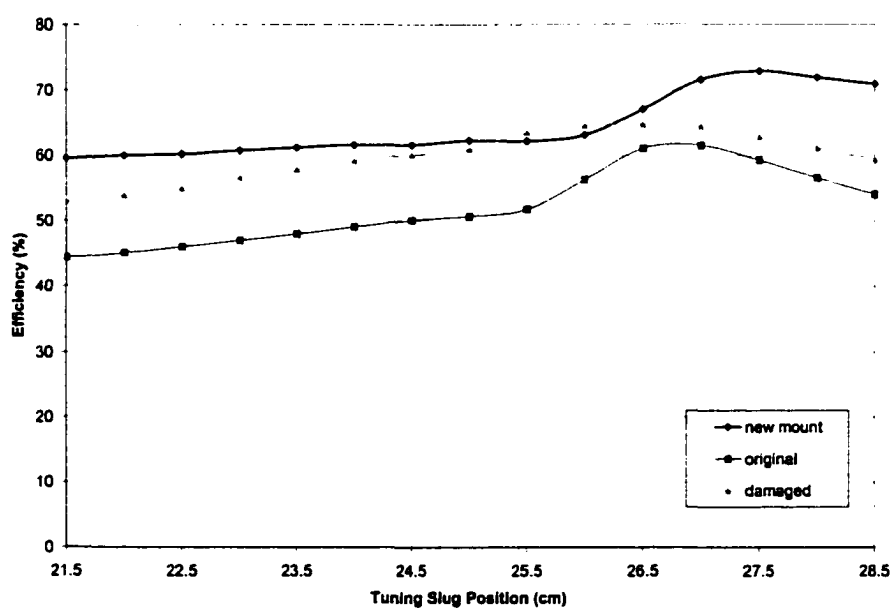

Figure A.4.3-3. Samsung 2M181 S/N 5194 Efficiency Performance History.

The corresponding output power curves are shown in Figure A.4.3-4. The adjustment in probe depth has resulted in an increase of maximum power from 737.1 to 919.0 W (almost 25%). The input power drawn on the supply is shown in Figure A.4.3-5. Because of the increased efficiency, the jump in power drawn is only ~5.4%.

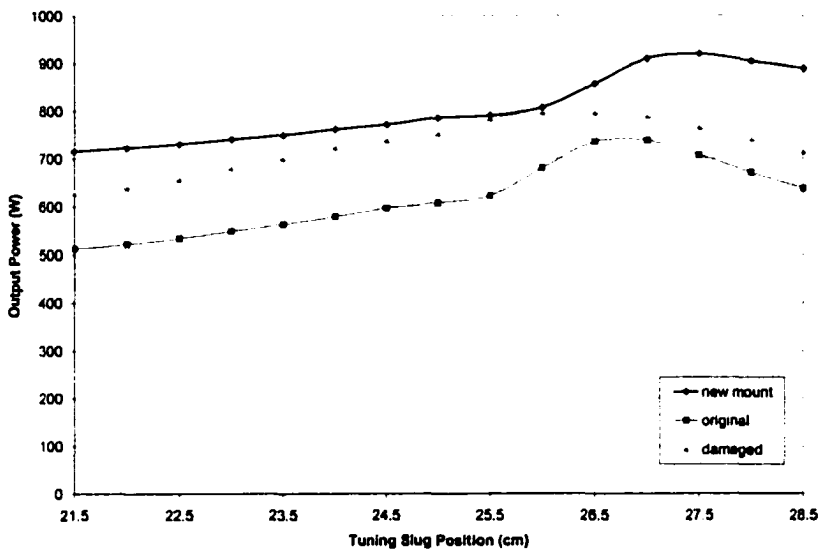

Figure A.4.3-4. Samsung 2M181 S/N 5194 Output Power Performance History.

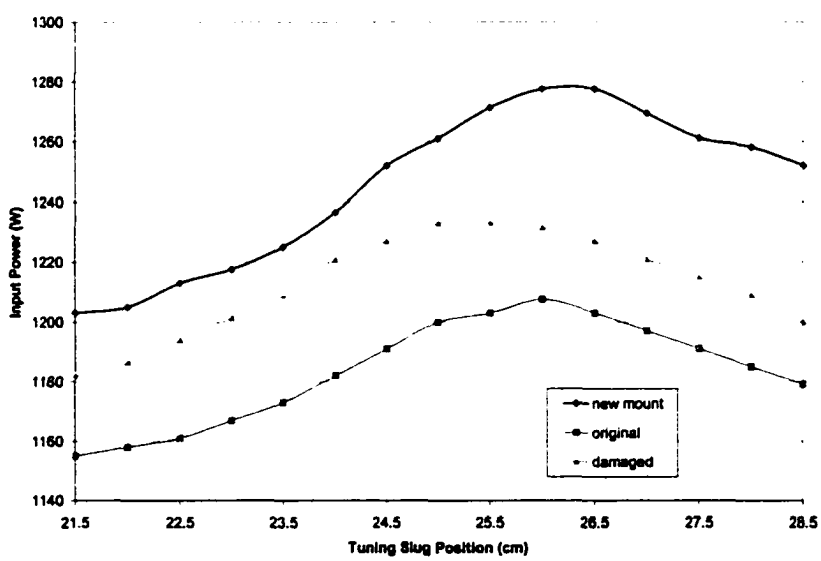

Figure A.4.3-5. Samsung 2M181 S/N 5194 Input Power Performance History.

The coupling between the probe and the waveguide may be modeled as an ideal transformer. From Section 4.2, the equivalent circuit diagram for one vane of the loaded magnetron is shown in Figure A.4.3-6.

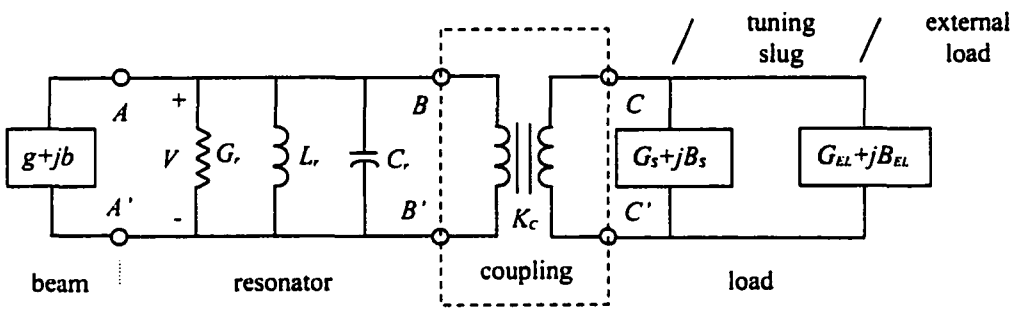

Figure A.4.3-6. Equivalent Circuit for a Class III MDA.

These parameters are defined by:

$Y_e = g + jb$ = electronic admittance of electron beam
V = RF voltage across vane tips
G_r = conductance of resonator
L = inductance of resonator
C = capacitance at vane tips
$Y_S = G_S + jB_S$ = admittance of tuning slug
$Y_{EL} = G_{EL} + jB_{EL}$ = admittance of external load
K_c = transformer constant between load and resonator.

The transformer constant *transforms* values of admittance across the probe boundary. This may alternately be written in terms of the transformer's turns ratio.

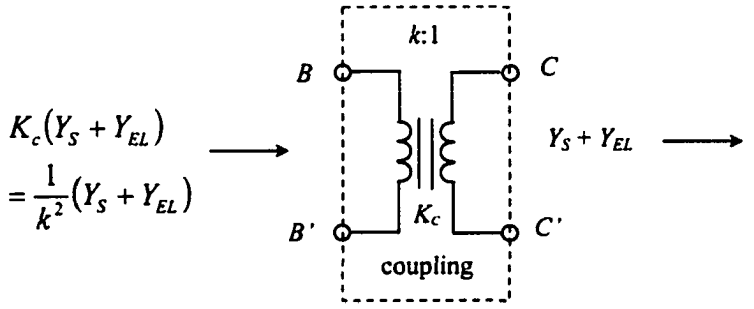

Figure A.4.3-7. Transformer Model for Magnetron RF Probe.

Increasing the coupling between the magnetron and probe increases the load admittance changes seen by the magnetron. This makes the magnetron more tunable, as the injected (or reflected) signals are coupled more strongly into the probe. It also increases the efficiency and power delivery capability of the magnetron.

Most magnetrons are tested using a standard size launching section, which may be constructed of waveguide up to WR-430 size. The magnetron performance should be examined in a variety of launching section sizes to determine these effects. This could ultimately drive the size of waveguide components used in the MDA.

A.4.4 Magnetron Comparison

This section describes performance differences between the primary magnetron used for baselining the MDA performance (Samsung 2M181 S.N. 5194) and two others of the same model. The purpose of this discussion is to highlight the performance diversity that may reasonably be expected between similar models or like models with a different usage history. This data is particularly relevant to the design of ESPAM-based phased arrays.

The single-axis beamsteering demonstration at UAF (Section 6.4) had identified a large difference in the free-running frequencies of the two ESPAM units. Both magnetrons

were of the same model, however this caused no real concern as the hardware configurations for the two units were quite different.

A.4.4.1 Performance of Magnetrons

During the MDA characterization it was found that the primary magnetron had been damaged, altering its operating characteristics (Appendix A.4.5). Since most of the data had been based upon this particular unit, another was introduced at this point. Baselining the performance differences between the units now might provide an easier transition.

The next step was to compare the operation of the two other Samsung 2M181 magnetrons in the MDA. The Class III OL MDA with tuning slug 2 (Table 5.4-1) was selected as a baseline. Each data set was run using power supply 1 at 300 mA anode current. The frequency response of the three units showed a surprising level of diversity, as shown in Figure A.4.4-1.

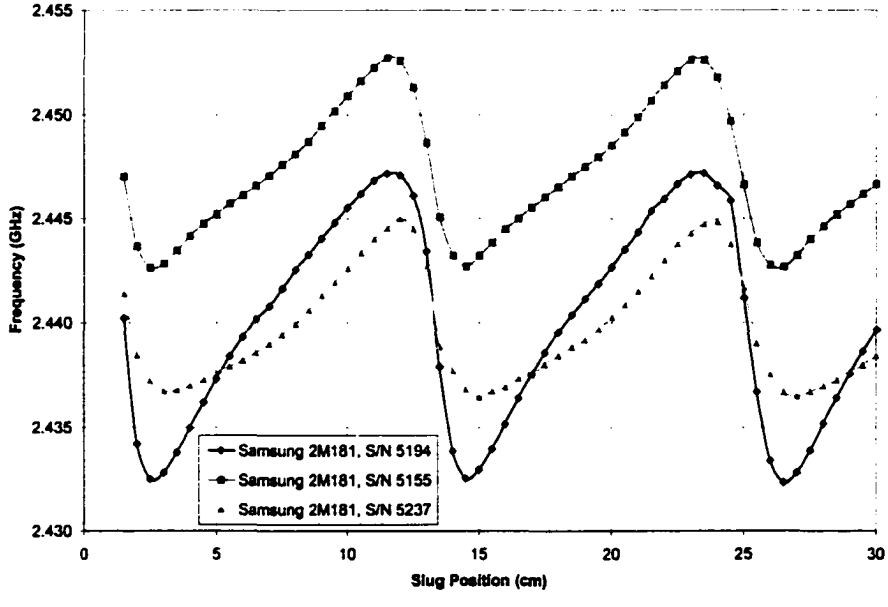

Figure A.4.4-1. Frequency Comparison for Samsung 2M181 Magnetrons. Data shown for I_{anode} = 300 mA, slug 2.

This comparison reveals significant differences between the magnetrons, both in locking range and in center frequency. Their center frequencies and bandwidths are summarized in Table A.4.4-1. S/N 5194 was the primary unit used throughout the MDA characterization effort and had been run heavily loaded for extended periods of time, as discussed in Appendix A.4.5. Even after sustaining the damage to the RF probe, this magnetron exhibited superior frequency characteristics. Prior to this, the bandwidth for this configuration had been even larger (20.05 MHz centered about 2.44193 GHz).

S/N 5155 had been part of Mr William Brown's own MDA configuration, which was provided to UAF for the purpose of comparing our results. This unit had undoubtedly been operated extensively over the years. Note that this was the same magnetron used in the slave ESPAM for the beamsteering demonstration (Section 6.4). Given the difference in frequency characteristics shown above, the 14 MHz separation between the ESPAM units becomes more understandable.

S/N 5237 had been in the possession of UAF for some time, but had not been used recently. The alignment pins in the mounting plate had been sheared, although the cause for this is not known. The plate consequently had to be machined prior to using this magnetron. This magnetron shared the same center frequency as S/N 5194, and therefore would provide a much easier frequency match for the 2-element array (given the same load impedances).

Next, the power characteristics of the magnetrons were examined. The corresponding efficiency curves are shown in Figure A.4.4-2. Again, the primary magnetron performed strongly alongside the others. Therefore, in this MDA configuration, S/N 5194 provided the best performance and was retained throughout the reminder of this effort.

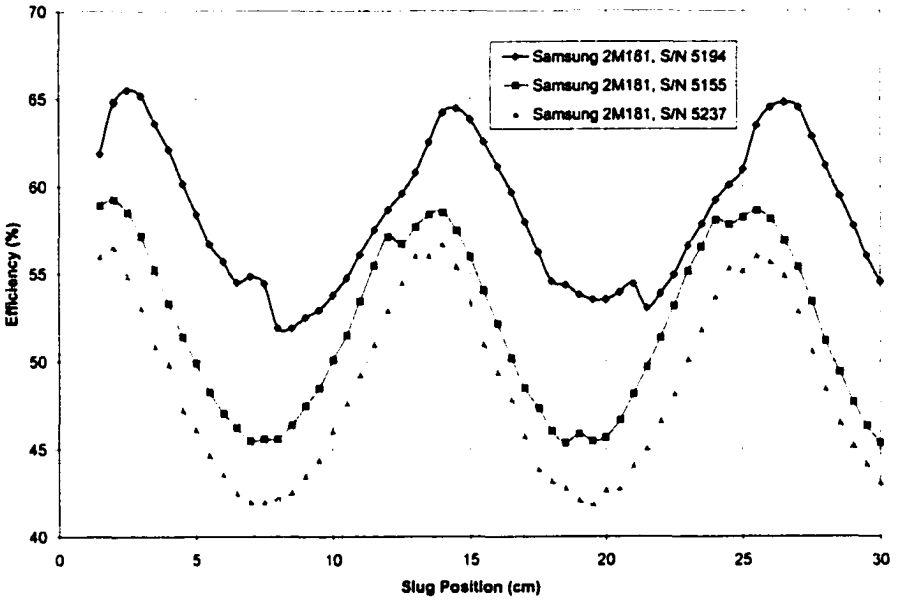

Figure A.4.4-2. Efficiency Comparison for Samsung 2M181 Magnetrons.

A summary of the performance obtained with the different magnetrons is given in Table A.4.4-1.

Table A.4.4-1. Comparative Frequency Characteristics of 2M181 Magnetrons.

Magnetron S/N	Average Frequency (GHz)	Bandwidth (MHz)	Maximum Efficiency (%)
5194	2.43989	14.83	65
5155	2.44709	10.09	59
5237	2.43975	8.55	56

Referring to Figure A.4.4-2, one point of curiosity is the differing locations of the peak efficiency. For S/N 5194, the peak power occurs at the minimum frequency point. For the other magnetrons, the peak is located in the middle of the frequency transition, as is generally the case. This phenomenon may help explain (or at least correlate) a number of

other interesting behaviors. Notice how the efficiency curve of S/N 5194 tends to bend around the curves for the other magnetrons. This appears to trace out a natural response of the magnetron to the load impedance provided. However, the variances in the internal construction (cavity sizes, vane sizes, RF probe) can force the magnetron to sometimes jump to another intersection of the power supply/load impedance curves. A diagram illustrating this action is shown in Figure A.4.4-3.

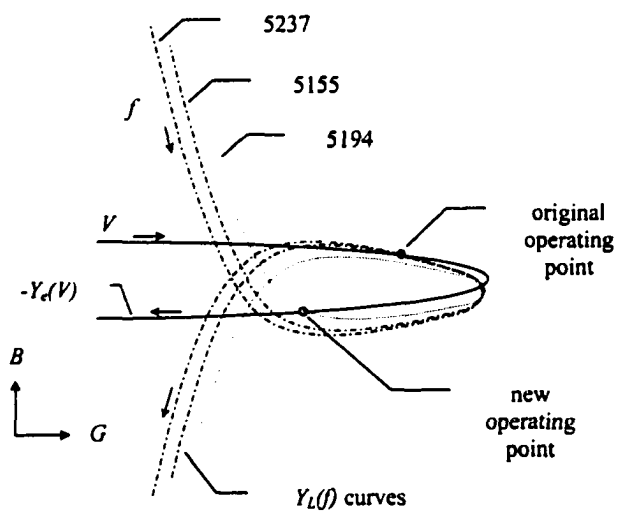

Figure A.4.4-3. Postulated Intersection of Load and Electronic Admittance Curves. Shows slightly different load from perspective of each magnetron.

Theoretical admittance curves are shown for the power supply and each of the three magnetrons. The slightly different load admittance curves account for the variations in the magnetron resonant circuit. This figure is much exaggerated for the data shown in Figure A.4.4-2.

A.4.4.2 Analysis of Results

Since Brown had characterized the magnetron with his MDA, this provided a data set to check our results against. This was of interest since our magnetrons exhibited such

different behavior in the UAF MDA. By showing the UAF MDA results for S/N 5155 agree with Brown's previous results, the performance of the other magnetrons may also be indirectly verified.

The frequency data in Figure A.4.4-1 supports the performance of Brown's previous results. At 300 mA, magnetron S/N 5155 provided about 10 MHz of frequency swing in the UAF MDA using slug 2 (Table 3.4-1). Brown had instead run his MDA using a slug size equivalent to slug 3. This was not done here because of the damage sustained to S/N 5194 (which was one reason for this magnetron comparison).

The frequency results in Figure 5.4-8 demonstrate that the frequency pulling range is proportional to the size of the slug. Using a scale factor of ~2 to account for a change from slug 2 to slug 3, then S/N 5155 should have been capable of producing ~20 MHz frequency bandwidth. This predicted value compares well with the 18 MHz demonstrated when used with Brown's MDA (see 300 mA curve in Figure A.4.4-4).

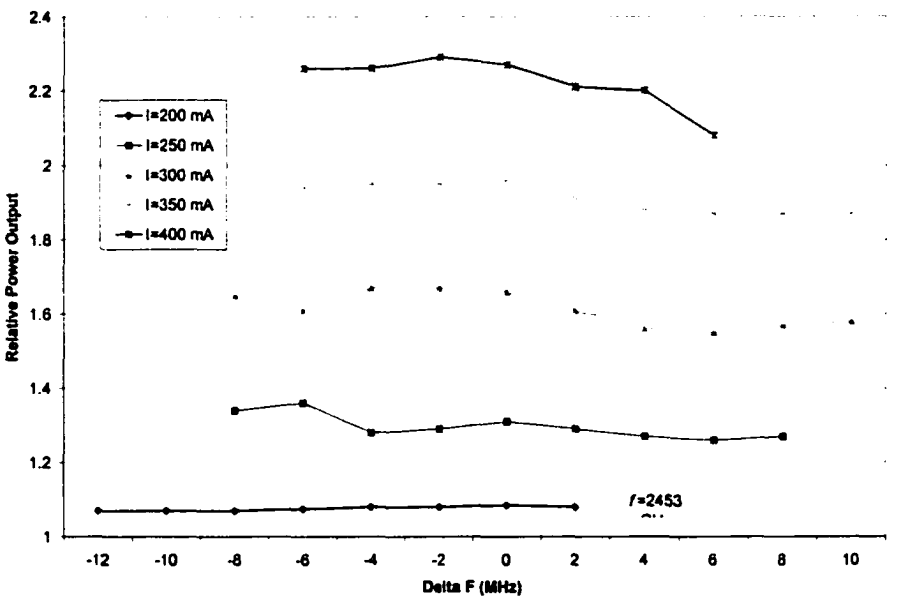

Figure A.4.4-4. Performance Results from William Brown's Class III MDA. Data shown for slug 3 [29].

Power measurements of S/N 5155 using the UAF MDA also compared favorably to Brown's configuration. Running the magnetron at 300 mA in Brown's MDA yielded an output power ranging from 1.55 to 1.67 units (mW) over a span of 18 MHz using slug 3. This data was taken in the sink region, which does not vary greatly for the 'normal' sink characteristics of S/N 5155. In the UAF MDA, the relative power ranged from 1.47 to 1.55 mW in the sink region over a span of 9.87 MHz using slug 2. The slopes of the resulting power versus frequency curves for magnetron S/N 5155 are equal to

$$\left.\frac{\Delta P}{\Delta f}\right|_{UAF} = 6.08\,\mathrm{mW}\cdot\mathrm{GHz}^{-1}, \qquad \left.\frac{\Delta P}{\Delta f}\right|_{Brown} = 6.67\,\mathrm{mW}\cdot\mathrm{GHz}^{-1}.$$

Therefore, the UAF frequency and power assessment of S/N 5155 agrees with Brown's results. Since this is the case, the UAF MDA may be considered an accurate test fixture for measuring the MDA performance. This validates the behavior of S/N 5194 throughout the characterization period.

Having established that S/N 5155 behaves similarly in the two MDA configurations, its performance may be measured against that of S/N 5194. The power versus frequency curves for both units are shown in Figure A.4.4-5.

In this figure, the probe output power of S/N 5155 varied by 6.08 mW/GHz (2900 W/GHz output power). By comparison, the slope of the power versus frequency curve for S/N 5194 was

$$\frac{\Delta P}{\Delta f} = \frac{1.66\,\mathrm{mW} - 1.46\,\mathrm{mW}}{2.44715\,\mathrm{GHz} - 2.43338\,\mathrm{GHz}} = 14.53\,\mathrm{mW}\cdot\mathrm{GHz}^{-1}. \qquad \text{(A.4.4-1)}$$

This is over 2x the variation for S/N 5155. In terms of the percentage power variation, this equates to

$$\Delta P(\%)\big|_{5155} = \frac{2(1.53-1.47)}{1.53+1.47} = 4.00\%, \qquad \text{(A.4.4-2a)}$$

$$\Delta P(\%)\big|_{5194} = \frac{2(1.66-1.46)}{1.66+1.46} = 12.82\%. \qquad \text{(A.4.4-2b)}$$

The large difference in these values is due to the intrinsic characteristics of the magnetrons, as shown in Figure A.4.4-2.

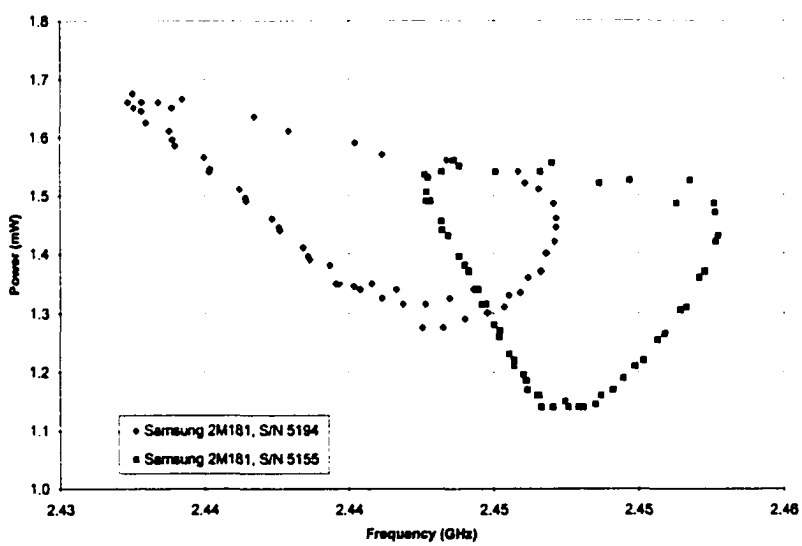

Figure A.4.4-5. Frequency versus Power for S/N 5155 and S/N 5194 in Class III MDA. S/N 5194 provides less power stability due to unique shape of sink region. Data sets for I_{anode} = 300 mA, slug 2.

The behavior of Samsung 2M181 S/N 5194 is unique since the power peak does not occur in the middle of the frequency transition region. Though this magnetron provides exceptional tuning range, the peak power occurs at the low end of the transition region. Therefore, the power is not nearly as stable across its sink region.

A.4.5 Magnetron Degradation

This section describes the effects of wear caused by low-level arcing, which eventually erodes the magnetron RF probe antenna. This erosion (or melting) of the probe gradually alters the magnetron performance over time. The purpose of this discussion is to quantify the change in performance noted, and to offer likely causes for the damage to the probe.

During the effort to characterize the effects of the MDA, one particular magnetron served as the primary unit for baselining performance (Samsung 2M181 S/N 5194). As part of characterizing and optimizing the MDA design, this magnetron has been operated for numerous hours at heavily loaded conditions. The performance of this magnetron as part of the MDA is well documented (Chapter 5). Magnetrons are generally tough, reliable device designed for years of operation if reasonably cared for. However, this unit has been pulled very hard into the sink region for extended periods of time, resulting in the high efficiency peaks noted in Figure 5.4-5.

In an attempt to verify this behavior, the data set was re-run with a water load. The peaks in power were not observed with the water load. A comparison of this data is shown in Figure A.4.5-1. Note the large difference in maximum efficiency obtained for the two loads (74.5% versus 56.0%).

The MDA performance is very sensitive to the exact hardware configuration used for particular combinations of waveguide size and operating frequencies. The inability to match the output power waveforms between the two loads eventually lead to repeating the measurements with the air-cooled load, as shown in Figure A.4.5-2.

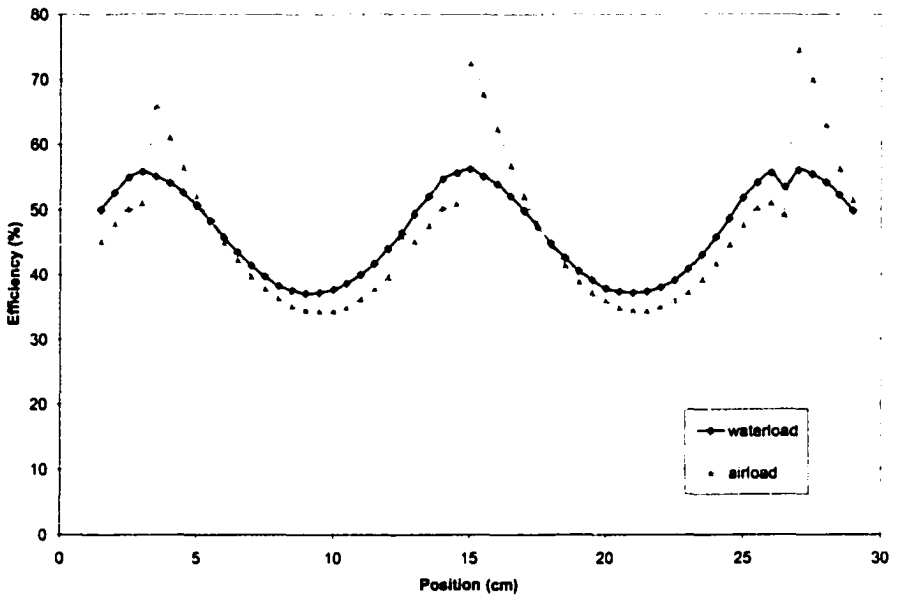

Figure A.4.5-1. Comparison of Output Power for Two Different Loads. Data shown is for slug 3 (Table 3.4-1).

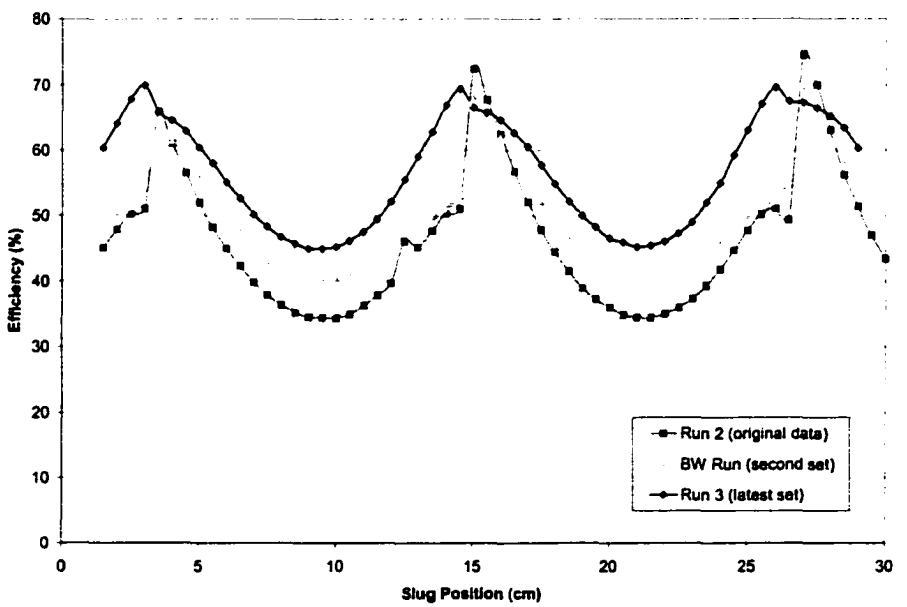

Figure A.4.5-2. Comparison of Output Power Over Time.

Comparison of the data sets reveals a gradual change in the power data. This shift resulted in increased power efficiency across most of the operating region, and decreased the efficiency in very narrow high efficiency regions. This same trend has also been noticed for tuning slugs 1 and 2. Though not as noticeable, the frequency data set also shows a definite shift over time. These differences are most apparent in the low efficiency regions opposite the frequency transition regions, as shown below.

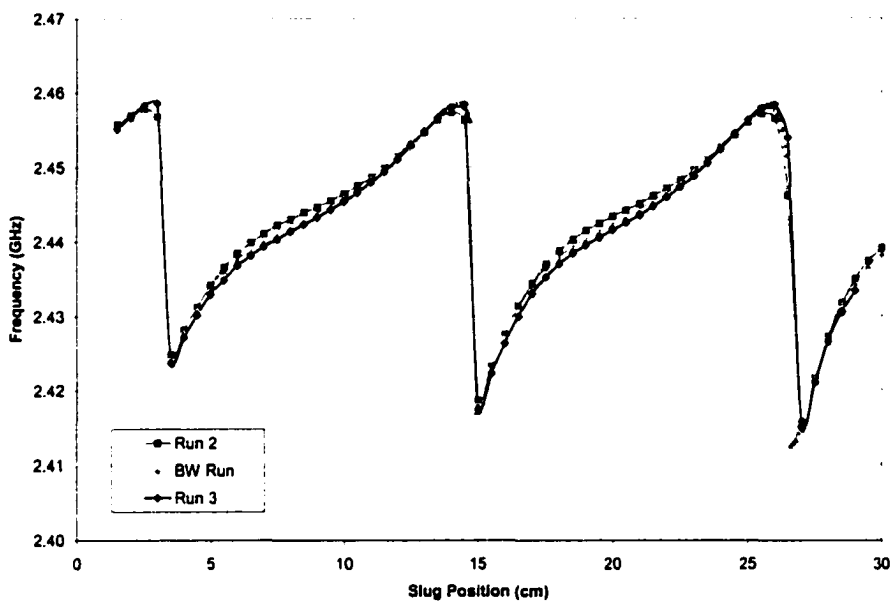

Figure A.4.5-3. Comparison of Operating Frequency Over Time.

The new frequency response of the MDA is shown in Figure A.4.5-4. Note that this curve shows the response for slug 2, vice slug 3 in Figure A.4.5-3. This data set shows a substantial clipping in the allowable frequencies for the MDA, much more than for the normal wear. This was the result of damage to the magnetron probe due to arcing. The arcing probably occurred at relatively low levels over an extended period of time. The damage was confirmed by examining the probe. The RF antenna had sustained some melting, which affected its radiation efficiency.

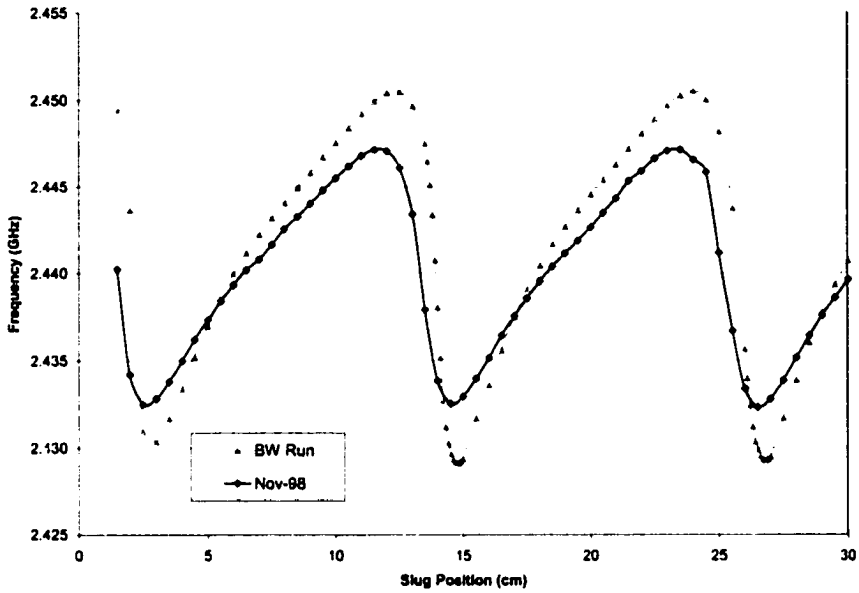

Figure A.4.5-4. Frequency Clipping due to Magnetron Damage.

However, it is not believed that the magnetron is damaged internally. In fact, this magnetron continued to be used throughout the remainder of the baselining effort, as it still displayed superior performance compared to the other two Samsung 2M181 units (Appendix A.4.4). Though the magnetron frequency response was slightly clipped, its power response was actually improved by the 'damage', as shown in Figure A.4.5-5.

Arcing causes the RF probe to change shape over time, and therefore changes the probe impedance. This may require adjustment of the shorting plate to optimize performance, as described in Appendices A.4.8.

The most likely cause of the damage seems to be the use of slug 3 for prolonged periods of testing. The low frequency points of the sink regions appear to be the most vulnerable to damage, as a buzzing noise was noted occasionally. This event seems to be related to destructive moding operation. In addition, this slug causes the highest impedance mismatch. Therefore, in the de-tuned range it causes the highest case temperatures due to reflected power.

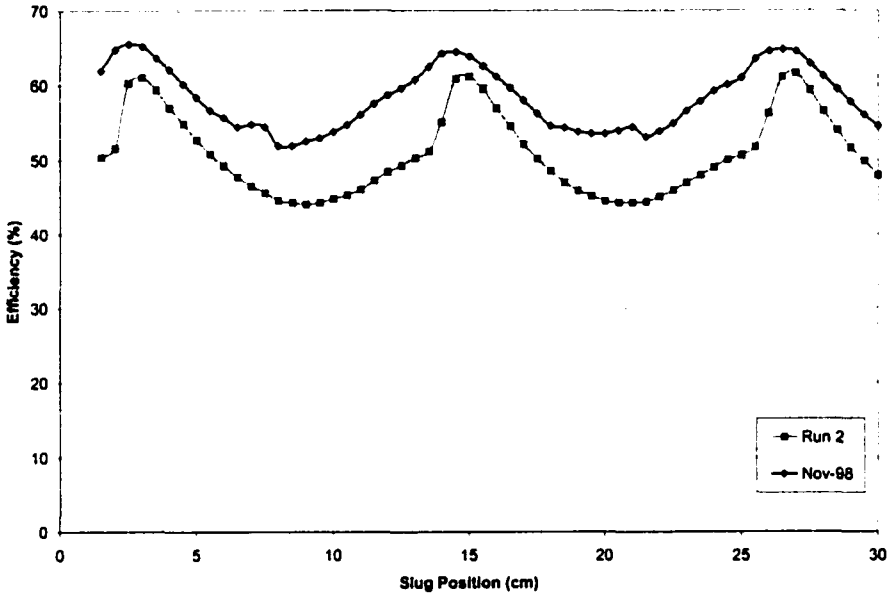

Figure A.4.5-5. Efficiency after Magnetron Damage. Response is improved.

The extended operation at 300 mA and lack of cooling may have also contributed to the damage. Some of the data sets run in support of the load power testing exceeded 10 hours continuous operation. Providing more cooling capacity in the lab may extend the life of the components to some degree.

Large tuning slugs provide a wide range of frequency tuning and can greatly increase the efficiency of the MDA. Unfortunately, extreme pulling may also damage the magnetron RF probe due to arcing. More study of this phenomenon is needed to assess the probability of such damage occurring for a given amount of tuning.

A.4.6 Moding

This section discusses the phenomenon of *moding* in the operation of the MDA. Moding refers to a number of different, but related situations where the operating point of the

magnetron is suddenly shifted. This discussion will limit the causes to those things affecting the steady state operation of a continuous wave (CW) magnetron.

Moding may occur at any phase of operation, either during starting up or normal operations. It is often seen as a result of changing the magnetron's operating parameters. This is caused by a change in the interaction between the magnetron and the load or power supply.

The impact of moding upon the hardware will vary according to its severity and frequency. The significance of this behavior also depends upon the application. Some possible results of moding include changes in frequency and power, break-lock condition in a phased array, changes (spikes) in input power, and damage to equipment.

Some examples of moding noted during this MDA characterization effort include: (1) startup of Hitachi 2M170 magnetron, (2) frequency jumps with large slugs, (3) disturbance effects (such as thermal changes), and (4) improper impedance matching (demonstrated by the National 2M107A-605 magnetrons).

A.4.6.1 Startup of Hitachi 2M170 Magnetron

This magnetron was used in the initial phases of the MDA characterization effort. Prior to that, it had been used as the primary microwave source for the UAF SABER Helicopter Project.

The 'normal' startup profile for a magnetron is shown in Figure 5.1-5. For the Hitachi magnetron in this MDA load configuration, the warming curve displayed an interesting characteristic, as shown in Figure A.4.6-1. After initially leveling out, the temperature would again rise quickly after approximately 10 minutes before reaching its final value. Of particular significance is the magnetron's frequency response to this shift, as shown in

Figure A.4.6-2. The magnetron follows an entirely different frequency profile after the jump occurs. This results in the final operating frequency being shifted by ~5.5 MHz.

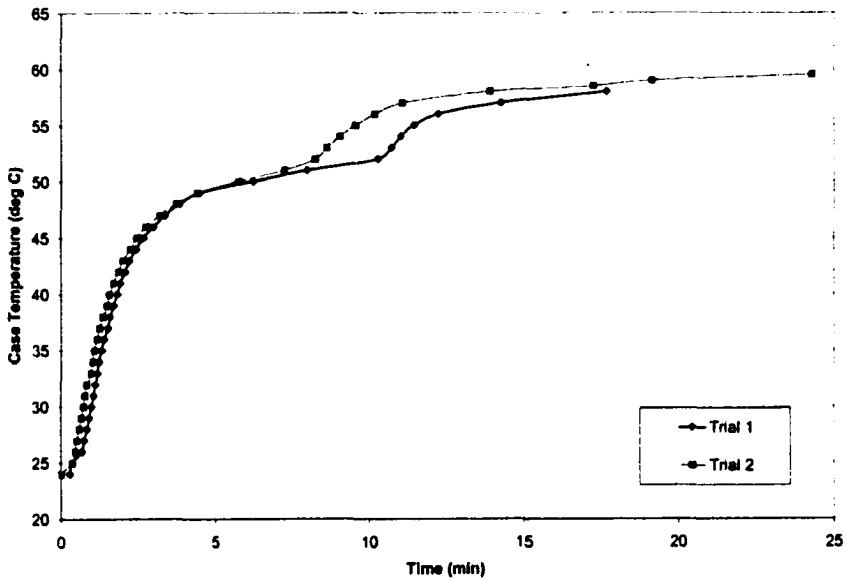

Figure A.4.6-1. Warming Curve for Hitachi 2M170 Magnetron.

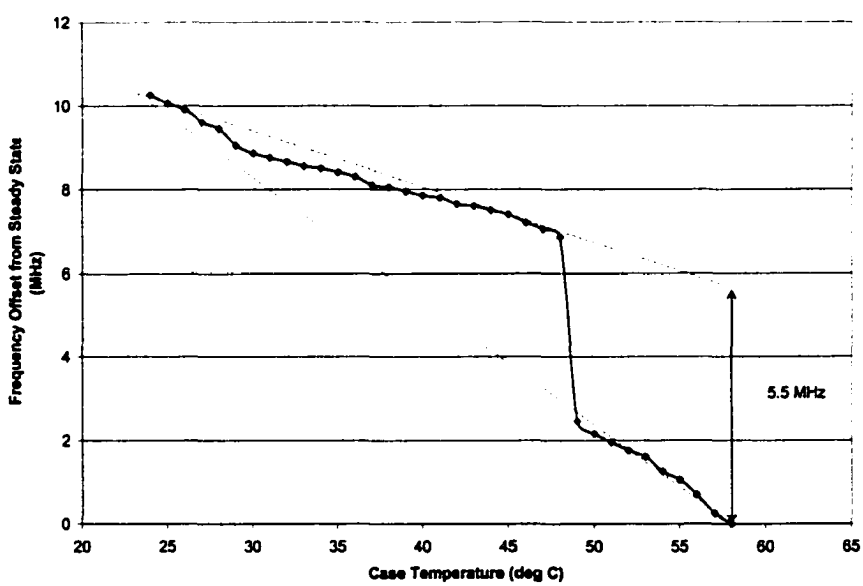

Figure A.4.6-2. Frequency Offset from Final Value for Hitachi 2M170 Magnetron During Warmup.

The mode shift also affects the efficiency of the magnetron. Its power curves are shown in the Figure A.4.6-3. The power supply jumps at the point of the mode change (51° C), causing the magnetron to operate a lower efficiency state. The steadily declining efficiency curve is accompanied by an increase in temperature, as expected.

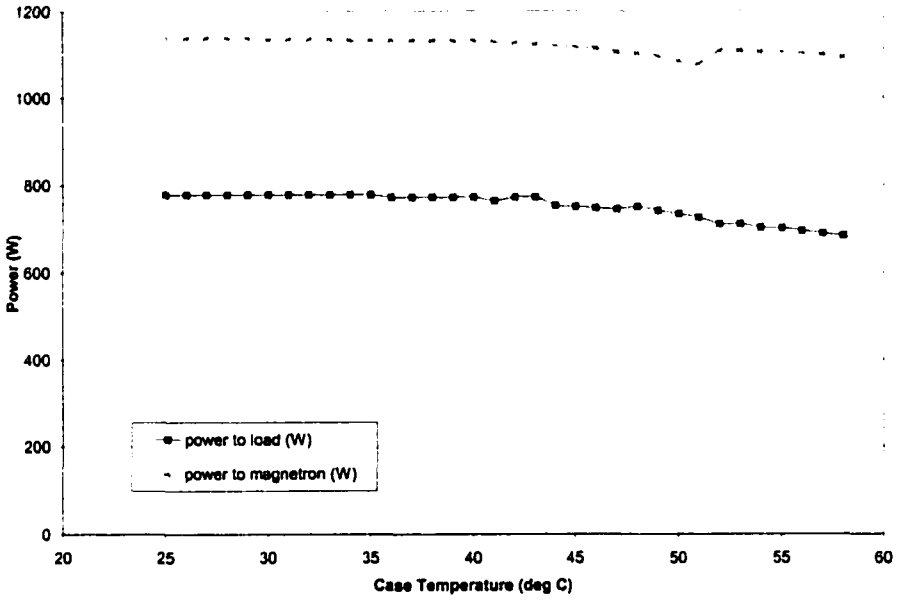

Figure A.4.6-3. Power Response for Hitachi 2M170 Magnetron.

The cause of this particular moding is thought to be the thermal loading placed upon the MDA. In general, any type of moding may be explained with the use of Figure A.4.6-4. The operating point of the MDA is defined by the intersection of the load admittance and power supply admittance curves. As the MDA components heat, their changing impedance causes the load admittance curve to shift. The magnetron operating point follows the intersection of these curves while it can. At some point, the intersection is broken and oscillation momentary ceases. The magnetron reestablishes oscillation at the next stable operating point having the lowest load conductance G_L (shown by gray dot).

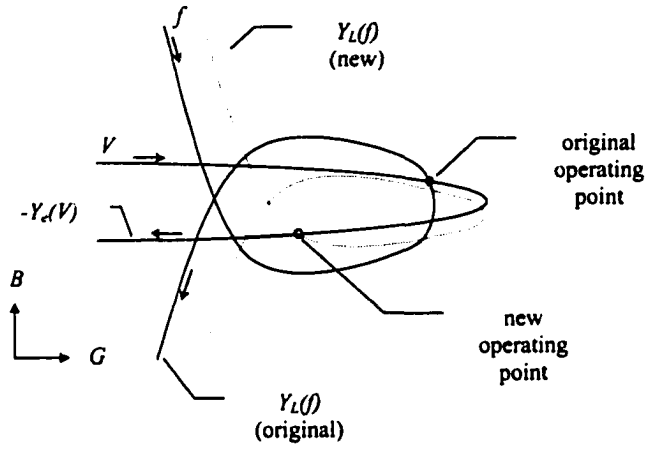

Figure A.4.6-4. Intersection of Load and Electronic Admittance Curves [15].

A.4.6.2 Frequency Discontinuities with Large Tuning Slugs

Large tuning slugs may cause a similar situation, where the frequency is forced to change values instantaneously. An example is shown for a Class III MDA in Figure A.4.6-5.

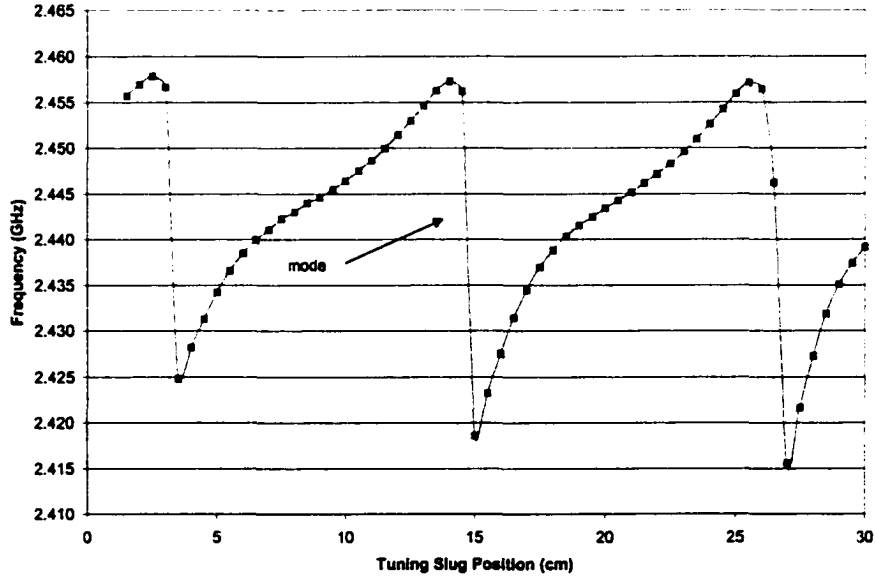

Figure A.4.6-5. Frequency Moding in Sink Region.

As the slug is moved along the low efficiency region, the admittance curves shown in Figure A.4.6-5 slide with respect to one another, but do not separate. Once the slug reaches the sink region, the intersection is broken and the magnetron must re-establish oscillation at the next intersection. Prolonged operation at this low frequency point is thought to have caused the damage to the primary magnetron (Appendix A.4.5).

In general, moding is referred to as *frequency* moding as this feature is usually the most prominent. However, moding is also evident in the power output for larger tuning slugs, as shown in Figure A.4.6-6. In this example, the power has jumped instantaneously by ~50% from its previous level. The peak efficiency is only sustained for a very narrow region of the sink. This type of moding is sometimes referred to as a resonant load.

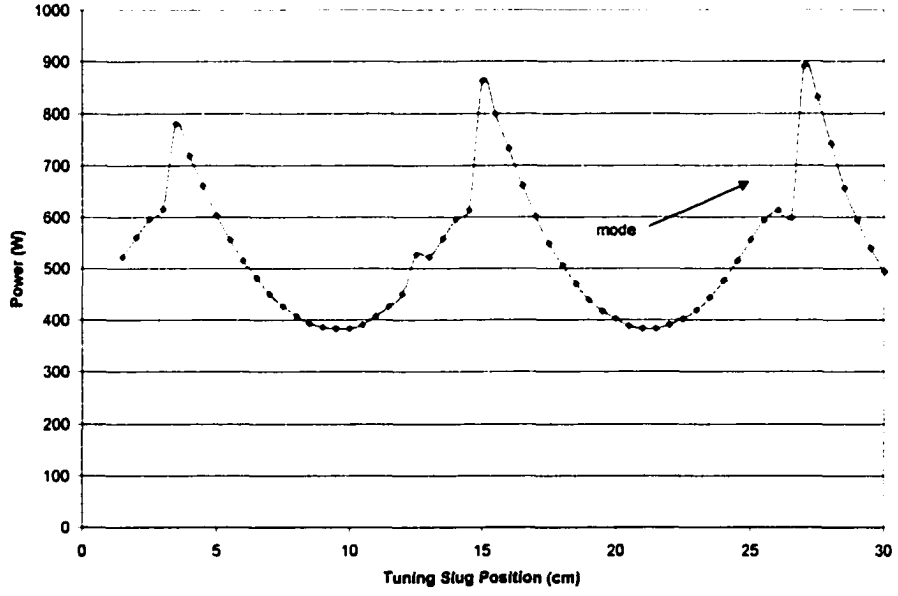

Figure A.4.6-6. Power Moding in Sink Region.

A.4.6.3 Moding Due to Disturbance Effects

The phenomena discussed so far have been relatively well behaved, in that they are predictable. However, this is not always the case. Throughout the MDA characterization

effort, the operating point has shown a tendency to shift for no apparent reason. Generally these shifts are relatively small and result in a power variation of ~3% (25W at 800 W operation). Some examples of the observed disturbances follow.

Example 1: 'Stable' Moding. In some cases, the magnetron's operating point may shift between two different curves, but with limited occurrence and relatively small amplitude change. This generally corresponds to operation in the low efficiency region of the tuning slug cycle. This behavior has been commonplace, particularly with larger tuning slugs. An example of this behavior is shown in Figure A.4.6-7.

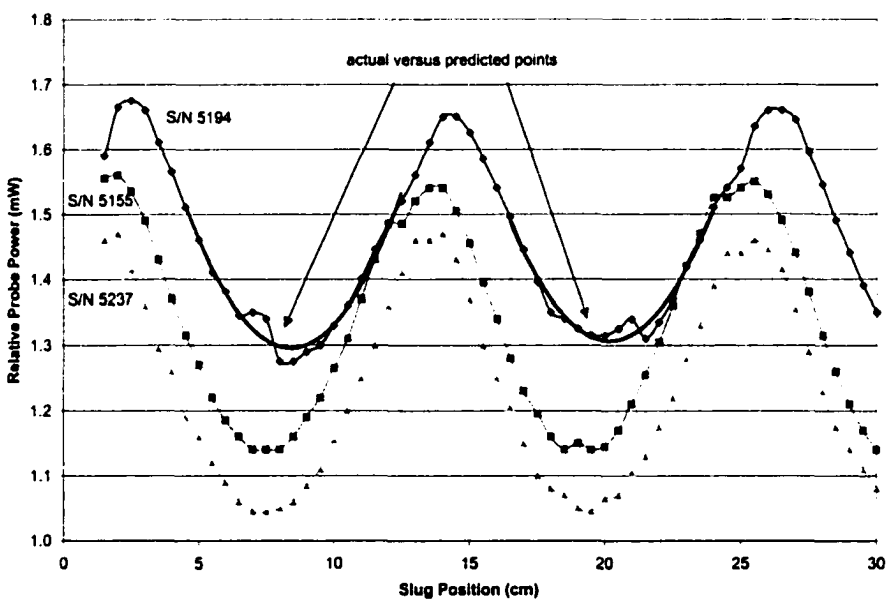

Figure A.4.6-7. Comparative Moding in Different Magnetrons. Data shown for I_{anode} = 300 mA, slug 2.

The upper curve shows the power response for the primary magnetron for the MDA characterization (Samsung 2M181 S/N 5194). The behavior displayed in the low efficiency regions is typical of that seen throughout the effort. Note the relative stability of the other two magnetrons in the same regions. This moding is caused by the

interaction of the particular magnetron and power supply. The behavior is lessened for operation at different power levels, as shown in Figure A.4.6-8.

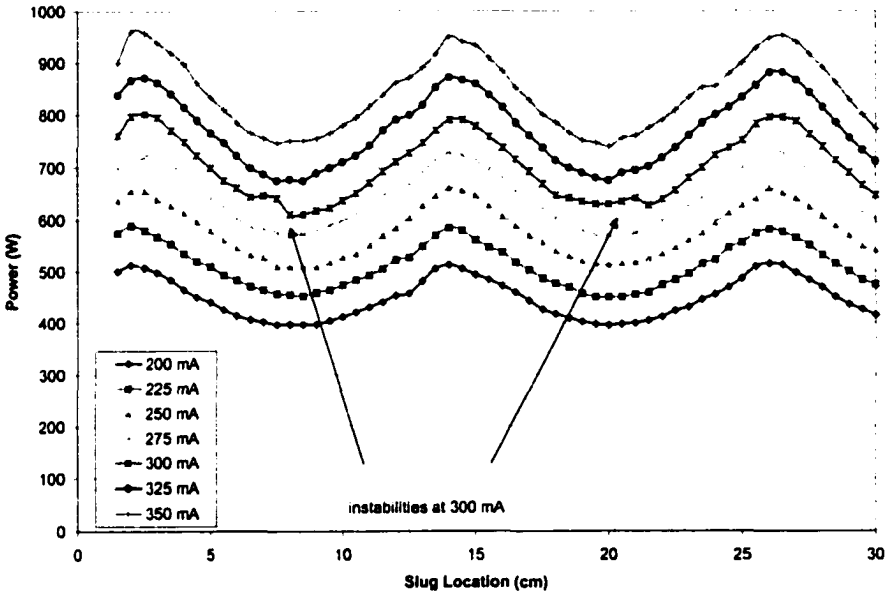

Figure A.4.6-8. Moding Caused by Instability of Power Supply.

Examining the power supply characteristics helps to explain the instabilities seen in the above figure. The *V-I* curve for the power supply driving this magnetron is shown in Figure 5.3-6. Operation at high power (350 mA anode current) also causes fluctuation in the low efficiency slug region due to the change in load impedance.

Example 2: 'Unstable' Moding. If the moding occurs near the sink region of the tuning cycle, the operating point may fluctuate more erratically and by a larger magnitude. This type of behavior was not seen often with the Samsung magnetron. When moding did occur, the duration was brief, making data capture difficult. In this example, the MDA displayed a tendency to operate at two different operating points for some tuning slug locations. One location of this phenomenon was at the bottom of the sink region, where the frequency is at a minimum and output power a maximum (Figure A.4.6-9). The moding yielded very low frequency data and correspondingly high power data. However,

attempts to reproduce this data failed – the MDA instead yielded the 'expected' values. This particular mode shift provided an increase of 2 – 3% in efficiency, as shown in Figure A.4.6-10.

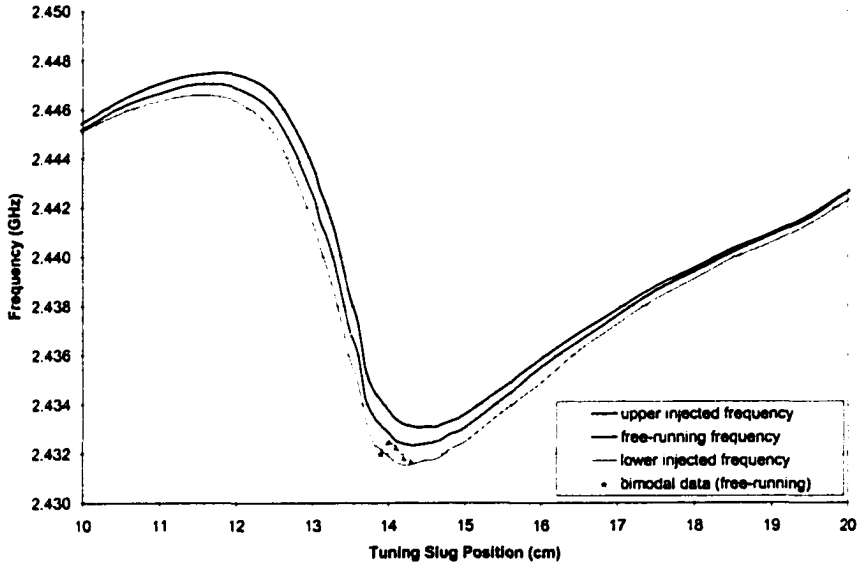

Figure A.4.6-9. Bimodal Frequency State in a Class III MDA.

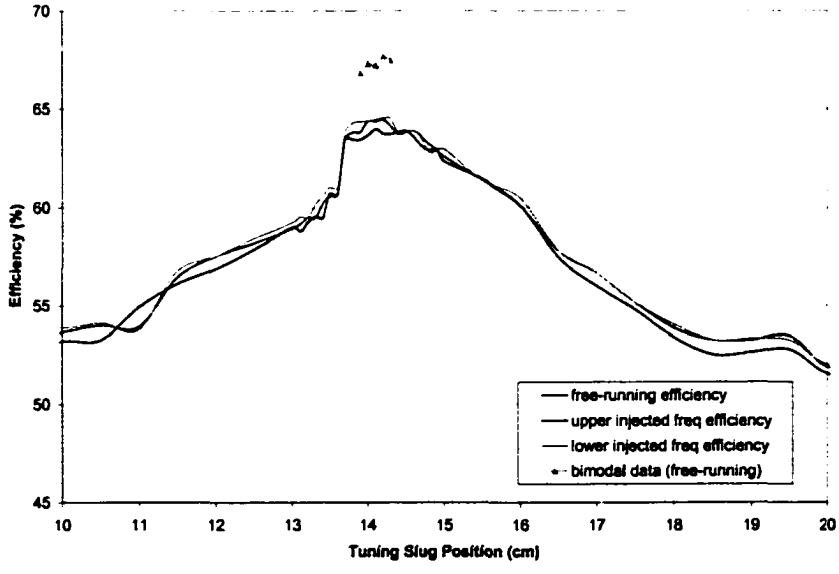

Figure A.4.6-10. Corresponding Bimodal Power State in a Class III MDA.

The moding shown in this set was also noted at other times and locations, but often could not be captured because of the brief duration. During this same data set, another occurrence of moding was seen directly opposite the first location (in the low efficiency region). This event was repeatable, but was not stable enough to take a good data set. The frequency in these unstable regions tended to jump about 200 kHz, with the output power jumping by ~25 W.

A.4.6.4 Moding Caused by Improper Impedance Matching

This subsection details a vivid example of moding encountered when attempting to integrate a new magnetron (National 2M107A-605) into the MDA. This was caused by a large impedance mismatch presented to the magnetron which had not so forcefully affected the Samsung 2M181 units.

One aspect of the MDA characterization effort was to compare the 'out-of-the-box' performance of four identical magnetrons. Through the course of the investigation, the magnetron has proven quite sensitive to the load and power applied. This is especially true for high efficiency operation in the sink region. Therefore, it was safe to assume that any differences between the magnetrons could produce noticeable results in performance.

Heavily supporting this hypothesis was the performance of three Samsung 2M181 magnetrons. These units had exhibited quite different operation with the same MDA hardware, as discussed in Appendix A.4.4. However, the usage history of these units was unknown, and therefore limited conclusions could be drawn.

Over the course of integrating these new magnetrons, much was learned about the MDA configuration. This particular effort launched the studies of the magnetron probe depth

(Appendix A.4.3) and the shorting plate location (Appendix A.4.8). Only the portions of these investigations directly relating to moding will be presented here.

Prior to altering the probe depth or repositioning the shorting plate, the new magnetrons did not operate well with the MDA. Of the three units tested, two of them exhibited distinct moding. The frequency response for one of these units in a Class II MDA is shown in Figure A.4.6-11.

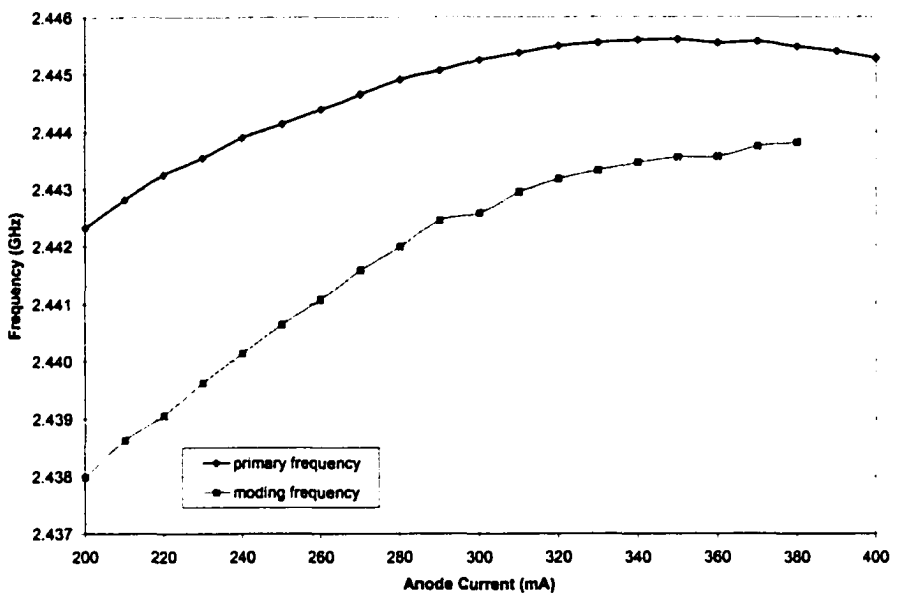

Figure A.4.6-11. Frequency versus Operating Power for National 2M107A-605 Magnetron (#4) in a Class II MDA. Upper curve shows 'stable' operating frequency, lower curve denotes unstable (momentary) value.

This magnetron exhibited moding nearly throughout the entire operating range. The primary frequency was that observed a majority of the time, while moding occurred almost instantly (less than 1 second in duration, but regularly). For lower operating powers, this moding occurred much more frequently (roughly every 5 seconds at 200 mA). As the operating power was increased, the rate of occurrence and the magnitude of the fluctuations diminished (roughly every 30 seconds at 350 mA).

The moding was resistant to load impedance changes, whether by frequency injection of slug tuning. The frequency response of this magnetron in a Class III MDA is provided in Figure A.4.6-12.

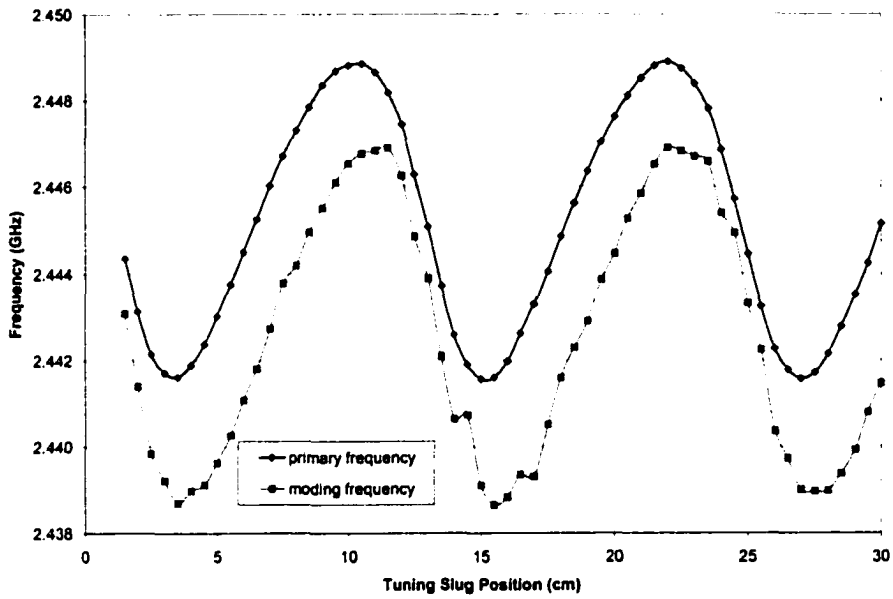

Figure A.4.6-12. Frequency Response versus Tuning Slug Position for National 2M107A-605 Magnetron (#4) in a Class III MDA. Upper curve shows 'stable' operating frequency, lower curve denotes transient value. Data shown for slug 1.

Moding occurred throughout the range of tuning, but was affected by the slug location. Sink regions yielded lower magnitude frequency shifts, but at a higher rate of occurrence. Larger tuning slugs may have stabilized at least a portion of the frequency range, but were not attempted.

The amount of frequency shift between the modes corresponds to the operating power level, as shown in Figure A.4.6-13. The magnitude of frequency shift is almost linear with input power. Lower power operation is less stable, with larger frequency changes

and higher rate of occurrence. Note that moding did not occur until the magnetron case had reached a temperature near steady state.

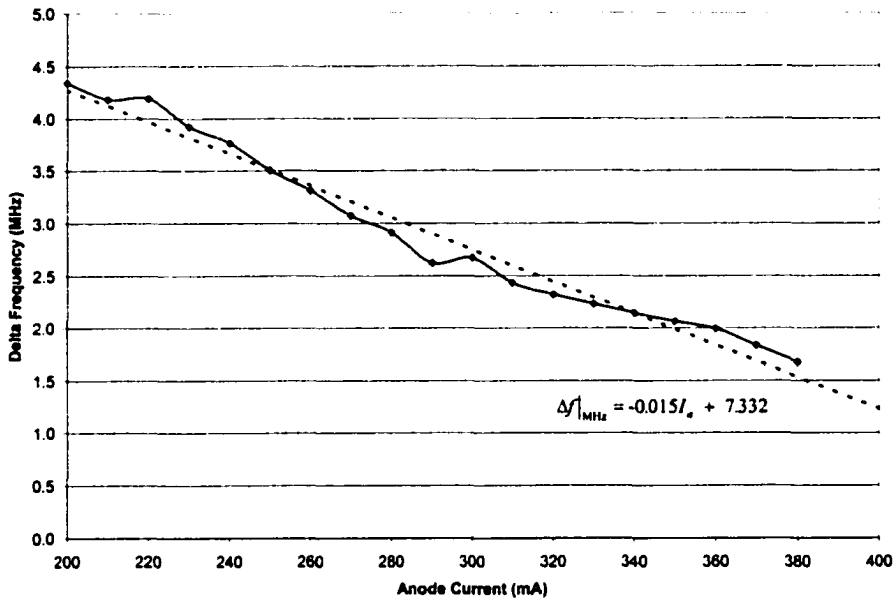

Figure A.4.6-13. Amount of Frequency Moding versus Operating Power.

The frequency shift also corresponds to the impedance presented to the magnetron, as shown in Figure A.4.6-14. Sink regions exhibit lower values for the moding, but with a higher rate of occurrence. The lower efficiency operating regions show more resistance to moding (lower rate of occurrence), but mode 'harder'. This behavior is somewhat surprising – the higher rate of occurrence for moding near the sink is expected, as the signal is in general less stable in this region. However, the lower magnitude of the moding in this region was not expected. This points to a higher dependency of the magnetron on load reflections than was anticipated. The most likely cause of this behavior would seem to be the temperature fluctuations of the waveguide components.

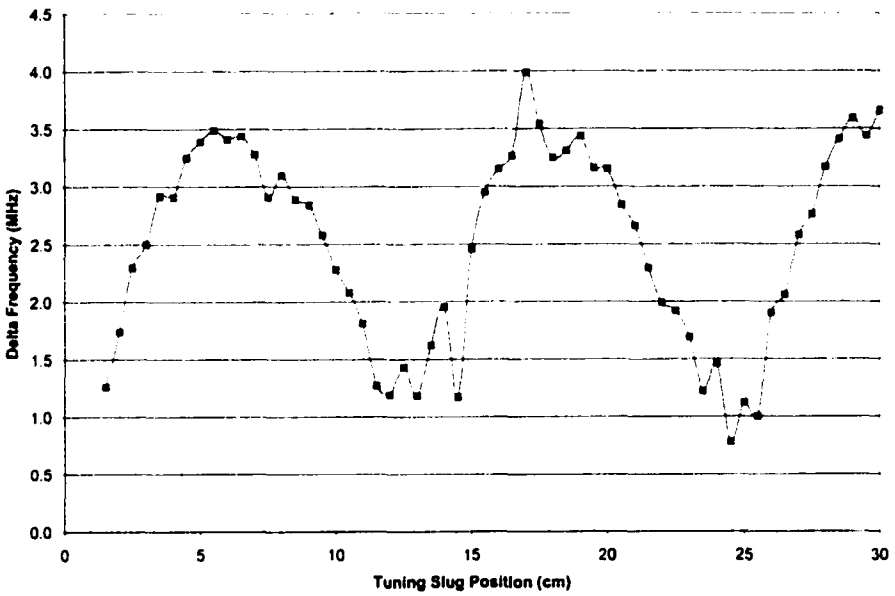

Figure A.4.6-14. Magnitude of Frequency Moding versus Slug Position.

Unfortunately, the power levels corresponding the above frequency data could not be recorded. The fluctuations occurred very quickly, not providing enough time to accurately read the analog meter. The magnitudes of the power fluctuations seemed to vary for a given operating point (constant load and power level). This behavior is attributed to physical limitations of the power meter. It appears that the power behaves quite similarly to the frequency — large changes in frequency correspond to large changes in power (as supported by the Rieke diagram). In general, output power surges of ~50 – 150 W corresponded to input power fluctuations in the range of 5 – 10 W.

The second tube examined performed more predictably in the MDA. However, it demonstrated unique behavior worth discussing. Figures A.4.6-15 and A.4.6-16 show two distinct modes of operation for this magnetron, which may help to explain earlier results.

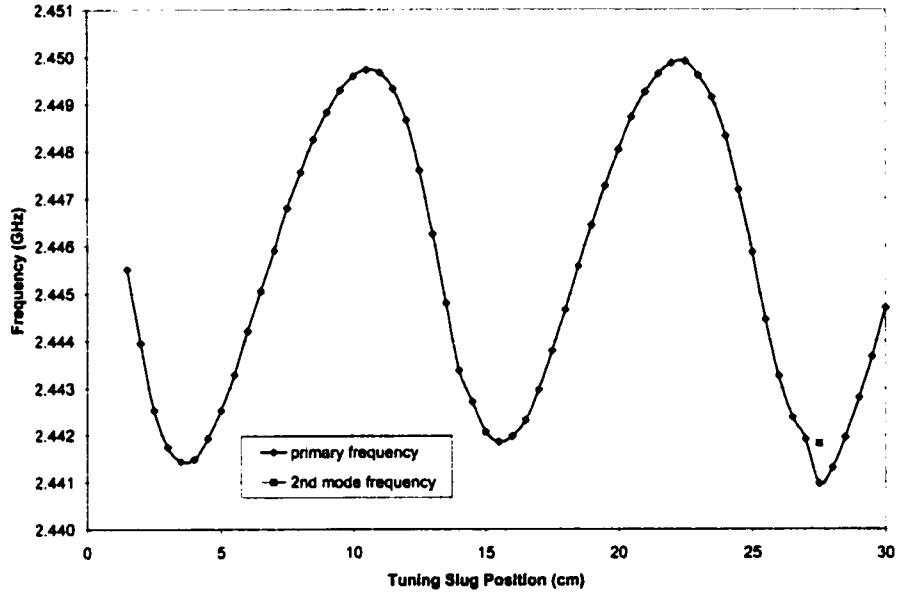

Figure A.4.6-15. Frequency versus Slug Position for 2M107A-605 (#3).

This frequency response exhibits the same type of moding shown in Figure A.4.6-10. The moded frequency point corresponds with the resonant power behavior shown below.

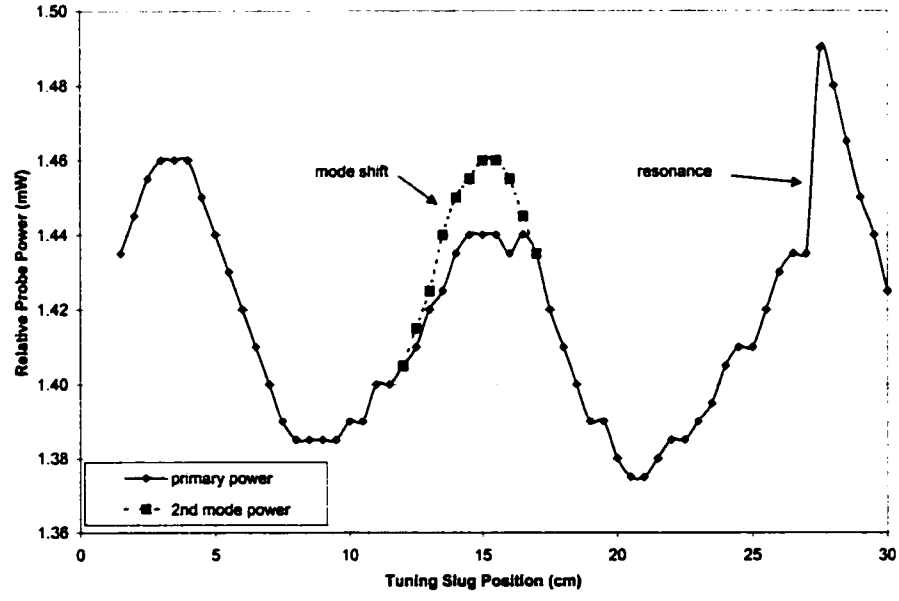

Figure A.4.6-16. Output Power versus Slug Position for 2M107A-605 (#3).

Note the inconsistency in the output power waveform given in Figure A.4.6-16. The solid line shows the initial power data taken. The dashed line denotes data retaken after magnetron moded at the end of peak. This magnetron exhibits two modes of operation in the same data set. One mode has a clipped power waveform with values below 1.44 mW and corresponding frequency minimums of about 2.442 GHz. This mode is fairly constant from cycle to cycle. The other mode has higher peak power output values and corresponding lower frequency values as the slug approaches the magnetron (at far right).

The probes on the National magnetrons are approximately ¼" shorter than the Samsung model (1/8" due to antenna length, 1/8" due to extension into tube). To center the antennas of these in the waveguide, a new mounting plate was constructed. This appeared to stop the moding in three of the four magnetrons — the remaining unit seems to mode regardless of probe depth or shorting plate location.

Adjusting the shorting plate permitted more of the magnetrons to operate without moding. The center frequency of the MDA load was far outside of the intended range of operation for these magnetrons (2.440 versus 2.460 GHz). Adjusting the plate to increase the operating frequency and centering the magnetron probe in the waveguide helped reduce moding.

Table A.4.6-1. Results of Adjustments on New Magnetron Operation.

	No change needed	Adjusted probe depth	Adjusted shorting plate
Tube 1	-	OK	
Tube 2	X	OK	OK*
Tube 3	OK		
Tube 4	X	X	X**

*Tube 2 was corrected by either changing probe depth or shorting plate location.
**Tube 4 did not operate properly in any configuration, with moding oscillations beginning at 55° C, though it appeared to be more stable with both corrections made.

Moding occurs for a variety of reasons. Some of these may be inevitable, such as the changing load impedance associated with motion of the tuning slug. Other causes should be minimized through stabilizing the MDA operating environment. Some preventative measures include (1) regulating the MDA temperature by operating into a waterload, (2) operating in a stable region of the power supply, and (3) operating slightly away from the 'deepest' portion of the high efficiency sink region.

The wide variation in performance shown by magnetrons of the same model was not anticipated. Some of this may be due to being tuned heavily into the sink region by the MDA load impedance. Though the MDA load was adjusted as much as possible, the magnetrons still behaved erratically. The National 2M107A-605 magnetron specification sheets call for it to be tested using a WR-430 launching section. It is possible that this magnetron is not able to operate into WR-284 waveguide directly. These results further support testing at larger waveguide sizes (WR-340 or WR-430).

A.4.7 Output Power

This section highlights the results of power correlation efforts undertaken, which was a significant part of the overall MDA characterization effort. This investigation was undertaken to verify the high efficiency peaks noted in the MDA data.

The high peaked resonant quality of the power response had been a curiosity. This was particularly true since the preliminary load temperature data did not support the resonant

power (or efficiency) behavior. A sample of the two waveforms is shown in Figure A.4.7-1.

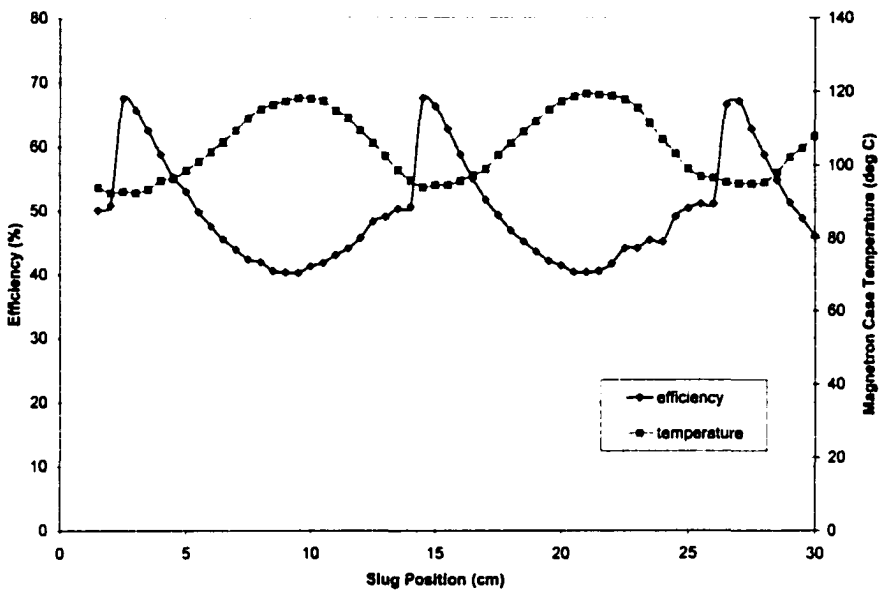

Figure A.4.7-1. Efficiency and Temperature Comparison for Quick Data Set.

For the initial data sets where temperature was recorded, the sets were taken without allowing the temperature of the magnetron to adequately stabilize. The thermal constant of the system was greater than anticipated, causing the data to be smoothed as shown above. Therefore, the magnetron temperature did not exhibit the same resonant qualities as the output power displayed.

The first part of the verification was an attempt to correlate the power meter measurements with an independent source. For this investigation, the hardware configuration used was a Class III MDA, as shown in Figure 3.4-3. The only difference was that the air-cooled load was replaced by a water-cooled load. By noting the water flow rate and heating of the water, an independent calculation of the power absorbed could be made. This calculation is provided in Section 3.1.

The results of the comparison are shown in Figure A.4.7-2.

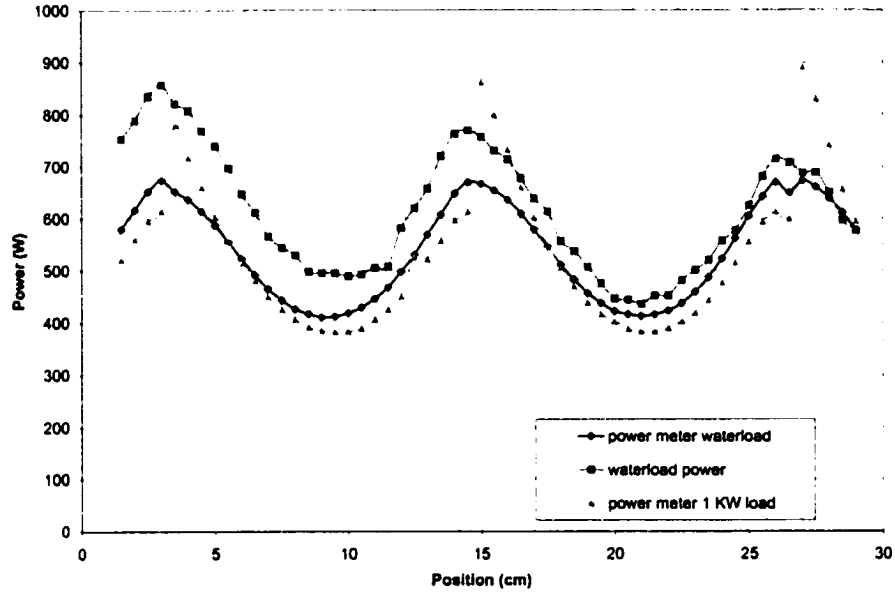

Figure A.4.7-2. Comparison of Air-Load and Water-Load Results. Data shown for I_{anode} = 300 mA, slug 3.

The waterload proved difficult to collect data without a constant pressure water source. Therefore power calculations were based upon averaged estimates of the waterflow and temperature differential data. Unfortunately, the fluctuations were rather high, rendering the data unusable for more than establishing the general power trend.

However, the output power read from the meter yielded a different waveform than that seen for the airload. The baseline waveforms agreed closely, but resonant peak was absent in the waterload data. This raised suspicion about the original airload data collected, which had been considered reliable to this point. Numerous data sets had provided linear relationships as to the amount of tuning available from different size slugs (Figures 5.4-8 and 5.4-9).

It was determined that the resonant waveform of the efficiency curves could be confirmed by temperature measurements made at the load and the magnetron. Taking accurate temperature data required the MDA to reach thermal equilibrium between data points. The amount of time needed was found to be a function of the tuning slug size, and was therefore only recorded when deemed necessary.

As part of the power investigation, the MDA was operated in numerous load configurations to ascertain whether the apparent efficiency resonance was real. In one experiment, the MDA was permitted to rest for 10 minutes between each data point (requiring a total of 10 hours per set). This was accomplished twice for each power supply. The comparative output power and load temperatures for these data sets are shown in Figure A.4.7-8.

Comparing the curves demonstrates that the shape is fairly well maintained between the output power and the load temperature. The load temperature exhibits the same resonant behavior seen in the power/efficiency plots, although with a lower relative peak magnitude. In addition, the magnetron case temperature displays a matching profile, as shown in Figure A.4.7-9.

To determine how well the output power and load temperature curves from Figure A.4.7-8 correlated, the expected load temperature was modeled. The heat energy absorbed by the load is given by

$$Q = mc\Delta T \tag{A.4.7-1}$$

where

Q = heat absorbed by load [J]
m = mass [kg]
c = specific heat capacity for load material $\left[\frac{\text{J}}{\text{kg} \cdot \text{deg K}}\right]$
ΔT = temperature differential [deg K].

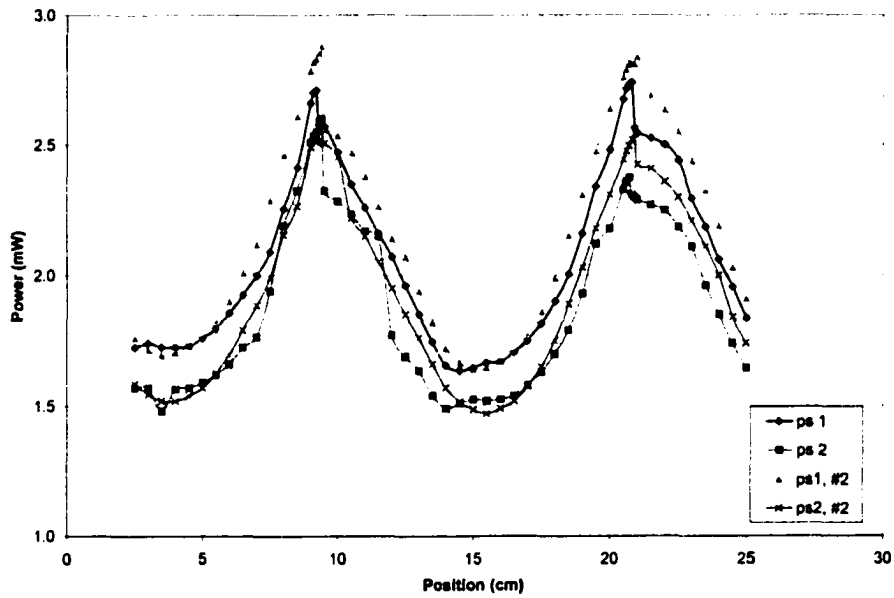

(a) Output Power versus Tuning Slug Position.

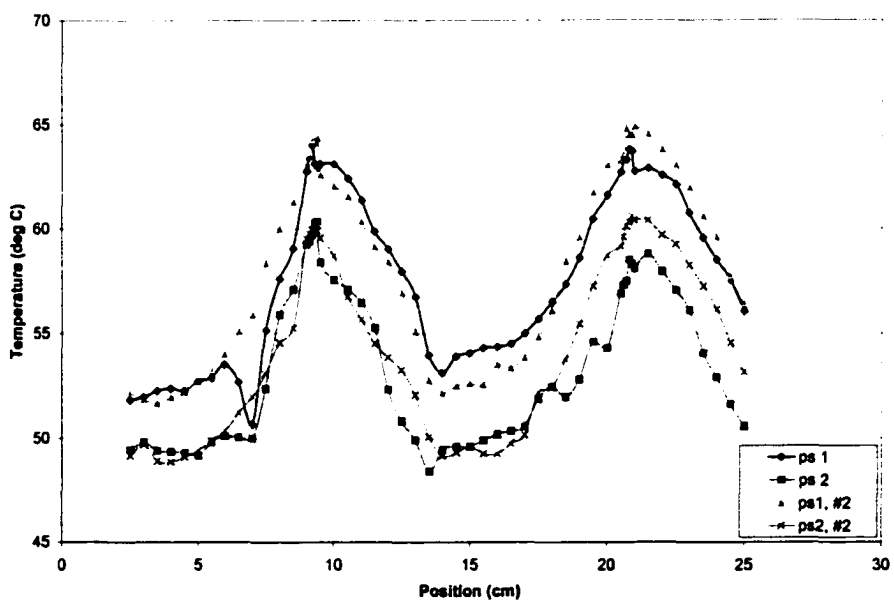

(b) Load Temperature versus Tuning Slug Position.

Figure A.4.7-8. Comparative Output Power and Load Temperature Plots.

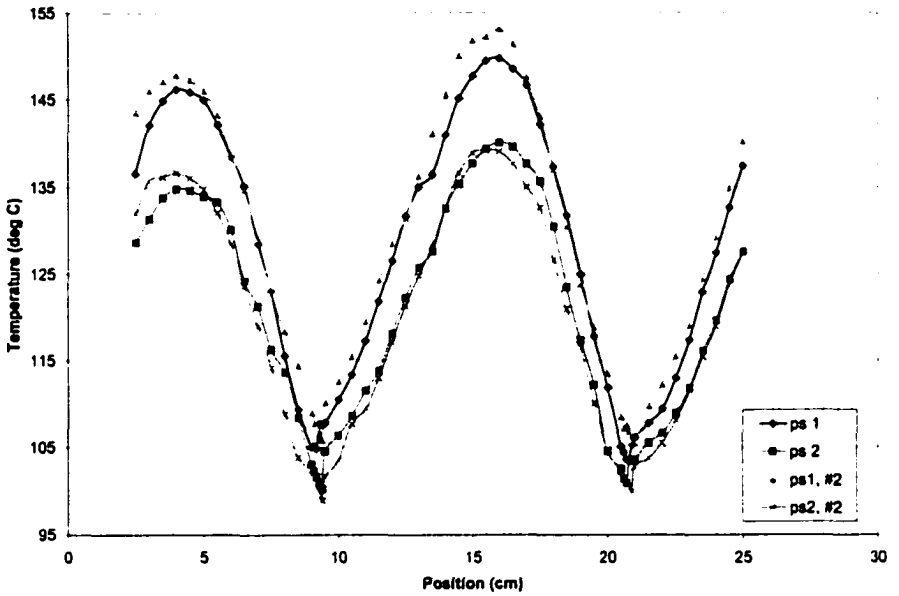

Figure A.4.7-9. Magnetron Case Temperature versus Tuning Slug Position. Corresponds to Figure A.4.7-8.

However, some of the variables in Equation A.4.7-1 would have to be estimated. If the load is constructed of aluminum, then the value for heat capacitance is $c = 900\ J \cdot kg^{-1} \cdot deg\ K^{-1}$. However, the actual material used is in question as the item is no longer manufactured. An alloy construction could vary the heat capacitance value somewhat. Also, it would be necessary to estimate the portion of the attached waveguide and circulator that act as the load, since they radiate a portion of the heat. These also have varying temperatures, depending upon their distance from the primary load interface.

Instead of proceeding in this fashion, it is noticed that the heat equation above is simply the relationship for a straight line. Noticing also that the empirical data relating the probe output power and load temperature satisfy the same relationship, the expected load temperature may be modeled. The modeled and actual data for the four sets is shown in Figure A.4.7-10.

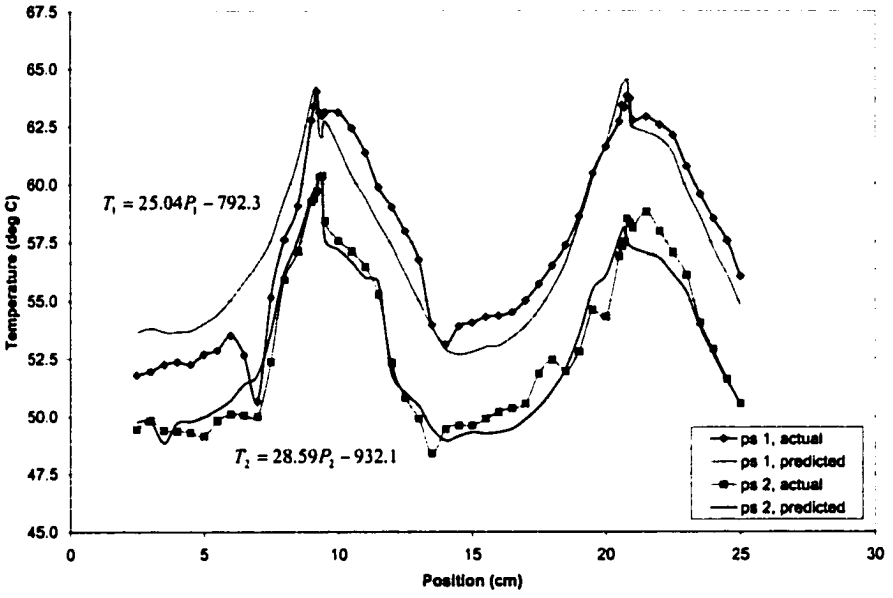

(a) first data run, each power supply

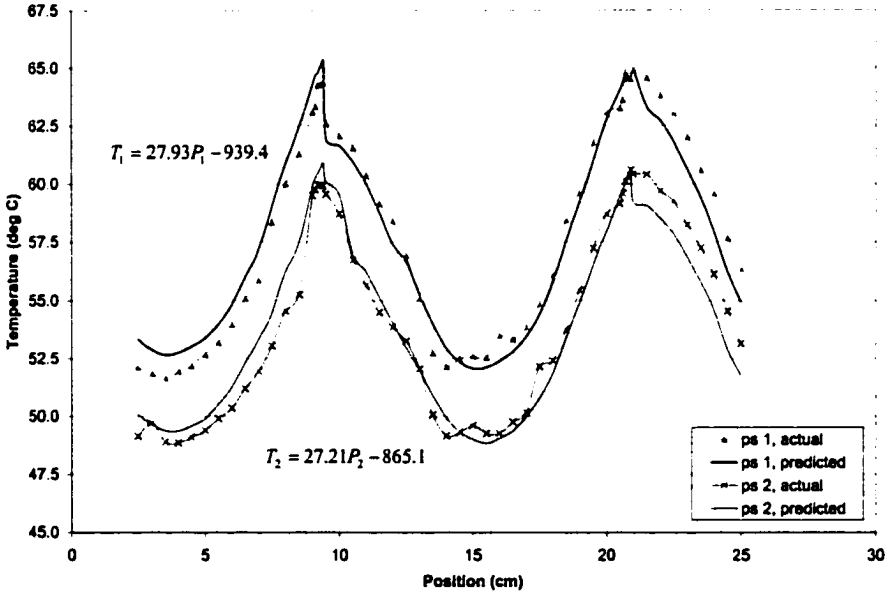

(b) second data run, each power supply

Figure A.4.7-10. Expected versus Actual Load Temperatures. Each plot shows one data run for each power supply. Actual data shown by data points. Modeled results based upon output probe power level, shown by smoothed curves.

These curves verify that a reasonably linear relationship exists between the output probe power and the load temperature. Therefore, the resonant peak in efficiency seen for large tuning slugs (Figure 5.4-6) is shown to be real.

The power/temperature comparison presented here supports the accuracy of the output waveform, as does the data seen throughout the characterization effort. The resonant feature of the power is a function of the waveguide size, slug size, shorting plate location, and a number of other factors. However, the exact magnitude of the resonant peak may be in question. This should be verified by operating the MDA into a precisely controlled waterload. A proposed design for such a system is given in Section 8.2. One particular experiment of interest would be an attempt to create the resonant power behavior for the waterload by adjusting the shorting plate (Appendix A.4.8).

Appendix A.4.8 Shorting Plate

This section discusses the effects of varying the shorting plate location in the magnetron launching section. This provides coarse tuning of the magnetron load impedance, which heavily affects the MDA operating characteristics.

A.4.8.1 Theory of Operation

The performance of the magnetron is not only dependent upon its own design and construction, but also upon the characteristics of the power supply and the load.

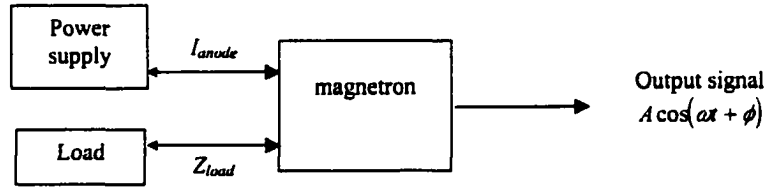

Figure A.4.8-1. Control Mechanisms for the Magnetron.

The interactions between these three components define the magnetron's operation. In this diagram, the interfaces are shown with arrows in each direction. The primary effect of the interaction is upon the magnetron, however, its behavior indirectly controls the behavior of the others. The effects of varying the input power are relatively straightforward and will not be discussed further here (see Section 5.3).

However, the interaction of the magnetron and the load is much more complex. The load consists of *anything* that affects the total impedance seen at the output of the magnetron RF probe. This includes the following items: (1) the primary load (air-cooled, water-cooled, or antenna), (2) the tuning slug size and location, (3) the injected reference signal, and (4) waveguide component characteristics and interfaces.

The last category encompasses many factors that influence the impedance. It includes device specific behavior of waveguide components, the effects of their impedance mismatches, and the size of the components. The waveguide size refers to its internal cross-section dimensions. The effects of this choice are discussed in Appendix A.4.2.

The size of the waveguide with respect to the magnetron is also dependent upon the proximity of the probe to any portion of the guide. Since the waveguide bounds the electromagnetic energy, it may be viewed as a resonant cavity coupled to an output load. The location of the shorting plate affects the phase of the signal reflected back to the magnetron probe. This reflected signal then is coupled back into the magnetron, affecting the total voltage to current ratio at the probe. The magnetron/load interface diagram is updated to show the shorting plate.

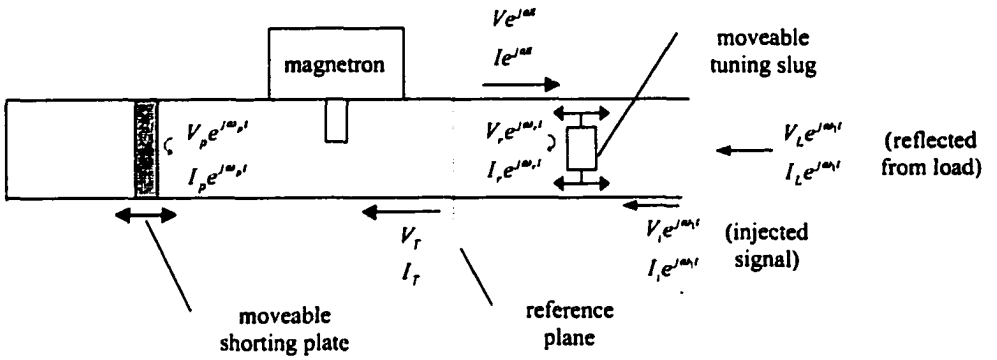

Figure A.4.8-2. Magnetron/Load Interface For a Class III MDA. Shows reflected signal from shorting plate.

This reflected signal has not been considered to this point, as it was not a parameter being varied. However, the location of the shorting plate provides considerable tuning over the magnetron.

The equations governing the operation of the magnetron from Section 4.2 are sufficient to explain this condition. The reflected voltage and current may be specified as a portion of the total load admittance presented to the magnetron.

A.4.8.2 Physical Configuration

The shorting plate was connected to a plunging rod via a threaded tap. A guide plate allowed the plunging rod to slide the shorting plate to the desired position. The guide also maintained the alignment of the plate within the waveguide. A diagram of the configuration is shown in Figure A.4.8-3.

The cap head screw on the bottom served as the position indicator for the shorting plate. It also helped to prevent any rotation of the shorting plate inside the guide. Additional slots were provided in the regions considered to be suitable operating locations for the

shorting plate. When the MDA was operated within reach of these slots, they were used to provide extra stability of the plate.

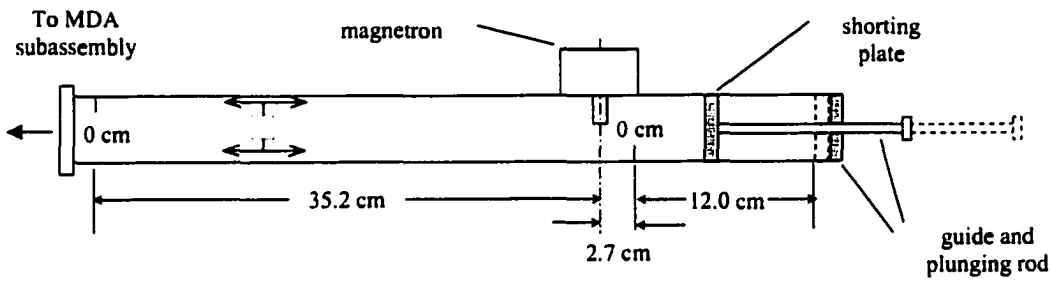

(a) side view

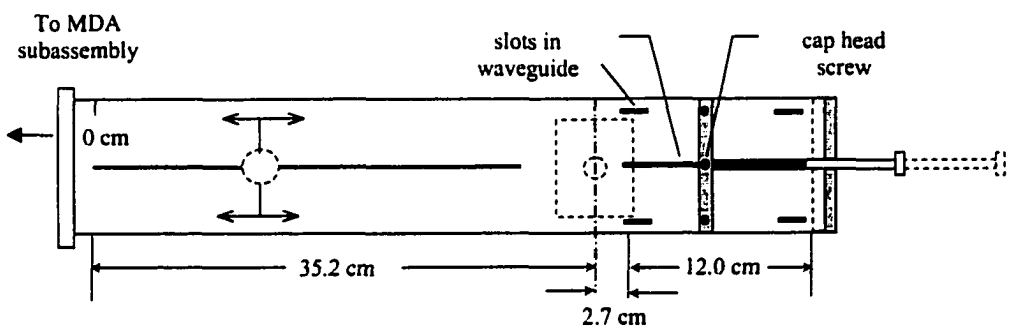

(a) bottom view

Figure A.4.8-3. Shorting Plate Adjustment Scheme.

Prior to this investigation, the shorting plate had been located in the position nearest the magnetron. This corresponded to a plate location of 0.0 cm on the scale shown in Figure A.4.8-3. This location was chosen because it provided the highest efficiency. It was also the closest point that the plate could be positioned to the magnetron at that time. Since then, the center slot has been lengthened to provide more tuning range.

A.4.8 3 Data Collected

The first subsection will discuss the effects of the plate on the operation of a magnetron and load, as described in Section 3.1. Then the combined tuning of the plate location

with a tuning slug will be examined for the Class III MDA. Note that all plate location measurements are given with respect to the shorting plate center. The plate is 0.5 cm in thickness, so the plate face is actually 0.25 cm closer to the RF probe. For the purposes of this discussion, the relative scale supplied should be sufficient. When necessary, the offset will be noted and incorporated into the analysis.

A.4.8 3.1 Effect of Shorting Plate on MDA

The data collection process for the shorting plate was similar to that of a tuning slug. For each data point, the plate was positioned and then the MDA was allowed to stabilize. Since the reflected signal from the plate was substantial, the MDA was given more time to reach thermal equilibrium (~3 minutes each point). To characterize the MDA with respect to this new parameter, the following data was collected as a function of shorting plate location: (1) operating frequency, (2) output power, (3) efficiency, and (4) magnetron case temperature. All data sets in this investigation were taken using power supply #1 set at 300 mA.

The plate location had a strong affect on the operating frequency of the MDA, as seen in Figure A.4.8-4. The position at the leftmost edge of the graph corresponds with the normal plate position used throughout testing (0.0 cm). The normal no-slug frequency corresponding to this point is ~2.442 GHz. Moving the plate away from the magnetron quickly increased the frequency, gaining over 10 MHz within 2.0 cm of motion. The curve quickly levels off and begins a less rapid descent, losing frequency at a rate of roughly 6 MHz over 4.0 cm.

Note that no data was taken between the positions of 6.0 and 10.0 cm in this set. This was due to a sharp decrease in output power and corresponding rise in magnetron case temperature (Figures A.4.8-5 and A.4.8-6). The value of 10.0 cm was obtained by first shutting the MDA off, then repositioning the shorting plate and resuming operation.

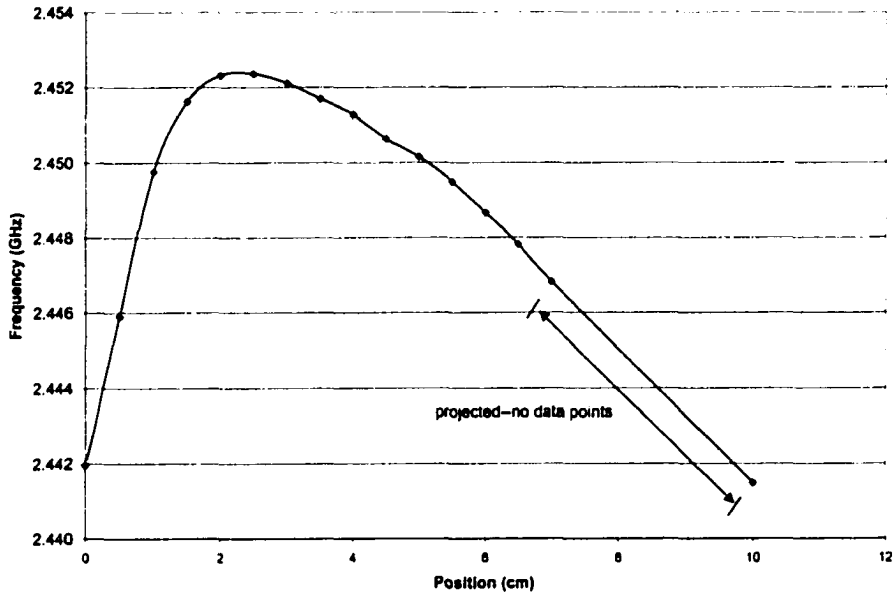

Figure A.4.8-4. Operating Frequency versus Shorting Plate Location.

This is explained by the standing wave pattern inside the waveguide. The *shorting* plate forces the electric field to be zero at that point and at ½ wavelength multiples from that point. A conceptual diagram of the standing wave pattern near the shorting plate is given in Figure A.4.8-5.

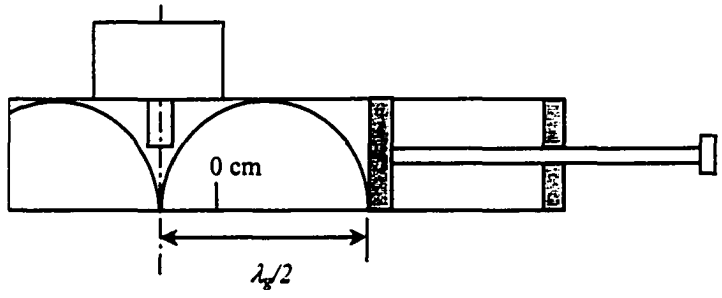

Figure A.4.8-5. Standing Wave Ratio Caused by Shorting Plate.

The wavelength in the guide is given by Equation A.4.2-1. For a frequency of 2.442 GHz, this is $\lambda_g|_{2.442\ GHz}$ = 23.30 cm. Therefore, the distance from the centerline of the

RF probe to the face of the shorting plate would be ~11.65 cm away. This corresponds to a launching scale reading of

$$\ell_{plate} \approx 11.65 - 2.7 + 0.25\,\text{cm} = 9.2\,\text{cm}.$$

Operation near this point will result in a nearly total reflection of power into the magnetron. Such operation would likely have catastrophic effects upon the magnetron and possibly the power supply. Data collected for load power and magnetron case temperature confirms the approaching condition.

The output power for the normal plate location (0.0 cm) used throughout the MDA characterization effort was shown to be roughly the maximum obtainable value. The power response for the MDA is shown in Figure A.4.8-6.

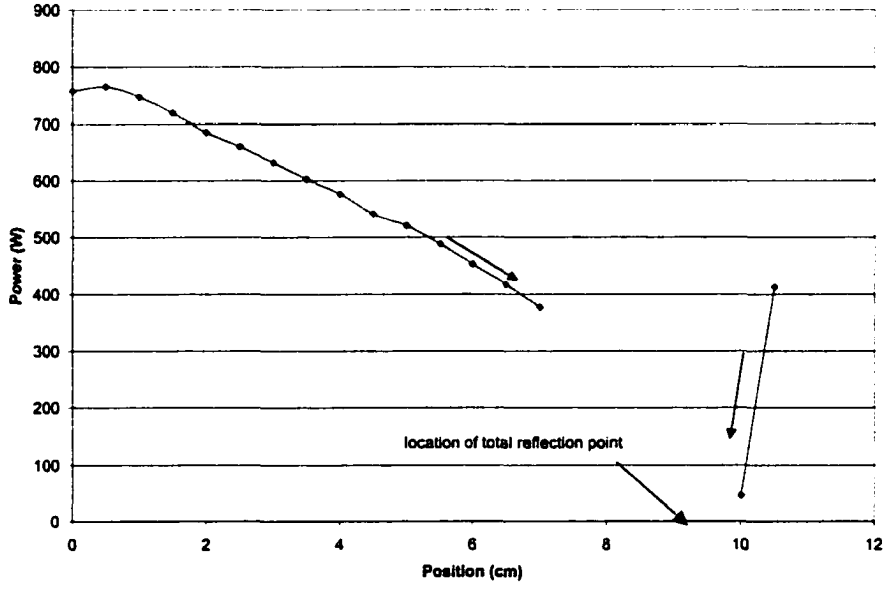

Figure A.4.8-6. Output Power versus Shorting Plate Location.

The power initially drops off linearly with the shorting plate location. Judicious selection of points ahead of time would have resulted in a narrower gap in the data. Power is

expected to drop linearly until in the proximity of the reflection point. The dropoff to the reflection point should be rapid, departing the linear curve at roughly 8.5 cm. This estimate is based upon the shape of the curve above, and by impedance measurements made subsequently (discussed later).

Arrows show the direction from which the reflection point is approached. The second set of points was initiated at 10.5 cm. The next point resulted in a near total reflection of the power. The power drop between these points is extremely sharp. As soon as this output power was noted, the situation was recognized and the power to the magnetron was shutoff. This did not permit the magnetron to stabilize, however, the output level was charted as it graphically displays the abruptness of the phenomenon.

The efficiency of the MDA follows the same curve, as shown in Figure A.4.8-7. Note that the point at 10.0 cm corresponds to ~4.3% efficiency.

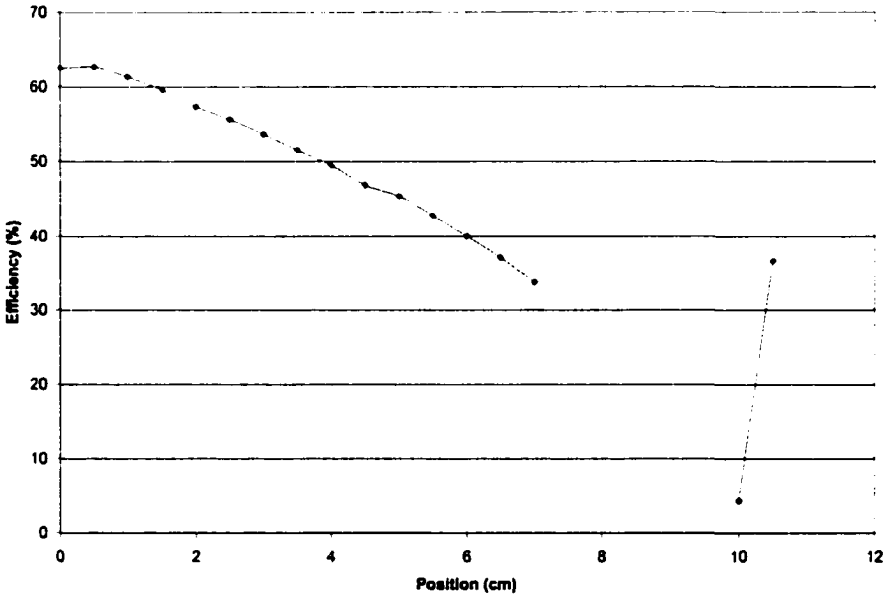

Figure A.4.8-7. Efficiency versus Shorting Plate Location.

In all of these graphs, the region corresponding to 7.5 to 10.0 cm was not explored, as it seemed to put severe loading on the magnetron. The decision to stop at 7.0 cm was made because of the abnormally high case temperature encountered. The magnetron temperature response is shown in Figure A.4.8-8. After operating merely a few seconds at 10.0 cm, the temperature had already reached 185 deg C. The data set was terminated immediately. This data set was not refined at the time because it had served its purpose.

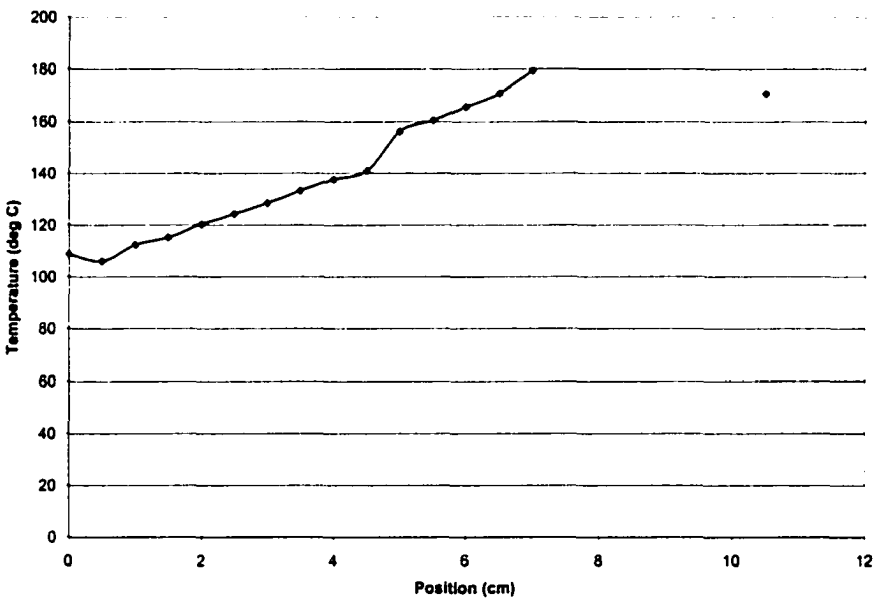

Figure A.4.8-8. Case Temperature versus Shorting Plate Location.

A.4.8 3.2 Combined Effects of Shorting Plate and Tuning Slug on Class III MDA

After the MDA was characterized with the shorting plate, it was desired to examine the combined effects of the plate with a tuning slug. It was postulated that the plate provides coarse tuning of the magnetron, while the tuning slug would fine-tune the response. The two methods should act linearly within the capabilities of the magnetron. If the responses can be combined, then the magnetron might be tuned even further into the sink region.

The data collection effort was a two step process. For each plate location, the tuning slug was varied to obtain a single data set. These were then combined to form a superset of data. The following families of curves describe the combined tuning effects on the Class III MDA: (1) operating frequency, (2) efficiency, (3) magnetron case temperature, and (4) output power versus frequency.

All data sets in this investigation were taken using power supply #1 set at 300 mA. The slug chosen for the characterization was slug 2, as it provides a fair amount of tuning without putting undue stress on the magnetron. With the combined effects of the plate, this would still have to watched closely.

The MDA had changed configurations since the last data set. The magnetron was damaged as a result of operation at very low frequency (Appendix A.4.5). As a partial result of this, the characterization of four new magnetrons was attempted (Appendix A.4.6). Difficulties in this process lead to an investigation of the magnetron probe depth and of the shorting plate location. Consequently, the magnetron mounting plate was modified to provide maximum coupling to the load (Appendix A.4.3). This changed the MDA's response to the shorting plate location.

In addition, subsequent data sets collected with the Class III MDA and by impedance measurements indicated another range of interest for the shorting plate. This range was located just to the left of the previous 0.0 cm mark (see Figure A.4.8-3). The slot was lengthened to permit the shorting plate to reach this region.

Because of these changes, the data sets are reviewed here. The new data set shows an increase in frequency range available, as expected. The jump in the two data sets at 0.0 cm is likely due to a slight offset in the plate positions for the two runs.

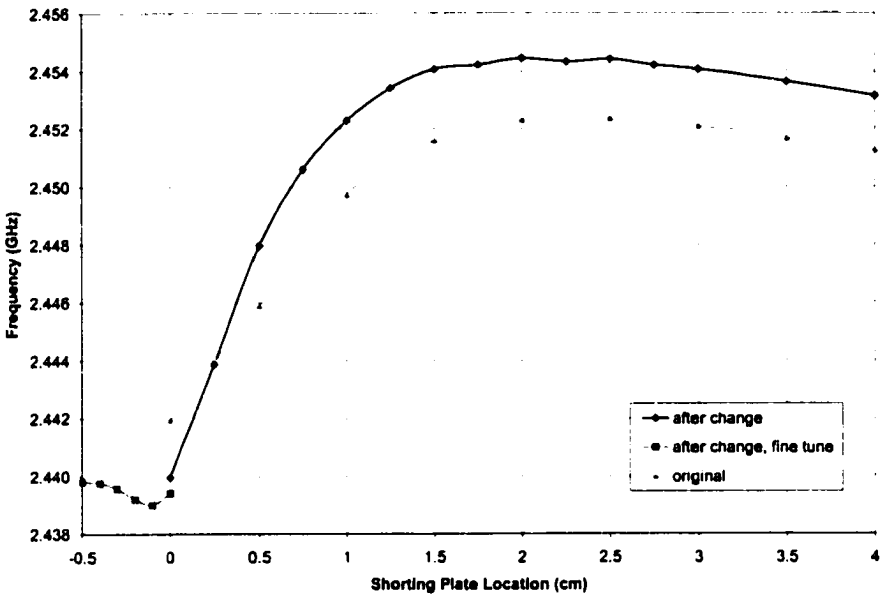

Figure A.4.8-9. Modified Frequency versus Shorting Plate Location.

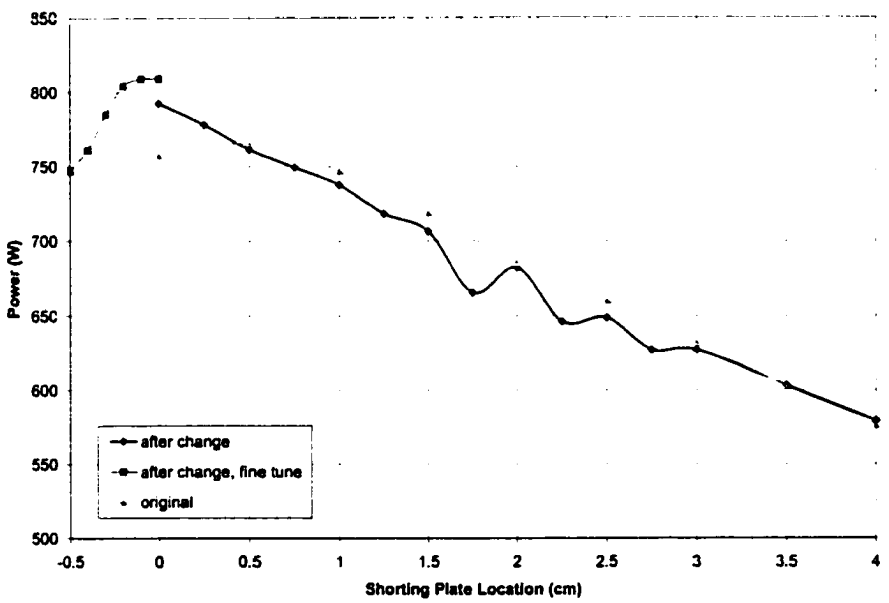

Figure A.4.8-10. Modified Output Power versus Shorting Plate Location.

The new configuration provides higher power output in the range of interest. However, it appears less stable between 1.5 to 3.0 cm.

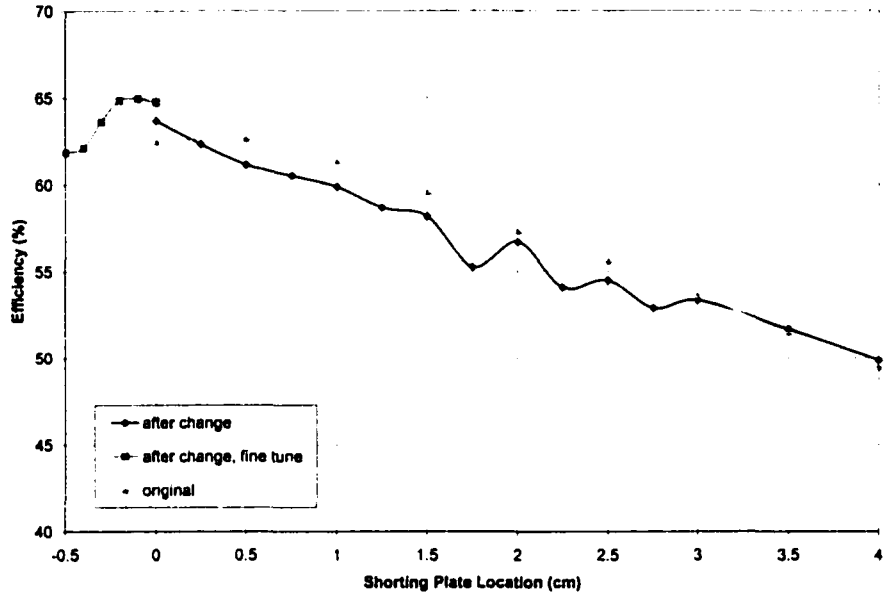

Figure A.4.8-11. Modified Efficiency versus Shorting Plate Location.

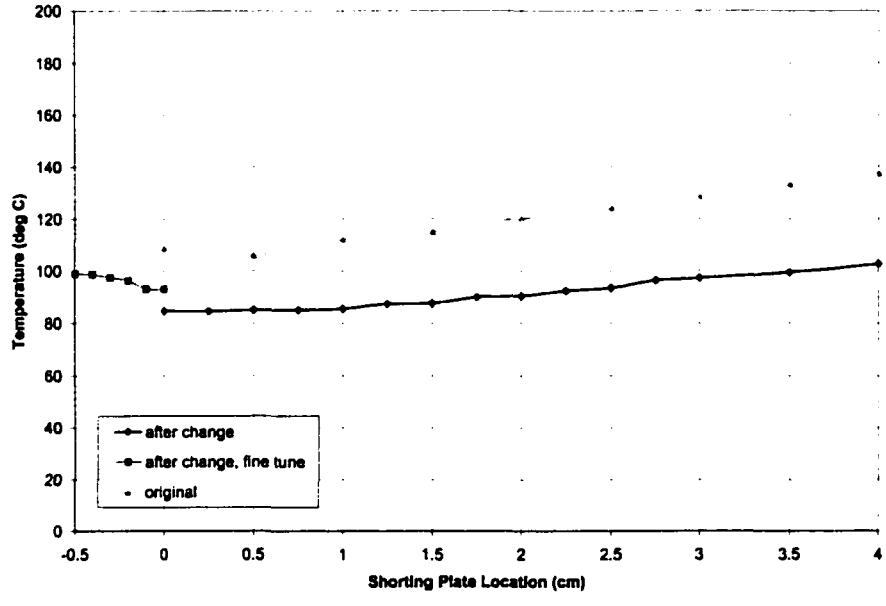

Figure A.4.8-12. Modified Magnetron Case Temperature versus Shorting Plate Location.

Efficiency appears to be only slightly improved, and only near the range of interest. Temperature shows a substantial improvement between the two configurations. This may be explained by the different heat sinking provided by the mounting schemes.

The above data sets provide some insight in placing the shorting plate. It is clear that the range of plate locations from –0.5 to 1.5 cm is a sink region for the magnetron. As was the case for the tuning slug, the peak efficiency is obtained for the lowest value of frequency (for this particular magnetron). The backside of the curve corresponds to the low efficiency range of a tuning slug. However, in this case, there is a *very* low efficiency point of operation.

For high efficiency operation, the plate should be placed near 0.0 cm, the original location. A slight advantage *might* be possible by cheating to the inside. However, the frequency in this range is low and may stress the magnetron. Backing the plate off 0.5 cm to the right would increase the frequency by 8 MHz, while only costing 2% in efficiency.

Finally, the combined effects of the shorting plate and the tuning slug may be examined. From earlier data sets, it was determined that the characteristics of the tuning slug also repeated every ½ guide wavelength. The entire range of effects may be viewed within the shorting plate range of –0.5 to 0.0 cm.

The frequency response caused by the shorting plate (the sink portion) is shown in Figure A.4.8-13. This region is located between – 0.5 to 2.0 cm, which correlates to a distance of 1.25 to 3.75 cm from the center of the RF probe to the face of the plate. Note that within this distance of 2.5 cm, the tuning slug shifts its sink region by ~6.0 cm. Between these points, the frequency pulling ability of the MDA oscillates from a low value (~12 MHz at –0.5 cm) to a high value (~25 MHz at 0.25 cm) and back to the lower value again (~9.5 MHz at 2.0 cm).

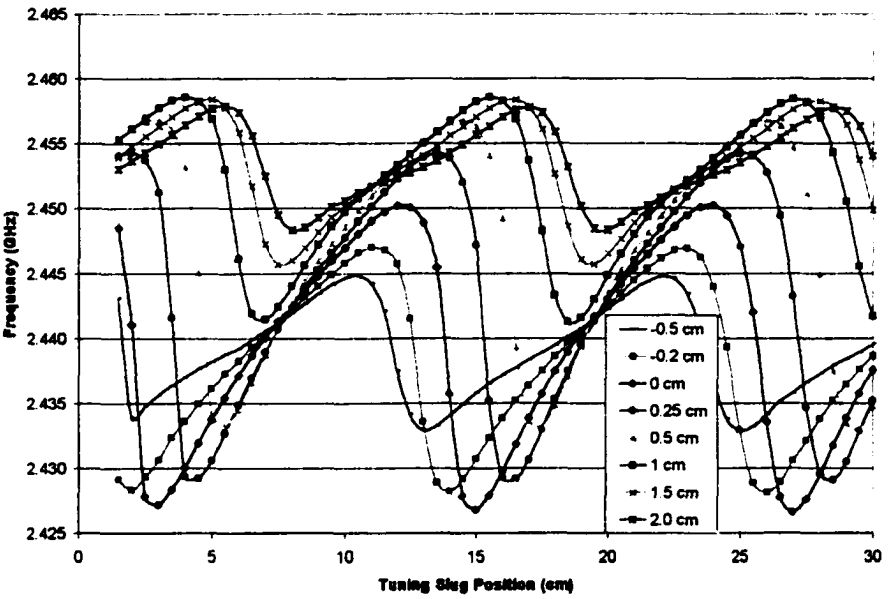

Figure A.4.8-13. Frequency Response for Class III MDA to Shorting Plate Location. Plate location shown by data in legend.

It is postulated that this effect is due to the relative shapes of the two frequency responses as shown below.

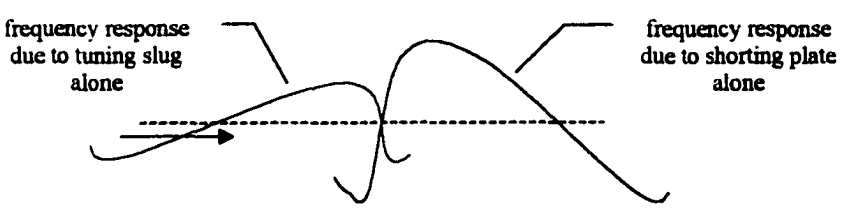

Figure A.4.8-14. Conceptual Diagram of Frequency Waveform Components.

This diagram is meant as a simplistic explanation for the shifting frequency patterns in the figure above. Each waveform has its own sink region associated with it. Generally, the shorting plate fixes the baseline frequency response according to its position. As the tuning slug is moved in relation to the shorting plate and the magnetron, the waveforms add constructively in some positions and destructively in others. Peak performance is

reached when of the two sink regions are aligned. This defines the maximum frequency tuning ability of the MDA.

The frequency pulling capability of the tuning slug at each shorting plate location may be plotted as follows.

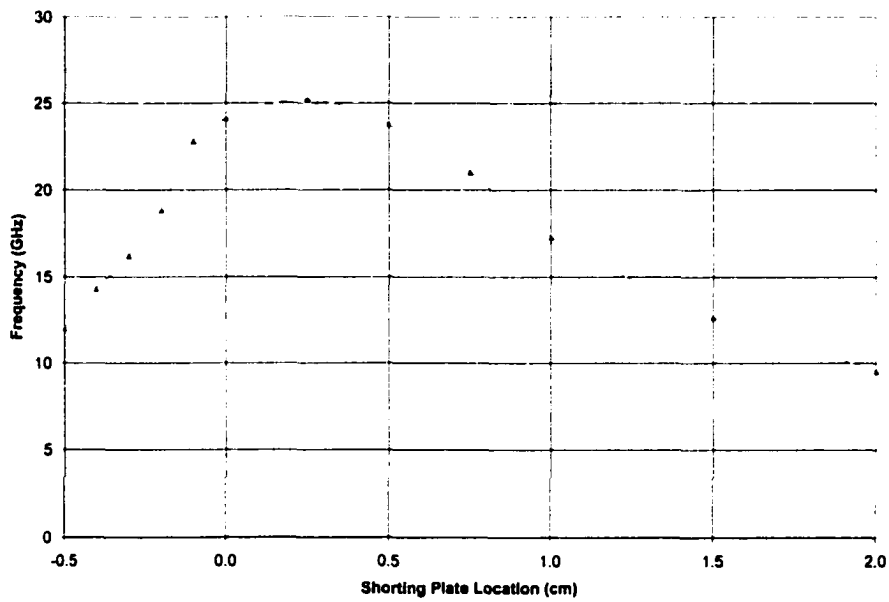

Figure A.4.8-15. Locking Bandwidth Possible for a Class III MDA versus Shorting Plate Location.

From the earlier analysis of the Class III MDA, there was found to be a correlation between the point of maximum locking bandwidth and the sink region for the magnetron. From the figure above, the sink would appear to be located with the shorting plate at 0.25 cm. From a power transmission standpoint, the sink is located at ~0.2 cm (see Figures A.4.8-11 and A.4.8-15).

The efficiency of the Class III MDA for different shorting plate locations is shown in Figure A.4.8-16. This figure shows that the maximum efficiency is obtained with the shorting plate located at – 0.2 cm. This yields a discrepancy of ~0.5 cm between the

points of highest efficiency and locking bandwidth. This is merely a function of this particular magnetron, as was seen in Section 5.2.1 and Appendix A.4.4. Note the formation of the resonant peaks as the plate approaches 0.0 cm. This phenomenon is not visible outside a band of ~2.0 cm, emphasizing the sharpness of the sink region.

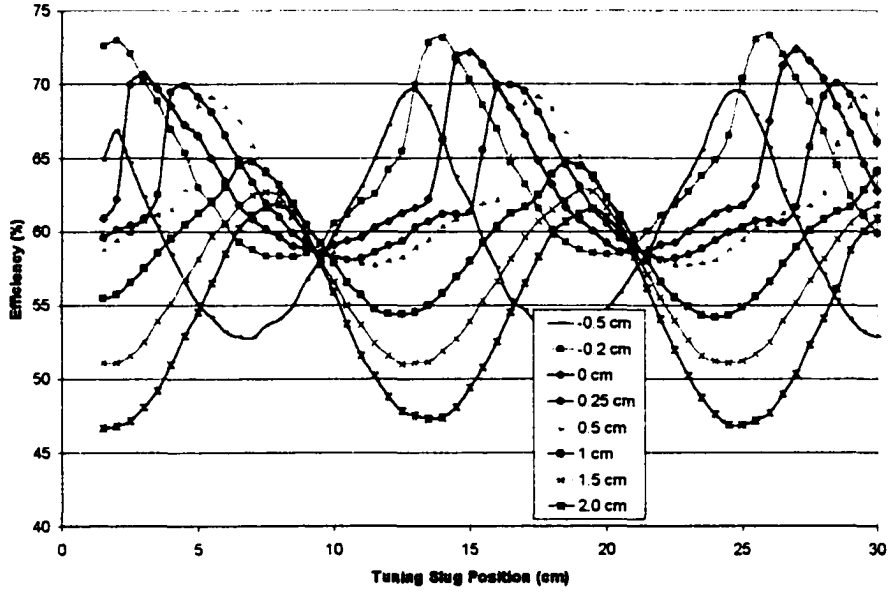

Figure A.4.8-16. Output Power Response for Class III MDA to Shorting Plate Location.

The magnetron case temperature measurements generally supported the others, as shown in Figure A.4.8-17. Since the absolute temperatures are dependent upon the thermal environment, they may vary between data sets. In this case, some offset is present between the two supersets of data (-0.5 cm to 0 cm and 0 cm to 2 cm) taken on different days. The temperature differences more accurately reflect the load characteristics over the data set. These show smaller variations in the magnetron temperature for operation near the center of the sink region.

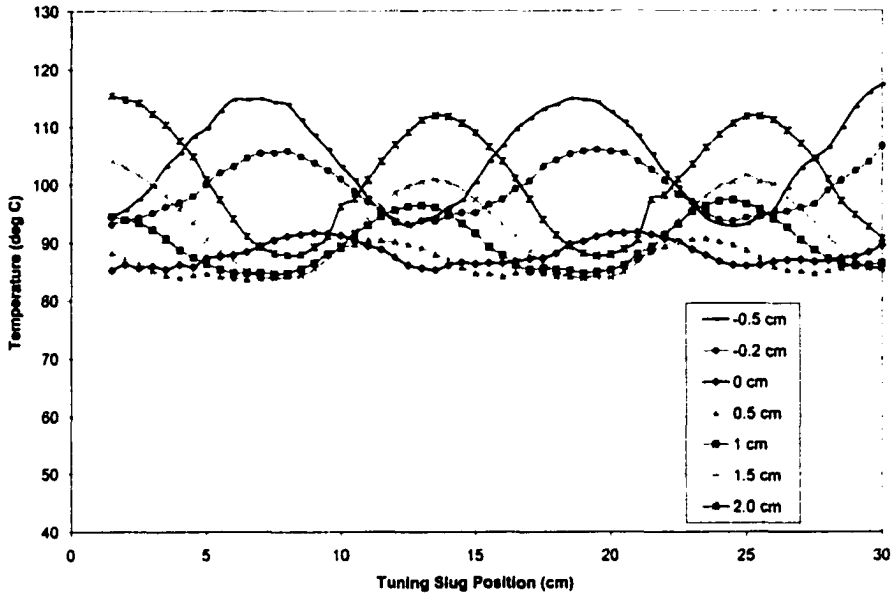

Figure A.4.8-17. Magnetron Case Temperature for a Class III MDA versus Shorting Plate Location.

The power versus frequency curves for the MDA give a good graphical estimate of where the sink is located. The curves near the sink region for the shorting plate are shown in Figure A.4.8-18. The flatter extended waveforms are characteristic of the MDA operating in the sink region, such as the curves depicting 0 and 0.5 cm. The flatness of the curve is a relative measure of the resistance offered to the RF circuit at different slug locations. Ideally, the curves would be a straight horizontal line, so that power would not vary with frequency. As the shorting plate moves out of the sink region, the tuning slug paths become rounder. This curve is the rectangular equivalent for the Rieke diagram. The quickness with which the envelopes are transformed from resistive to primarily reactive and back is a measure of the magnetron's sensitivity to the sink presented by the plate.

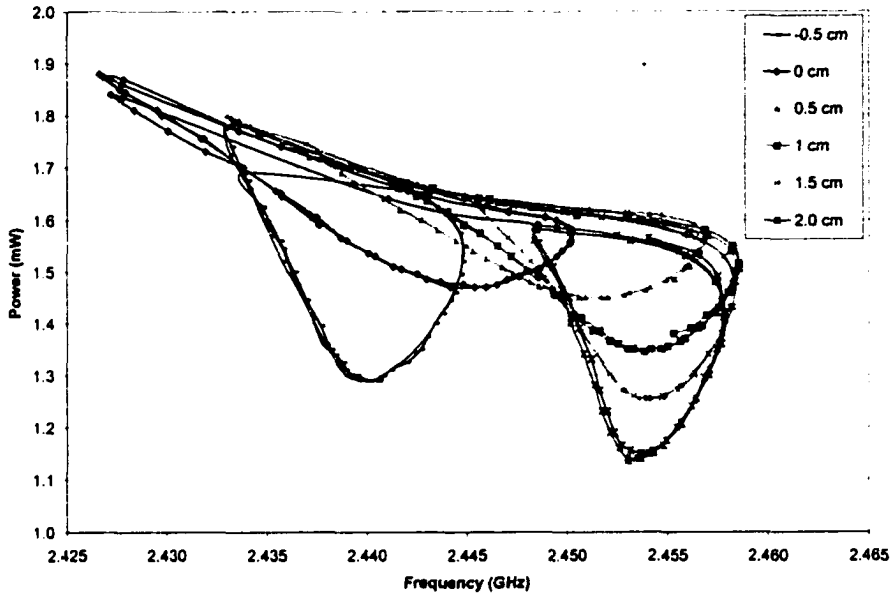

Figure A.4.8-18. Output Power versus Frequency Curves for a Class III MDA due to Shorting Plate Location.

A.4.8.3.3 Impedance Measurements

In earlier measurements of the load impedance, a coax-to-waveguide adapter was used (Figure 4.3-7). However, this method cannot account for the changes in the shorting plate location. Instead, a test probe emulating the magnetron RF probe was fabricated. This was constructed by cannibalizing one of the Samsung magnetrons. The probe attaches to the waveguide at the magnetron mounting plate in the same fashion as the magnetron. Details of the probe are provided in Appendix A.4.1.

The combined load impedance data was then plotted on the Smith Chart. To show the difference seen in the measurements using this homemade probe versus the previous coax/waveguide adapter method, the plots for two slugs are given for each method.

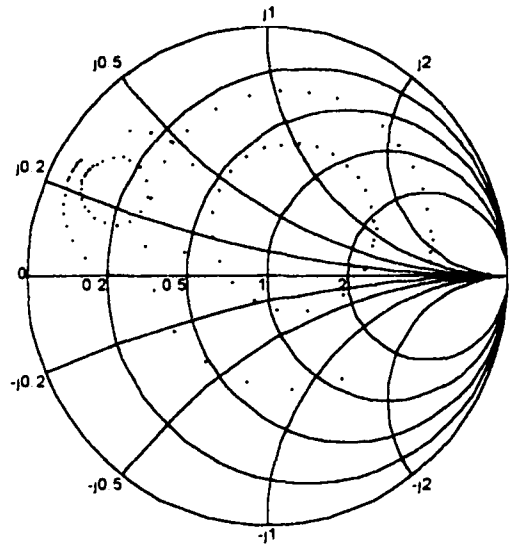

Figure A.4.8-19. Comparison of MDA Impedance Traces for Two Different Probes. Blue circles taken by previous coax/waveguide adapter; red circles resulting from new magnetron type probe. Both sets show data for slugs 2 (inner) and 3 (outer).

As can be seen, the two probes yield quite different patterns. The coax-to-waveguide adapter couples more of the RF energy, and therefore provides larger patterns. The homemade probe couples relatively little energy in comparison. The coax-to-waveguide adapter also shows the sink region being located toward the bottom right of the graph, whereas the homemade probe shows this in the upper left portion of the circles.

For precise measurements, it is necessary to utilize a probe with the same antenna shape as the magnetron being tested. The probe must also be tuned and calibrated according to specifications. However, much may still be learned by studying the relative influences of the shorting plate and tuning slug. This may be accomplished with data from a simple probe such as was shown in Figure A.4.8-19.

The combined effects of the shorting plate and tuning slug are shown below.

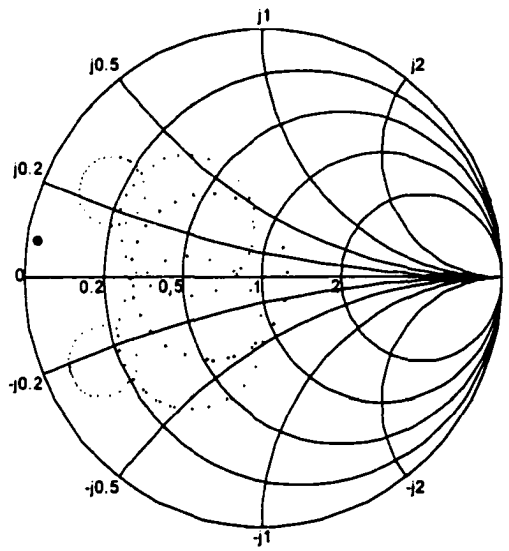

Figure A.4.8-20. Effect of Shorting Plate and Slug on a Class III MDA. View of impedance circles for slug 2 from magnetron probe. Shorting plate was changed in 2.0 cm increments. Beginning with upper left circle (0.0 cm), circles move clockwise around the plot. Curves were plotted for a constant frequency of 2.45 GHz, and will therefore vary from the actual performance of the magnetron.

Note the changing effect of the tuning slug versus that of the shorting plate for different plate locations. The slug causes a relatively large change in impedance with the plate located at 4.0 cm (large circle centered on real axis), but has almost no effect at 10.0 cm (small black circle). The large circle represents operation in a de-tuned region, with lower power efficiency. The black circle predicts MDA operation where almost all power is reflected back at the magnetron. All previous sets of data have been taken at plate location 0.0 cm, as this point has yielded the most efficient (no slug) operation. This then infers the location of the sink to be near the upper left circle.

However, to understand the effect of the impedance on the MDA performance, it is necessary to take numerous data points and then overlay the MDA contours of constant

power and frequency. This would create a Rieke diagram for the MDA, similar to the one shown in Appendix A.4.1. This was not accomplished for this effort, however, some performance inferences may be drawn simply by visualizing the placement of the sink region. The sink is located to the upper left of the diagram, in the vicinity of the 0 cm circle. From this point the lines of constant frequency radiate outward and the lines of constant power cross these perpendicularly. Therefore, a relatively small impedance change in the sink region may cause more change in the MDA performance than a larger circle placed elsewhere.

Note that areas corresponding to large impedance changes may drastically affect the magnetron performance when near the sink region. The constant step size of 2.0 cm in Figure A.4.8-19 results in a much large rotational change when near the sink region (note the relative change from 8 to 10 cm, vice that of 2 to 4 cm). Examining this motion provides insight into the sensitivity of the MDA at different load locations.

Finally, to accurately plot the location of the impedance points, it is necessary to account for the value of frequency corresponding to slug location. This is used to index a lookup table, which provides the exact value of impedance. The spacing of these points shows the location of the magnetron sink region. Figure A.4.8-21 compares the spacing of points for the actual MDA operation versus a simplified constant-frequency case.

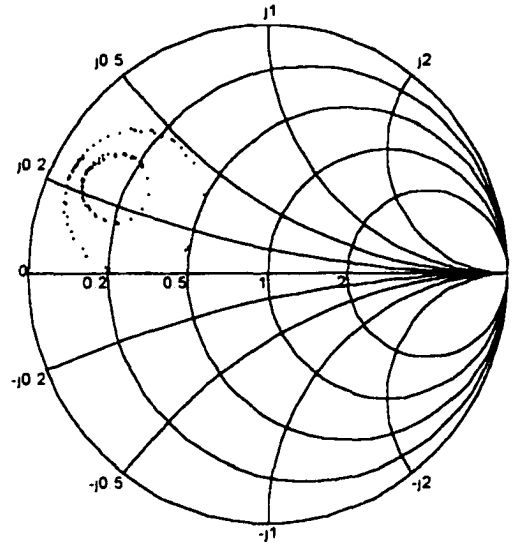

Figure A.4.8-21. Comparison of Constant Frequency Impedance Points versus Actual Frequency Points. Red points depict constant frequency; blue represent actual points.

The performance data from this section indicates that a small range of shorting plate locations will provide optimum MDA performance. The plate may be adjusted slightly within this range to satisfy system requirements for operating frequency, output power, and tuning bandwidth. The exact location chosen will also depend upon the characteristics of the particular hardware used for the MDA.